Inaugural dissertation

for

obtaining the doctoral degree

of the

Combined Faculty of Mathematics, Engineering and Natural Sciences

of the

Ruprecht - Karls – University

Heidelberg

Presented by

M.Sc. Luisa Maria Mateus Abreu

born in: Viseu, Portugal

Oral examination: 23/10/2024

Unraveling metabolic responses

of $CD4^+$ T cells with single-cell metabolomics

Referees: Prof. Dr. Ana Martin-Villalba
Dr. Michael Zimmermann

"Nothing is too wonderful to be true, if it be consistent with the laws of nature, and in such things as these, experiment is the best test of such consistency."

Michael Faraday

ACKNOWLEDGMENTS

I want to start by thanking my supervisor, Theodore Alexandrov, for giving me the opportunity to work on such an exciting project in such a good environment as EMBL. This was a challenging road with many obstacles, but it also gave me the scientific confidence and independence I was missing before starting my PhD journey.

Secondly, I want to thank my parents for always being present despite being far away and for supporting me. I would not have been writing my dissertation today without their early efforts. I also want to thank my brother for supporting me in his unique way.

The podium would not have been completed without thanking my boyfriend, Alex. He was my main support during my PhD journey and always reminded me to take care and breathe. He also made me forget about the work and challenges whenever we were together, and I am very grateful for that. His extra dedication during the writing period of this dissertation was essential, and I will never forget it.

I also want to thank all the past and present members of the Alexandrov team for being such great colleagues and always ready to help. More specifically, I would like to thank Shahraz for welcoming me and always answering all kinds of questions. I want to thank Bishoy for all the nice conversations and for always being supportive. I also thank Sharath for the nice late lunches with random facts and unexpected tangents. I want to thank Nastia for understanding me and for all the good times running experiments.

Finally, I want to thank the rest of my family for always being so enthusiastic about everything. And also every other person who has been around throughout these 5 years and made life outside the lab a little easier.

ABSTRACT

The field of immunometabolism, which explores how metabolism regulates the function of immune cells, has emerged over the past decade. The available metabolomic methods require a large amount of biological material and only provide bulk measurements that miss details like cell heterogeneity or rare populations. The recent advances in the single-cell omics field aim to provide a response to these drawbacks. HT-SpaceM is a high-throughput single-cell metabolomics method that combines light microscopy with MALDI-Imaging Mass Spectrometry. This dissertation aims to characterize the metabolic requirements of human primary $CD4^+$ T cells *in vitro* with HT-SpaceM. $CD4^+$ T cells are a heterogeneous population that plays a key role in regulating and coordinating the adaptive immune response. The activation of these cells, which is triggered by antigen presentation, is the starting point for proper immune function and is heavily supported by a metabolic shift. Naïve $CD4^+$ T cells exhibit a quiescent oxidative metabolic profile that, upon activation, is remodeled in favor of glycolysis to support proliferation and differentiation. The metabolic profiles of $CD4^+$ T cells after activation and modulation with several compounds were measured at the single-cell level with HT-SpaceM. The detection of unique metabolites in cells modulated with different drugs helped unravel the mechanism of action of these compounds. Activated $CD4^+$ T cells exhibited higher levels of asparagine, proline, and glutaminolysis metabolites than the naïve state. The high intensities of orotic acid and L-dihydroorotic acid in cells treated with antimycin A revealed a potential effect of this complex III inhibitor on the pyrimidine *de novo* biosynthesis. The increased detection of phosphoribosyl pyrophosphate and ribose 5-phosphate in cells treated with the anti-inflammatory drug methotrexate resulted from the impairment of the purine *de novo* biosynthesis caused by this drug. The metabolic modulation of activated $CD4^+$ T cells also enabled the generation of a single-cell atlas of metabolic states that covered key metabolic pathways such as glycolysis and respiration. The projection of activated cells treated with Janus kinase inhibitors on the atlas revealed that these drugs have a heterogeneous effect and affect the purine synthesis pathway. The results of this thesis help advance the fields of single-cell metabolomics and immunometabolism by describing a method for characterizing the metabolic states of $CD4^+$ T cells at the single-cell level and providing insights regarding the metabolic mode of action of different inhibitors.

ZUSAMMENFASSUNG

Der Bereich des Immunometabolismus, der untersucht, wie der Stoffwechsel die Funktion von Immunzellen reguliert, hat sich im letzten Jahrzehnt entwickelt. Verfügbare metabolomische Methoden erfordern eine große Menge an biologischem Material und liefern nur Bulkmessungen, denen Details wie die Heterogenität von Zellen oder seltene Populationen entgehen. Die jüngsten Fortschritte im Bereich der Einzelzell-Omik zielen darauf ab, diese Nachteile zu überwinden. HT-SpaceM ist eine Hochdurchsatz-Metabolomikmethode für Einzelzellen, die Lichtmikroskopie mit MALDI-Imaging-Massenspektrometrie kombiniert. Ziel dieser Dissertation ist es, die metabolischen Anforderungen von menschlichen primären CD4+ T-Zellen in vitro mit HT-SpaceM zu charakterisieren. CD4+ T-Zellen sind eine heterogene Population, die eine Schlüsselrolle bei der Regulierung und Koordinierung der adaptiven Immunantwort spielt. Die Aktivierung dieser Zellen, die durch Antigenpräsentation ausgelöst wird, ist der Ausgangspunkt für eine geeignete Immunfunktion und wird durch eine Stoffwechselumstellung stark unterstützt. Naive CD4+ T-Zellen weisen ein ruhiges oxidatives Stoffwechselprofil auf, das bei der Aktivierung zugunsten der Glykolyse umgestellt wird, um die Vermehrung und Differenzierung zu unterstützen. Die Stoffwechselprofile von CD4+ T-Zellen nach Aktivierung und Modulation mit verschiedenen Substanzen wurden mit HT-SpaceM auf Einzelzell Ebene gemessen. Der Nachweis einzigartiger Metabolite in Zellen, die mit verschiedenen Wirkstoffen moduliert wurden, trug dazu bei, den Wirkmechanismus dieser Verbindungen zu entschlüsseln. Aktivierte CD4+ T-Zellen wiesen im Vergleich zum naiven Zustand höhere Konzentrationen von Asparagin-, Prolin- und Glutaminolyse-Metaboliten auf. Die hohen Konzentrationen von Orotsäure und L-Dihydroorotsäure in Zellen, die mit Antimycin A behandelt wurden, zeigten eine mögliche Wirkung dieses Komplex-III-Inhibitors auf die Pyrimidin-De-novo-Biosynthese. Der erhöhte Nachweis von Phosphoribosylpyrophosphat und Ribose-5-Phosphat in Zellen, die mit dem entzündungshemmenden Medikament Methotrexat behandelt wurden, ist auf die durch dieses Medikament verursachte Beeinträchtigung der Purin-De-novo-Biosynthese zurückzuführen. Die metabolische Modulation aktivierter CD4+ T-Zellen ermöglichte auch die Erstellung eines Einzelzell-Atlas der Stoffwechselzustände, wichtiger Stoffwechselwege wie Glykolyse und Atmung abdeckt. Eine Projektion von aktivierten Zellen, die mit Januskinase-Inhibitoren behandelt wurden, auf dem Atlas zeigte, dass diese Medikamente eine heterogene Wirkung haben und den Purinsyntheseweg beeinflussen. Die Ergebnisse dieser Arbeit tragen dazu bei, die Bereiche Einzelzell-Metabolomik und Immunometabolismus voranzubringen, indem sie eine Methode zur Charakterisierung des Stoffwechselzustands von CD4+ T-Zellen auf Einzelzellebene beschreiben und Erkenntnisse über die metabolische Wirkungsweise verschiedener Inhibitoren liefern.

TABLE OF CONTENTS

LIST OF ABBREVIATIONS AND ACRONYMS

2-DG	2-Deoxy-D-glucose
2-DG6P	2-Deoxy-D-Glucose-6-Phosphate
9AA	9-Aminoacridine
ADP	Adenosine Diphosphate
AMP	Adenosine Monophosphate
AMPK	5' AMP-Activated Protein Kinase
ATP	Adenosine Triphosphate
AZ67	AZ-PFKFB3-67
BBKNN	Batch Balanced K Nearest Neighbors
cAMP	Cyclic AMP
CTV	CellTrace Violet
DAN	1,5-Diaminonaphthalene
DMSO	Dimethyl Sulfoxide
ESI	Electrospray Ionization
ETC	Electron Transport Chain
FAO	Fatty Acid Oxidation
FAS	Fatty Acid Synthesis
FBP	Fructose 1,6-Biphosphate
FCCP	Carbonyl Cyanide-p-trifluoromethoxyphenylhydrazone
FDR	False Discovery Rate
FSC	Forward Scatter
G6P	Glucose 6-Phosphate
GABA	Gamma-Aminobutyric Acid
GLUT1	Glucose transporter 1
HPLM	Human Plasma-Like Medium

IMP	Inosine Monophosphate
LC-MS/MS	Liquid Chromatography-Tandem Mass Spectrometry
LN2	Liquid Nitrogen
MALDI	Matrix-Assisted Laser Desorption Ionization
MS	Mass Spectrometry
MSI	Mass Spectrometry Imaging
mTOR	Mammalian Target of Rapamycin
MTX	Methotrexate
NADH	Nicotinamide Adenine Dinucleotide
NEDC	N-(1-naphthyl) Ethylenediamine Dihydrochloride
OXPHOS	Oxidative Phosphorylation
PBMCs	Peripheral Mononuclear Cells
PCA	Principal Component Analysis
PDL	Poly-D-Lysine
PFA	Paraformaldehyde
PLL	Poly-L-Lysine
PPP	Pentose Phosphate Pathway
PRPP	Phosphoribosyl Pyrophosphate
P/S	Penicillin-Streptomycin
RT	Room Temperature
SSC	Side Scatter
SIMS	Secondary Ion Mass Spectrometry
UMAP	Uniform Manifold Approximation and Projection

1 INTRODUCTION

1.1. Immune System: an overview

The immune system protects the body against pathogens and tumors while maintaining tissue homeostasis. This protection is mediated by a complex network of cells that develop in the bone marrow from hematopoietic stem cells. These progenitors differentiate into two lineages: myeloid and lymphoid. The myeloid lineage differentiates into monocytes, neutrophils, eosinophils, basophils, and mast cells, while Natural killer cells, B lymphocytes, and T lymphocytes develop from a common lymphoid progenitor. The immune response is orchestrated in distinct phases by the two main arms of the immune system: innate and adaptive. The myeloid lineage and the Natural Killer cells mediate the innate response, while T and B lymphocytes are responsible for adaptive immunity [1].

The innate immune system is the first line of defense against pathogens, providing a fast response to infection. The innate immune cells express receptors that recognize conserved molecular patterns present in pathogens. This interaction triggers the innate response and can result in phagocytosis of the pathogens. The innate system takes only minutes or hours to act upon infection. However, the provided response is unspecific and insufficient to stop most pathogens [2]. On the other side of immunity, T and B lymphocytes express pathogen-specific receptors as a result of somatic gene recombination during early development. Lymphocytes have to undergo a very long and strict process of selection that culminates with the maturation into naïve cells. [3] The differentiation process is only complete when these inactivated cells encounter a pathogen presented by cells from the innate immune system. This interaction provides the co-stimulatory signals required for activation and differentiation into effector cells that can efficiently target the pathogen by producing cytokines and antibodies. When the immune response ceases, most lymphocytes will undergo apoptosis. However, a small subset will differentiate into memory cells [4]. The time required by the adaptive immune system to develop a response to a primary challenge is 10 to 14 days. In case of reinfection, the response time is faster due to the presence of memory cells, taking only 3 to 4 days to develop [5]. The adaptive immune system exhibits higher specificity than the innate side. However, it also takes much longer to orchestrate a response that depends on signals provided by the innate system. Thus, immunity is a complex process that requires a balanced response of its two arms.

1.2. $CD4^+$ T cells: the orchestrators of immunity

T and B lymphocytes, or T and B cells, are the key perpetrators of the adaptive immune response, although with different roles. B cells can differentiate into plasma cells and produce antibodies, while T cells orchestrate and execute the immune response by producing cytokines [6]. The development of T cells starts in the bone marrow, where hematopoietic stem cells differentiate into thymocytes. The maturation of thymocytes to naïve T cells is a tightly regulated process that takes place in the thymus. During this differentiation process, self-reactive thymocytes are deleted, and the selected cells differentiate into two subsets with distinct roles: $CD4^+$ T cells and $CD8^+$ T cells [7]. The main function of $CD4^+$ T cells or helper T cells is to regulate and coordinate the immune response by producing cytokines and chemokines that will recruit and activate other immune cells. On the other hand, $CD8^+$ T cells or cytotoxic T cells target and kill pathogens and infected cells [8].

The development of a naïve $CD4^+$ T cell is only completed after the encounter with their cognate antigen. This process, also known as activation, will trigger the differentiation into different subsets of effector cells with distinct functions [9]. The effector subsets of $CD4^+$ T cells can be divided into two lineages: conventional T helper cells (Th) cells and regulatory T cells (Tregs). The Th cells can be subdivided into four main subsets: Th1, Th2, Th17, and T follicular T helper (Tfh). Each subset orchestrates a different type of immune response. The Th1 subset coordinates the immune response against intracellular pathogens (e.g., viruses, bacteria), while the Th2 subset mediates the response to large extracellular pathogens (e.g., helminths). Th17 cells also coordinate the immune response against extracellular pathogens (e.g., bacteria and viruses). Finally, the Tfh subset has the distinct role of helping B cells produce antibodies [10]. On the other hand, Tregs maintain immune homeostasis by promoting immunosuppression while preventing autoimmunity and chronic inflammation [11]. Autoimmune diseases develop when tolerance to self-antigens is lost, which results in immune responses that target healthy tissues and cause progressive damage. Conventional Th cells have been extensively linked to developing and maintaining autoimmune diseases due to their role in orchestrating the immune response [12]. Conversely, the number and function of Tregs are impaired in many autoimmune diseases [13]. Although there is strong evidence of the role of $CD4^+$ T cells in promoting autoimmunity, the mechanisms driving loss of tolerance and disease remain to be unraveled.

1.3. Metabolism: the key to proper immune function

The term immunometabolism can be defined as the set of metabolic processes that regulate the immune function [14]. The increased interest in understanding this intersection between metabolism and immunity and how it can be applied in disease treatment (e.g., cancer, autoimmunity) resulted in the emergence of the Immunometabolism field over a decade ago [15], [16]. However, the pioneering studies that aimed to characterize the metabolic requirements of lymphocytes were carried out more than 40 years ago. These early studies concluded that lymphocytes depend on glycolysis, OXPHOS, and lipid synthesis for proper proliferation [17], [18]. This preceded the identification of the CD4 and the CD8 molecules and the subsequent identification of the naïve and memory subsets [9]. Although these findings apply to the bulk lymphocyte population in the human peripheral blood, the main conclusions are still valid today.

The current model accepted in the immunometabolism field indicates that naïve cells are metabolically inert and must engage in a remodeling program to respond to activation. The observed metabolic burst ceases when the immune response stops, with remaining memory cells exhibiting a quiescent profile [19]. This metabolic pattern can also be observed during thymocyte's tightly regulated maturation into naïve T cells. In the thymus, the thymocytes oscillate between a quiescent and an active metabolic state. The quiescent progenitors rely on oxidative phosphorylation (OXPHOS), and the transition to a glycolytic profile is required to support proliferation but not differentiation. The naïve T cells exhibit a quiescent metabolic profile similar to their progenitors, requiring low levels of anabolic precursors and energy to survive [20]. Naïve cells rely on OXPHOS fueled by the breakdown of fatty acids and pyruvate oxidation in the tricarboxylic acid (TCA) cycle [21]. This strategy is thought to promote long-term survival without compromising the readiness of these cells [22].

Upon activation, the quiescent naïve cells quickly switch to a metabolic profile where aerobic glycolysis is predominant. Although this process might seem less advantageous regarding the final energetic yield, glycolysis is 100 times faster than OXPHOS. Thus, the preference for glycolysis can be a more efficient strategy, provided glucose is available. Besides generating energy, glycolysis also provides building blocks to fuel other key metabolic pathways (i.e., nucleotide, fatty acid, and amino acid synthesis) [23]. Fatty acid oxidation (FAO), predominant in naïve cells, is replaced upon activation by fatty acid

synthesis (FAS), which provides building blocks for membrane lipid synthesis during proliferation [24]. The uptake of glutamine is also rapidly increased upon stimulation, and its consumption through glutaminolysis provides metabolic intermediates required for protein, nucleotide, and fatty acid synthesis [25], [26]. Thus, the metabolic remodeling observed upon activation results from the increased demand for energy and biosynthetic precursors, which are required to support cellular proliferation, differentiation, and effector function [27].

The activated T cells that survive the shutdown of the immune response differentiate into long-lived memory cells ready to respond upon reinfection [24]. Memory cells switch back to a metabolic profile where FAO is predominant. This is essential for the proper development and survival of memory cells [28]. The different metabolic profiles between the two $CD4^+$ T cell lineages are one fine example of how metabolism is linked to immune function. FAO is responsible for promoting the immunosuppressive function of Tregs. Meanwhile, the conventional Th cell subsets (particularly Th1, Th2, and Th17) heavily rely on glycolysis and require high amounts of glucose and glutamine to exert their functions [29].

Recent studies have challenged the established and accepted concepts in the immunometabolism field. Activated $CD4^+$ and $CD8^+$ T cells were reported to have distinct metabolic profiles. $CD4^+$ T cells exhibited enhanced mitochondrial activity compared to $CD8^+$ T cells. The increased glycolytic profile of $CD8^+$ T cells allowed them to grow and proliferate faster than $CD4^+$ cells [30]. The different subsets of memory $CD8^+$ T cells have also been reported to use distinct metabolic strategies. Tissue-resident and central memory $CD8^+$ T cells rely on FAO, while effector memory cells are more metabolically active and use glycolysis and OXPHOS. It remains to be elucidated if this is also true for memory $CD4^+$ T cells [31].

The metabolism of T cells is also being investigated in the context of disease, especially in conditions where T cell function is dysregulated, like autoimmunity. $CD4^+$ T cells from patients with Rheumatoid Arthritis have been reported to fail to engage in glycolysis upon activation. The consumption of glucose is done through the pentose phosphate pathway (PPP) instead. The mitochondrial activity of these cells is also reported to be low. On the other hand, $CD4^+$ T cells from patients with Systemic Lupus Erythematosus (SLE) exhibit high mitochondrial mass and activity, consequently resulting

in higher oxidative stress. Nevertheless, glycolysis is still the preferred pathway and the main driver of effector function in SLE $CD4^+$ T cells [32]. On the opposite side of the disease spectrum are the effector T cells that target cancer cells. Competition for nutrient uptake is often observed in the tumor microenvironment. The metabolic deprivation that T cells suffer significantly impacts their function, which results in tumor survival [33]. A more comprehensive understanding of immunometabolism could be essential for developing new therapies in conditions like autoimmunity, where the immune function is dysregulated, or cancer, where the immune function is suppressed. The field of immunometabolism has been speedily growing, with the reported studies helping unravel the metabolic configurations that regulate immune cell function. However, many questions remain to be explored, particularly in the context of disease and therapy.

1.4. Capturing the metabolism of immune cells: current technologies

The dynamism and complexity of cellular metabolism have posed significant challenges when studying this field. However, the continuous technological advancements have facilitated the understanding of metabolic processes. One remarkable example of this progress is the (re-) emergence of the immunometabolism field. The current techniques in this field cover a wide range of cellular processes linked to metabolism, from metabolite uptake measurements to transcriptomics [34]. The standard and commonly used technology in the immunometabolism field is the Seahorse extracellular flux analyzer. This assay is used to assess the activity of glycolysis and OXPHOS in live cells by measuring the extracellular acidification rate and oxygen consumption rate, respectively. The cell population is treated with metabolic inhibitors of these two pathways, with the outcome providing insights into the metabolic state (i.e., glycolytic or oxidative) [35]. However, the ability to detect only glycolysis and OXPHOS is one of the main limitations of this technology [36].

The intracellular metabolic measurements are typically carried out using nuclear magnetic resonance (NMR) or mass spectrometry (MS). The latter is more commonly preferred due to its higher resolution and sensitivity, especially when combined with liquid or gas chromatography. Liquid chromatography with tandem mass spectrometry (LC-MS/MS) provides steady-state measurements of the intracellular metabolites. Untargeted LC-MS/MS provides a readout of hundreds of metabolites, which is essential for

exploratory studies. Meanwhile, the targeted mode quantifies a pre-set group of metabolites with high sensitivity [37]. However, metabolite levels do not necessarily correlate with the pathway's activity, so analyzing steady-steady measurements can be challenging. This limitation can be overcome by combining stable isotope tracing with targeted MS. This technique provides information on metabolic fluxes and pathway activity. However, the cost and high level of specialization prevent it from being a suitable alternative for many researchers [38].

The Seahorse assay and LC-MS/MS provide a reliable and established readout of the metabolic profiles of immune cells. However, these techniques also have some significant limitations. First, both require a large amount of sample material or cell number, which can be challenging to obtain when working with patient samples or rare populations. Second, the bulk measurements miss details like cell heterogeneity hidden behind the population averages. This is perhaps the most limiting factor of these two techniques since the immune response is complex and might be oversimplified with the exclusive use of bulk techniques [39]. This limitation can be overcome with single-cell techniques such as flow cytometry or transcriptomics, which can provide information on population heterogeneity.

Flow cytometry is the single-cell technique more widely used to characterize immune cell populations. This technique uses antibodies conjugated with fluorophores to identify markers that differ among the various immune cell types. Additionally, it can also be used to detect metabolic enzymes and other metabolic-related parameters, such as glucose uptake and lipid levels [37]. The low cost and easy access to the technology are some of the main advantages flow cytometry offers. On the other hand, the limited number of detected markers that need to be pre-selected are some of the main disadvantages of this technique [39]. Thus, flow cytometry is a great complementary validation technique but not suitable for profound metabolic studies. Flow cytometry is the foundation for other multiplexed techniques like mass cytometry, also known as CyTOF (cytometry by time-of-flight). This single-cell technique uses mass spectrometry to detect antibodies conjugated to metal isotopes and can detect up to 40 proteins [37]. Although mass cytometry offers higher coverage and throughput than traditional flow cytometry, it is more costly and less widely available [39].

The field of single-cell omics has emerged over the past decade with the development of technologies that can profile the transcriptome, proteome, and metabolome. Although the number of cells required is not necessarily lower than in the bulk techniques, the capacity to provide detailed information about the heterogeneity of a given population made single-cell techniques a desirable alternative [40]. The single-cell RNA sequencing (scRNA-seq) method was the first omics modality implemented. The ability of this method to provide information about the entire transcriptome of individual cells and identify cell types in heterogeneous populations makes it the most commonly used untargeted single-cell technology in the immunometabolism field. Despite providing unbiased results, scRNA-seq has limitations, including the limited number of cells that can be analyzed per sample and the disparities between mRNA and protein levels [41]. Single-cell technologies can have impactful applications. The continuous development and improvement of single-cell technology capacities have facilitated the development of single-cell atlases. These comprise the vast information provided by single-cell technologies that range from cell types to disease markers. Single-cell atlases are becoming a valuable tool to understand fundamental cellular mechanisms in disease. However, the most useful application of single-cell atlases lies in medicine, where they could revolutionize diagnostics, drug discovery, and treatment selection.

Although quite informative, these single-cell techniques have one main limitation: the indirect measure of the metabolism. Enzyme and mRNA levels do not directly correlate with pathway activity and flux. Thus, these single-cell techniques can only provide a limited context of the metabolic state of immune cells. The most accurate and detailed profiling of the metabolic heterogeneity among different cell types can only be achieved with single-cell metabolomics despite its main limitation of only measuring the steady states of metabolites. This branch of the single-cell omics field is still underdeveloped compared to transcriptomics but is growing rapidly. However, the currently developed methods are not scalable or ready for technology transfer, which limits their application to other fields, such as immunometabolism [36].

1.5. Single-cell metabolomics: state of the art

The interest in single-cell metabolomics is not recent, and in fact, the first attempts to develop a robust method started almost two decades ago [42]. Despite the long-term enthusiasm and constant breakthroughs, multiple challenges have prevented single-cell metabolomics from accompanying the exponential burst observed for single-cell transcriptomics. Similarly to bulk metabolomics, the main technique used in single-cell metabolomics is MS. The sensitivity and resolution of MS analyzers have significantly increased in the past decades due to continuous technological advancements. However, the small volume of a single cell and the resulting low metabolite concentrations have been the main challenges in developing a single-cell metabolomics method [43]. Additionally, different metabolites have different intracellular concentration ranges and ionization efficiency. The latter is the cause of the detected intensities not correlating with the intracellular metabolite concentrations. Thus, without including internal standards or calibration curves, single-cell metabolomics cannot quantify the absolute metabolite concentrations, but the intensities detected are comparable between different conditions [44]. Recent increases in reports of successful single-cell metabolomics studies show that these challenges can be overcome. However, the developed methods have no standard strategy, with each reporting a different approach to sample preparation, data acquisition, and analysis [45].

Electrospray ionization (ESI) is the most used ionization technique in single-cell metabolomics. This technique generates ions after applying a high voltage to a liquid at atmospheric pressure [46]. In most applications, the cells are resuspended and inserted sequentially into a capillary for ESI, enabling the detection of all metabolites present in a cell. However, this approach cannot provide morphological, phenotypical, or spatial information [45]. These limitations prevent it from being suitable for directly studying mixed populations, either isolated from biological samples or in a co-culture.

Mass spectrometry imaging (MSI) is a technique that maps the spatial distribution of metabolites on a given sample. In this technique, a tissue section or cells adhered to a substrate are sampled by an ionization source under vacuum or atmospheric pressure conditions. The generated ions are then transferred to the MS analyzer for detection and relative quantification. The resulting raw spectra are converted into an image, depicting the relative intensity of each metabolite detected in each pixel of the analyzed area [47].

The number of single-cell metabolomics methods based on MSI has been increasing due to the spatial resolution provided by this technique. The MSI ionization techniques primarily used in single-cell metabolomics are secondary ion mass spectrometry (SIMS) and matrix-assisted laser desorption ionization (MALDI). SIMS can achieve subcellular resolution and has been used to detect energy molecules, nucleotides, and lipids at the single-cell level [45]. On the other hand, MALDI can only achieve cellular resolution, but it can be easily combined with different techniques such as microscopy [48], [49]. Thus, MALDI Imaging Mass Spectrometry (MALDI-imaging MS) can, in combination with microscopy, provide spatial, morphological, and phenotypical information, which is a great advantage compared to SIMS or even ESI. However, only lipids have been successfully detected at the single-cell level with MALDI. This is a significant limitation, especially compared to ESI, which can detect nucleotides, amino acids, sugars, and lipids. On the other hand, MALDI can analyze a significantly higher number of cells than ESI in a similar amount of time, making it more suitable for high-throughput applications [45].

The increasing number of studies reporting new single-cell metabolomics methods indicates that the field is growing and progressing rapidly. However, significant improvements are still required before establishing a standard method. First, it is necessary to increase the sensitivity and improve the detection of metabolites and small molecules, which is still a big gap among imaging methods. The throughput of samples and cells analyzed in a single run must also be optimized to avoid technical differences and batch effects [50]. Finally, data processing and analysis are currently done using in-house developed scripts and custom software [45]. Thus, the data analysis step would benefit from implementing a standardized and reproducible pipeline, making data acquired with similar ionization methods comparable.

There are multiple potential applications of a robust single-cell metabolomics method in the immunometabolism field. For example, in the context of autoimmunity, where the metabolism of immune cells might be altered. Single-cell metabolomics could help understand why patients react differently to established therapies and even help select the appropriate one. Another example would be understanding the heterogenous tumor microenvironment and the metabolic response of specific immune cell subsets. This would also provide insights into new therapeutic targets and the selection of the most efficient therapies for different tumors [36].

1.6. SpaceM: a method for single-cell metabolomics

SpaceM is a single-cell metabolomics method developed by the Alexandrov team that combines two techniques: MALDI-imaging MS and light microscopy [51]. SpaceM was designed to detect lipid species and provide phenotypical and morphological information. The method was validated in co-cultures of human cancer epithelial cells (HeLa) and mouse fibroblast cells (NIH3T3) by predicting the cell type based on the metabolic profile. SpaceM also captured lipidomic heterogeneity in differentiated human hepatocytes commonly used as an *in vitro* model of nonalcoholic steatohepatitis and nonalcoholic fatty liver disease.

In this method, the cells are cultured in four-well glass slides compatible with both MALDI-imaging MS and microscope systems. After culturing, the metabolic state of the cells is preserved with fixation, which can be followed by fluorescent staining. The slides are then washed in a volatile solvent to remove non-intracellular molecules that could interfere with the MS analyzer signal. After desiccating the samples, some fiducial marks are drawn with a permanent marker.

The entire slide is scanned using an optical microscope to acquire the pre-MALDI microscopy images. These are important to determine the position of the cells inside the wells and the spatial relationships with other neighbors. The pre-MALDI microscopy images also provide information on cell morphology and, when fluorescent staining is included, on the phenotypic properties. Following this, the samples are sprayed with an appropriate chemical matrix, an essential step in MALDI-imaging MS. The sample is then loaded to the ionization source, where the matrix will absorb the MALDI laser energy and generate the ions for MS. The throughput of SpaceM is higher than that of other methods because four individual wells are acquired in one run. Additionally, sampling around 1000 cells per hour is another advantage of this method.

The MS imaging data is uploaded to the cloud-based platform METASPACE for annotation [52]. The Alexandrov team also developed this computational engine that matches the detected mass-to-charge ratios (m/z) to metabolites and lipids from public databases (e.g., HMDB, LIPID MAPS). The result is a list of the annotated ions and the corresponding spatial images with the intensity distribution for each pixel. The laser-ablated slides are scanned again using light microscopy to acquire the post-MALDI images.

These provide information on the areas scanned during MALDI-imaging MS since the laser leaves clear ablation marks on the applied matrix.

The obtained data from both techniques is processed and integrated using the open-source software developed by the team, also named SpaceM. The software first stitches the pre and post-MALDI microscopy images. Then, it segments the cells and the ablation marks in the stitched pre and post-MALDI images, respectively. Following this, the spatial images for each metabolite annotated by METASPACE are matched to the segmented ablation marks. Finally, the stitched pre- and post-MALDI images are registered using the pen mark fiducials, which leads to the overlap of the ablation marks with the segmented cells. This step identifies which cells were sampled during MALDI-imaging MS and matches the corresponding ion intensities to each cell. The single-cell data is then ready to be further analyzed and interpreted. Thus, SpaceM is an accessible and transferable single-cell method because it relies on commercially available instrumentation with no customization required. The sample requirements are compatible with standard cell culture procedures. Finally, open-source software can promote community collaboration, which, in the end, would help standardize data format and advance the field.

2 OBJECTIVES

The main objective of the project presented in this dissertation is to develop a method for single-cell metabolomics that can be applied in the immunometabolism field. The metabolic heterogeneity of the immune response is understudied because no single-cell metabolomic method has been successfully applied to immune cells. This project aims to fill that gap by developing a method to capture the metabolic states of naïve and activated $CD4^+$ T cells at the single-cell level. $CD4^+$ T cells were chosen for their key role in coordinating the immune response. The well-studied dichotomy between naïve and activated cells was the ideal model for method development. In this dissertation, I will present a new version of the SpaceM method developed by the Alexandrov team. This version, HT-SpaceM, has increased throughput and new software that several team members helped generate. The second main objective of this dissertation is to explore the capacity of HT-SpaceM to detect the metabolic states of $CD4^+$ T cells that have been modulated with metabolic inhibitors. The third aim is to create a single-cell atlas of metabolic states of $CD4^+$ T cells based on the data provided by HT-SpaceM. The single-cell atlas can then be used to resolve the mode of action of drugs with unknown metabolic effects.

3 MATERIALS AND METHODS

Reagents and Materials

Table 1 – List of reagents and materials and the respective manufacturer.

Product	Manufacturer
RPMI with L-Glutamine, HEPES, and Phenol Red	Gibco
Heat-Inactivated Fetal Bovine Serum (Origin: Brazil)	Gibco
Sodium Pyruvate	Gibco
Non-Essential Amino Acids	Gibco
Penicillin-Streptomycin	Gibco
Ficoll Paque Plus	Cytiva
Leucosep Tubes	Greiner Bio-One
50 mL Falcon Tubes	Corning Life Sciences
1.8 mL Nunc Cryogenic Tubes	Thermo Fisher Scientific
Mr. Frosty Freezing Container	Thermo Fisher Scientific
Trypan Blue	Bio-Rad Laboratories
Cell Counting Slides for TC10/TC20 Cell Counter	Bio-Rad Laboratories
EasySep Human Naïve CD4+ T Cell Isolation Kit II	StemCell Technologies
EasySep Magnet	StemCell Technologies
The Big Easy EasySep Magnet	StemCell Technologies
14 mL Falcon Round Bottom Tubes	Corning Life Sciences
Dynabeads Human T-Activator CD3/CD28	Gibco
ImmunoCult Human CD3/CD28 T Cell Activator	StemCell Technologies
ImmunoCult Human CD3/CD28/CD2 T Cell Activator	StemCell Technologies
ImmunoCult-XF T Cell Expansion Medium	StemCell Technologies
Human Plasma-Like Medium	Gibco
24-Well Nunc Cell-Culture Treated Multidishes	Thermo Fisher Scientific
96 Well Round (U) Bottom Plate (TC Surface)	Thermo Fisher Scientific
Dimethyl Sulfoxide	VWR International
2-Deoxy-D-glucose	Sigma-Aldrich
Antimycin A	Sigma-Aldrich
AZ-PFKFB3-67	MedChemExpress
Baricitinib	MedChemExpress
BPTES	Sigma-Aldrich
CBR-5884	Sigma-Aldrich
Cyclosporine	Adooq Bioscience
Etomoxir	Sigma-Aldrich
FCCP	Sigma-Aldrich
Gossypol	Biomol
Metformin	Sigma-Aldrich

Methotrexate	Thermo Fisher Scientific
MK8722	MedChemExpress
Mycophenolic Acid	Biomol
Oligomycin A	Sigma-Aldrich
PF-02545920	Adooq Bioscience
PF-05175157	MedChemExpress
Rapamycin	Sigma-Aldrich
Rotenone	Sigma-Aldrich
STF-31	Sigma-Aldrich
Telaglenastat	Adooq Bioscience
TEPP-46	Sigma-Aldrich
Tofacitinib	MedChemExpress
Torin 1	Adooq Bioscience
WZB-117	Sigma-Aldrich
CellTrace Violet Cell Proliferation Kit	Invitrogen
LIVE/DEAD Fixable Near-IR Dead Cell Stain Kit	Invitrogen
Brilliant Violet 711 Anti-Human CD3 Antibody	BioLegend
FITC Anti-Human CD4 Antibody	BioLegend
Brilliant Violet 605 Anti-Human CD45RA Antibody	BioLegend
PerCP Anti-Human CD45RO Antibody	BioLegend
PE Anti-Human CD25 Antibody	BioLegend
Brilliant Violet 785 Anti-Human CD69 Antibody	BioLegend
DRAQ7 Dye	Invitrogen
1.5 mL Eppendorf Safe-Lock Tubes	Eppendorf
SuperFrost Plus Adhesion Slides	Fisher Scientific
Ethanol	Merck Millipore
Poly-L-Lysine Solution (150,000-300,000 Da)	Sigma-Aldrich
Poly-L-Lysine Solution (84,000 Da)	Sigma-Aldrich
Poly-D-Lysine	Gibco
Collagen from Human Placenta	Sigma-Aldrich
Acetone	Merck Millipore
Acetic Acid 96%	VWR International
ProPlate Multi-Well Chambers	Grace Bio-Labs
Paraformaldehyde 16%	Thermo Fisher Scientific
Ammonium Acetate	Merck Millipore
1,5-Diaminonaphthalene	Sigma-Aldrich
9-Aminoacridine	Sigma-Aldrich
N-(1-naphthyl) ethylenediamine dihydrochloride	Sigma-Aldrich
Acetonitrile	Merck Millipore

Biological Samples

Buffy coats produced from the peripheral blood of healthy donors were obtained from the German Red Cross (Deutsches Rotes Kreuz). The received buffy coats were anonymized by the German Red Cross, including the gender and age of the donors. The project and the use of human material were approved by the EMBL Bioethics Internal Advisory Committee.

Peripheral Mononuclear Blood Cell Isolation and Cryopreservation

Buffy coats were diluted 1:1 in RPMI (modified with L-glutamine, HEPES, and phenol red) supplemented with 1% heat-inactivated fetal bovine serum (HI FBS) and 1 mM EDTA. Ficoll Paque Plus was added to Leucosep tubes and centrifuged for 1 minute at 1000g. The RPMI-diluted buffy coats were then added to the Leucosep-Ficoll tubes and centrifuged at 800g for 20 minutes with acceleration set to 6 and brakes set to 0. After gradient centrifugation, the peripheral blood mononuclear cell (PBMC) layer was extracted to a 50 mL Falcon tube using a Pasteur pipette and diluted with RPMI supplemented with 1% HI FBS and 1 mM EDTA. The PBMCs were centrifuged at 400g for 5 minutes with both acceleration and brakes set back to 9. The supernatant was discarded, and the PBMCs were resuspended in RPMI with 1% HI FBS and 1 mM EDTA. The PBMCs were aliquoted, diluted 1:1 in trypan blue, and counted using a TC20 automatic cell counter. The centrifugation step was repeated, and the resultant supernatant was removed. The PBMCs were resuspended to a concentration of 300 x10^6 cells/mL in HI FBS with 10% dimethyl sulfoxide and divided into 1.8 mL Nunc cryogenic tubes. The PBMCs were transferred to a -80°C freezer and slowly cooled at an optimal rate of -1°C minute using a Mr. Frosty Freezing Container. After 24 hours, the frozen vials were stored in a liquid nitrogen tank (at -165°C) until further use.

Naïve $CD4^+$ T cell Isolation

The frozen PBMCs were thawed in a water bath at 37°C for 5 minutes and then carefully transferred to a 50 mL Falcon tube. Pre-heated RPMI supplemented with 10% HI FBS and 1% Penicillin-Streptomycin (P/S) was added dropwise to the 50 mL Falcon tube until topped up. The PBMCs were centrifuged at 400g for 5 minutes, and the supernatant

was discarded. Then, the PBMCs were resuspended in FACS Buffer (PBS + 2% HI FBS + 1 mM EDTA) and aliquoted for counting. The aliquots were diluted 1:1 with trypan blue, and the cells were counted using a TC20 automatic cell counter. The PBMCs were centrifuged again at 400g for 5 minutes. After discarding the supernatant, the cells were resuspended in FACS Buffer to a concentration of $50x10^6$ cells/mL. The naive $CD4^+$ T cells were isolated from the PBMCs following the EasySep Human Naïve $CD4^+$ T Cell Isolation Kit II instructions.

$CD4^+$ T cell Activation, Modulation, and Culturing

Freshly isolated naïve $CD4^+$ T cells were topped up with RPMI supplemented with 10% HI FBS and 1% P/S and centrifuged at 400g for 5 minutes. The supernatant was discarded, and the naïve $CD4^+$ T cells were resuspended in RPMI supplemented with 10% HI FBS, 1% sodium pyruvate, 1% non-essential amino acids, and 1% P/S. The naïve $CD4^+$ T cells were aliquoted, diluted 1:1 with trypan blue, and counted using a TC20 automatic cell counter**.** After counting, the cell suspension was adjusted to a concentration of $2x10^6$ cells/mL. The naïve $CD4^+$ T cells were either left unstimulated or were stimulated with CD3/CD28 Dynabeads. The activated cells were further divided and treated with 25 modulators (Table 1) with different concentrations (Table 9 in the Results chapter). The unstimulated, stimulated, and modulated $CD4^+$ T cells were cultured in a Nunc 24-well plate at a final concentration of $1x10^6$ cells/mL for 72 hours at 37°C with 5% CO2. In one particular experiment, different media and stimulation were tested in addition to RPMI and Dynabeads. However, the remaining culturing conditions were the same. The other tested media were ImmunoCult-XF T Cell Expansion Medium and Human Plasma Like Medium supplemented with 10% HI FBS. Similarly, the other tested stimulations were soluble anti-CD3/CD28 and soluble anti-CD3/CD28/CD2.

Slide Etching and Coating

The glass slides were initially etched in-house using the ZEISS Microbeam (Carl Zeiss AG). The laser dissection microscope was operated with the PalmRobo software (Carl Zeiss AG). The etching was performed using a layout with 4 columns and 10 rows, and manual focusing was necessary between elements. The layout was designed based on

the dimensions of the incubation chambers used during the cell adhesion step (mentioned below). In total, 40 square wells (3000x3000 microns) and their unique IDs were etched in each slide. The wells were spaced 4500 microns apart, both horizontally and vertically. The increased demand for etched slides eventually justified requesting this service from a professional company (Workshop of Photonics). After etching, all the slides were thoroughly washed with H2O and 70% ethanol before further use.

The etched slides were coated with poly-L-lysine or poly-D-lysine solutions (0.1 mg/mL) for 1 hour at room temperature. After incubation, the slides were thoroughly washed with H2O (Millipore quality) three times. The slides were dried at room temperature overnight or at least 2 hours before use. Collagen powder was reconstituted in 0.1 M acetic acid to a final concentration of 1 mg/mL. The etched slides were coated with the collagen solution overnight at room temperature. Following incubation, the collagen solution was removed, and the slides were left to dry overnight before being used. The poly-L-lysine, poly-D-lysine, and collagen-coated slides were sterilized for 15 minutes with UV light in a cell culture hood before use. In some experiments, the slides were not coated. Instead, the slides were washed with acetone and dried overnight before being used.

$CD4^+$ T cell Adhesion and Sample Preparation

After culturing the cells for 72h, the conditions stimulated with CD3/CD28 Dynabeads were collected in Falcon round bottom tubes. Each well was washed 2 times with PBS. The Falcon round bottom tubes were placed in an EasySep magnet for 1 minute to separate the cells from the magnetic beads. The supernatant containing the cells was transferred to a new Falcon tube. The cells were centrifuged at 400g for 5 minutes. The supernatant was discarded, and the $CD4^+$ T cells were resuspended in RPMI without any supplements. Aliquoted cells were diluted 1:1 in trypan blue and counted with a TC20 automatic cell counter. The unstimulated cell suspension was adjusted to a final concentration of $0.5x10^6$ cells/mL with RPMI. The stimulated and modulated conditions were adjusted to a final concentration of $0.3x10^6$ cells/mL when viability was higher than 70%. Otherwise, if viability was lower than 70%, the final concentration for these conditions was $0.5x10^6$ cells/mL.

The etched slides were attached to the 64-well ProPlate chambers following the manufacturer's instructions. Then, 50 µL of cell suspension was pipetted into each well,

following a layout that randomized the order of the different conditions. The $CD4^+$ T cells were left to adhere to the glass slides for 2 hours at room temperature. After this incubation, the RPMI was carefully removed, and the wells were washed with PBS. In some experiments, the $CD4^+$ T cells were fixed with 4% Paraformaldehyde diluted in PBS for 10 minutes. After removing the Paraformaldehyde solution, cells were rewashed with PBS. However, the fixation step and washes with PBS were skipped in most experiments.

The glass slides were carefully detached from the ProPlate chambers. Then, the slides were washed by dipping 9 times in 100 mM Ammonium Acetate. The washed slides were dried in a vacuum desiccator for 30 minutes. The slides were imaged with a microscope (described below), then vacuum packed and stored in a -80°C freezer until further use.

Brightfield Microscopy

The microscopy images were acquired with a Nikon Ti-E inverted microscope (Nikon Instruments) connected to an Orca Flash 4 V2 (Hamamatsu Photonics) camera. The microscope was operated using the NIS Elements software (Nikon Instruments). The 10x magnification was achieved with the objective CFI Plan Apo 10x Lambda (Nikon Instruments). After focusing the cells in the brightfield channel, the Köhler illumination was adjusted to ensure even illumination across the entire field of view. The whole slide was focused and imaged using a custom script created with the JOBS plug-in module, capturing consecutive tiles with 20% overlap in the brightfield channel. Additionally, several images of areas outside the slide were acquired for flatfield correction. This protocol was used for both pre and post-MALDI microscopy.

Matrix Preparation and Application

The frozen slides were thawed in a vacuum desiccator for 30 minutes. The matrix solutions were prepared and applied to the slides using an HTX TM-Sprayer (HTX Technologies LLC). The solvent, concentration, and spraying parameters used for each matrix are resumed in **Table 2**. In some experiments, a mix of 1,5-diaminonaphthalene (DAN) and 9-aminoacridine (9AA) was used instead. DAN was dissolved in 70% acetonitrile to a final concentration of 7 mg/mL. While 9AA was dissolved in 70% acetonitrile to a final concentration of 10 mg/mL. Then, DAN and 9AA were mixed in a

9:1 ratio. The DAN:9AA matrix mix was sprayed on the slides using the parameters shown in **Table 2**.

Table 2 – Details for matrix preparation and spraying.

Matrix	Solvent	Concentration	Spraying Parameters
1,5-Diaminonaphthalene	70% Acetonitrile	7 mg/mL	Temperature = 80°C Number of passes = 7 Flow rate = 0.05 mL/min
9-Aminoacridine	70% Methanol	10 mg/mL	Temperature = 75°C Number of passes = 10 Flow rate = 0.07 mL/min
N-(1-naphthyl) Ethylenediamine Dihydrochloride	70% Acetonitrile	10 mg/mL	Temperature = 95°C Number of passes = 10 Flow rate = 0.05 mL/min
1,5-Diaminonaphthalene + 9-Aminoacridine	70% Acetonitrile 70% Acetonitrile	7 mg/mL 10 mg/mL	Temperature = 80°C Number of passes = 7 Flow rate = 0.05 mL/min

MALDI-Imaging Mass Spectrometry

The sprayed slides were imaged on an AP-SMALDI5 ion source (TransMIT) coupled to a Q Exactive Plus mass spectrometer (Thermo Fisher Scientific). The sprayed slides were mounted on a proper slide adapter and loaded into the AP-SMALDI5 source. The integrated software, SMALDIControl (TransMIT), controlled parameters like the laser focus, the distance between the ablated spots (pixel size), and the coordinates of the acquisition area. In SMALDIControl software, the sampling area of each well had to be set manually and individually. So, the Alexandrov team developed a software that connected to SMALDIControl. In this software, all 40 wells in the etched slides could be acquired in one single run. The software also featured a calibration function for the laser focus. The only parameter still controlled by the SMALDIControl was the laser attenuation. The MALDI parameters were varied between experiments until optimized settings were found. However, in most experiments, the attenuator was set to 32, the pixel size was 20 µm, and the number of pixels acquired in each area was 2500.

The ions generated in the AP-SMALDI5 source were redirected to be analyzed in the Q Exactive Plus mass spectrometer. This instrument was also controlled by an integrated software, Tune (Thermo Fisher Scientific). The Tune software also had multiple parameters (e.g., scan parameters, source parameters) that were tweaked to find the optimal detection settings. In most experiments, the analysis was performed in full scan mode over a mass range of 100-400 m/z, with a resolving power of 140000 and using negative polarity. The source parameters were also optimized, and in most experiments, the spray voltage was set to 3.1 kV, the capillary temperature to 250°C, and the RF level to 50. After sampling the entire slide, the post-MALDI microscopy images were acquired (described above).

Data Processing and Annotation

The data generated with pre and post-MALDI microscopy and MALDI-imaging MS was processed and integrated using in-house software (SpaceM-HT 1.0) compatible with the high-throughput requirements of 40-well slides. Each well had to be processed individually in the original SpaceM software (described in the Introduction section). In contrast, all 40 wells were processed in the same workflow with SpaceM-HT. All the steps described below were performed using the SpaceM-HT software.

The RAW file generated with Tune software was split and converted to the mzML format using MSConvert [53]. The centroided mzML files for each acquired well were converted to the imzML format using the imzMLConverter software [54]. The imzML files were uploaded to the cloud-engine METASPACE for metabolite annotation against the HMDB (v4) and CoreMetabolome (v3) databases. Pre and post-MALDI microscopy images were stitched using the BigStitcher plug-in available in Fiji, an open-source image analysis software [55]. The ablation marks in the stitched post-MALDI microscopy images were segmented using a Grid Fit tool implemented in the HT-SpaceM software. The cells in the pre-MALDI microscopy images were segmented with Cellpose using the cyto2 model [56]. Then, the pre and post-MALDI microscopy images were registered using the etched well IDs as reference. The cell deconvolution step was performed using a method that selected the ablation mark with the biggest overlap for each cell. The final single-cell data individual files matched the acquired wells and contained the intensities of the ions present in each sampled cell.

Following this, ion-cell localization was evaluated using an area-normalized Manders Colocalization Coefficient, a metric developed by the Alexandrov team. This metric was developed to identify and select intracellular ions in SpaceM data. Then, a custom database was created based on the ions selected and added to METASPACE. The SpaceM data was reprocessed with the created custom database, resulting in single-cell files that only contained ions identified as intracellular.

Data Analysis

The single-cell metabolomics data was analyzed with Outer-SpaceM, a Python package developed by the Alexandrov team, and Scanpy [57]. Metabolites not present in 'Metabolic Pathways' maps from the Kyoto Encyclopedia of Genes and Genomes were excluded from analysis, with some exceptions. This resulted in a final number of 180 metabolites. Then, the cell filtering and normalization steps were done using the Scanpy package. Cells with less than 40 detected metabolites were also excluded from analysis, and wells with less than 100 cells were removed. The total intensity of the cells was normalized to 10000. The data was transformed using the natural logarithm. The effects of running replicates across different slides were regressed out. Then, the data was scaled. The outlier wells were identified using a linear dimensionality reduction method and unsupervised clustering. Principal component analysis (PCA) was performed for each condition on the selected 180 metabolites, considering only the first 10 components. Then, the neighborhood graph was calculated using 15 neighboring points. Unsupervised clustering was performed with the Leiden algorithm using the minimal resolution of 0.1. The replicate wells assigned to unique clusters were identified as outliers and removed.

Integration and alignment of different batches were done using the batch balanced k nearest neighbors (BBKNN) method [58]. PCA was then performed using the selected 180 metabolites. The neighborhood graph was constructed using the top 10 principal components and 15 neighboring points. Then, dimensionality reduction was performed with uniform manifold approximation and projection (UMAP). Unsupervised clustering was performed using the Leiden algorithm with the resolution parameter set between 0.1 and 0.5. Differential expression analysis between conditions or Leiden clusters was performed using the non-parametric Wilcoxon rank-sum test. The abovementioned methods were all performed with the functions provided by the Scanpy package. Both

technical and biological variability were evaluated with a function from the Outer-SpaceM package that calculated the Euclidean distance between the technical replicates.

The single-cell metabolomics atlas was generated using a pipeline similar to the one described above. BBKNN was used to integrate data from different batches, and then metabolites detected in less than 1% of the cells were removed. PCA was then performed using the filtered 141 metabolites. The neighborhood graph was constructed using 15 neighboring points and the first 10 principal components. Dimensionality reduction was performed with UMAP, followed by Leiden clustering with a resolution of 0.9. Metabolic states were assigned to the Leiden clusters based on the conditions they overlapped with. The projection of the query data and mapping of the Leiden labels was performed using the Scanpy function "ingest".

The other plots in the Results chapter that were not mentioned above were all generated with the Python package Seaborn [59]. These include plots like the boxplots with metabolite intensities shown in the Results section 4.3 and the scatterplot plots with flow cytometry results in section 4.7.

Flow Cytometry

In some experiments, naïve $CD4^+$ T cells were analyzed with Flow Cytometry rather than HT-SpaceM. There was an extra step after isolation and before culturing for naïve $CD4^+$ T cells used in Flow Cytometry assays but not in HT-SpaceM. The cells were resuspended in PBS to a concentration of $1x10^6$ cells/mL and stained with CellTrace Violet (0.1:1000) for 20 minutes at 37°C. After incubation, the dye was quenched for 5 minutes at 37 °C by adding RPMI with 10% HI FBS and 1% P/S. The cells were then centrifuged at 400g for 5 minutes. After discarding the supernatant, the naïve $CD4^+$ T cells were counted, activated, and modulated as described above. The cells were also cultured as described above with one small modification using 96-well plates instead.

After 72 hours of culturing, the cells were centrifuged in the 96-well plate at 400 g for 5 minutes. The supernatant was discarded, and the $CD4^+$ T cells were resuspended in PBS and centrifuged again at 400 g for 5 minutes. The supernatant was discarded, and the cell pellet was resuspended in PBS and stained with Live/Dead Fixable Near-IR (1:1000) for 10 minutes at 37°C. After incubation, FACS Buffer was added to the cells, which were then

centrifuged at 400 g for 5 minutes. The supernatant was discarded, and the cell pellet was resuspended in FACS Buffer. The $CD4^+$ T cells were stained with CD4-FITC (1:200), CD3-BV711 (1:100), CD45RA-BV605 (1:100), CD45RO-PerCP (1:100), CD25-PE (1:600) and CD69-BV785 (1:200) for 30 minutes at 4°C. After incubation, FACS Buffer was added to the cells, which were then centrifuged at 400 g for 5 minutes. The supernatant was discarded, and the $CD4^+$ T cells were resuspended in FACS buffer.

Flow cytometry was performed using a FACSymphony A3 Cell Analyzer (BD). The collection channels (laser + bandpass filter wavelength) selected were: 488-530/30 (FITC), 405-710/50 (BV711), 405-604/40 (BV605), 488-710/50 (PerCP), 561-586/15 (PE), 405-810/40 (BV785), 405-431/28 (CellTrace Violet) and 640-780/60 (Live/Dead Near-IR). The $CD4^+$ T cells were analyzed using a High Throughput Sampler (BD) compatible with 96-well plates. Forward and Side Scatter were used to discriminate cells from debris and select singlets. The viability of all conditions was assessed by measuring the expression of Live/Dead Near-IR. The isolation quality was determined by measuring the expression of CD3, CD4, CD45RA, and CD45RO in the unstimulated condition. The efficacy of CD3/CD28 stimulation and the impact of the modulators on activation and cell proliferation was evaluated by measuring the expression of CD25, CD69, and CellTrace Violet. The data was acquired using the BD FACSDiva Software (BD) and later analyzed with FlowJo v10.9 (FlowJo LLC). In the first experiments, the cell viability was assessed with DRAQ7 before switching to Live/Dead Near-IR. The same staining procedure was followed for DRAQ7 as described for Live/Dead Near-IR (37°C, 10 minutes, 1:1000), and the selected collection channel was 640-780/60.

Liquid Chromatography-Mass Spectrometry

The single-cell results of some conditions were structurally validated with LC-MS/MS. The experimental workflow for naïve $CD4^+$ T cell isolation, activation, modulation, and culturing was the same as described above. After 72 hours of culturing, the cells from the stimulated conditions were separated from the magnetic activation beads as described above. Following this, the cells were centrifuged at 400g for 5 minutes. The supernatant was discarded, and the CD4+ T cells were resuspended in PBS. Aliquoted cells were diluted 1:1 in trypan blue and counted with a TC20 automatic cell counter. Each condition was divided into the maximum possible number of technical replicates, each

containing $1x10^6$ million cells. The cells were centrifuged at 400g for 5 minutes. The supernatant was discarded, and the cell pellets were stored in the -80°C freezer until further use.

The rest of the bulk metabolomics protocol described here was done by a postdoc from the Alexandrov team, Svitlana Dekina. The thawed cell pellets were extracted by adding zirconia beads and a solvent mixture of acetonitrile: methanol: water (Chemsolute) in a ratio of 2:2:1, along with internal standards. The samples were homogenized thrice for 30 seconds and then were incubated at -20°C for 10 minutes to facilitate protein precipitation. The resulting mixtures were centrifuged at 14000g for 15 minutes at 4°C. The supernatants were transferred to new tubes 1.5 mL Eppendorf tubes. The quality control samples were prepared by pooling 20 µL from each sample following the metabolomics Quality Assurance and Quality Control Consortium guidelines [60]. The control blank samples were prepared following the same protocol but using Ultra LC-MS grade water (Chemsolute) instead of the cell pellets.

LC-MS/MS analysis was performed on a Vanquish Horizon UHPLC system (Thermo Fisher Scientific) coupled to an Orbitrap Exploris 240 mass spectrometer (Thermo Fisher Scientific). Chromatographic separation was performed on an Atlantis Premier BEH Z-HILIC column (Waters) at a 0.25 mL/min flow rate. The column temperature was maintained at 40°C, the autosampler temperature was set to 4°C, and the sample injection volume was 5 µL. Untargeted metabolomics was performed using a full scan over a mass range of 60-900 m/z, with a resolving power of 120000 in negative heated-electrospray ionization mode. Then, data-dependent acquisition was performed to obtain MS/MS fragment spectra. The resolving power was set to 15,000, the scan time to 22 ms, the stepped collision energies to 30/50/70%, and the cycle time to 900 ms. For the ion source parameters, the spray voltage was set to -3000 V, sheath gas to 30, auxiliary gas to 5, sweep gas to 0, ion transfer tube temperature to 350°C, and vaporizer temperature to 300°C. The data was processed using Compound Discoverer 3.3 (Thermo Fisher Scientific).

4 RESULTS

4.1. Experimental Overview and Action Points

The main goal of this project was to develop a single-cell method to characterize the metabolome of $CD4^+$ T cells. This was achieved by adapting the protocols of the novel single-cell metabolomics method, SpaceM. However, this involved optimizing and changing multiple steps of the original SpaceM pipeline. This was necessary because of the differences between the cellular properties of $CD4^+$ T cells and the cells used in the original method. These challenges will be described in more detail in the following section, but I will highlight the main ones now. To run SpaceM, it is absolutely necessary to have adhered and dried cells on a glass slide. However, naïve $CD4^+$ T cells grow in suspension, which made the adhesion step the first challenge to tackle. The second challenge was related to the cell size because SpaceM was developed for bigger cells like HeLa and hepatocytes. Since naïve $CD4^+$ T cells are smaller, this decreased the sensibility and detection of the method. Thus, it was necessary to find solutions to compensate for this. Finally, the third challenge was related to the target molecules, which were metabolites. SpaceM was initially developed to detect lipids but was not demonstrated to work for metabolite detection. Thus, it was also necessary to find strategies to enhance metabolite detection. These three main challenges made adapting the original SpaceM method necessary, as shown in **Figure 1**. The steps of the experimental workflow and the original SpaceM pipeline are represented in green boxes. The red boxes and sunbursts highlight the steps that had to be optimized to develop a single-cell metabolomics method for $CD4^+$ T cells. Thus, the critical optimization steps were: establishing the appropriate cell culture model, testing different adhesion strategies, evaluating the optimal preservation method, choosing the appropriate chemical matrix, and optimizing the technical parameters. This resumes the most time-consuming part of my project and was essential to obtain the biology-focused results that will be presented later.

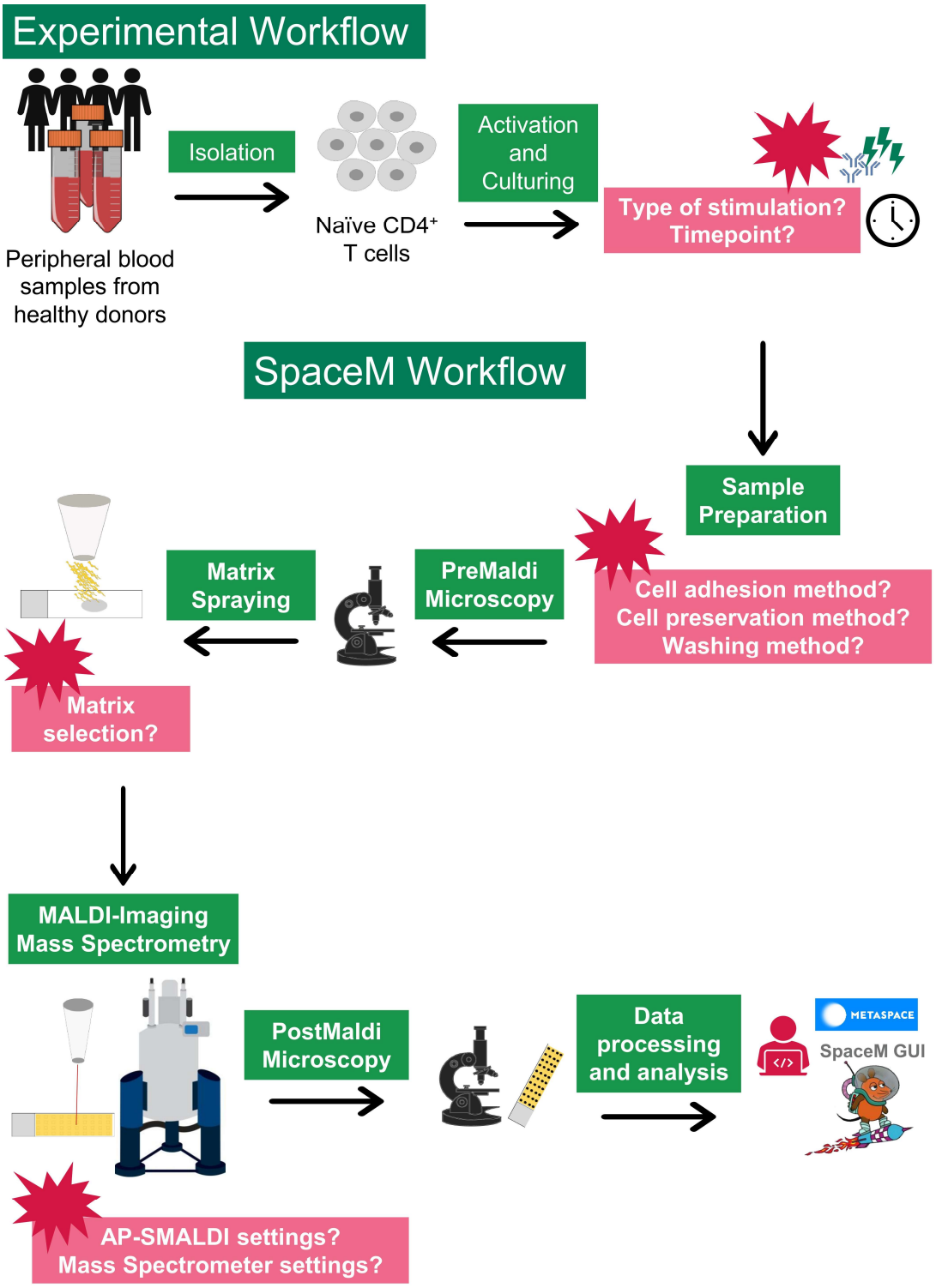

Figure 1 – Experimental and SpaceM workflows. The green boxes in the experimental workflow indicate the essential steps for cell isolation and culturing. The red boxes indicate the parameters that were optimized to establish the cell culture model. Similarly, the green boxes in the SpaceM workflow highlight the steps of the original method. The red boxes indicate the parameters that had to be changed in specific steps of the original method.

4.2. $CD4^+$ T cell Activation and Culturing

The first step towards single-cell metabolomics was to set up a reliable and functional cell culture model to study $CD4^+$ T cell activation. The source cell material consisted of samples of peripheral blood donated by healthy individuals to the German Red Cross. After donation, the whole blood samples are processed and, through centrifugation, divided into different parts (red blood cells, platelets, plasma, and buffy coats). Of all these products, only buffy coats cannot be used for medical purposes because these contain blood leukocytes (i.e., granulocytes, monocytes, and lymphocytes). [61] Thus, upon donor consent, the buffy coats can be used for research. The buffy coats still contain a significant amount of red blood cells and plasma, so further density gradient centrifugation is required upon receiving them. This step separates low-density cells like the peripheral blood mononuclear cells (PBMCs), where T cells are present, from the plasma, the red blood cells, and the granulocytes [62].

The frequency of T cells in human PBMCs is approximately 50%, and $CD4^+$ T cells are also dominant among the T cell subpopulation, with a frequency of roughly 70%, making buffy coats a great source of these cells [63]. The characterization of the PBMC population isolated from the buffy coats used in this project was done using flow cytometry. For this, 4 well-characterized surface markers were used. At the first level, CD3 was used to identify the total T cells, while CD4 was used as a differential marker among this population. CD45RA was used to determine the frequency of naïve cells among $CD3^+CD4^+$ cells, while CD45RO revealed the amount of memory cells [64]. **Figure 2** demonstrates the gating strategy and the frequency of cell subpopulations in PBMCs isolated from buffy coats. Lymphocytes can be separated from monocytes without any surface marker using the two optical detectors, Forward and Side Scatter (FSC and SSC, respectively) [65]. FSC intensity can be directly correlated with cell diameter, making it a good measure of cell size, while SSC provides information regarding the internal complexity of the cells or granularity [66]. Monocytes exhibit higher size and granularity than lymphocytes, translating into higher FSC and SSC. In the example strategy gate from one single donor, the frequency of lymphocytes is 50%, while the frequency of monocytes is 12% **(Figure 2A**) [67]. The significant amount of debris in the sample can be characterized by low FSC and low to high SSC [66]. If only the cell populations are considered (not shown), the counts of lymphocytes and monocytes translate to roughly 80% and 20% of total events, which reflects the frequencies previously reported for these populations [63].

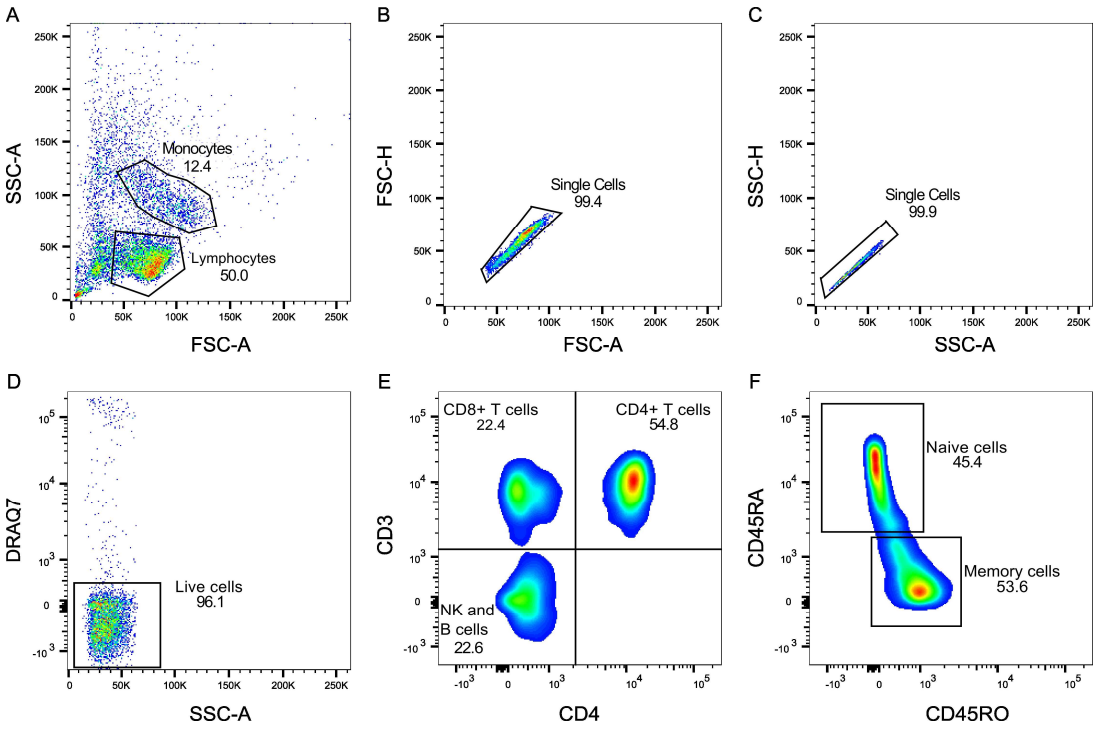

Figure 2 – Frequency of different cell types in PBMCs from one donor. **(A)** Lymphocytes were separated from monocytes based on the SSC and FSC. **(B)**, **(C)** After gating on the lymphocyte population, double discrimination was applied to select the single cells. **(D)** The viability marker DRAQ7 was used to select only live cells. **(E)** The percentage of $CD4^+$ T cells, $CD8^+$ T cells, B cells, and NK cells among the live lymphocytes was determined with CD3 (T cell marker) and CD4. **(F)** After gating on the $CD4^+$ T cell population, the percentage of naïve and memory cells was determined through the expression of CD45RA (naïve marker) and CD45RO (memory marker).

After gating on the lymphocyte population, the height and area parameters of FSC and SSC were used to select single cells, excluding debris, doublets, or clumps, which in this case (**Figure 2B-C**) was minimal. DRAQ7 is a viability dye that selectively stains cells with a compromised membrane and dead cells [68]. This way, the cell population with a negative DRAQ7 signal can establish the last gate before phenotypical characterization. In the presented example, most cells were alive and included in the live cell gate (**Figure 2D**). The expression of CD3 and CD4 proteins can be used to characterize and identify the lymphocyte subpopulations. Among the population of live cells, 54.8% of the cells were double positive for CD3 and CD4 and thus were identified as $CD4^+$ T cells. The population

of $CD8^+$ T cells, which only express CD3, accounted for 22.4% of all lymphocytes, while 22.6% of cells were double negative for both CD3 and CD4 and were identified as B cells and Natural Killer Cells (**Figure 2E**). The frequency of naïve cells among the $CD4^+$ population was 45.4% ($CD45RA^+CD45RO^-$), which is within the expected range in healthy adults [69].

The frequency of lymphocyte populations circulating in the peripheral blood varies from individual to individual. For all the 100 donors processed in this project, the amount of $CD4^+$ T cells was 35-60% of all lymphocytes, while naïve cells accounted for 40-60% of total $CD4^+$ (data not shown). After isolating the total PBMC population from the received buffy coats through a density gradient centrifugation, another round of isolation is necessary to obtain the naïve $CD4^+$ T cells. For this step, a negative selection method with commercial kits was chosen where the unwanted cells were removed. The PBMC population was incubated with surface antibodies specific for non-naïve $CD4^+$ T cells. After a short incubation, magnetic particles that bind the surface antibodies used in the first step were added. Upon placing the PBMC population on a specific magnet, the unwanted cells migrated toward the wall of the tube while the target cells (naïve $CD4^+$ T cells) remained in suspension.

After isolating the naïve $CD4^+$ T cells, the same protocol and gating strategy used to characterize the lymphocyte populations for each donor was used to evaluate the quality of purification. In **Figure 3**, the purity of the cell population after isolation from one donor is shown. The used isolation kits provided high-quality (98.5% viable cells) and highly purified $CD45RA^+CD45RO^-$ naïve cells (99.1%) among the $CD3^+CD4^+$ population (97.4% of live cells). Additionally, the expression of CD69 and CD25, activation markers in lymphocytes, was measured to provide additional confidence regarding the phenotype of the isolated population, which turned out to be double negative for these markers as expected [70].

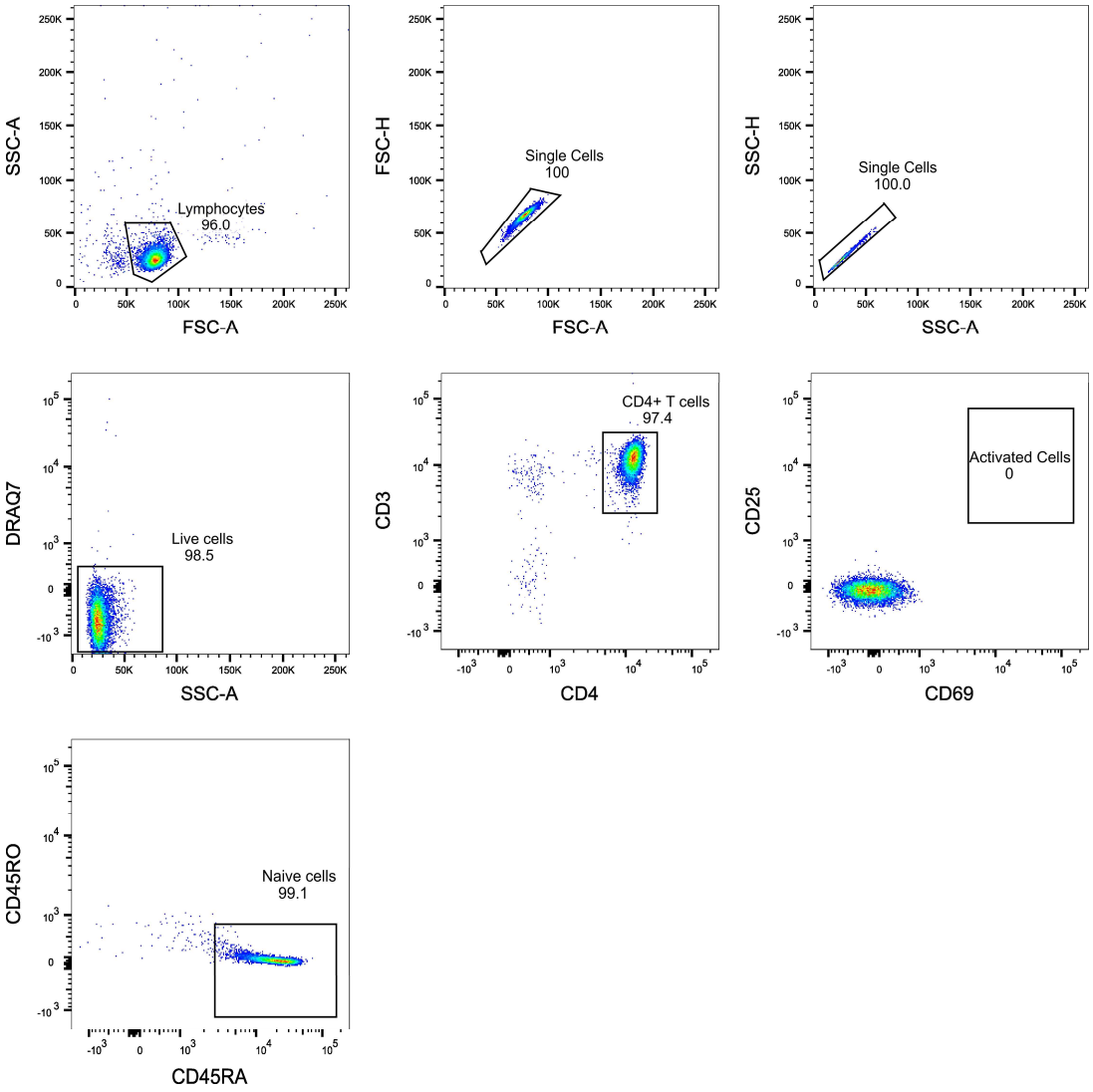

Figure 3 – Purity of naïve $CD4^+$ T cell population after isolation from one donor. Lymphocytes were separated from debris using the SSC and FSC. Then, double discrimination was applied to select the single cells among the lymphocyte population. The viability marker DRAQ7 was used to select only live cells. The isolation quality was determined by checking the percentage of $CD4^+$ T cells that were naïve. The $CD4^+$ T cell population was identified using the CD3 and CD4 markers. After gating on the $CD3^+CD4^+$ T cell population, the percentage of naïve cells was determined through the positive expression of CD45RA and negative expression of CD45RO.

Once the isolation protocol was established, the next logical step was setting up a fitting cell culture model to answer the main questions proposed in this project. Since the objective was to characterize the metabolic remodeling upon activation at the single-cell level, it seemed appropriate to start by studying the time dynamics of T-cell activation and decide on a relevant time point. Naïve $CD4^+$ T cells require at least 20h of continuous signaling to commit to proliferation [72]. The first main division occurs only 36-48h after initial stimulation, and thus, the most commonly used protocol to study activation takes 3 days of cell culturing and incubation [73], [74]. Considering this, multiple time points had to be tested to determine the optimal stimulation period. Freshly isolated naïve $CD4^+$ T cells were incubated with magnetic beads coupled to anti-CD3 and anti-CD28 antibodies. These two signals are essential to trigger T cell activation in the body, and it has been established that these are also required to mimic this process *in vitro* [71]. Stimulated cells were cultured in RPMI supplemented with heat-inactivated FBS. The time points of stimulation chosen were: 0 hours (non-stimulated control), 2 hours, 4 hours, 16 hours, 24 hours, 72 hours, 120 hours.

The activation state at each time point was evaluated with Flow cytometry by checking the expression of the markers CD69 and CD25 in $CD3^+CD4^+$ cells **(Figure 4A)**. The chosen markers have different kinetics, with CD69 expression being upregulated shortly 4 hours after stimulation, while it can take 12-24 hours to detect CD25 expression. Additionally, cell proliferation was tracked with the intracellular dye CellTrace Violet (CTV). The dye is expected to be symmetrically divided between the daughter cells upon division, leading to a continuous decrease in intensity between generations [75]. This intensity difference allows each new peak to be associated with a new generation (**Figure 4B**).

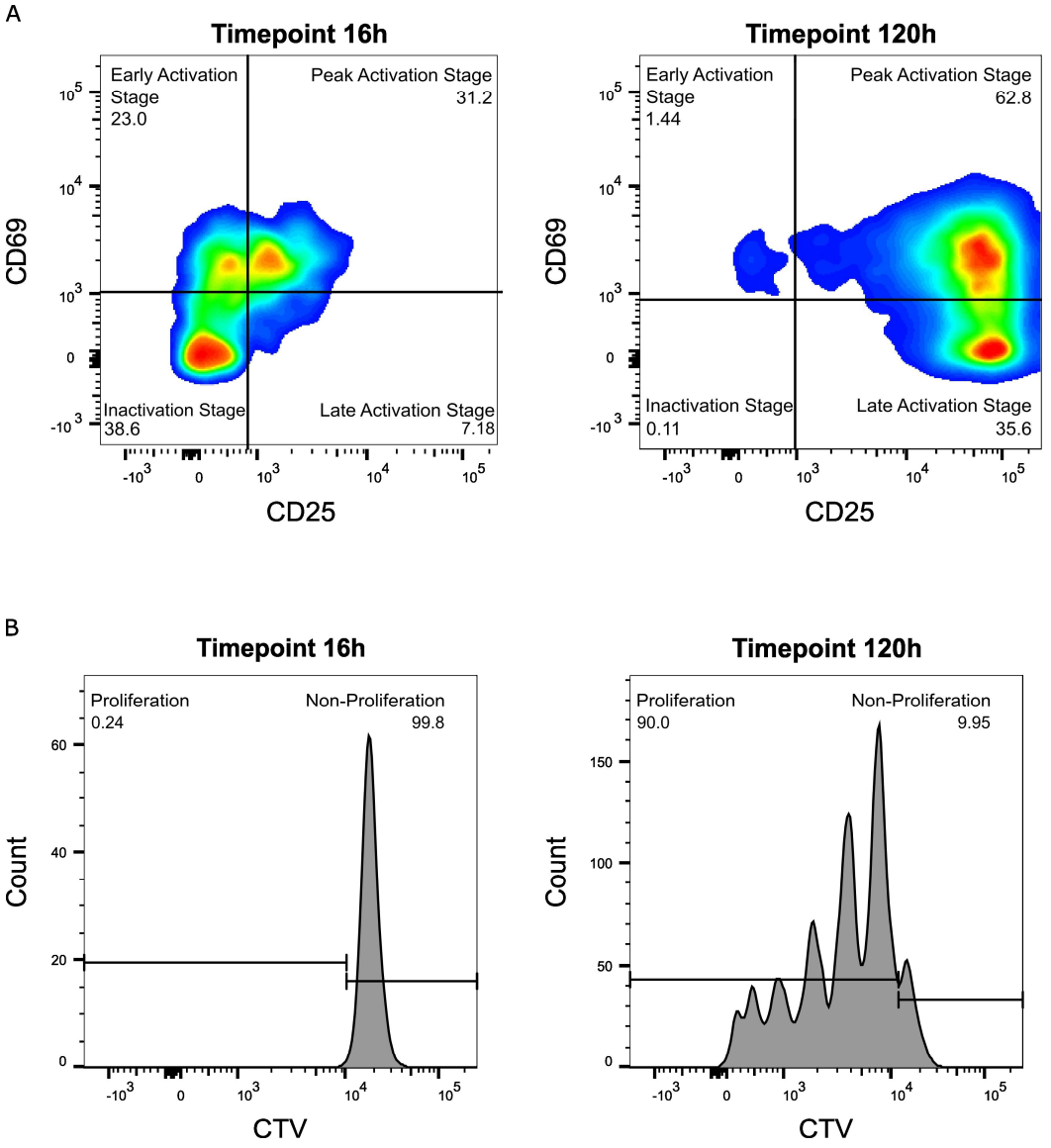

Figure 4 – Activation and proliferation stages after stimulation of naïve $CD4^+$ T cells from one donor. The gating strategy shown previously was used to select the live $CD3^+CD4^+$ T cells. **(A)** CD69 and CD25 were used to define four stages of activation. **(B)** CTV peaks were used to determine the percentage of cells that proliferated. One early and one late time point are shown here to demonstrate how the activation and proliferation dynamics change.

Four activation stages were defined according to the expression of the markers in $CD3^+CD4^+$ cells: Inactivation ($CD25^-D69^-$), Early Activation ($CD25^-D69^+$), Peak Activation ($CD25^+D69^+$), Late Activation ($CD25^+D69^-$) **(Figure 4A)**. The expression of CD69 (Early Activation) can be observed only 4h after stimulation, while CD25 expression can be detected only after 16h (**Figure 5A**), as reported before [70]. After 24 hours, practically all cells are committed to activation, with only a small percentage of cells remaining inactivated and the Early Activation population starting to decline. The two proliferation stages were defined based on the peaks of CTV (**Figure 4B**). The first and most intense CTV peak was defined as the Non-Proliferation stage, while all the other peaks were defined as Proliferation. The first division round occurs between 40h and 48h after stimulation (**Figure 5B**). However, significant proliferation is only observed 72h post-stimulation, with 70% of cells dividing at least once. Considering both activation and proliferation results, I proceeded with 72h of stimulation. This time point provided a heterogeneous population of cells in their Peak and Activation stage, with most having successfully divided at least once.

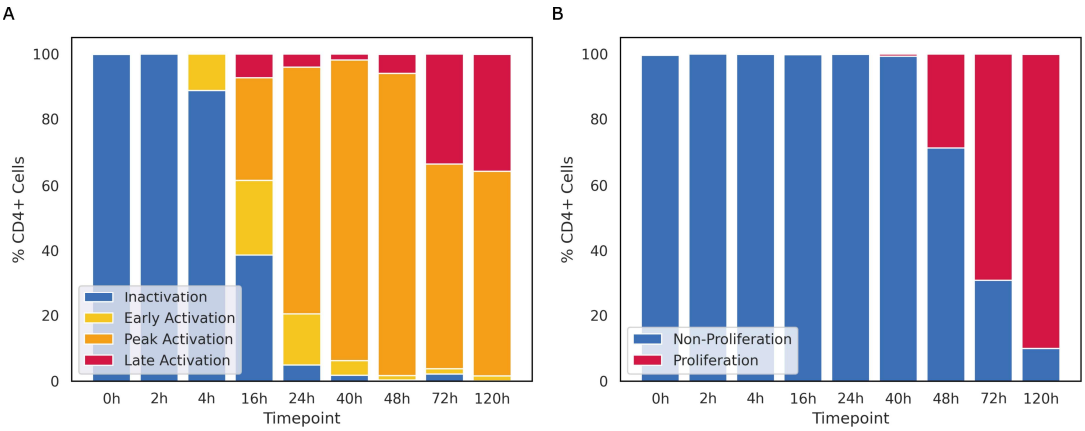

Figure 5 – Activation and proliferation stages of stimulated $CD4^+$ T cells at different time points from one donor. **(A)** Percentage of total $CD3^+CD4^+$ T cells at each activation stage at a given time point. The activation stages were determined based on the expression of CD69 and CD25: Inactivation ($CD25^-D69^-$), Early Activation ($CD25^-D69^+$), Peak Activation ($CD25^+D69^+$), Late Activation ($CD25^+D69^-$). **(B)** Percentage of total $CD3^+CD4^+$ T cells that have proliferated at a given time point. The proliferation stages were determined based on the number and intensity of CTV peaks: Non-Proliferation (first and most intense peak), Proliferation (remaining peaks).

The last and final step for setting up the cell culture model was determining the appropriate stimulation method and culture media. The first aim was to select the most efficient type of stimulation. So, two commonly used products in T cell activation were compared: magnetic beads coated with anti-CD3 and anti-CD28 (Dynabeads) versus a soluble version of these antibodies (ImmunoCult). In addition, a combination of anti-CD3 and anti-CD28 with anti-CD2 (ImmunoCult + CD2) was also included. CD2 has been previously reported as a costimulatory molecule. In other words, it was reported as a second signal required after TCR stimulation, similar to CD28. Thus, it plays a key role during activation and might enhance it [76].

The second aim was to compare different cell culture media (RPMI, ImmunoCult, HPLM) and determine the most suitable one to study T-cell activation. RPMI was the first synthetic medium to be used for *in vitro* leukocyte expansion, and it's still the most commonly used medium [77], [78]. Thus, RPMI was included in these experiments and was further supplemented with heat-inactivated FBS, sodium pyruvate, and non-essential amino acids [79]. The second chosen medium was ImmunoCult-XF T cell Expansion Medium (ImmunoCult), which did not require serum supplementation and was developed for optimal T cell expansion [80]. The third chosen option was Human Plasma-Like Medium (HPLM), a medium designed to mimic the metabolite composition of the human plasma. However, heat-inactivated FBS is still required as a supplement [81]. The main difference between the three selected media is the metabolite composition and concentration. The glucose concentration is 2 times higher in RPMI and 4 times higher in ImmunoCult medium than in HPLM. Meanwhile, the glutamine concentration is 4 and 8 times higher in RPMI and ImmunoCult medium compared to HPLM [80]. Given the drastic differences between the composition of the selected media, I wondered if this, along with the type of stimulation, impacted the activation and proliferation state of the cells when culturing them for the time point chosen in the previous experiment (3 days or 72 hours).

The activation stages were defined using the same criteria described above, with the presented results reflecting the percentage of $CD3^+CD4^+$ cells present in each stage (**Figure 4A**). Few cells were detected in the Inactivation and Early Activation Stages after 72h of stimulation, but this was expected (**Figure 6A**). The percentage of cells in the Peak or Late Activation stages highly depended on the type of medium used but not on the stimulation. More than 60% of naïve $CD4^+$ T cells cultured in ImmunoCult medium were in the Late Activation stage regardless of the type of stimulation used. While for cells cultured in RPMI, only 26-35% were in the late activation stage, and this value decreased to 16-20% with HPLM. Considering the percentage of cells in the Late Activation stage, the best stimulation for both RPMI and ImmunoCult medium was Dynabeads, while for HPLM, it was ImmunoCult + CD2.

To interpret the proliferation results, each CTV peak was assigned to a different generation, with the most intense peak being assigned to Generation 0. The results show the percentage of $CD3^+CD4^+$ cells in each generation (**Figure 6B**). Naïve $CD4^+$ T cells stimulated and cultured in HPLM had the slowest division rates after 72h, with 19.6-25.6% of cells not dividing (Generation 0) and most belonging to Generation 1 and thus having divided only once (43.3-52.4%). Culturing the cells in either RPMI or ImmunoCult medium resulted in the most effective proliferation, with fewer cells in Generation 0 and most in Generation 3. The only exception was the combination of ImmunoCult + CD2 stimulation with RPMI, where a significant number of cells (30.8%) did not divide after 72h.

The activation and proliferation were mainly affected by the chosen medium rather than the stimulation method. Similar results have been observed before for human $CD4^+$ T cells, with the cells adapting metabolically depending on the medium used for expansion [80]. Considering that the main goal was to study T-cell activation and build a single-cell atlas of metabolic states for future drug discovery, it seemed appropriate to choose HPLM, given its similarity to the native body condition. However, the delivery of HPLM was quite unreliable, with some orders taking 3 months to arrive. Thus, I had to proceed with RPMI instead since it was the most similar option to HPLM [81]. RPMI was supplemented with heat-inactivated FBS, non-essential amino acids, and sodium pyruvate. This was intended to enrich RPMI with essential metabolites that are present in human plasma and HPLM, like alanine, cysteine, and sodium pyruvate [81]. Since all the stimulation methods tested had very similar effects and did not impact the activation or proliferation of cells, I decided to proceed with Dynabeads.

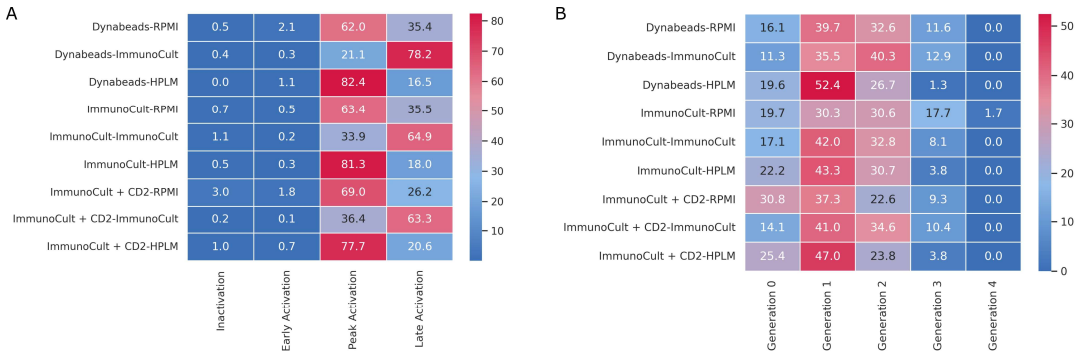

Figure 6 - Activation and proliferation stages of $CD4^+$ T cells from one donor stimulated and cultured under different conditions. **(A)** Heatmap showing the percentage of total $CD3^+CD4^+$ T cells at each activation stage for different stimulation and culturing conditions. The activation stages were determined based on the expression of CD69 and CD25: Inactivation ($CD25^-D69^-$), Early Activation ($CD25^-D69^+$), Peak Activation ($CD25^+D69^+$), Late Activation ($CD25^+D69^-$). **(B)** Heatmap showing the percentage of total $CD3^+CD4^+$ T cells present in the dividing generations for different stimulation and culturing conditions. The different generations were determined based on the intensity of CTV peaks: generation 0 was assigned to the most intense peak.

In summary, in this section, I have demonstrated that PBMCs are a good source of naïve $CD4^+$ T cells. Most donors had 14% to 36% of naïve $CD4^+$ T cells among the lymphocyte population. I have also shown that the population of naïve $CD4^+$ T cells isolated from PBMCs exhibited a purity of 95-97%. Finally, I have also investigated the parameters for optimal activation and proliferation of $CD4^+$ T cells. HPLM was identified as the best option to use as a culture medium due to its similarity to the human plasma composition. However, since the delivery of this reagent was unreliable, I had to choose RPMI as it was the second-best option. The RPMI was further supplemented with sodium pyruvate and non-essential amino acids. I have also determined that the type of stimulation (soluble vs magnetic beads) did not significantly change the activation or proliferation of CD4+ T cells. Thus, I chose magnetic dynabeads since these are the most commonly used method for stimulating human CD4+ T cells. Finally, the stimulation and culturing time was 72 hours. This time point was sufficient for more than half of the cells to divide while still being in a highly activated state.

4.3. SpaceM for CD4$^+$ T cells: adapting and improving the original method

4.3.1. From Cytospin to ProPlates: increasing throughput and decreasing variability

The successful setup of the activation and culture model allowed me to proceed to the next step, which was adapting the protocols of SpaceM to CD4$^+$ T cells. The original SpaceM sample preparation protocol consisted of adhering cells to glass slides compatible with the Widefield Nikon Ti-E microscope and the AP-SMALDI system. This was followed by fixation with 4% paraformaldehyde (PFA) and several washes in a volatile solvent like Ammonium Acetate to remove any medium components and avoid crystallization, finishing with the desiccation of the entire slide. SpaceM was developed for naturally adherent cells that would survive the harsher steps of the sample preparation protocol, and it had been only tested for bigger cells (20-40 µm diameter). Naïve CD4$^+$ T cells do not naturally adhere to any surface when in culture and have a diameter of 5 µm that expands only to 10 µm after activation [82], [83]. The reduced size of these cells was a concern in this project because metabolite concentration depends on the cytosol volume [84]. Thus, the two main anticipated challenges were cell adhesion and sensitivity.

There have been many reported successful methods for T cell immobilization, either with substrates commonly used in other cell types (e.g., poly-l-lysine, laminin, collagen type IV, and fibronectin) or with specific surface markers (i.e., CD3 and CD45) [85]–[88]. However, there was still a concern about the strength of the adhesion and whether the cells would survive the harsh washes necessary during the SpaceM protocol. Besides the methods mentioned above, a particular one has been extensively used for depositing immune cells onto glass slides: Cytopsin [89]. This method involves centrifuging cells onto a glass slide from a given cell suspension while removing all the liquid. The result is a perfect cell monolayer with intact morphology. The main drawback of this method is the throughput. While with the original SpaceM protocol, it was possible to have 4 individual samples per glass slide, with Cytospin, only one sample per slide was possible.

Naïve CD4$^+$ T cells were isolated from the peripheral blood of 2 healthy donors and divided into either Naïve or Activated conditions. The latter was stimulated with anti-CD3 and anti-CD28, and both conditions were cultured in RPMI for 72 hours. Cells were cytospined onto glass slides using a standard protocol for immune cells (30 minutes at

1000g). $CD4^+$ T cells were then desiccated before proceeding with the standard SpaceM protocol. This involved spraying the cells with 1,5-Diaminonaphthalin (DAN), a chemical matrix commonly used to detect metabolites and lipids in negative mode [90]. Given the exploratory nature of the whole project, a wide mass range of 100 to 1000 mz was scanned, and data annotation was done with METASPACE. The acquired data resulted from a single round of sample ionization with no further ion fragmentation performed. In other words, the acquired results only measured the mass of the molecules detected but had no additional information on their structure, meaning that isomers cannot be individually discerned. Multiple molecules are often assigned to a single ion, even when using databases explicitly curated for the metabolome (i.e., CoreMetabolome) [91]. The primary example of this limitation is glucose and its numerous isomers. In the results presented in this dissertation, I chose to report only one of the many candidate molecules annotated by METASPACE to make it easier to interpret. The choice of the reported molecules was supported by literature research, with frequently the most common metabolite or the most relevant one being chosen. In this dissertation, the reported metabolites with known isomers are all signaled with an asterisk.

The detection of small molecules was suboptimal in these experiments, with a low number of metabolites detected. Nevertheless, relevant metabolites like aspartic acid*, glutamic acid*, and glutathione could still be detected (**Figure 7A**). The results presented here reflect another issue besides the low throughput of Cytospin: reproducibility. For both analyzed donors, the detection of the three metabolites was quite variable between technical replicates. For example, aspartic acid* was only detected in half of the technical replicates of the Naïve condition in donor 15. The detection of glutamic acid* was more consistent between technical replicates. However, there was still relatively high variability concerning the intensity measured for each replicate. On top of that, the number of metabolites detected in donor 15 was half the number detected in donor 2 (**Figure 7B**). This showed that even though Cytospin was a pretty convenient method and very likely the most effective one in seeding $CD4^+$ T cells onto glass slides, the low throughput and the high variability made it necessary to look for another method.

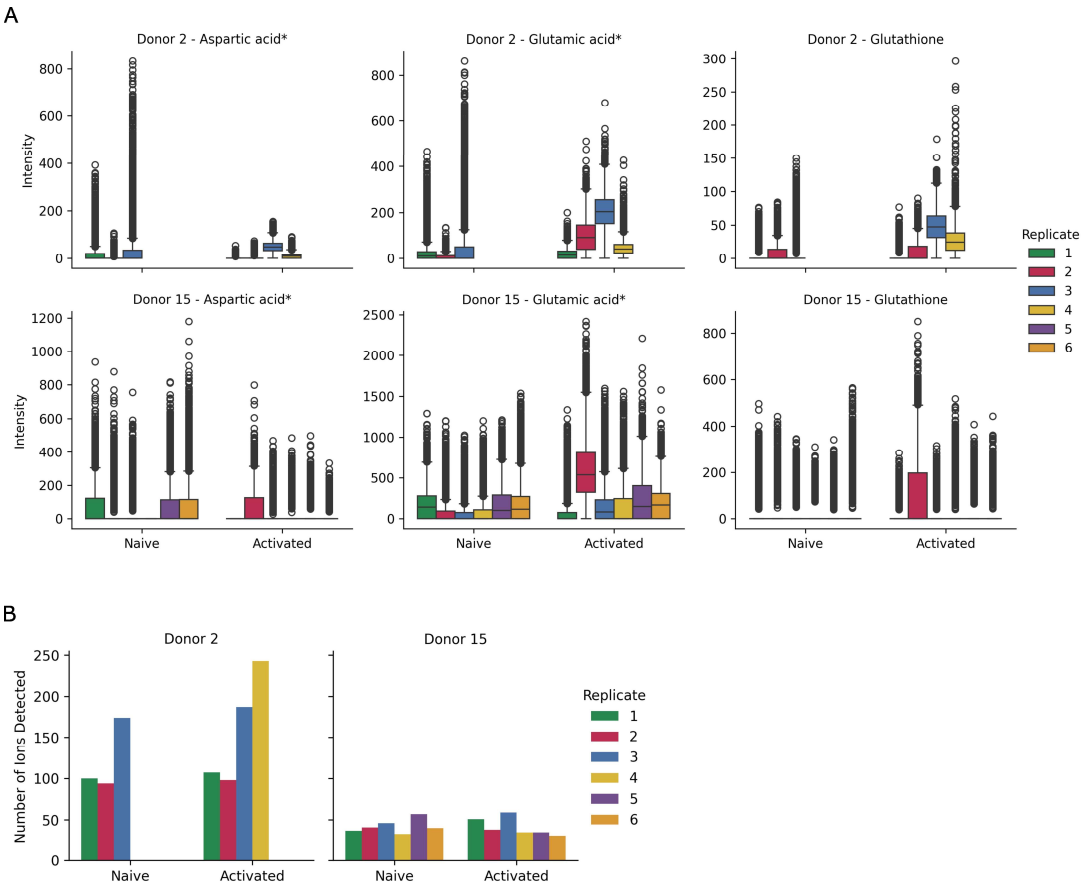

Figure 7 – Metabolites detected in naïve and activated CD4$^+$ T cells from two donors seeded with Cytopsin. The slides were sprayed with DAN and acquired in negative mode. The acquisition parameters included varying the laser attenuator between 33 and 36, setting the RF level to 50, capillary temperature to 150°C, and spray voltage to 3.1 kV. The sum intensity of the ions detected in each pixel was normalized to 10000. **(A)** Normalized single-pixel intensity of three metabolites. The asterisk indicates metabolites with known isomers. **(B)** Number of ions annotated for each replicate with CoreMetabolome (v3) database.

When searching for an alternative method to Cytospin, the main requirement was a multi-well system to avoid reproducibility issues. The method used in the original SpaceM protocol consisted of 4-well glass slides with incubation chambers that could be removed after cell adhesion (commercially known as Nunc™ Lab-Tek™ II Chamber Slide™ System). This removal step is necessary because a plain glass slide with no protrusions is required for the AP-SMALDI system. This would have been a great alternative to Cytospin, provided the cells could adhere. However, another solution was found before testing the Lab-Tek system. The found alternative, commercially named "ProPlate Multi-Well

Chambers", had higher throughput, with 64 reusable wells (**Figure 8A**). However, due to the spatial restrictions of the AP-SMALDI stage, only 40 wells out of the 64 could be reached and thus used. This was still better than any of the other available options.

One of the most critical features of SpaceM is the registration of pre and post-MALDI microscopy images, which is essential for signal deconvolution. The solution used to align both pre- and post-MALDI images in the original method relied on fiducial marks that delimited the corners of the wells. These were usually drawn by hand when using Lab-Teks or Cytospin slides. However, this was not possible with ProPlates, given the small size of the wells (3x3mm). This led to an additional step in the SpaceM pipeline, where 40 squares would be etched on plain glass slides before being attached to the ProPlates. Unique IDs were also etched on the top left corner of each square to easily identify the wells during processing and analysis. These were composed of one letter (A-J) that identified the row and one number (1-4) that identified the column (**Figure 8B**). Initially, each user etched their slides using a widefield microscope with an integrated laser (Widefield Zeiss MicroBeam). However, when the demand for such etched slides increased, this service was requested from a professional company. The implementation of the ProPlates in the SpaceM pipeline and the need to analyze multiple wells triggered the development of a new version of the method: HT-SpaceM.

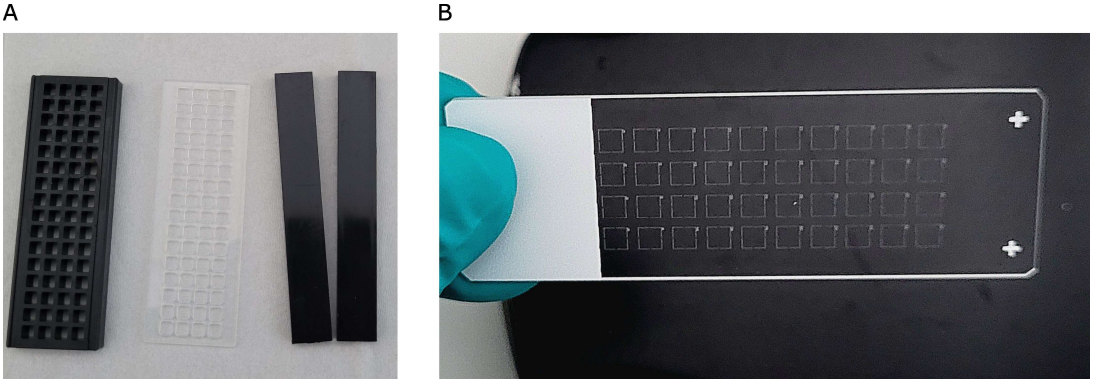

Figure 8 – Multi-well slides used in the HT-SpaceM pipeline. This system consists of multi-well chambers attached to glass slides. **(A)** Commercially available reusable multi-well chambers with 64 wells (ProPlate Multi-Well Chambers). **(B)** Custom-etched slides with 40 wells and unique well IDs. The dimensions of the wells match the dimensions of the multi-well chambers.

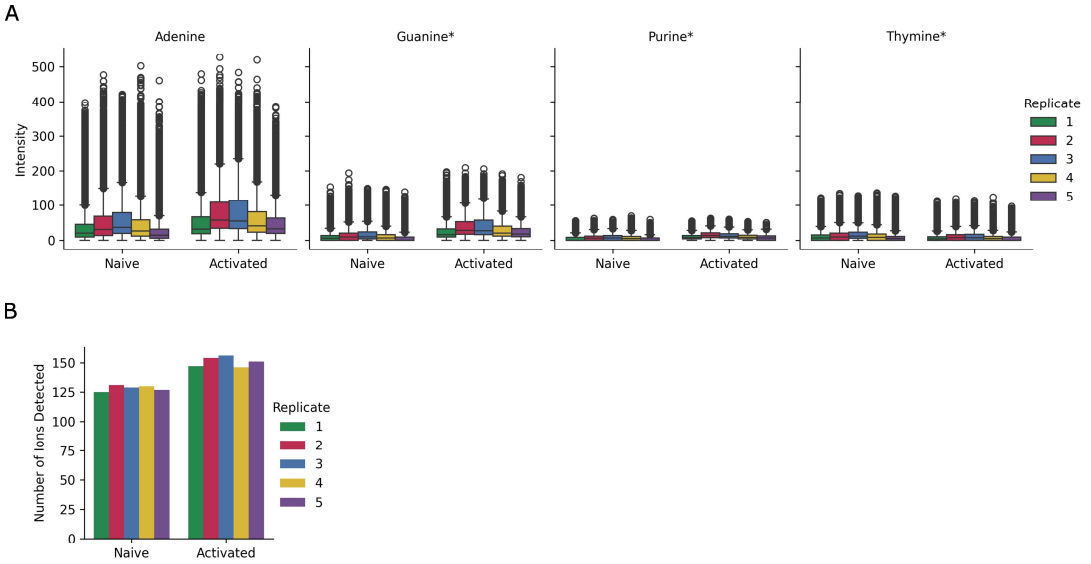

Figure 9 - Metabolites detected in naïve and activated CD4$^+$ T cells from one donor (D21). The slides were sprayed with NEDC and acquired in negative mode. The acquisition parameters included the laser attenuator set to 27, RF level to 50, capillary temperature to 150°C, and spray voltage to 3.1 kV. The sum intensity of the ions detected in each pixel was normalized to 10000. **(A)** Normalized single-pixel intensity of four metabolites. The asterisk indicates metabolites with known isomers. **(B)** Number of ions annotated for each replicate with CoreMetabolome (v3) database.

The new protocol required another method for cell adhesion. According to the available literature, poly-l-lysine (PLL) coating of slides/plates is one of the most used methods for T-cell adhesion [92]. One particular protocol published in 2017 reported that 30 minutes was enough for lymphocytes to adhere to PLL-coated coverslips when resuspended in PBS [93]. Since the goal was to study the metabolism and interfere with it as little as possible, this seemed like a correct approach due to the fastness of adhesion. The first attempt to run this protocol worked well, with naïve and activated CD4$^+$ T cells strongly adhering to the PLL-coated glass slides, surviving a wash with PBS, then fixation with 4% PFA, and a last wash with Ammonium Acetate. The matrix chosen for small molecule detection was N-(1-naphthyl) ethylenediamine dihydrochloride (NEDC) and not DAN as in the previous experiments. The change in the matrix was motivated by other internal results in our group and in an earlier study, where NEDC was very accurate for

small molecule detection in mouse tissues [94]. The number of metabolites detected was relatively low, consisting mainly of purine and pyrimidine molecules (**Figure 9A**). Metabolites such as aspartic acid*, glutamic acid*, or glutathione were not detected, contrary to the previous experiment. However, reproducibility was much more consistent (**Figure 9B**), with all replicates having the same number of ions detected and similar intensities for each metabolite. The key factors when deciding to proceed with this method were the high throughput potential and the consistent reproducibility between technical replicates. However, it was still necessary to further optimize the sample preparation method due to the low amount of metabolites detected. The results indicated that 125-150 ions were detected in each replicate. This was misleading due to the broad coverage of the database used (CoreMetabolome), which included many bacterial and exogenous metabolites (i.e., part of the human exposome). Detecting such metabolites in a controlled and isolated environment like *in vitro* cell culture is not expected. The annotation of such molecules was taken carefully, and it was presumed that many were false positives. In addition to this, cell adhesion was also inconsistent when the protocol presented here with PLL was repeated for other donors. In other words, the homogenous adhesion observed in this experiment could not be further reproduced. The following steps involved optimizing two key points: sample preparation (i.e., cell adhesion) and metabolite detection. In summary, in this section, I have presented the first main change introduced in the SpaceM pipeline when adapting this method to $CD4^+$ T cells. The old low-throughput slides were switched to high-throughput ones with 40 wells.

4.3.2. Robust adhesion of $CD4^+$ T cells to glass slides: the first milestone

Cell adhesion was the priority since it is one of the first and essential sample preparation steps. The protocol described previously involving PLL was quite inconsistent, and it was often the case that some of the wells would be fully covered with cells in the same slide while others would be half empty. This issue was not majorly associated with the condition (Naïve or. Activated) or the spatial distribution of the wells (row or column). Thus, my approach to this question was to test multiple adhesion methods described in the literature or previously used in our laboratory. To make the results more objective and straightforward to interpret, I have defined an “Adhesion Score” that reflects the efficacy of the tested method. Only five values were defined to avoid overcomplicating the score

(0, 25, 50, 75, 100). A score of 0 means that none of the wells were at least half-covered with cells for a given slide, while a score of 25 means that only 25% of the wells in the slide were half-covered with cells. The same logic is applied to the rest of the score values.

The only exception was the first optimization experiment, which tested many parameters in a given slide. For this experiment, the score applies to a single well instead of a whole slide, reflecting the percentage of adhesion within that well. A score of 0 indicates no cells adhered, while 75 means that 75% of the well is covered with cells. As mentioned above, many methods have been successfully used in the adhesion of $CD4^+$ T cells. There was a particular method that I wanted to avoid that involved immobilizing $CD4^+$ T cells with anti-CD3 because the strong activation induced by this molecule could compromise the Naïve condition [88].

Since PLL is one of the most commonly used protocols for T cell adhesion and had previously worked with these cells, it was the main method used in this first optimization experiment. Only one slide was used in this experiment, meaning each well had a unique combination of the tested parameters (**Table 3)**. In this experiment, three different parameters were tested: PLL type, PLL concentration, and cell concentration. Two types of PLL commonly used for cell adhesion that differ in molecular weight were tested here. The PLL type with a lower molecular weight is less viscous and easier to handle, while the high molecular weight one provides more binding sites. In addition, the concentration of the PLL solution used was also tested. The standard and commercially available concentration is 0.1 mg/mL. However, some manufacturers often recommend diluting it two times before using it. The third parameter tested was the cell density. $CD4^+$ T cells require cell-to-cell contact and high density for proper activation and proliferation [95]. Thus, I also wondered if cell density would compromise the adhesion and what the lower limit would be.

Table 3 – First adhesion experiment with optimization of three parameters and the respective score.

Molecular Weight (Dalton)	Concentration (mg/mL)	Cell Density (10^6 cells/mL)	Adhesion Score
Low (84 kDa)	0.1	0.25	75
Low (84 kDa)	0.1	0.5	100
Low (84 kDa)	0.05	0.25	75
Low (84 kDa)	0.05	0.5	100
High (150-300 kDa)	0.1	0.25	75
High (150-300 kDa)	0.1	0.5	75
High (150-300 kDa)	0.05	0.25	100
High (150-300 kDa)	0.05	0.5	100

Naïve $CD4^+$ T cells were activated for 72h, resuspended in PBS, and seeded onto a ProPlate system attached to a glass slide. Following a similar protocol used before, the cells were left to adhere for 30 minutes at 4°C and then fixed for 10 minutes with 4% PFA before desiccation. The fast incubation time, the solvent, and the temperature chosen aimed to interfere with the metabolic state of the cells as little as possible. The results showed no significant difference between the low (84 kDa) and high molecular weight PLL (150-300 kDa). Higher cell density resulted in a perfect score for the low molecular weight PLL, while the concentration did not seem to impact adhesion. The opposite effect was observed for the high molecular weight PLL. There, the lower concentration of PLL resulted in a perfect score independent of the cell density. The main limitation of this experiment was the lack of technical replicates for each one of the combinations tested. Nevertheless, I proceeded with the protocol that seemed more adequate. The high molecular weight PLL was chosen due to its theoretically higher number of binding spots. For both concentration and cell density, the lower options were selected. Low cell density is essential for SpaceM processing. Ideally, monolayers of cells should be avoided for better signal deconvolution, and this was achieved with lower cell density without impacting adhesion, as demonstrated in the results. Thus, I have proceeded with a protocol that used 0.05 mg/mL of high molecular weight PLL and a cell density of $0.25x10^6$ cells/mL.

The new adhesion protocol was tested for multiple donors, and unfortunately, it was never consistent. The same issue reported above was still observed. Wells seeded with cells from the same condition would have inconsistent adhesion outcomes. Eventually, I repeated the adhesion protocol and switched to PBS supplemented with Ca^{2+} and Mg^{2+}. The two cations are essential for adhesion and are not present in the regular PBS formulation [96]. However, there was no improvement in cell adhesion compared to before (data not shown). Given the inconsistency observed, a new optimization experiment was necessary.

The second adhesion optimization experiment was done with PBMCs instead of activated $CD4^+$ T cells. This choice was because isolating just PBMCs from peripheral blood samples was faster, easier, and less expensive than $CD4^+$ T cells. In addition to that, PBMCs are mainly composed of T and B cells, which are both naturally non-adherent cells. These details made PBMCs an optimal model for optimization experiments. All the tested slides were coated with high-weight PLL (150-300 kDa), and the concentration chosen was 0.05 mg/mL. The main goal of this optimization experiment was to find another method for cell sedimentation and slide washing. Thus, it was tested whether spinning down the cells for 5 minutes after seeding into the wells would provide higher efficacy. This was compared against the standard protocol of letting the cells adhere by gravitation for 30 minutes in PBS. Another reason for the poor and inconsistent adhesion results observed could be the washing method. The standard method involved separating the ProPlate from the slide and dipping the latter in a beaker with Ammonium Acetate at least 3 times. I suspected that this procedure could be too harsh for $CD4^+$ T cells. Thus, a new washing method that involved carefully pipetting the Ammonium Acetate solution into the wells was tested. These slides were dried in the desiccator, and the ProPlates were still attached to the slides. Thus, in this experiment, five parameters were optimized: adhesion method (gravitation vs. centrifugation), adhesion time (5 vs. 30 minutes), adhesion temperature (4°C vs. RT), washing method (dipping vs. pipetting), and drying method (ProPlates on vs. ProPlates off).

The adhesion score for this experiment (**Table 4**) reflects the number of wells per slide successfully seeded, with a score of 100, meaning that all the wells are at least fully covered with cells. The slides were desiccated for 30 minutes after the seeding and washing steps. After desiccation, it was already possible to conclude that leaving the ProPlates attached to the slides during this step was not ideal. These slides had many crystal structures

(data not shown) that mainly accumulated around the well edges. These were probably PBS crystals since Ammonium Acetate is volatile. This indicated that washing by pipetting Ammonium Acetate in and out is inefficient in removing the medium/solution used during seeding. Thus, this washing option had to be discarded. Cell adhesion by centrifugation had the perfect score of 100, making it a suitable alternative to the standard method of gravitation (score of 75). This method consisted of seeding the cells onto the ProPlate system and then centrifuging it using a plate holder. Unfortunately, the centrifugation method was as inconsistent as the gravitation method when I tried reproducing it for $CD4^+$ T cells from other donors.

Table 4 - Second adhesion experiment with optimization of five parameters and the respective score.

Adhesion Method	Adhesion Time	Adhesion Temperature	Washing Method	Drying Method	Adhesion Score
Gravitation	30 min	4°C	Dipping	ProPlates off	75
Gravitation	30 min	4°C	Pipetting	ProPlates on	50
Centrifugation	5 min	RT	Dipping	ProPlates off	100
Centrifugation	5 min	RT	Pipetting	ProPlates on	75

It was still unclear what the origin of the inconsistency of cell adhesion between different slides and donors was. The following optimization experiment still focused on the two main suspects: adhesion and washing methods (**Table 5**). For this experiment, both naïve and activated $CD4^+$ T cells were used, and the isolation and culture protocols followed were the same as mentioned previously. The slides used were coated with PLL at a concentration of 0.05 mg/mL. In the previous experiments, cells were resuspended and seeded in PBS. However, given the inconsistency of the results, I started to hypothesize whether the prolonged incubation in PBS (30 minutes) could affect cell viability and adhesion. This was tested by seeding cells and letting them adhere by gravitation in either PBS or RPMI. While the adhesion score of cells seeded in PBS was 25, the RPMI score was 75. The poor adhesion score for cells seeded in PBS reflected the previous inconsistency and the better score for cells seeded in RPMI seemed to be a good alternative worth trying. However, it was evident that adhesion by gravitation was not the most

successful method. Thus, I tried another method that simultaneously addressed the adhesion and washing problems, and it was based on Cytospin. This method consisted of seeding the cells and centrifuging the ProPlate system facing upwards for 5 minutes. After this, the ProPlate system was placed in the plate holder facing down and centrifuged for 5 more minutes; this step was named Reverse Centrifugation. The objective was to let the cells adhere during the first centrifugation and remove all the liquid with the second one. The choice of medium did not impact cell adhesion when cells were centrifugated. On the other hand, the force used did affect the results, with 1000g leading to the best adhesion score. However, a significant amount of debris and ruptured cells was observed with this method regardless of the force used. There was an additional set of experiments where the force was reduced to 100g and 50g (data not shown). However, this resulted in the liquid not being efficiently removed, and on top of that, cell debris was still observable. Thus, Reverse Centrifugation was not suitable for cell adhesion, so I had to search for an alternative.

Table 5 - Third adhesion experiment with optimization of five parameters and the respective score.

Adhesion Method	Adhesion Medium	Adhesion Time	Adhesion Temperature	Washing Method	Adhesion Score
Gravitation	PBS	30 min	4°C	Dipping	25
Gravitation	RPMI	30 min	4°C	Dipping	75
Centrifugation – 400g	PBS	5 min	RT	Reverse Centrifugation	50
Centrifugation – 400g	RPMI	5 min	RT	Reverse Centrifugation	50
Centrifugation – 1000g	PBS	5 min	RT	Reverse Centrifugation	75
Centrifugation – 1000g	RPMI	5 min	RT	Reverse Centrifugation	75

One positive outcome of the abovementioned experiment was the improved adhesion when RPMI was used. For the fourth adhesion experiment, I focused on parameters that had been overlooked before, such as temperature and time of adhesion. The previous settings were 4°C and 30 minutes, respectively. The low temperature aimed to arrest the metabolism, while the short incubation time was chosen due to the poor survival of cells incubated in PBS for long periods. It has been reported that 30 minutes is enough for PBMCs to adhere to PLL-coated plates [93]. However, the possibility that $CD4^+$ T cells would require more time to adhere strongly had to be considered. Since I switched to RPMI,

the adhesion time was no longer a restriction, and longer periods were tested. In addition, the incubation temperature was increased to 37°C since most protocols recommended it [88], [97], [98]. For this experiment, naïve and activated $CD4^+$ T cells were cultured using the protocol described before. Naïve and activated cells were resuspended in RPMI and let to adhere at 37°C as indicated in **Table 6**. This experiment mainly aimed to optimize the adhesion by testing different incubation times and using a gentler method for washing (flushing instead of dipping). Increasing the adhesion time from 15 or 30 minutes to 1, 3, or 24 hours did not significantly improve adhesion. In addition, the slides with shorter adhesion times (15 min, 30 min, 1h) were flushed with Ammonium Acetate using a pipette. Although gentler than the standard wash of dipping the slides in a beaker, this method did not help improve the adhesion score.

Given the inconsistent results, the choice of PLL as the adhesion substrate also started to be heavily questioned. One of the studies mentioned above reported that lymphocytes adhered to plastic surfaces without coating after 30 minutes of gravity sedimentation [93]. Thus, it was worth trying this approach and evaluating if $CD4^+$ T cells would adhere to glass without any coating. Another issue frequently observed in the successfully seeded wells was an "edge effect". In other words, the cell distribution was not homogeneous within the wells, and the cells mainly adhered around the edges, leaving the center empty. A valid method to avoid this effect is pre-incubating the plates/slides at room temperature (RT) for 2 hours before culturing at 37°C [99]. In this experiment, an incubation of 30 minutes at RT followed by 30 minutes at 37°C was used to compare cell adhesion in PLL-coated with non-coated slides (**Table 6**). The adhesion score of non-coated slides was significantly superior to that of PLL-coated slides. The edge effect was also lower in these slides, confirming that the incubation at RT was a valid approach. Since increasing the incubation time or the temperature did not improve adhesion with PLL and all the previous attempts were unsuccessful, I stopped coating the slide with it. Instead, I switched to using non-coated slides, given the preliminary results observed in the fourth optimization experiment.

Table 6 - Fourth adhesion experiment with optimization of four parameters and the respective score.

PLL Coating	Adhesion Time	Adhesion Temperature	Washing Method	Adhesion Score
+	15 min	37°C	Flushing	50
+	30 min	37°C	Flushing	25
+	1h	37°C	Flushing	50
+	3h	37°C	Dipping	50
+	24h	37°C	Dipping	0
-	1h	RT + 37°C	Flushing	75
+	1h	RT + 37°C	Flushing	25

Although counterintuitive, the new adhesion method without coating offered more consistent results. However, the adhesion was still an issue with the slides having some wells empty and others fully seeded. One last optimization was designed to solve this issue in an experiment divided into different parts. The first part compared the non-coated slides with slides coated with Poly-D-Lysine (PDL), which, contrary to PLL, cannot be digested by proteases, and this could explain the poor adhesion observed before [100]. In addition to this, another adhesion method was tested based on using centrifugation to deposit the cells. Thus, in the first part of the experiment, I aimed to optimize the coating method (PDL vs. no coating) and the adhesion method (30 min centrifugation vs. 5 min centrifugation + 30 min adhesion). The naïve and activated cells resuspended in RPMI were seeded onto the wells, and the ProPlates were centrifuged for 5 or 30 minutes. The shortest centrifugation time was followed by a 30-minute incubation at RT (**Table 7**). No improvement was observed for either using a long centrifugation for cell deposition or doing a short centrifugation followed by gravitation. The adhesion score in PDL-coated slides was higher than in non-coated ones. However, it was still suboptimal. Thus, neither the PDL nor the centrifugation methods tested were suitable alternatives to the gravitation without coating method. The second part of the experiment aimed to test $CD4^+$ T cell adhesion to collagen. Both naïve and activated cells resuspended in RPMI were seeded onto the ProPlates and incubated for 4 hours at 37°C in either collagen-coated or non-coated slides. The collagen coating did not significantly improve the adhesion. The adhesion score of cells seeded on collagen was 25, while cells seeded on non-coated slides had a higher score of 50. Thus, collagen was also not a suitable alternative for cell adhesion.

Table 7 - Fifth adhesion experiment with optimization of four parameters and the respective score

Coating Method	Adhesion Method	Adhesion Time	Adhesion Temperature	Adhesion Score
-	Centrifugation + Gravitation	5 min + 30 min	RT	0
-	Centrifugation	30 min	RT	0
PDL	Centrifugation + Gravitation	5 min + 30 min	RT	25
PDL	Centrifugation	30 min	RT	25
-	Gravitation	4h	37°C	50
Collagen	Gravitation	4h	37°C	25

Given the time restrictions, stopping the optimization experiments and choosing a protocol was necessary. The method selected for adhesion was gravitation in non-coated slides. Even though the results were not optimal, this method still offered the highest consistency of all tested ones. Given the low adhesion score observed when cells were incubated for 4 hours at 37°C, the chosen adhesion temperature was RT. The adhesion time was increased to 2 hours instead of the typical 30 minutes and 1 hour. This change finally solved the adhesion problems, and no further optimization experiments were necessary. Thus, the final protocol consisted of taking both naïve and activated $CD4^+$ T cells resuspended in RPMI and seeding them onto the ProPlates attached to plain glass slides. The cells adhered at RT for 2 hours before detaching the ProPlates from the slides. These were then fixed with 4% PFA for 10 minutes, dipped in a beaker with Ammonium Acetate, and desiccated for 30 minutes. In **Figure 10**, the microscopy images show both naïve and activated $CD4^+$ T cells from 3 different donors after desiccation. Microscopy results showed that activated cells were bigger than naïve cells. However, the size did not affect the adhesion, with both naïve and activated cells having consistent results with the chosen protocol. Considering this, the seeding density was adjusted according to the cell size. Naïve $CD4^+$ T cells were seeded at a concentration of $0.5x10^6$ cells/mL (25k cells per well), while activated cells were seeded at a concentration of $0.3x10^6$ cells/mL (15k cells per well). In conclusion, in this section, I optimized the adhesion method to the glass slides attached to the ProPlate system. The optimal protocol found after many optimizations used plain glass slides and required the cells to adhere for 2 hours at RT.

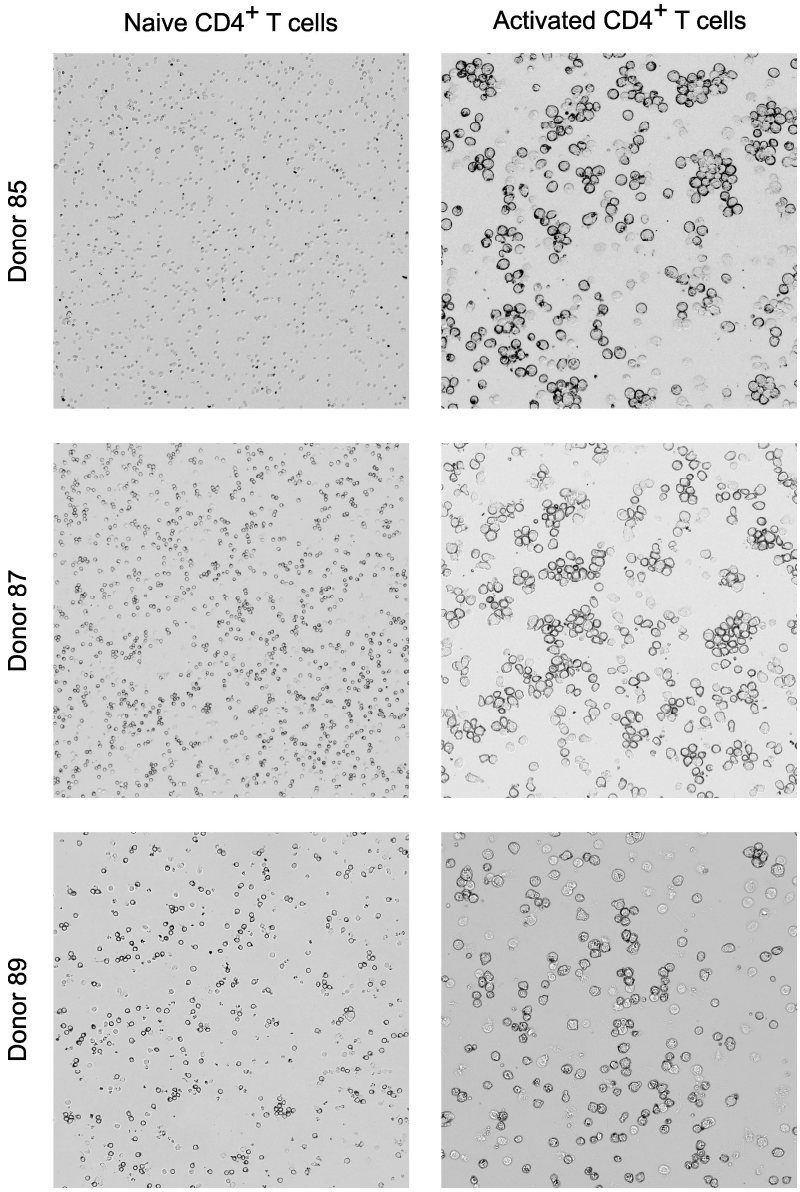

Figure 10 – Microscopy images (10x magnification) of desiccated naïve and $CD4^+$ T cells from three donors.

4.3.3. Reproducible sample preparation method: the second milestone

The successful implementation of the adhesion method allowed me to focus on the next challenge: reproducibility. The initial experiments with the new adhesion protocol revealed a high variability among the metabolites detected for naïve and activated cells. The matrix chosen for these experiments was DAN due to its good performance in detecting amino acids, carboxylic acids, and nucleotides [101]. The measured metabolites exhibited huge variability in both detection and intensity across experiments run over consecutive months (**Figure 11A**). Interestingly, the total number of metabolites detected did not correlate with the poor detection observed for some metabolites (**Figure 11B**). This is the case of glutamine* and aspartic acid*, which were optimally measured in the experiment with fewer total ions detected. This made me wonder whether some step during the cell preparation protocol was causing this variability. The main hypothesis was that the fixation step with 4% PFA between adhesion and desiccation was causing metabolite leakage. This was supported by previous reports that PFA can potentially increase the permeability of the cell membrane [102].

It was essential to test this hypothesis, and in case it was confirmed, it was necessary to find a suitable alternative to fixation. The simplest solution was skipping the fixation step and directly desiccating the cells after adhesion. However, it was uncertain whether the time necessary to remove all the water from the cells would cause significant metabolic changes since these would still be alive. Thus, a second solution was conceived: dipping the glass slides in liquid nitrogen (LN2) to snap-freeze the cells before desiccation. For the pilot experiment, PBMCs were isolated from the peripheral blood of 3 different donors and seeded onto the ProPlates attached to glass slides as described before. After adhesion, the cells were either: fixed with 4%PFA, washed with Ammonium Acetate and desiccated; or only washed with Ammonium Acetate and desiccated; or washed with Ammonium Acetate, snap frozen with LN2 and desiccated. The results showed that except for adenine, no other metabolite could be consistently detected across 3 different donors in cells fixed with PFA, confirming the previous results (**Figure 12A**). On the other hand, only glucose 6-phosphate* (G6P) could not be consistently detected in cells that were either desiccated or snap-frozen with LN2. This proved that the initial hypothesis was correct, and the permeability resultant from PFA fixation led to the leakage of small molecules. The use of PFA had to be skipped, so the remaining question was which alternative to choose. Both methods had similar results regarding metabolite detection and intensity. However, both

methods exhibited significant differences in metabolite co-localization and spatial distribution in single-pixel images from this data provided by METASPACE (**Figure 11B**). While in just desiccated cells, adenine was colocalizing with glutamic acid* and glutathione, in snap-frozen cells, adenine was anti-colocalizing with these two metabolites. This suggested that both glutamic acid* and glutathione were detected outside the cells, possibly due to membrane disruption caused by LN2.

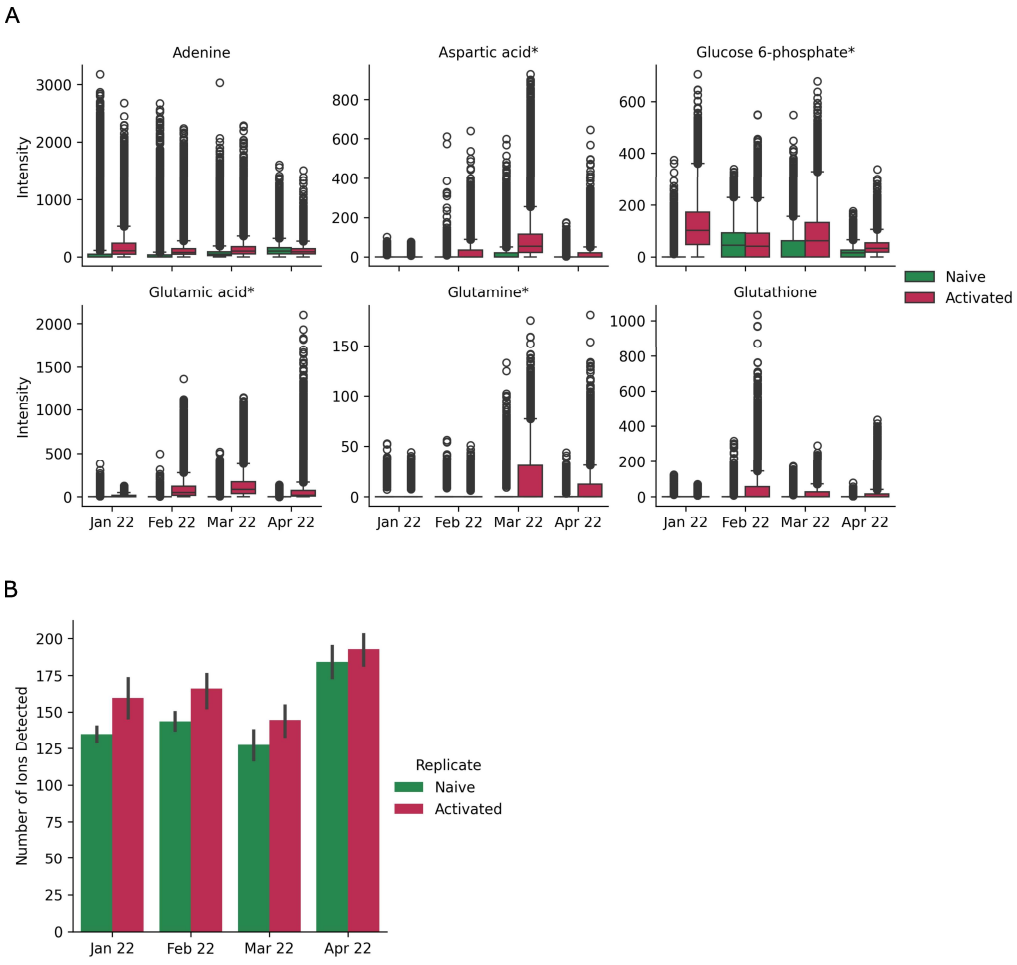

Figure 11 - Metabolites detected in naïve and activated CD4^{+} T cells from different donors across different experiments. The slides were sprayed with DAN and acquired in negative mode. The acquisition parameters included the laser attenuator set to 29, RF level to 50, capillary temperature to 350°C, and spray voltage to 3.1 kV. The sum intensity of the ions detected in each pixel was normalized to 10000. **(A)** Normalized single-pixel intensity of six metabolites. The asterisk indicates metabolites with known isomers. **(B)** Number of ions annotated for each replicate with CoreMetabolome (v3) database.

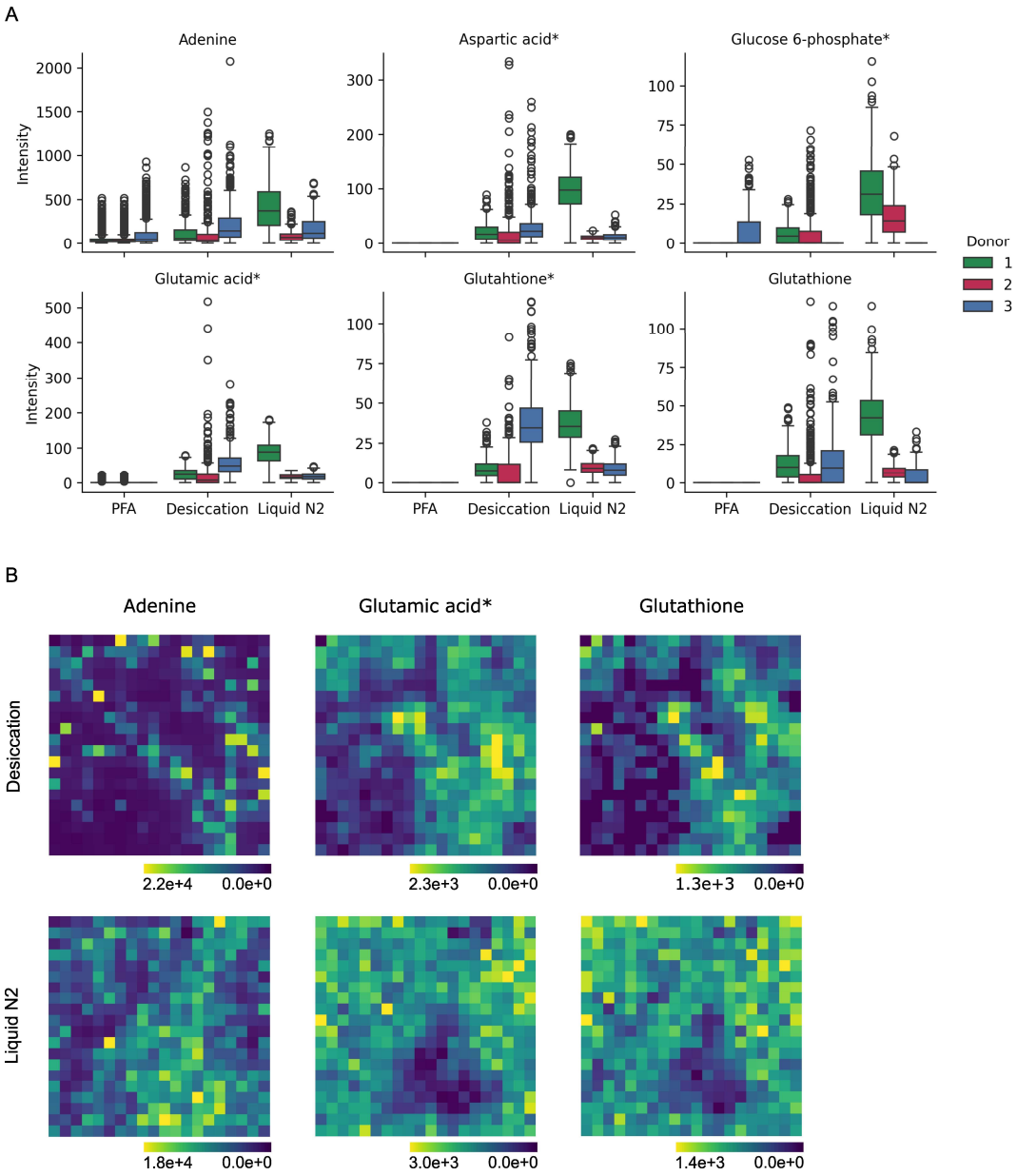

Figure 12 - Metabolites detected in PBMCs cells from three donors for different sample preservation methods. The slides were sprayed with DAN and acquired in negative mode. The acquisition parameters included the laser attenuator set to 29, RF level to 50, capillary temperature to 350°C, and spray voltage to 3.1 kV. The sum intensity of the ions detected in each pixel was normalized to 10000. **(A)** Normalized single-pixel intensity of six metabolites. The asterisk indicates metabolites with known isomers. **(B)** Spatial distribution images of three metabolites provided by METASPACE .

Before making the final decision, the same experiment was run for both naïve and activated CD4$^+$ T cells from one donor. The PFA fixation condition was skipped, so the metabolite detection was mainly compared between desiccated and snap-frozen cells (**Figure 13**). The results showed that the detection between both methods was quite comparable. The poor detection of G6P* in activated cells preserved with desiccation was surprising. However, it was not a reason for concern since it was well detected in both naïve cells and PBMCs, and most likely, other factors affected these results. Given the delocalization concerns in LN2-preserved samples, I chose the desiccation method for sample stabilization. In summary, in this section, I have demonstrated that PFA fixation caused metabolite leakage and was the reason for inconsistent results across different experiments. I have introduced another change to the original SpaceM protocol by skipping PFA fixation and directly desiccating the cells after adhesion.

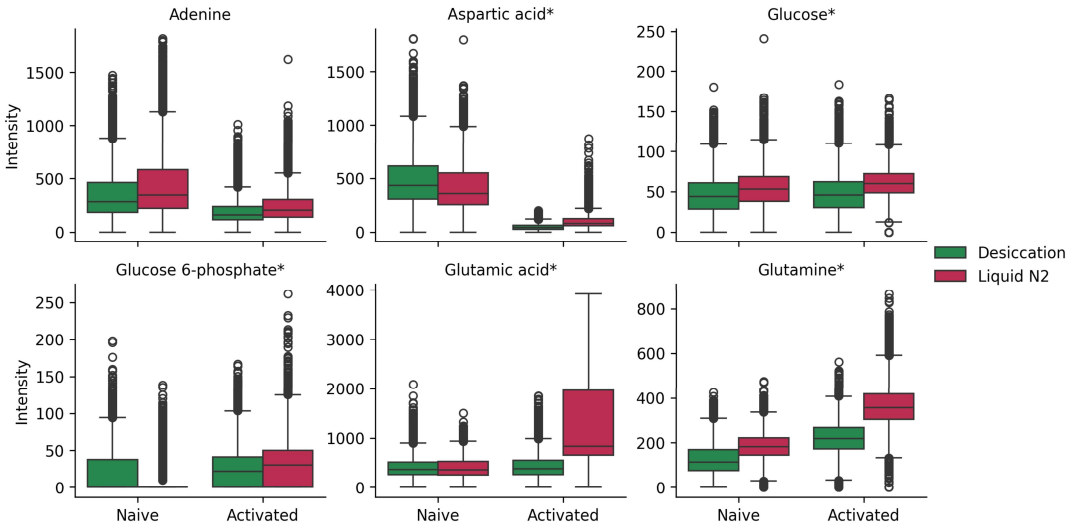

Figure 13 - Metabolites detected in naïve and activated CD4$^+$ T cells preserved using the desiccation or LN2 method. The slides were sprayed with DAN and acquired in negative mode. The acquisition parameters included the laser attenuator set to 29, RF level to 50, capillary temperature to 350°C, and spray voltage to 3.1 kV. The sum intensity of the ions detected in each pixel was normalized to 10000. The asterisk indicates metabolites with known isomers

4.3.4. Improved detection and increased coverage: the third milestone

The change in the sample preparation protocol mentioned in the previous section was a significant breakthrough that improved metabolite detection. However, it was still possible to optimize the signal further. The three main factors I focused on were the chemical matrix, the mass spectrometer parameters, and the MALDI parameters. The chemical matrix and polarity choice will determine the type of molecules detected. These are the two most critical parameters for detection, while the other parameters are more helpful in improving and tuning the signal. The negative polarity is the most efficient mode for the detection of many small molecules (e.g., amino acids, carboxylic acids, nucleotides), and the commonly used matrices for this purpose are NEDC, DAN, and 9-Aminoacridine (9AA) [90], [94], [103], [104]. The additional parameters that can be fine-tuned include, but are not limited to, the capillary temperature and the S-lens RF level. The MALDI-imaging MS pipeline starts with spraying the chemical matrix onto the sample. The coated sample is then placed in the MALDI source and ionized with the assistance of a laser while a spray voltage is applied to help redirect the ions to the Mass Spectrometer [105]. After ionization, the sample is redirected to a heated inlet, where the vaporization and transition from atmospheric pressure to vacuum occur [106]. The primary function of the S-lens is to focus the ionized molecules into a beam after leaving the inlet for optimal transmission to the mass analyzer [107]. In addition, the MALDI source also contains two parameters that could influence the intensity of the signal: attenuator and pixel size. The first acts as a filter for the laser power and measures the angle of attenuation applied [108]. The lower the attenuator level, the higher the laser power will be. However, excessive laser power can cause unwanted fragmentation, and the ideal value might depend on the matrix used [109]. Finally, the pixel size and the laser diameter determine the spatial resolution. The smaller the pixel size, the higher the resolution, which results in less sensitivity [110].

All the parameters mentioned above were tested in activated $CD4^+$ T cells isolated from different donors and cultured as described before. The negative mode was a clear choice since the main target was the detection of small molecules. However, it was necessary to choose the appropriate matrix from the three mentioned options (DAN, NEDC, 9AA). It is important to disclaim that the first experiment was performed in cells fixed with 4% PFA because it was run before the sample preparation protocol was finalized. The main goal of the first experiment was to compare the three matrixes commonly used for small molecule detection in negative mode. In addition to that, different attenuator

levels were tested to understand the optimal range for each matrix. The other parameters (e.g., S-lens RF level and capillary temperature) were set to standard values commonly used in the laboratory and optimized only later. **Figure 14** shows the intensity of four primary metabolites for each matrix and different attenuator levels. The slide sprayed with the DAN matrix exhibited higher coverage than the others, with the optimal attenuator level ranging from 29 to 31. Similar to previous results, NEDC was great for detecting Adenine but no other metabolites. The results for 9AA were ambiguous, with decent detection of G6P* but very low detection of the other metabolites. However, the results should be taken carefully as they could have been heavily influenced by each slide being differently affected by the fixation step.

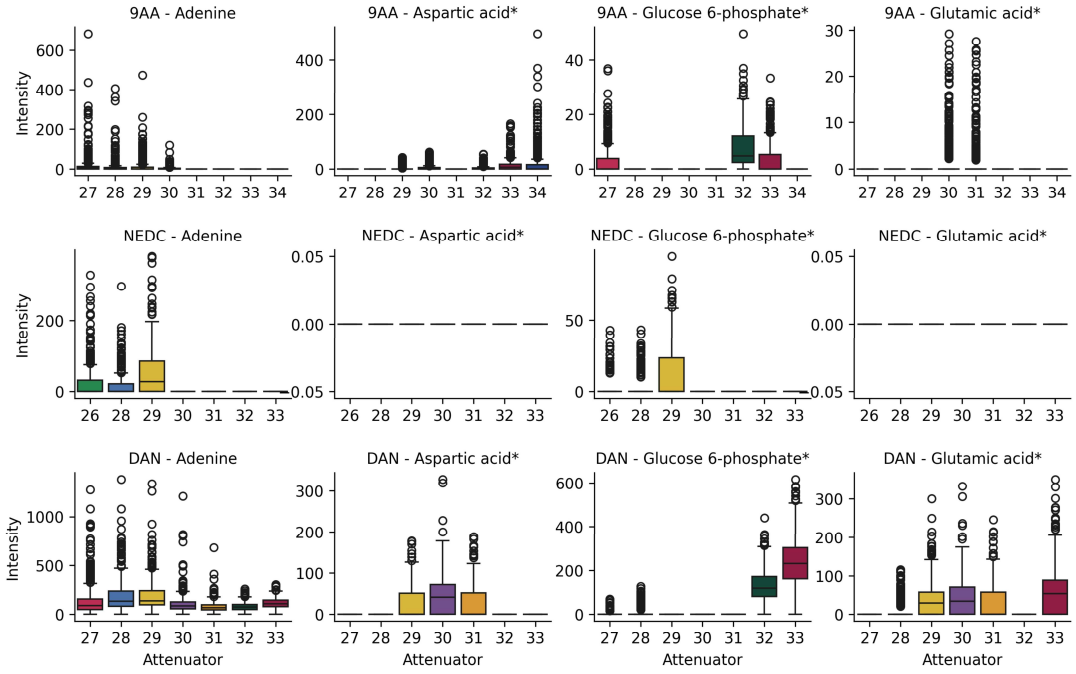

Figure 14 - Metabolites detected in activated $CD4^+$ T cells sprayed with different matrices. The slides were sprayed with DAN, NEDC or 9AA and acquired in negative mode. The acquisition parameters included RF level to 50, capillary temperature to 150°C, and spray voltage to 3.1 kV. The sum intensity of the ions detected in each pixel was normalized to 10000. The asterisk indicates metabolites with known isomers

The experiment that followed was run on non-fixed and activated cells, with attenuator, pixel size, capillary temperature, and S-lens RF level being thoroughly tested in both DAN and 9AA matrices. The decision to drop NEDC was supported by data available on METASPACE from a project run by other group members in collaboration with other imaging laboratories [111]. In that project, they evaluated the detectability of multiple chemical classes in different matrices in both negative and positive polarity. The results are summarized and available for public consultation. These showed that DAN and 9AA were significantly better than NEDC at detecting small molecules (i.e., carboxylic acids, amino acids, nucleotides, and carbohydrates). The methodology followed in the experiment was quite simple. I started by setting each parameter (attenuator, pixel size, capillary temperature, RF level) to the default value used in other metabolomics protocols in our group. Then, each parameter was tested individually and sequentially. Thus, at the beginning of the experiment, the attenuator level was set to 29, the pixel size to 20 μm, the capillary temperature to 150°C, and the RF level to 50.

The standard inlet capillary temperature used in other protocols in the group was 150°C. However, higher values are commonly used in the literature, with a study showing that the intensity of glutamine doubled when the temperature was increased from 150°C to 250°C [112]–[114]. Thus, the capillary temperature was the first parameter to be optimized, and the chosen test values were 150°C, 250°C, and 350°C (**Figure 15**). The effect of each temperature value was evaluated by checking how the intensity of four key metabolites was affected (aspartic acid*, glucose 6-phosphate*, glutamic acid *, glutamine*). In general, the intensity of the selected metabolites was very similar across different temperatures for both matrices (**Figure 15A**). However, increasing the temperature significantly improved the intensity of aspartic acid* and G6P* in cells sprayed with DAN. On the other hand, increasing the temperature resulted in lower intensity of adenine and glutamine* when the matrix was 9AA. The increased temperature did not affect the ion intensities significantly. However, it did affect the number of ions, with higher capillary temperature resulting in more molecules detected (**Figure 15B**). Thus, I set the capillary temperature to 350°C and moved on to optimize the following parameter.

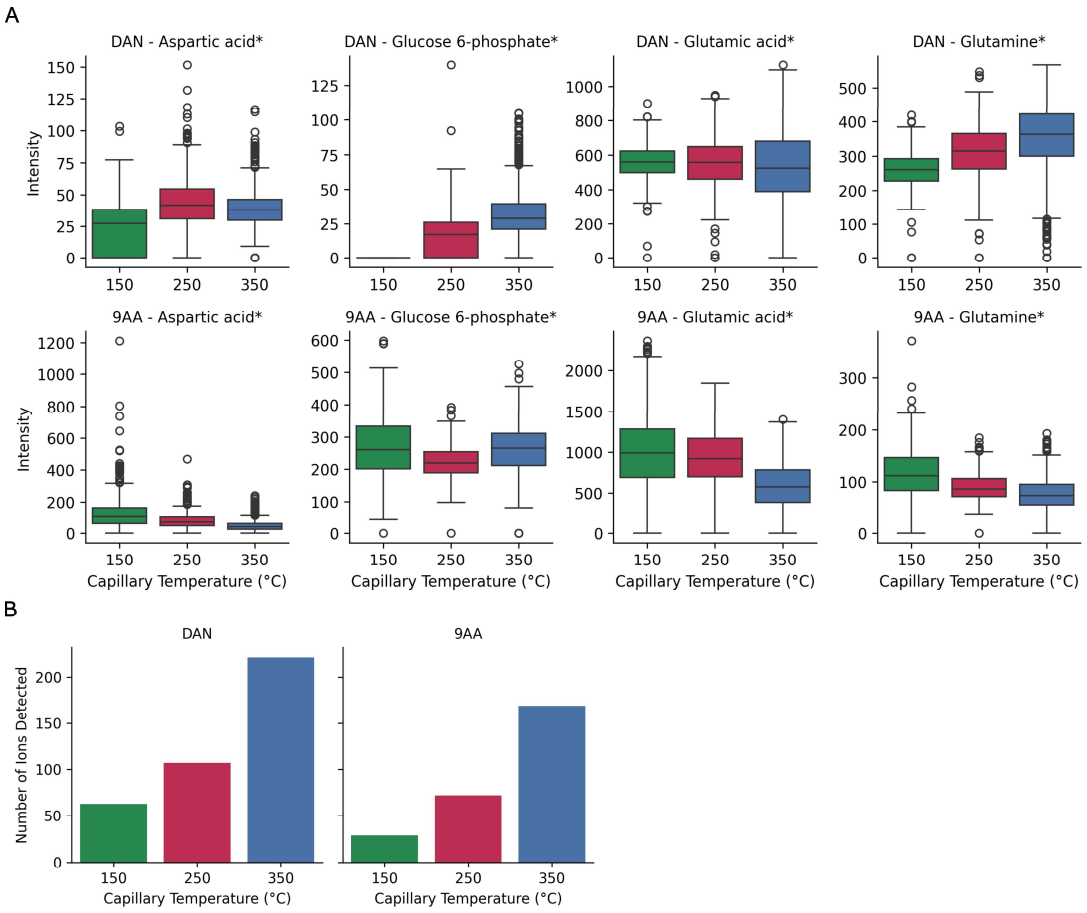

Figure 15 - Metabolites detected in activated CD4$^+$ T cells for different capillary temperatures. The slides were sprayed with DAN or 9AA and acquired in negative mode. The acquisition parameters included the laser attenuator set to 29, the RF level to 50, and the step size to 20. The sum intensity of the ions detected in each pixel was normalized to 10000. **(A)** Normalized single-pixel intensity of four metabolites. The asterisk indicates metabolites with known isomers. **(B)** Number of ions annotated with CoreMetabolome (v3) database.

The second parameter to be optimized was the S-lens RF level, which is a radiofrequency. Usually, the level used for metabolites is 50, however, some studies report values as 65 or 80 [107], [112], [115]. **Figure 16A** shows how the different RF levels tested (50, 60, 70) affected the intensity of the four example metabolites. Contrary to the capillary temperature, increasing the RF level did not significantly improve metabolite detection. Only the intensity of G6P* in the DAN matrix positively increased with the RF level increase. The opposite trend was observed for glutamic acid* and glutamine* in 9AA and DAN, with higher intensities detected when the RF level was only 50. Interestingly, increasing the RF level resulted in decreased ions detected, so I proceeded with the standard value of 50 (**Figure 16B**).

After optimizing the mass spectrometer-related parameters (capillary temperature and RF level), only the two MALDI-related parameters were left to optimize: pixel size and attenuator. The pixel size is the distance between two laser ablation marks, and sensitivity can drop with smaller size values [116]. The standard size used in the group protocols was 20 µm, which was compared with a lower and higher value (15 and 25 µm). The changing pixel size did not significantly affect the intensity of the example metabolites (**Figure 17A**). The only exception was glutamic acid* and glutamine* in cells sprayed with DAN, with the highest intensity at 20 µm. Similar to before, the main difference observed was in the number of ions detected, with step size 15 µm yielding half the ions detected at step size 20 µm (**Figure 17B**). Thus, the step size was set to 20 µm, and only the attenuator remained to be optimized.

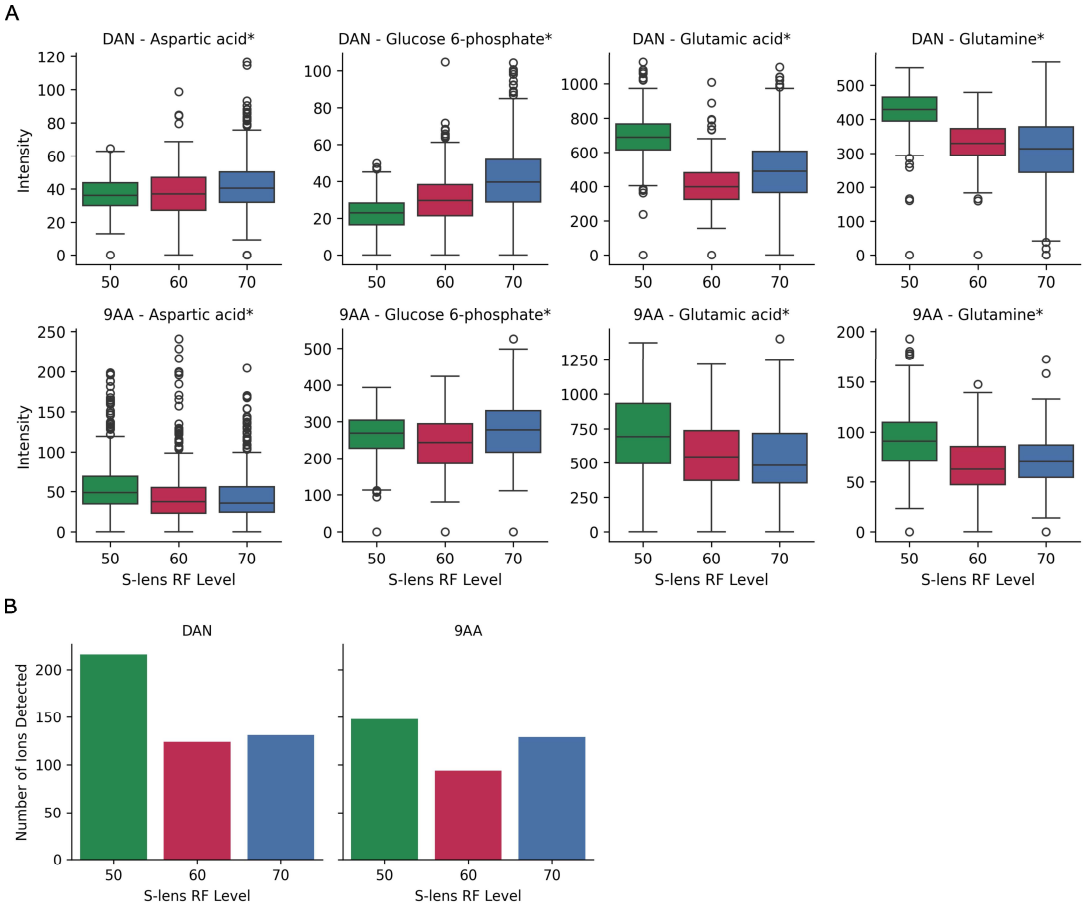

Figure 16 - Metabolites detected in activated CD4⁺ T cells for different RF levels. The slides were sprayed with DAN or 9AA and acquired in negative mode. The acquisition parameters included the laser attenuator set to 29, the capillary temperature to 350, and the step size to 20. The sum intensity of the ions detected in each pixel was normalized to 10000. **(A)** Normalized single-pixel intensity of four metabolites. The asterisk indicates metabolites with known isomers. **(B)** Number of ions annotated with CoreMetabolome (v3) database.

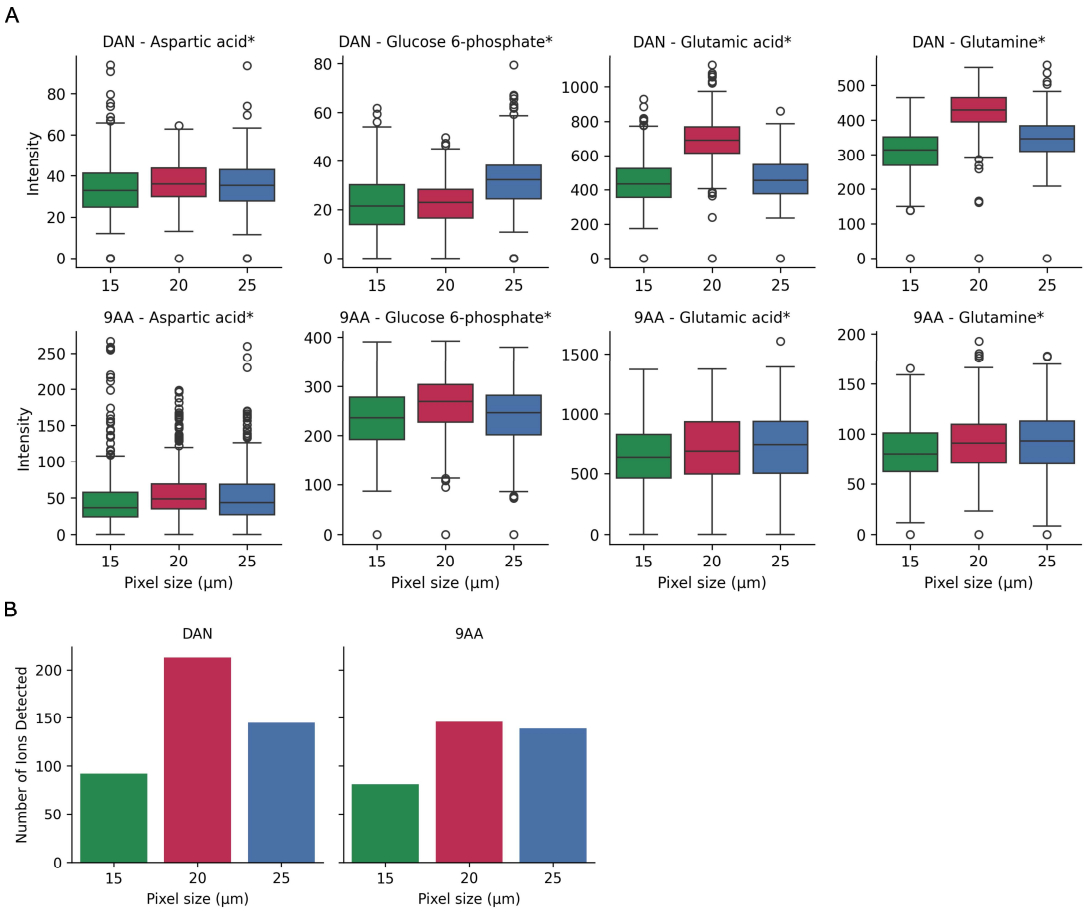

Figure 17 - Metabolites detected in activated CD4^{+} T cells for different step sizes. The slides were sprayed with DAN or 9AA and acquired in negative mode. The acquisition parameters included the laser attenuator set to 29, the capillary temperature to 350, and the RF level to 50. The sum intensity of the ions detected in each pixel was normalized to 10000. **(A)** Normalized single-pixel intensity of four metabolites. The asterisk indicates metabolites with known isomers. **(B)** Number of ions annotated with CoreMetabolome (v3) database.

Thus, the last parameter to be optimized was the attenuator level. Similar to before, a wide range of levels was selected to be tested in both matrices. These values were selected based on protocols available in the group. The typical attenuator value used in the group for metabolomics studies is 29-30, while for lipidomics studies is 33-34 or even higher. The results in **Figure 18A** showed little difference in the metabolite intensities measured with different attenuators in cells sprayed with DAN, except for the extreme values of the tested range. The higher attenuator level of 33 (i.e., lower laser power) resulted in the loss of the aspartic acid* and G6P* signal. On the other hand, attenuator level of 28 was also correlated with lower intensity of glutamine* and glutamic acid*. In cells sprayed with 9AA, the intensity of the example metabolites increased with the attenuator level. Lower attenuator levels (29-31) worked better for the DAN matrix, while higher attenuator levels (31-33) were ideal for 9AA. However, similar to the previous results, the intensity of the metabolites did not correlate with the number of ions detected, at least for 9AA (**Figure 18B**). Considering the number of ions detected, the ideal attenuator level for DAN and 9AA was 29. Before deciding on the attenuator, it was necessary to check how the ablation marks looked for each attenuator level (**Figure 19**). One of the main requirements of the SpaceM processing pipeline is clear ablation marks that can be segmented. This is essential to assign the metabolite intensities to the single cells correctly. Unfortunately, the attenuator levels of 29 or 30 resulted in overlapping ablation marks, making it difficult to segment them individually. Thus, it was necessary to proceed with higher attenuator levels (31-32), which meant compromising the number of ions detected.

All the parameters were optimized, and the only decision left was which matrix to choose. Both matrices performed very similarly in detecting the example metabolites. Thus, I wondered which ions were uniquely detected by each matrix (**Table 8**). It turned out that many interesting metabolites were uniquely detected by either one of the matrices. The logical choice would be the matrix that yielded more ions, which was DAN. However, that meant missing molecules like fructose 1,6-biphosphate* (FBP) or citric acid*. Likewise, choosing 9AA would mean missing glucose* or fumaric acid*. Since it was impossible to run both matrices due to time restrictions, I wanted to test if it would be possible to combine them.

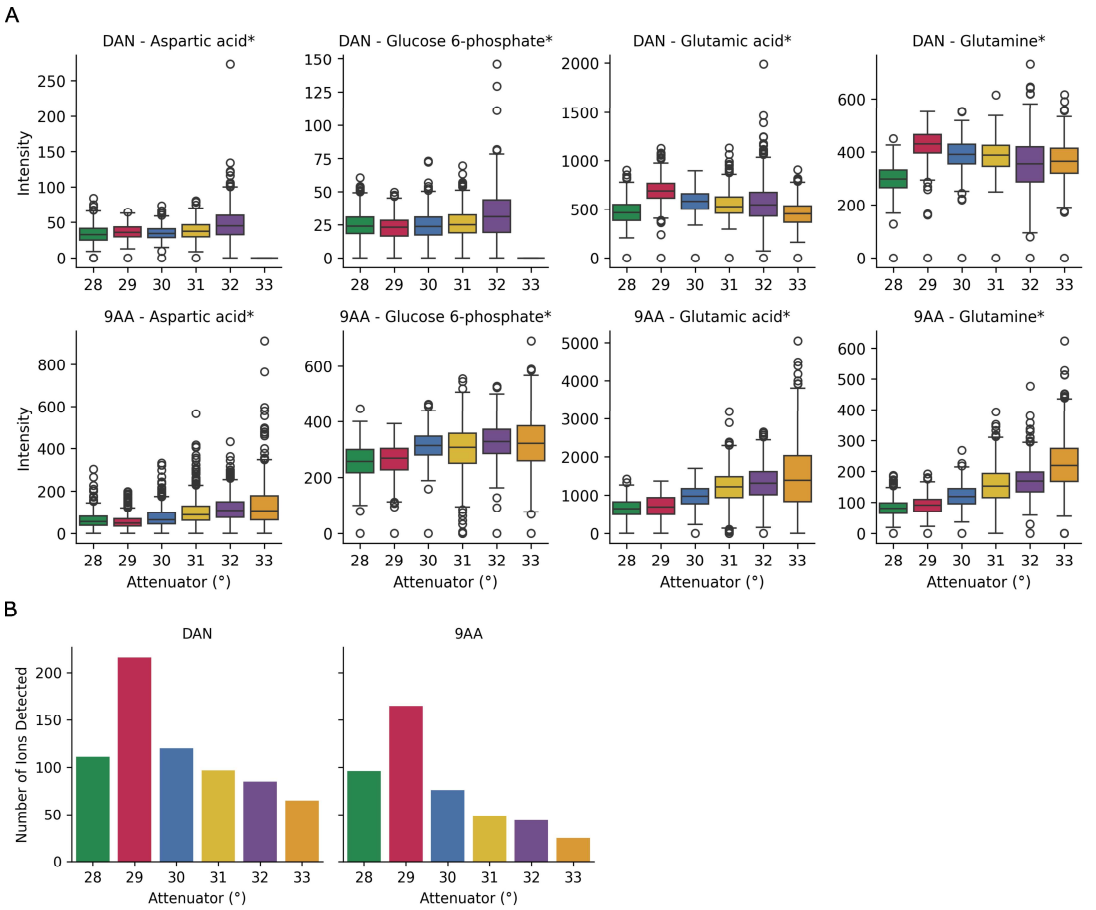

Figure 18 - Metabolites detected in activated $CD4^+$ T cells for different attenuator levels. The slides were sprayed with DAN or 9AA and acquired in negative mode. The acquisition parameters included the RF level set to 50, the capillary temperature to 350, and the step size to 20. The sum intensity of the ions detected in each pixel was normalized to 10000. **(A)** Normalized single-pixel intensity of four metabolites. The asterisk indicates metabolites with known isomers. **(B)** Number of ions annotated with CoreMetabolome (v3) database.

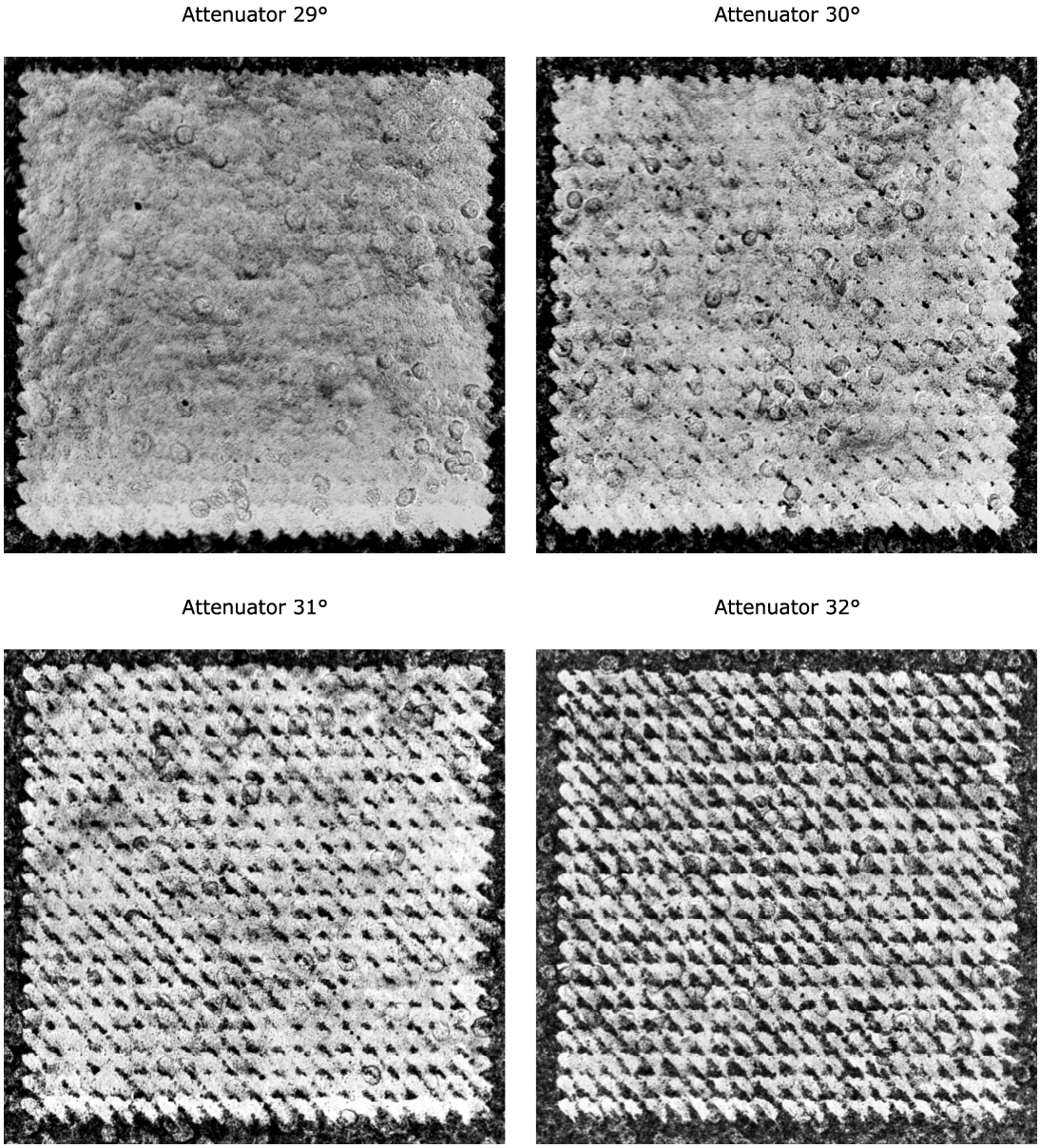

Figure 19 – Microscopy images (magnification 10x) of ablation marks for different attenuator levels.

Table 8 – Metabolites uniquely detected by DAN or 9AA.

DAN	9AA
Kynurenine*, Adenosine*, Kynurenic acid*, 5'-Methylthioadenosine, N-Acetylneuraminic acid*, Methionyl-Phenylalanine*, Arachidonic acid*, O-Phosphoethanolamine, Serine, **Fumaric acid***, Threonic acid*, L-Threonine*, Valine*, Methionine*, C5H11NO3S, Ornithine, Ribitol*, Hypoxanthine*, Xanthine*, L-Dihydroorotic acid, Itaconic acid*, Glutaric acid*, 2-Hydroxyglutaric acid*, Proline*, L-Glutamic gamma-semialdehyde*, Formiminoglutamic acid*, C6H10O2, 2-Methyl-3-ketovaleric acid, 4-Acetamidobutanoic acid*, **Glucose***, Leucine*, Lysine, Sorbitol-6-phosphate, Urocanic acid*, 4-Imidazolone-5-propionic acid*, Oxoadipic acid*, Pimelic acid*, 2-Pyrocatechuic acid*, N-a-Acetylcitrulline*, Ethyl hexanoate*, 4-Hydroxyphenylacetaldehyde*, Pyridoxal*, Tyrosine*, Phenylpyruvic acid*	Cyclic AMP*, Inosine monophosphate, Guanosine monophosphate*, Norophthalmic acid*, Acetylphosphate*, Phosphoglycolic acid, 2-Phosphoglyceric acid*, Glycerol 3-phosphate*, Uracil*, Succinic acid*, Malic acid*, N-Acetyltaurine*, L-Glutamic acid 5-phosphate, Deoxyribose 5-phosphate*, Ribulose 5-phosphate*, Phosphoribosyl pyrophosphate, 6-Phosphonogluconо-D-lactone*, 6-Phosphogluconic acid*, **Fructose 1,6-bisphosphate*, Citric acid***, N-Formyl-L-glutamic acid*, 3-Dehydroquinate*, Glutarylglycine*, Sedoheptulose 7-phosphate*, 5-Acetylamino-6-formylamino-3-methyluracil, N-Acetylglucosamine 6-phosphate*, Uridine 2',3'-cyclic phosphate, Uridine 5'-monophosphate*, Cytidine monophosphate*, AICAR, Pyrophosphate

Combining MALDI matrices is not a novel method but is not the most common approach. The mix of two matrices has been successfully used for improved detection of peptides, lipids, glycans, and small molecules [117]–[120]. There were no reports of improving small molecule detection with a combination of DAN and 9AA on negative mode in the literature when I started to consider this approach. However, the use of this combination in lipid detection has been recently reported [121]. Given that the mentioned publication was not available when this idea was envisioned and the experiments run, it is still safe to claim that the mix of DAN with 9AA was a novel approach in imaging and small molecule detection.

Since there was no previous reference about combining DAN with 9AA, it was necessary to test different mixture ratios to understand how they affected the individual metabolites. The chosen ratios of DAN:9AA were 1:1, 10:1, 20:1, and 100:1. Keeping DAN as the main matrix and trying different dilutions of 9AA can be justified by the superior number of ions detected by DAN. The parameters used were the same as

determined during the optimization, except for the attenuator and the capillary temperature. As mentioned, the attenuator was changed to 31 because of the overlapping of ablation marks for lowed attenuators. The capillary temperature was changed to 250°C instead of 350°C because the higher value resulted in lower metabolite intensity with 9AA, as shown in the previous section. This was a very discussable choice, but not unreasonable. The new experiments were run in activated cells from one donor. The results in **Figure 20A** show how the different ratios affected the intensity of metabolites uniquely detected by DAN (glucose*) and 9AA (citric acid* and FBP*). The higher dilution of 9AA (1:100) resulted in a higher intensity of aspartic acid*, glutamic* acid, and glutamine*; however, it was not enough to detect FBP*. Unfortunately, citric acid* could still not be properly detected with any ratio. Adenine was only detected when the DAN:9AA ratio was 1:1 or 1:10. Thus, this reduced the choice of these two ratios. Since all metabolites had a lower intensity when the dilution was 1:1, the final choice was the 1:10 ratio. This choice was also supported by more ions being detected with this ratio (**Figure 20B**).

The attenuator level of 31 yielded great results, with around 80 ions detected. However, the ablation marks still overlapped at this level, as shown in **Figure 19**. Thus, it was necessary to test if increasing the attenuator would be possible with the DAN:9AA mix (10:1 ratio) without affecting the results. This would be the last optimization experiment before moving into the biological questions. The objective was to check if higher attenuator values (32 and 33) yielded similar detection to lower ones (30 and 31). The results showed that all metabolites had similar intensities for low and high attenuator levels (**Figure 21A**). The only exception was adenine, which could not be detected when the attenuator level was increased to 33. The number of ions detected with the attenuator level of 32 was not much lower than at 31 (**Figure 21B**). On the other hand, a significant drop in the number of ions was detected when the attenuator level was changed to 33. Thus, proceeding with attenuator 32 seemed the best option for optimal ablation marks without compromising the detection.

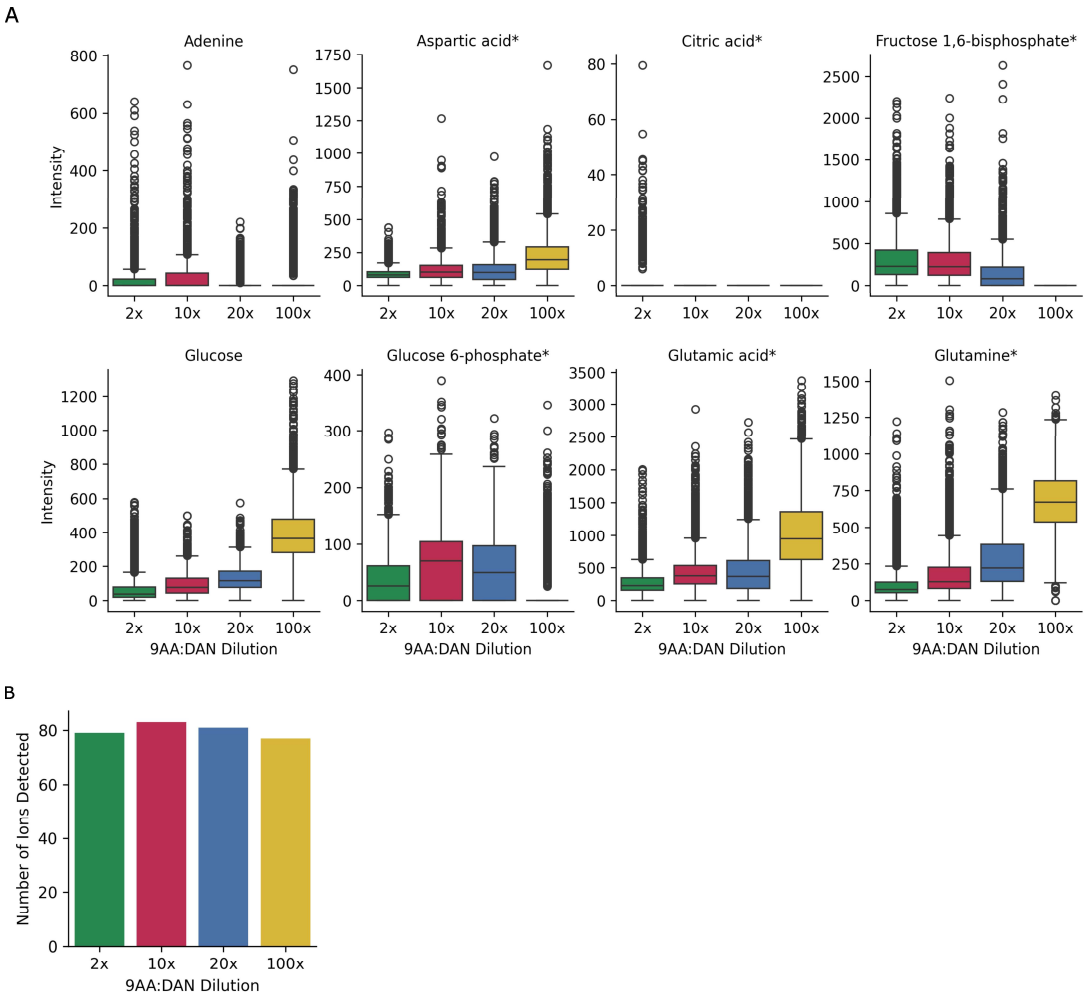

Figure 20 - Metabolites detected in activated CD4^{+} T cells for different DAN:9AA mix ratios. The slides were sprayed with a mix DAN with 9AA and acquired in negative mode. The acquisition parameters included the RF level set to 50, the capillary temperature to 250, and the attenuator level to 31. The sum intensity of the ions detected in each pixel was normalized to 10000. **(A)** Normalized single-pixel intensity of six metabolites. The asterisk indicates metabolites with known isomers. **(B)** Number of ions annotated with CoreMetabolome (v3) database.

This last experiment ended a long journey of multiple optimizations using activated cells. Thus, before moving into the biological questions, it was essential to show how the chosen protocol performed in another condition. $CD4^+$ T cells were isolated from the peripheral blood of one donor and cultured for 3 days. The cells were either kept at their naïve state or activated with anti-CD3 and anti-CD28. After culturing, the abovementioned adhesion and MALDI-imaging MS protocols were followed. The results showed that all the metabolites detected in activated cells were also detected in naïve cells, except for FBP* (**Figure 22A**). However, this was not a concern since activated $CD4^+$ T cells exhibit enhanced glycolysis, a pathway that fructose 1,6-biphosphate is part of [122], [123]. Unfortunately, citric acid* could not be well detected in both naïve and activated conditions, which showed that the detection of this ion was inconsistent. The number of ions detected in naïve condition was slightly lower than in activated cells (**Figure 22B**). Around 200 ions were detected in both conditions, which was an improvement compared to the previous optimization results. This can be explained by the area sampled (1000 µm) in this experiment being bigger than the area (400µm) sampled in the previous experiments. This could mean more cells were sampled, resulting in more metabolites detected, especially less frequent ones. In summary, this section concludes the long set of optimization experiments. Here, I demonstrated that DAN and 9AA detect metabolites differently in $CD4^+$ T cells and that choosing one implies compromising and missing information. Thus, I developed a novel method for small molecule detection by mixing the DAN with 9AA. Mixing these matrices resulted in the detection of molecules uniquely detected by one of the matrices. Thus, the method was finally ready to answer biological questions. This coincided with the transition of the original SpaceM software to the HT-SpaceM software developed by other team members. This was also a game-changer factor because it allowed me to easily process the hundreds of individual wells that were acquired in the experiments that followed. Thus, the only question left was if HT-SpaceM could characterize other aspects of $CD4^+$ T cell metabolism and give reproducible results.

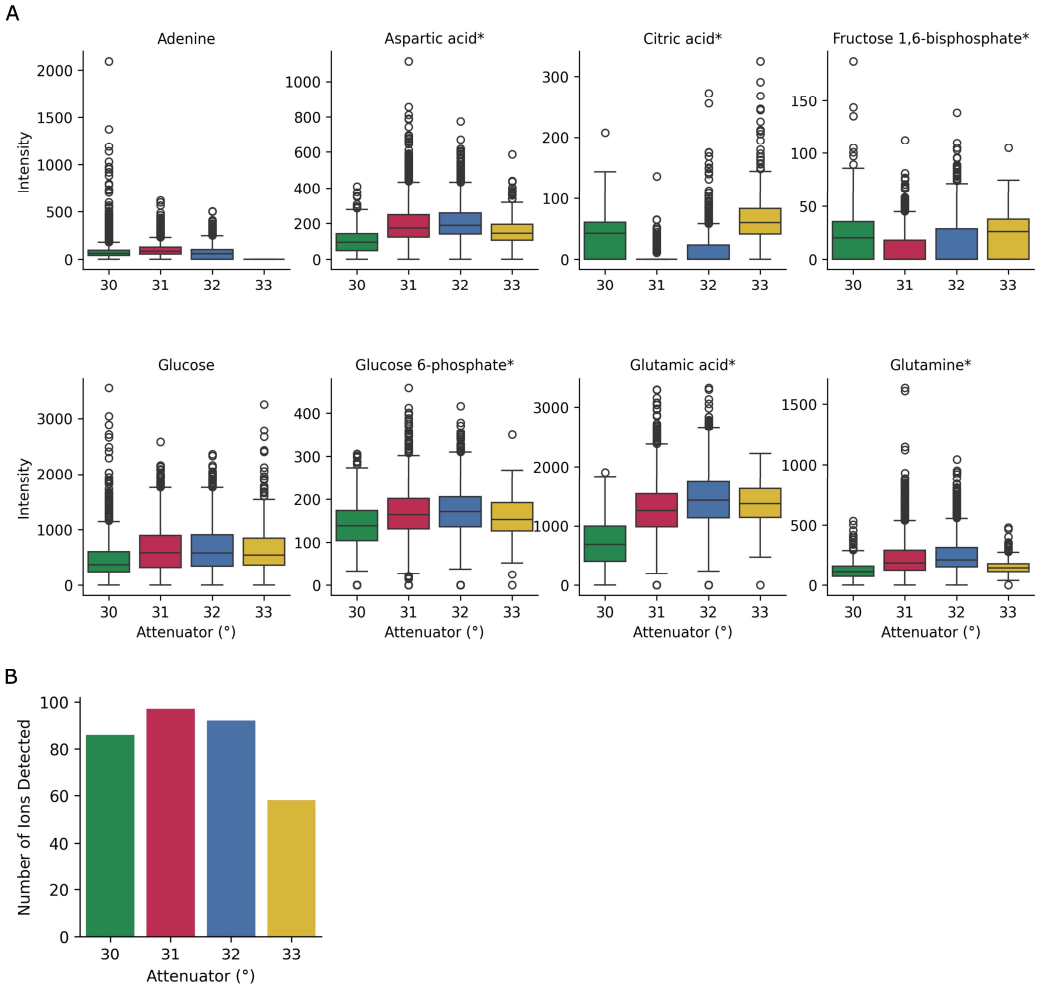

Figure 21 - Metabolites detected in activated CD4$^+$ T cells for different attenuator levels. The slides were sprayed with a mix of DAN with 9AA (10:1 ratio) and acquired in negative mode. The acquisition parameters included the RF level set to 50 and the capillary temperature to 250. The sum intensity of the ions detected in each pixel was normalized to 10000. **(A)** Normalized single-pixel intensity of six metabolites. The asterisk indicates metabolites with known isomers. **(B)** Number of ions annotated with CoreMetabolome (v3) database.

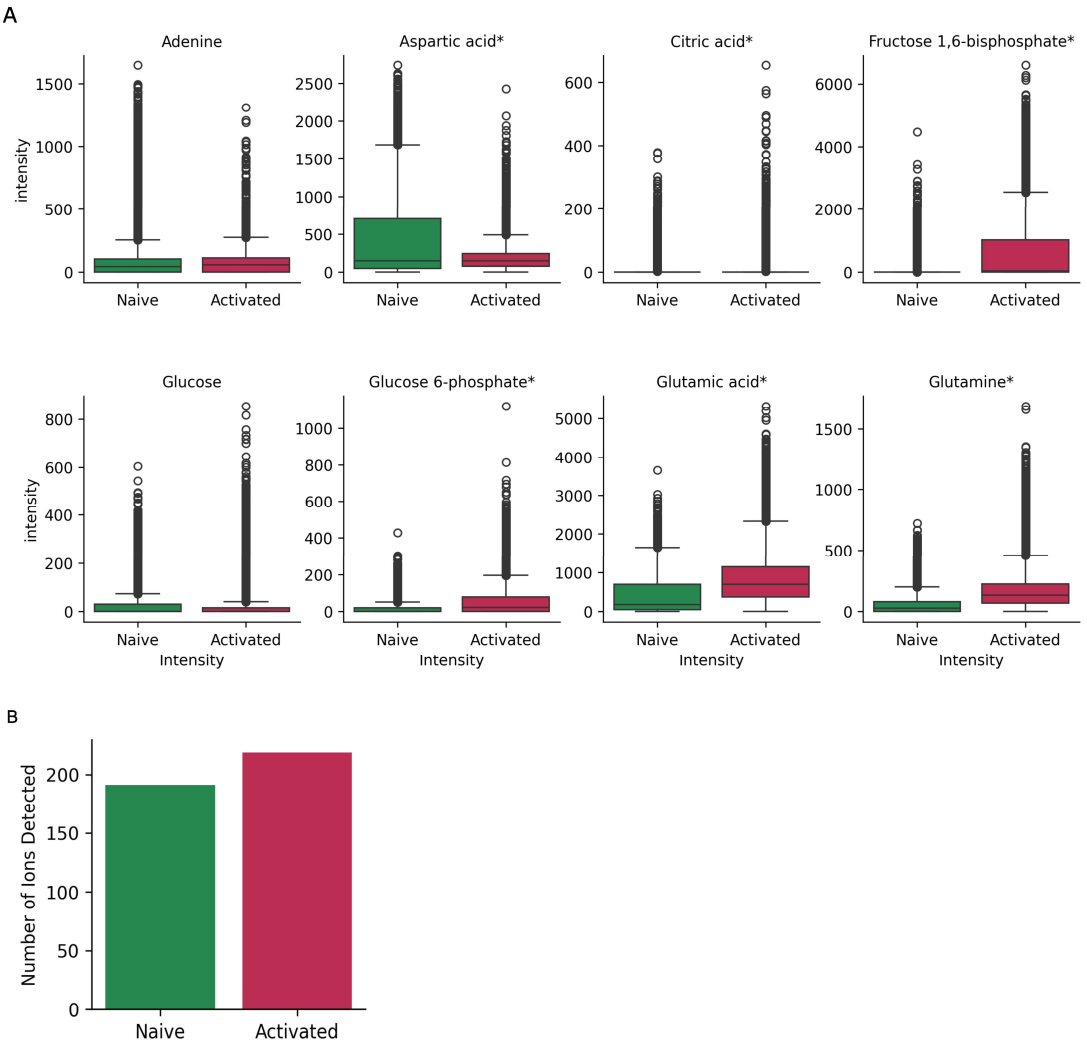

Figure 22 - Metabolites detected in naïve and activated $CD4^+$ T cells for the DAN:9AA mix. The slides were sprayed with a mix of DAN with 9AA (10:1 ratio) and acquired in negative mode. The acquisition parameters included the RF level set to 50, the capillary temperature to 250, and the attenuator level to 31. The sum intensity of the ions detected in each pixel was normalized to 10000. **(A)** Normalized single-pixel intensity of six metabolites. The asterisk indicates metabolites with known isomers. **(B)** Number of ions annotated with CoreMetabolome (v3) database.

4.4. Characterizing the metabolomic profile of CD4$^+$ T cells at the single-cell level with HT-SpaceM

4.4.1. Selecting the modulators for the proof-of-concept experiment

The success of the optimization experiments, along with the demonstration that metabolite detection was possible in naïve and activated cells, allowed me to focus on the main objectives: activation and modulation. Since the culturing and activation model was already established, the main focus relied on finding the appropriate modulator to validate HT-SpaceM as a method to characterize the metabolic states of CD4$^+$ T cells. It seemed logical to choose modulators used in other metabolic assays like Seahorse, which has been extensively used to study the metabolism of T cells [98], [124]. In this assay, glycolysis is inhibited with 2-deoxy-D-glucose (2-DG), a glucose analog that competes for binding to hexokinase. The resultant molecule, 2-deoxy-D-Glucose-6-phosphate (2-DG6P), can bind to but not be metabolized by the second enzyme in glycolysis, phosphohexose isomerase. The accumulation of 2DGP inhibits both mentioned enzymes and, consequently, the whole pathway [125]. The assay also typically uses three respiration inhibitors: rotenone, antimycin A, and oligomycin. The first is a complex I inhibitor that prevents the transfer of electrons from nicotinamide adenine dinucleotide (NADH) to ubiquinone [126]. Since the electron transport chain (ETC) has an additional supply of electrons resulting from the oxidation of succinate into fumarate catalyzed by complex II, rotenone is used in combination with Antimycin A, a compound that blocks the electron transfer within complex III [127], [128]. Thus, this combination results in complete disruption of the ETC. Oligomycin A is a naturally occurring compound that inhibits the last step of OXPHOS by blocking the conversion of adenosine diphosphate (ADP) to adenosine triphosphate (ATP) catalyzed by ATP synthase [129]. Last but not least, there is also Carbonyl cyanide-p-trifluoromethoxyphenylhydrazone (FCCP), a compound that uncouples oxygen consumption from ATP synthesis by facilitating proton leak across the mitochondrial membrane [130]. FCCP has a bimodal role because it initially promotes respiration but ends up inhibiting it after long exposures [131].

The five metabolic modulators used in the Seahorse assay were the perfect candidates to evaluate the capacities of HT-SpaceM. The effect of these compounds on the activity of glycolysis and OXPHOS can be observed under 30 minutes of incubation in this assay. So, I wondered if it would be possible to reproduce this with HT-SpaceM and see changes in

the metabolome so quickly. I have performed pilot experiments where the naive $CD4^+$ T cells were activated for three days following treatment for 30 minutes with these inhibitors and then analyzed with HT-SpaceM. However, no significant changes at the metabolite level were observed for any inhibitors except 2-DG (data not shown). In fact, a study reported that significant effects on metabolism were only observed in $CD4^+$ T cells treated with oligomycin for at least 48 hours [132]. Others reported that stimulation combined with oligomycin incubation can significantly impact the activation and proliferation of T cells [133], [134]. Thus, all these studies used a different approach, where $CD4^+$ T cells were treated with inhibitors during activation and not after. Since the metabolic shift is observed when naïve cells are transitioning to activated cells, it seems logical that any modulation will be more effective during this phase than at a later stage when a metabolic plateau has been reached. Thus, it was necessary to pivot the main question from how activated $CD4^+$ T cells can be modulated to how modulation upon activation affects the metabolic remodeling of these cells.

There was only one last question: which concentration should be chosen for each modulator? One study reported that oligomycin and rotenone at a concentration of 0.1 or 1 μM significantly impact the activation and proliferation of $CD4^+$ T cells [134]. The concentration range typically used in the Seahorse assay for the mitochondria modulators in these cells is 0.5-1.5μM [135], [136]. However, these values were optimized for short-time incubations. Since I was interested in observing a long-term effect without significantly impacting the cell's survival, the concentration chosen for all the mitochondrial inhibitors was 0.1 μM. The concentration of 2-DG used in the Seahorse assays is considerably higher, ranging from 10 to 100 mM [135], [137], [138]. However, the concentration used for long exposures in $CD4^+$ T cells that successfully suppresses glucose intake and activation goes from 1 to 10 mM [132], [139]. Thus, 5 mM was the final concentration of 2-DG added to the cells. In the Seahorse assay, there is a step where glucose supplementation happens to determine the glycolysis rate. The cells must be first incubated in a medium depleted of glucose for this to work correctly [140]. The concentration of glucose supplemented in the Seahorse assay is usually 10 mM, the same amount present in RPMI [80], [135]. The glucose supplementation in this experiment had a different goal since the incubation time was longer, and the effect observed in Seahorse assays could not be mimicked. In addition to the 10 mM of glucose already present in the medium, an extra 10 mM was added. The objective was to understand if the extra glucose

would significantly change the metabolism of $CD4^+$ T cells. Moreover, the modulators were dissolved in either H2O or Dimethyl sulfoxide (DMSO). Thus, it was also necessary to include a condition with these solvents for vehicle control.

Table 9 summarizes the concentration of the 5 chosen modulators**.** This table also provides information about the modulators used in the subsequent experiments. The process of selecting and testing these additional modulators and their function will be covered later in this dissertation. These 20 modulators had to be run in separate batches due to the limited number of conditions and replicates that could be fitted in one slide. Nevertheless, the logical thing would be to integrate the individual batches and analyze all these conditions together. However, I could not find a method to efficiently correct the variation observed between batches run across different months. When I tried integrating all modulators, the result was missing information and details captured when analyzing the batches individually. Thus, the additional 20 modulators will be presented and discussed per batch in this dissertation. In summary, one glycolysis inhibitor (2-DG) and four mitochondrial modulators (Rotenone, Antimycin A, Oligomycin A, and FCCP) were selected to conduct the proof-of-concept experiment that would test the HT-SpaceM capacities to capture metabolic modulation in $CD4^+$ T cells.

Table 9 – Modulators tested in $CD4^+$ cells and the respective target enzymes and used concentrations.

Compound	Target	Concentration
2-Deoxy-D-glucose	Phosphohexose Isomerase	5 mM
Antimycin A	Mitochondrial Respiratory Complex III	0.1 µM
AZ-PFKFB3-67	6-Phosphofructo-2-Kinase/ Fructose-2,6-Bisphosphatase 3	1 µM
Baricitinib	Janus Kinase	1 µM
BPTES	Glutaminase	5 µM
CBR-5884	Phosphogluconate Dehydrogenase	1 µM
Cyclosporine	Cyclophilin	1 µM
Etomoxir	Carnitine Palmitoyltransferase-1	5 µM
FCCP	Mitochondrial Membrane Proton Gradient	0.1 µM
Gossypol	Bcl-2-like Protein 1	µM
Metformin	- Mitochondrial Respiratory Complex I - 5' AMP-Activated Protein Kinase - Glycerol-3-phosphate Dehydrogenase	5 mM

Methotrexate	Dihydrofolate Reductase	1 µM
MK8722	5' AMP-Activated Protein Kinase	1 µM
Mycophenolic Acid	Inosine-5'-monophosphate dehydrogenase	
Oligomycin A	ATP Synthase	0.1 µM
PF-02545920	Phosphodiesterase 10A	1 µM
PF-05175157	Acetyl-CoA Carboxylase	1 µM
Rapamycin	Mammalian Target of Rapamycin	1 µM
Rotenone	Mitochondrial Respiratory Complex I	0.1 µM
STF-31	Glucose Transporter 1	1 µM
Telaglenastat	Glutaminase	5 µM
TEPP-46	Pyruvate Kinase M2	1 µM
Tofacitinib	Janus Kinase	1 µM
Torin 1	Mammalian Target of Rapamycin	1 µM
WZB-117	Glucose Transporter 1	1 µM

4.4.2. Designing the proof-of-concept experiment and selecting the metabolite database

The entire workflow of the proof-of-concept experiment can be seen in **Figure 23**. This detailed workflow of the experimental design and the HT-SpaceM pipeline was followed for all the other experiments as well. Naïve $CD4^+$ T cells were isolated from the peripheral blood of 3 healthy donors and cultured for 72 hours in RPMI supplemented with HI FBS, sodium pyruvate, and non-essential amino acids. Except for the Naïve condition, all the remaining cells were stimulated with anti-CD3/CD28 during this incubation. The stimulated cells were also divided into 8 conditions that included the control condition (Activated), the vehicle control conditions (H2O, DMSO), the modulators (2-DG, RotAA, Oligomycin A, FCCP), and the glucose supplementation (Glucose). After the prolonged incubation and treatment for 72 hours, the cells were collected and seeded onto the glass slides as described before. The 9 conditions had to be randomly distributed into the 40 wells etched on the glass slides. This meant it was impossible to have an even distribution of the 9 conditions. The naïve and 4 modulator conditions were given more wells (5), followed by the activated, the glucose supplemented, and the DMSO-treated cells (4), and finally, the H2O-treated cells (3).

After seeding the cells, the HT-SpaceM experimental pipeline was followed, as shown in **Figure 23**. It started with pre-MALDI microscopy, then MALDI-imaging MS, and ended with the post-MALDI microscopy. Then, during the processing part of the HT-SpaceM pipeline, the detected ions were annotated, the cells and ablation makers were segmented, and the cell deconvolution was performed. The final output is the single-cell data, which contains information on all the ions detected in the cells acquired for each well.

The ions detected for each well were initially annotated with METASPACE against CoreMetabolome (version 3), a database created by a previous member of the Alexandrov team. Annotating datasets with METASPACE has the significant drawback of missing peaks that are present in the raw spectrum. This happens because the annotation process depends on the percentage of false positives calculated for each possible annotation, also defined as False Discovery Rate (FDR). Only ions with an FDR below 50% are reported to the METASPACE user. In HT-SpaceM data generated in this project, this FDR thresholding resulted in ions being often inconsistently annotated even among technical replicates (wells from the same donor and same condition). The solution to circumvent this issue consisted of creating a custom database and using that for annotation instead. The report of the ions present in custom databases is not dependent on the FDR threshold. Using a custom database resulted in more consistency of the ions detected across replicates, at the expense of having false positives.

Creating a custom database consists of compiling all the ions detected in at least one well from one condition. Then, a filter is applied to select only intracellular ions, which do not need to be present in all cells. The metric used for this is named Normalized Manders Colocalization Coefficient, and a previous member of the Alexandrov team established it specifically for SpaceM data. The selected intracellular ions will be used to create a database that will be uploaded to METASPACE. After this, the single-cell data is reprocessed and finally ready for analysis. Thus, it became standard practice to use custom databases in the group due to the inconsistency mentioned. The data presented in this dissertation was also annotated with a custom database and was not subject to FDR thresholding, which means that it might include some false positives.

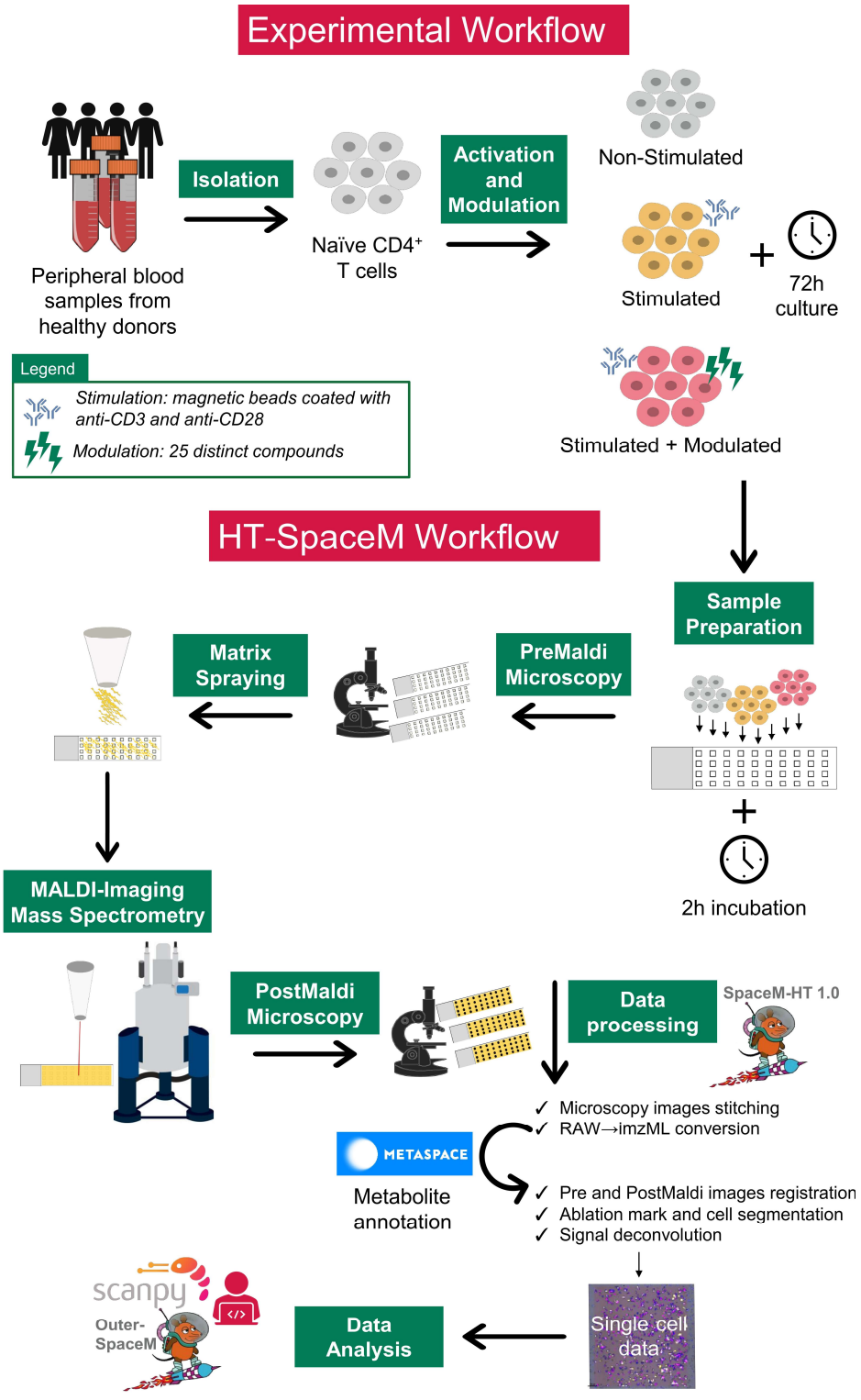

Figure 23 – HT-SpaceM workflow: from the bench to the desk.

The custom database is always based on the metabolites present in the standard databases available on METASPACE that are initially used to annotate the single-cell data. It is also possible to create a custom database from scratch with metabolites of interest, but this is not the standard procedure, especially in projects like these with such an exploratory nature. Thus, the choice of the initial database used for annotation will significantly affect the ions included in the custom database, so it should be carefully chosen. In this project, CoreMetabolome was chosen to initially annotate the single-cell data because this database gathers the core metabolites and lipids in mammals. However, CoreMetabolome still includes many metabolites that are part of the exposome or even some without a clear role. This was also observed in the metabolites included in the custom database.

Since I was interested in mainly detecting metabolites that would either be endogenous or participate in metabolic reactions, I have introduced another level of curation. This involved taking all the metabolites in the custom database and keeping the ones present in the 'Metabolic Pathways' maps from the Kyoto Encyclopedia of Genes and Genomes (KEGG). These maps cover the global cell metabolism, and the present metabolites from the custom database were identified using the web application iPath3.0 [141]. All the metabolites from the custom database that were not mapped were individually checked. And I have opted to keep some of them based on their source (endogenous) or function. Examples of this include cyclic AMP* or oleic acid*, which do not participate in metabolic reactions but are intracellular metabolites with known functions.

The original database used, CoreMetabolome, had over 500 annotated metabolites (**Figure 24**). The size of the custom database generated with the intracellular filtering method described was 310 metabolites. This number was reduced to 164 KEGG-identified metabolites. The addition of the hand-selected metabolites resulted in a curated database with 180 metabolites. This curated database also included metabolites with many isomers. Similarly to what happened in the previous sections, I will only report one of the isomers to make the results clearer. The full composition of the curated database used can be consulted in Appendix A. The information provided there includes all molecular formulas present in the database along with their candidate molecules (known isomers) and the reported ones.

Reprocessing the single-cell data with the curated database was the last step before moving to the final part of the HT-SpaceM pipeline: data analysis. As mentioned before, the number of technical replicates per condition that could be included in one slide was limited and uneven. This made preparing and running multiple slides per donor necessary when possible. This was done to prevent an eventual scenario where one or more wells had to be removed from the analysis, leaving some conditions with only a few wells and, thus, fewer cells. Multiple factors commonly affect the acquisition of individual wells, including errant spraying, improper laser focus, or inefficient solvent removal, which can result in variability among replicates. The reproducibility of HT-SpaceM had never been checked in this project, so there was no indication of how often these external factors affected the individual wells. Thus, before even diving into the biological context, it was essential to understand the technical variability among the wells and slides and how this affected the reproducibility of conditions and donors.

In summary, in this section, I have presented the general workflow of HT-SpaceM, which was followed for all the experiments mentioned in the next sections. I have also described a step in the pipeline that can significantly influence the interpretation of the results: the selection of the database used for annotation and filtering of intracellular metabolites. This must be done during processing and before starting the data analysis. Since the main goal was to characterize the metabolic configurations of $CD4^+$T cells, the detected metabolites not present in the KEGG 'Metabolic Pathways' were filtered out. Once this was done, the single-cell data was ready to start the analysis. Finally, I have also raised one of the main questions to be evaluated in the proof-of-concept experiment: the reproducibility of HT-SpaceM. This was still an open question that needed to be investigated before starting to look into any biological questions.

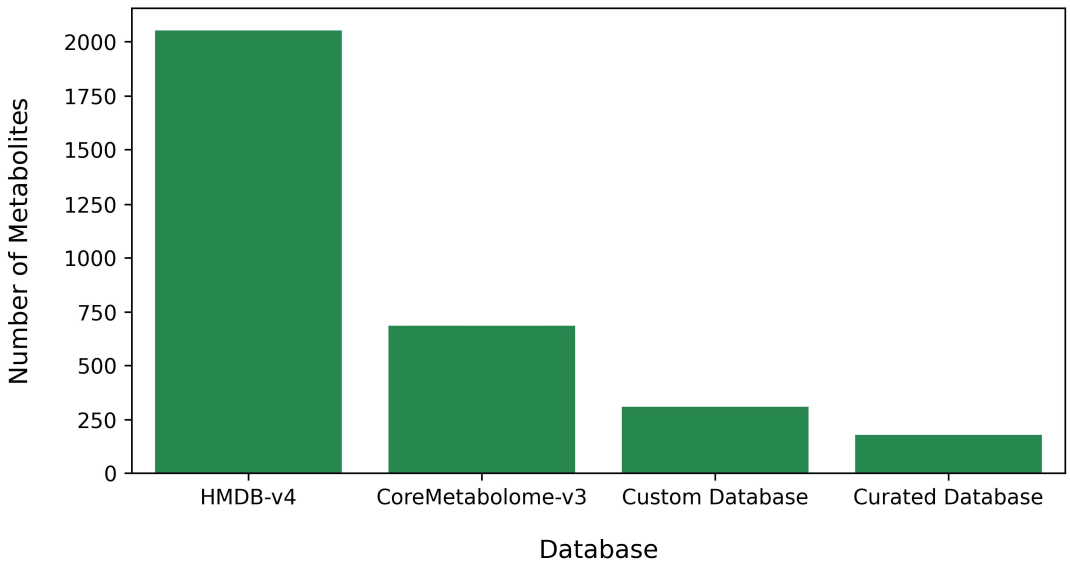

Figure 24 – Number of metabolites detected in $CD4^+$ T cells using different databases.

4.4.3. Evaluating the reproducibility and correcting for possible batch effects

The first main goal of the analysis was to evaluate the reproducibility that could be achieved with HT-SpaceM and how to correct for potential issues. This was evaluated for 5 slides from a single donor (D89). This was the only donor with enough cells to prepare more than two slides and was the ideal test case for this purpose. These five slides were seeded with the nine conditions mentioned above simultaneously. Since the biological material used in the five slides was the same, all the wells in all the slides that belong to the same condition could be classified as technical replicates. What could prevent them from being technical replicates were the next steps. After adhesion and PreMaldi microscopy were done, the slides were frozen until needed. Each slide was thawed, sprayed, and run on a different date since each had to be individually loaded in the MALDI source. Each one of these steps could be a source of variation. Thus, it was necessary to start by evaluating if there were any batch effects between slides and if wells from the same condition but different slides could be treated as technical replicates.

The data obtained from each well of the five slides was concatenated into an extensive dataset with 86,391 cells and 180 ions. The package used for analysis is named Outer SpaceM and was developed by a previous member of the Alexandrov team. Outer SpaceM

has its foundations in Scanpy, the Python package developed by the Theis group to analyze single-cell gene expression data [57]. Scanpy was also extensively used in the analysis pipeline. The quality control steps revealed that most cells had at least 40 metabolites (results not shown). Nevertheless, some filtering was still applied to ensure the high quality of the data used. All cells with less than 40 metabolites and all the metabolites present in less than 1% of all cells were excluded using the filtering function from Scanpy. In addition to that, all the wells with less than 100 cells were removed. This resulted in 69,009 cells and 152 metabolites.

The filtered data was normalized so that the sum of all ions in each cell had a total intensity of 10,000. The data was then transformed using the natural logarithm to reduce skewness. This was followed by a scaling step where, for each ion, the mean is subtracted from the expression, which is then divided by the standard deviation. This step ensures that all ions have the same weight in the downstream steps so that highly variable or highly expressed ions do not dominate the analysis. There is no consensus regarding using this step in the single-cell community [142]. However, previous results in this project showed that it is essential for cluster separation (data now shown).

Then, Principal Component Analysis (PCA) and Uniform Manifold Approximation and Projection (UMAP) were used for data dimensionality reduction and visualization. Because of the complexity of the dataset, the non-linear method, UMAP, provided a better visualization (**Figure 25A**). Then, the reproducibility was assessed using two methods: Euclidean distances and Leiden clustering. A previous member of the Alexandrov team developed the first method that can be represented in one plot, as shown in **Figure 25B**. This method calculates the mean pairwise distance between replicates of the same condition (D_{REP}). In this context, one replicate is one well, meaning that one replicate will contain several cells. The intra-distance for each condition can be observed in the bottom row of white circles in **Figure 25B**. The size and value inside the other circles represent the pairwise distance between the condition of interest (x-axis) and the other conditions (y-axis), denoted as D_{BIO}. Additionally, a ratio between the D_{BIO} and D_{REP} is calculated and transformed using the binary logarithm for easier visualization. The circles that contain the D_{BIO} information are colored according to the ratio calculated. A negative value, represented by the red color, means the distance between the technical replicates (intra-distance) is higher than their distance to other conditions (inter-distance). This indicates that the technical variability is higher than the biological variability. The other method used

to assess reproducibility was the Leiden algorithm, developed to detect clusters in complex networks [143]. The idea was to check whether any clusters were specific to single slides. This could pinpoint if one of the slides was different than the rest. Thus, the first method was used to identify the conditions with potentially high technical variability, while the second was used to identify the potential outlier slides.

The UMAP visualization in **Figure 25A** shows how the cells from different slides clustered for each condition. A clear trend was observed: slides 2 and 3 were clustering apart from the others. Moreover, one of the identified clusters by the Leiden algorithm was uniquely composed of cells from slides 2 and 3 (**Figure 25C**). This indicated that slides 2 and 3 could be outliers. Finally, the reproducibility of the technical replicates did not look great (**Figure 25B**). Most conditions exhibited high intra-distances. Besides that, the intra-distance for each condition was generally higher than the inter-distance to others, except for the Naïve condition. This indicated that the technical variability was higher than the biological one.

The clustering difference observed for slides 2 and 3, along with the poor technical replicate distance, indicated differences between slides, or in other words, a possible batch effect. Linear regression is one of the most common and simpler ways of correcting for a batch effect. This method removes the unwanted variation by adjusting the expression values of metabolites in each cell [144]. The only caveat is that the source of variation (covariate) has to be known, which is not always so obvious. Since this function is already available in Scanpy, it seemed like the ideal method to test first. In this case, I chose to remove the effect of the covariate "slide". Regressing out the effect of slide positively affected the clustering by bringing the cells from different slides closer (**Figure 26A**). Leiden clustering showed that the distribution of the slides among the clusters was more balanced (**Figure 26C**). However, there was still a cluster exclusive to slides 2 and 3. The linear regression also reduced the distance between technical replicates (**Figure 26B**). This was enough to see some changes in the plots, with some dark red circles becoming lighter, which meant that technical variability was being decreased.

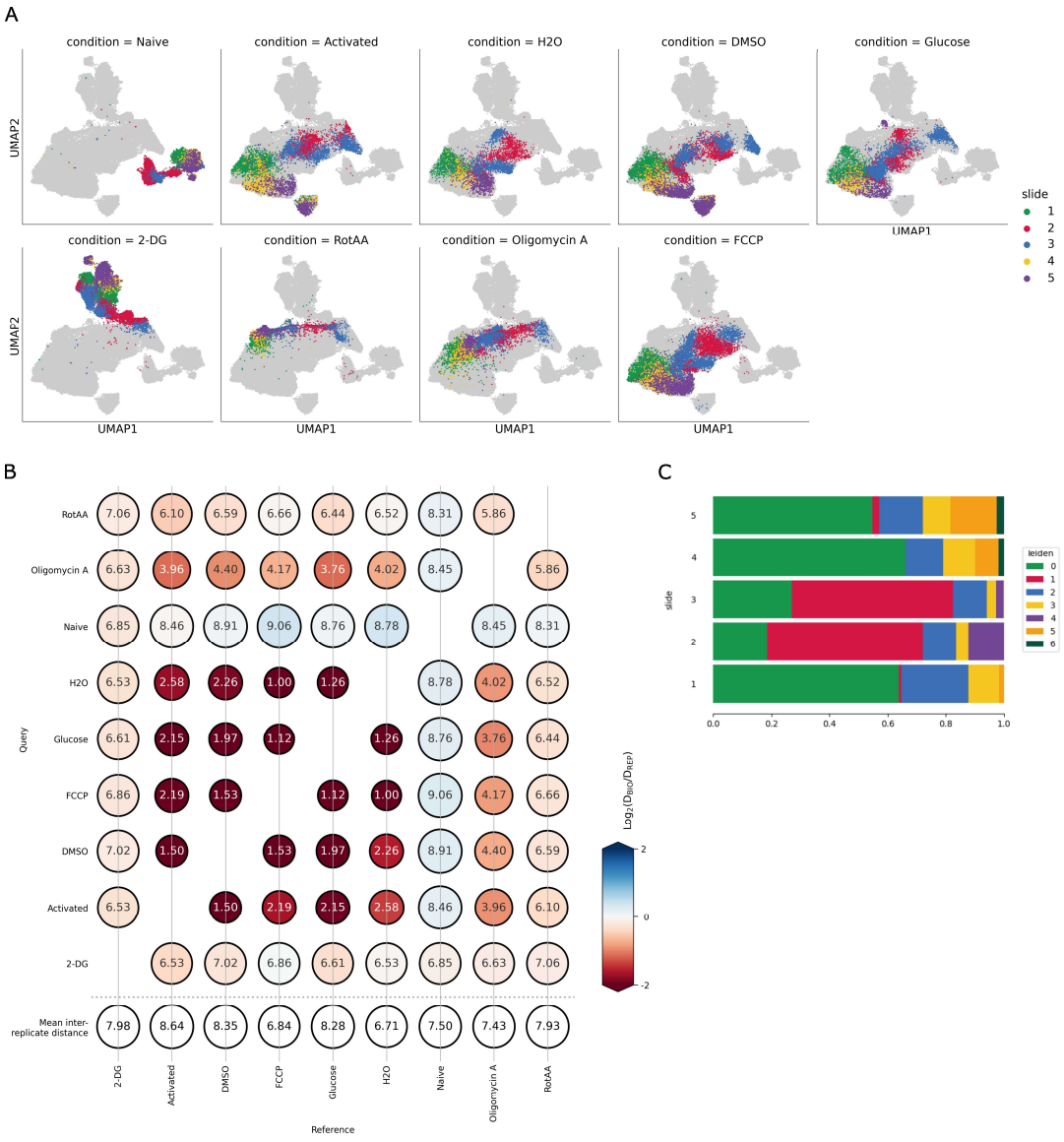

Figure 25 – Evaluating the reproducibility between multiple slides of one donor. **(A)** UMAP visualization of 69,009 cells and 152 metabolites. **(B)** Intra-label vs. inter-label distance plot. The intra-condition distances are represented in the bottom row. The inter-condition distance is represented in the colored circle. A red circle indicates that the intra-condition distance is lower than the inter-condition distance. **(C)** Visualization of the distribution of slides within the identified Leiden clusters (resolution=0.1).

The linear regression helped to reduce the variability in the data. However, some variability associated with slides 2 and 3 could not be removed. Thus, I have decided to remove slides 2 and 3 from the analysis, which was only possible because I still had 3 slides left. Naturally, it would have been possible to keep correcting the variation with other methods. However, this did not seem necessary, and I preferred not to distort the data further. The linear regression was still applied when the analysis was run on the 3 remaining slides. It was clear from **Figure 25** that there was also some variation between slides 1, 4, and 5, although much lower. Thus, linear regression became one of the standard steps in the analysis pipeline when integrating multiple slides.

Removing slides 2 and 3 significantly improved the results, as shown in **Figure 27**. Visualization with UMAP showed that the three slides were mixing very well for each condition (**Figure 27A)**. Most of the conditions were separated into well-defined clusters. There was also a significant reduction in the intra-condition distances, but not inter-condition ones, which actually increased in some cases (**Figure 27B)**. This showed that the technical variability was also reduced, and the biological differences were no longer hidden. This was the confirmation that removing the problematic slides was a good solution. However, it was also possible to notice that some conditions were split into multiple clusters. Thus, looking into outliers on a more detailed scale was necessary by going from the slide to the well level. In summary, in this section, I have demonstrated that there is some technical variability between slides that might come running them separately. On the one hand, it is difficult to pinpoint the origin of this variability and prevent it. On the other hand, it is possible to correct it. Here, I demonstrated that linear regression can correct variability between slides from the same donor.

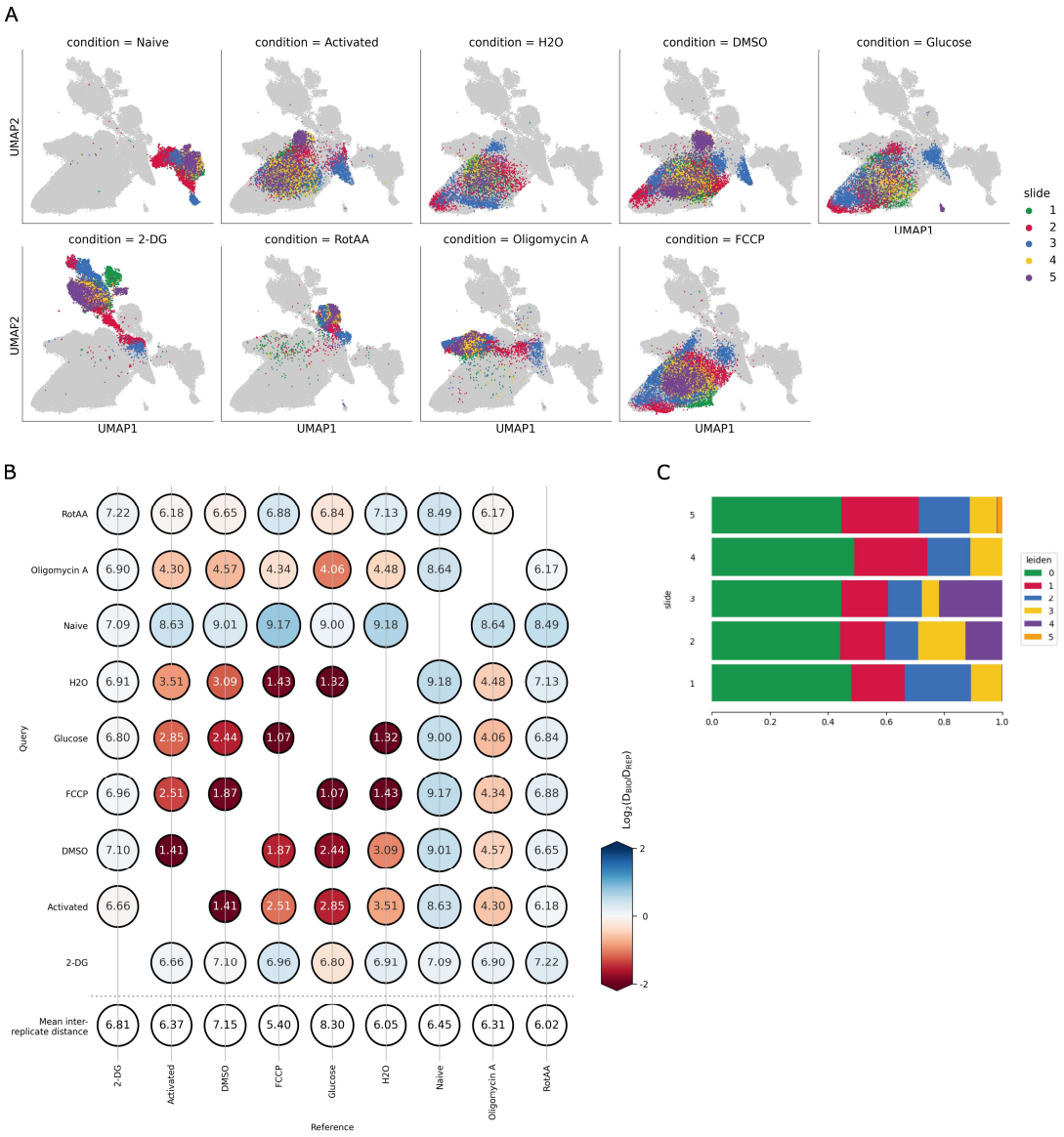

Figure 26 – Evaluating the reproducibility between multiple slides of one donor after applying linear regression. **(A)** UMAP visualization of 69,009 cells and 152 metabolites. **(B)** Intra-label vs. inter-label distance plot. The intra-condition distances are represented in the bottom row. The inter-condition distance is represented in the colored circle. A red circle indicates that the intra-condition distance is lower than the inter-condition distance. **(C)** Visualization of the distribution of slides within the identified Leiden clusters (resolution=0.1).

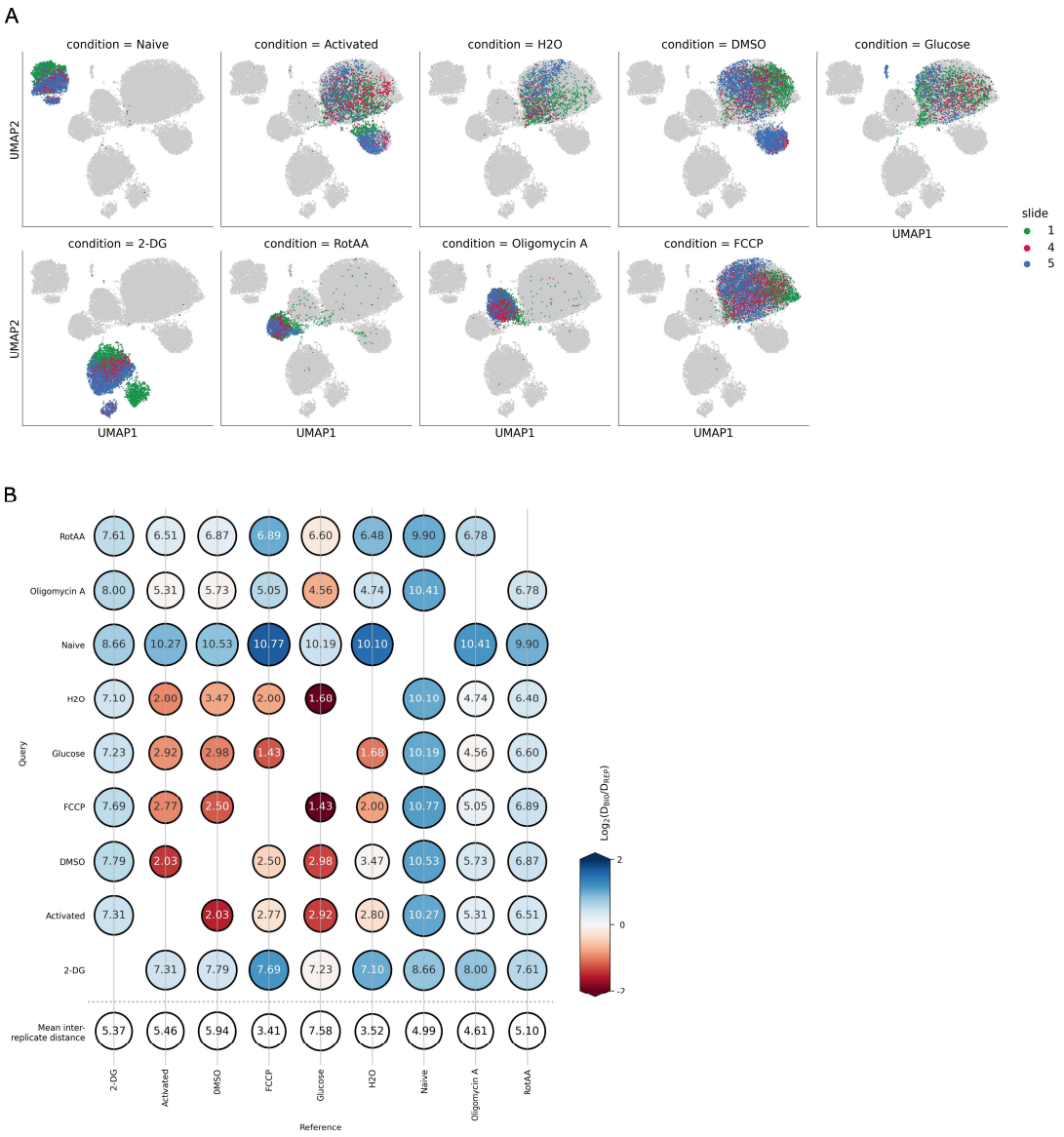

Figure 27 – Evaluating the reproducibility between multiple slides of one donor after removing two slides. **(A)** UMAP visualization of 35,762 cells and 152 metabolites. **(B)** Intra-label vs. inter-label distance plot. The intra-condition distances are represented in the bottom row. The inter-condition distance is represented in the colored circle. A red circle indicates that the intra-condition distance is lower than the inter-condition distance.

4.4.4. Identifying and removing outliers among technical replicates

In the single-cell field, an outlier is usually defined as a cell presenting an aberrant number of total counts, genes, or mitochondrial fraction [145]. These outlier cells can be easily identified and removed with the functions provided by packages like Scanpy. This can be very effective, but it is not enough in the context of HT-SpaceM data. The filtering functions help remove outlier cells or metabolites, but these do not work when the issue happens on the expression level. For example, cells from an entire well from one condition may pass the filtering threshold because they express the minimum number of metabolites set. However, the expression of some metabolites detected in those cells can be significantly lower or higher than that of other wells in the same condition. The commonly used filtering functions cannot detect situations like this. Since the wells of one condition are all technical replicates, this variability cannot be considered biological. This gets even more complex because sometimes only the expression of a few ions is affected. One could devise criteria to select and remove the outlier wells manually. However, that solution would become unpractical in a scenario where hundreds of wells were acquired, just like in this project. Thus, I started to wonder how I could integrate outlier detection into the analysis pipeline and remove the outliers in a more automated way.

PCA-based methods are commonly used for outlier detection when the other filtering functions are insufficient [146], [147]. The PCA tends to be chosen over other options because it is a linear method that retains the variance and the global structure of the data, making it easier to understand and interpret [148]. In the context of HT-SpaceM, PCA usually failed to provide useful visualizations due to the complexity of the data with so many cells and conditions. Thus, the UMAP was always the preferred alternative for any visualization. However, visualization with PCA was very informative when only one condition was considered due to the reduced complexity. Thus, PCA was a valid visualization for outlier detection in HT-SpaceM data. The next question was how to identify the wells that should be removed. This is usually done visually by assessing which points or samples are further away from the other replicates [146]. This can be fine with only a few points but impossible with thousands of points, which is the case in single-cell analysis. This strategy also raised a second question: How to define a cutoff value for the PCA distance? Thus, this approach was still very subjective, so I searched for more objective methods. The first solution I found was based on the Silhouette Score, which measures the clustering quality. This method evaluates how well-separated the clusters are

by measuring the distance between the points of two separate clusters. A score close to 1 means that the cluster is well-separated. A score of 0 indicates that the distance between the points in that cluster is similar to the distance to other points in a different cluster. Finally, a score below 0 indicates that the points have been assigned to the wrong cluster [149]. This seemed like the ideal method to detect outliers for this data. The objective was to calculate the silhouette score for each technical replicate (each well) and remove the ones with high scores. However, this raised another question: How to you choose the cutoff value? This resulted in an additional step that involved Z-scoring the data. This method standardizes the data and calculates how far a given point is from the population mean [150]. In this case, I was interested in identifying replicates with a score that was positively but not negatively higher than the mean. Thus, a cutoff of 1.645 was applied. Any replicate with a z-score above this value would be located beyond the 95^{th} percentile and automatically flagged as an outlier.

The steps for outlier detection consisted of first visualizing the PCA and then calculating the silhouette score and finding the outliers. **Figure 28** summarizes this procedure in the Activated condition. The PCA plot was divided into 3 columns, each corresponding to one of the slides for easier visualization (**Figure 28A)**. The different colors represent the acquired wells in each slide. Most of the replicates were grouped in one big cluster. However, there was also a second cluster only populated by 1 or 2 replicates from each slide. The silhouette score calculated for each replicate was closer to 0 than 1 (**Figure 28B)**. Z-scoring the data and applying the mentioned cutoff only resulted in one outlier detected. The outlier replicate was represented in green, while the normal distributed replicates were in grey. The proposed method only found one outlier (replicate 1 from slide 1), which was coincidentally also one of the replicates in the smaller cluster. The method effectively detected that specific outlier in the smaller PCA cluster. However, I wondered why it did not detect the remaining replicates in that cluster. In fact, all of them had negative silhouette scores, which indicated that they were so well mixed that the metric considered them to be assigned to the wrong cluster. This revealed one main limitation of the method. Potential outlier wells that were well mixed among them, although separated from the main population, would not be flagged as outliers because their silhouette score would be low. The solution to this would be to implement a step where the distribution of the replicates into the populations observed in PCA would also be considered when calculating the

silhouette score. However, I couldn't find a way to achieve that and had to consider other options.

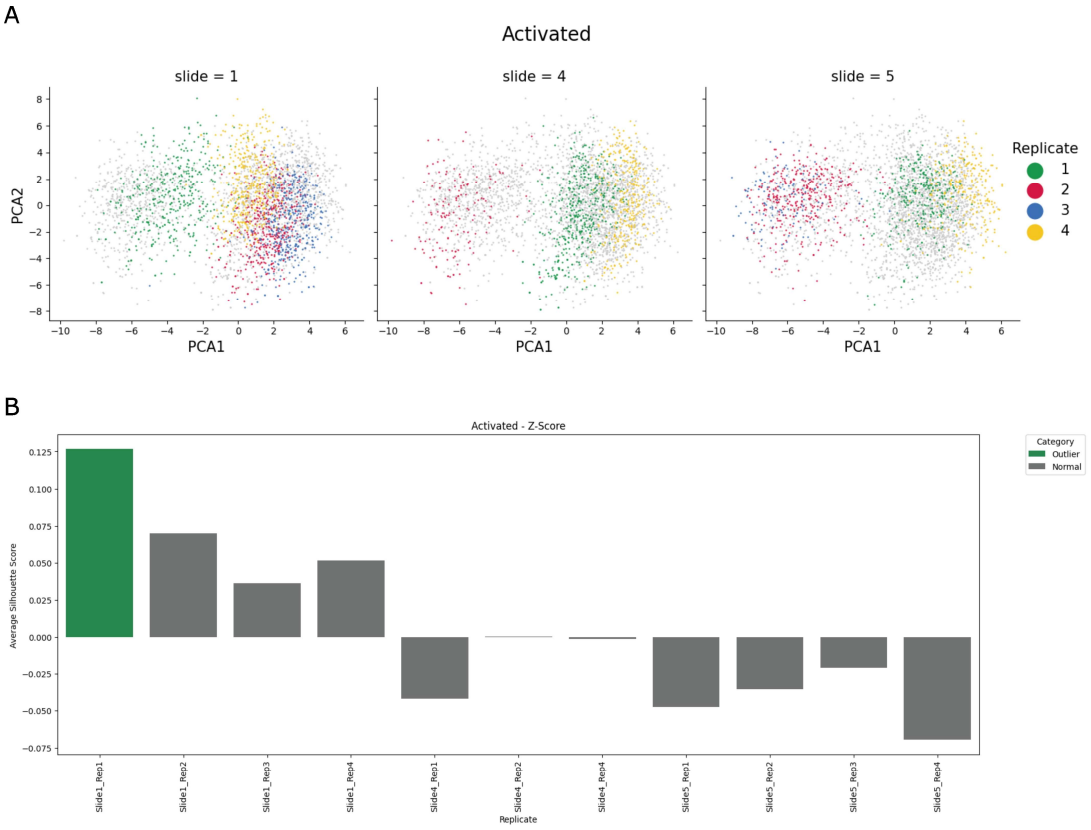

Figure 28 – Method I for removing outliers based on Silhouette scoring. **(A)** PCA visualization per condition colored by technical replicates (wells) of each slide. **(B)** Silhouette score of each technical replicate. The z-scoring function was applied to detect the scores that deviated from the mean. Outliers are highlighted in green.

The ideal solution would be to develop another method involving unsupervised clustering. This would guarantee unbiased and objective results. The goal was to find a simple method that would be easy to integrate into the pipeline. So, I decided to apply the same approach used to detect outlier slides. The data was clustered using the Leiden algorithm with the resolution set to the lowest value to avoid overclustering, which could bias the interpretation. Then, the outliers were identified by evaluating the distribution of the replicates in the different clusters. **Figure 29** shows the results of the new method for the same condition used in the previous example. One of the advantages of this new method was that the clustering results could also be visualized in the PCA plot. Thus, the PCA plot was divided into 3 columns, each corresponding to one slide, and the cells were colored according to the cluster they were assigned to (**Figure 29A)**. The unsupervised clustering found 2 main clusters and 3 smaller ones. The main Leiden clusters aligned perfectly with the two main populations observed in the PCA plot. **Figure 29B** shows the percentage of cells assigned to each cluster per replicate. This further confirmed what was observed in the PCA plot: the replicates in different populations were very distinct. There were 7 replicates assigned to the main cluster, while only 4 were driving the other one. Thus, I have removed all these 4 replicates as they seemed to be outliers. I could have explored different ways to support my decision by, for example, checking the main markers of these clusters. However, given the exploratory nature of this project, it would not help. There are also no guidelines or best practices available for single-cell metabolomics to help with such decisions. Thus, this was a valid approach with a significant limitation: one had to assume that the main population was the normal one. On the other hand, there is a considerable advantage when compared to the silhouette method: more than one outlier could be detected simultaneously. Overall, this revealed that HT-SpaceM is a reliable method. However, reproducibility could be optimized as 4 out of 11 wells were removed in this example.

The outlier detection method was repeated for all the remaining conditions, with 18 out of 83 wells removed. This removed the split observed before in the UMAP for some conditions. This indicated that the split was likely driven by the replicates removed (**Figure 30A**). The main impact of outlier removal was observed when the distance between replicates of the same condition was calculated (**Figure 30B**). The significant reduction observed in some conditions (e.g., 2-DG or Glucose) resulted in an improved ratio between the intra and inter-distance. In summary, I showed that HT-SpaceM data has some variability due to the experimental setup. This can usually be corrected with linear

regression. However, in isolated cases where this is not possible, other methods are necessary to remove the problematic wells. Removing outlier wells is essential to reduce the technical variability without compromising the biological one.

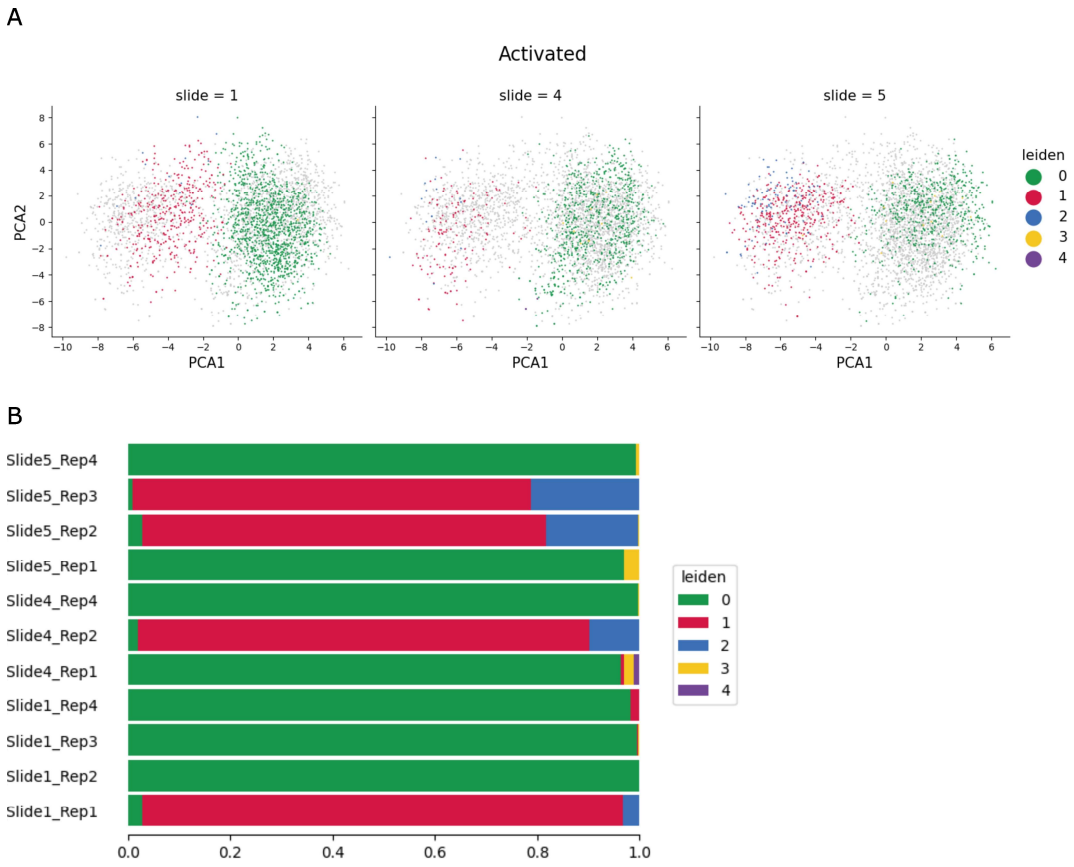

Figure 29 – Method II for removing outliers based on unsupervised clustering. **(A)** PCA visualization per condition colored by Leiden clusters. **(B)** Visualization of the distribution of technical replicates (wells) within the identified Leiden clusters (resolution=0.1).

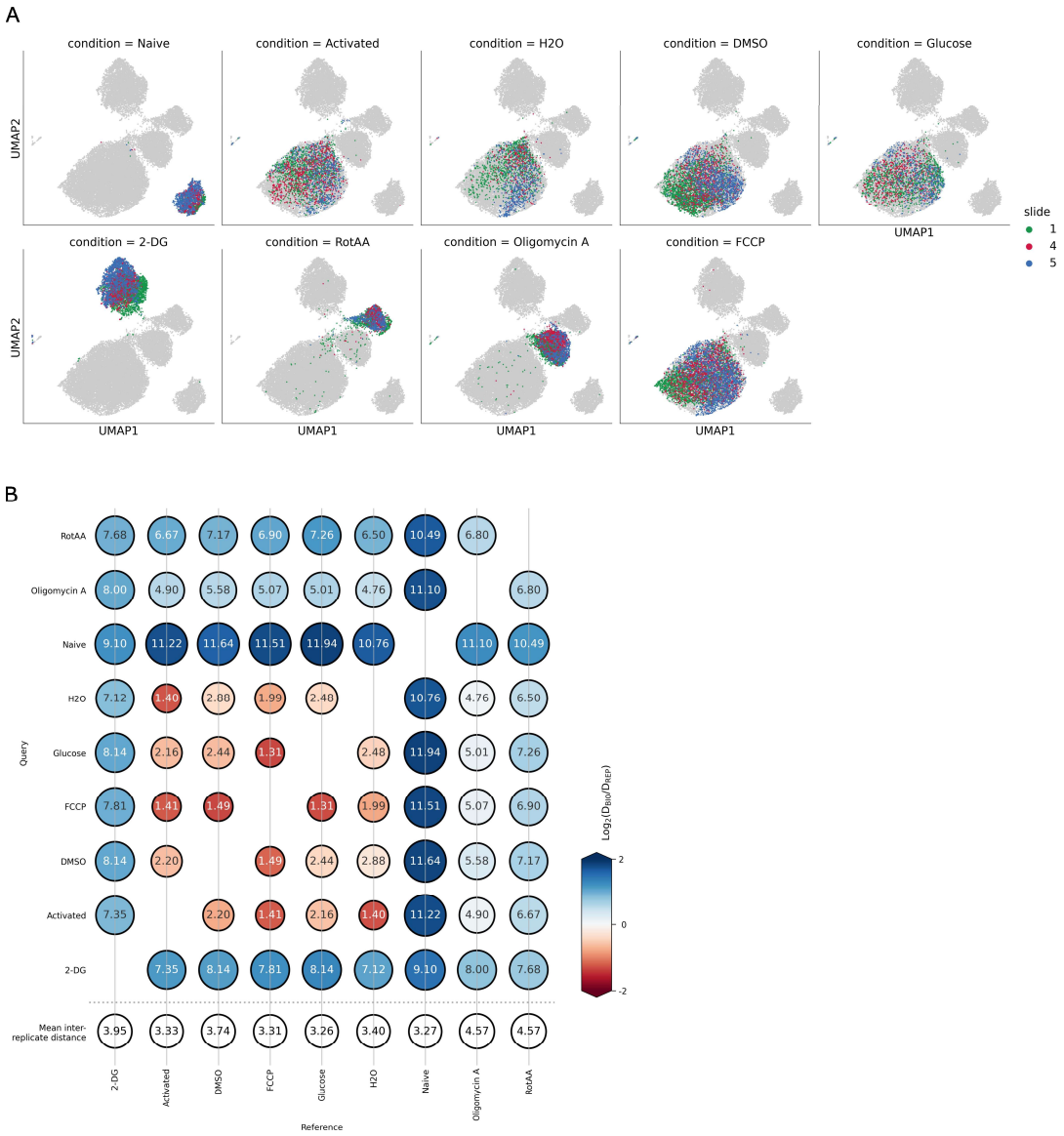

Figure 30 - Evaluating the reproducibility between multiple slides of one donor after removing outliers wells. **(A)** UMAP visualization of 29,294 cells and 152 metabolites. **(B)** Intra-label vs. inter-label distance plot. The intra-condition distances are represented in the bottom row. The inter-condition distance is represented in the colored circle. A red circle indicates that the intra-condition distance is lower than the inter-condition distance.

4.4.5. Validating HT-SpaceM as a method for metabolite detection in $CD4^+$ T cells with reference metabolic modulators

4.4.5.1. Visualizing the data and evaluating reproducibility

The same outlier-removing method described in the previous section was applied to the other 2 donors individually. Then, all the wells were concatenated into an extensive dataset with 121,940 cells and 143 ions. The same filtering and processing steps were followed as before. The filtering applied removed cells with less than 40 ions and wells with less than 100 cells. The 116,148 filtered cells were normalized to a total intensity of 10,000. The data was transformed using the natural logarithm and then scaled. Linear regression was also applied, and the variable "slide" was appointed as the source of variation, and then the data was scaled. This step exposed one significant limitation of the experiment: the slide design. Since there were 9 conditions and 3 donors in this experiment, it was not possible to fit everything in one slide while having at least 3 technical replicates. Thus, a decision had to be made between prioritizing conditions or donors. Prioritizing the latter would result in having all three donors in one slide with fewer conditions and fewer technical replicates. At the time of the experiment, it was still very uncertain whether there was high reproducibility between slides. Choosing to prioritize donors could mean that not all conditions would be comparable. Thus, I have decided to prioritize conditions instead, have all the conditions per donor in one slide, and maximize the number of technical replicates. Because of this design, each donor was cofounded with the variable slide. There were multiple slides per donor, but only one donor per slide. This meant that the linear correction of the variability observed across slides could conceal any potential donor biological variability.

The reproducibility across donors was very high (**Figure 31A**). When calculating the intra- and inter-condition distances, each well from each condition of each donor was considered a technical replicate. The intra-condition distances were relatively low, indicating that there was high reproducibility between the donors. The intra-condition distance was slightly higher than in previous results for the single donor, which was not unexpected. On the other hand, the inter-distance condition decreased, but the biological variability was still higher than the technical one, except for the Activated, H2O, DMSO, FCCP, and Glucose conditions. This was also observed in the UMAP plots, where these conditions formed one big population (**Figure 31B**). The UMAP plot, colored by condition

and donor, showed an excellent mixing of all donors except for one D85 in Activated and DMSO conditions (**Figure 31C**). The poor separation observed for the Activated, H2O, DMSO, FCCP, and Glucose conditions indicated either considerable technical variability among them or no biological difference between them.

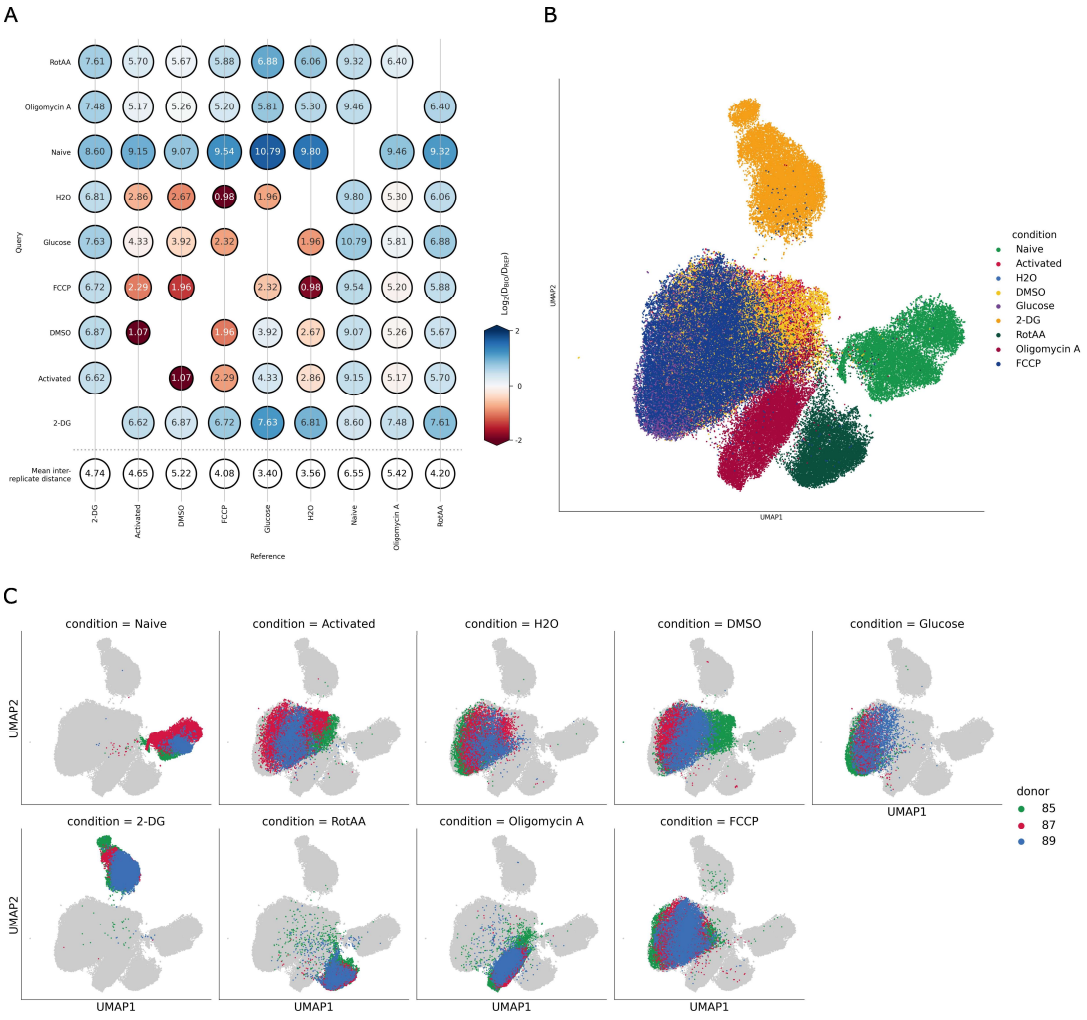

Figure 31 – Evaluating the reproducibility between different donors. **(A)** Intra-label vs. inter-label distance plot. The intra-condition distances are represented in the bottom row. The inter-condition distance is represented in the colored circle. A red circle indicates that the intra-condition distance is lower than the inter-condition distance. **(B), (C)** UMAP visualization of 116,148 cells and 143 metabolites.

The first option seemed very unlikely because the intra-distance calculated for these conditions was relatively low. Except for the DMSO condition, where the intra-distance was a bit high. However, it was still lower compared to other conditions with defined clusters like Naïve or Oligomycin A. On top of that, Glucose and H2O had the lowest intra-distance of all conditions and were still in this situation. Thus, it all indicated that the issue I was observing was biological. This was supported by the fact that the 3 affected conditions were the Activated and vehicle control conditions (DMSO, H2O). The poor inter-distance and clustering between these conditions indicated that the vehicles used did not affect the metabolism, which was a positive result. On the other hand, this also meant that adding extra glucose to the cells or incubating them with FCCP had no effect. Or at least the method could not measure this effect as the number of molecules detected is limited compared to the whole metabolome. In summary, the UMAP visualization hinted at the possibility that some compounds did not have a measurable effect. However, overall, the three donors were quite reproducible and clustered well together.

4.4.5.2. Identifying the marker metabolites and evaluating the metabolic effect

The UMAP visualization showed that there were metabolic differences between most conditions. So, it was essential to determine which metabolites were driving these differences, and for this, a differential expression analysis was performed. This analysis aims to identify quantitative changes between experimental groups using statistical tests. The method chosen for statistical analysis depends on the data distribution. The t-test is usually chosen when the data is normally distributed, while the Wilcoxon rank-sum is used when the distribution is skewed. Differential analysis is widely used among the single-cell community and is available in packages like Scanpy [151]. Thus, it was straightforward to integrate this into the analysis pipeline. Since the HT-SpaceM data contains many zeros, the distribution of most metabolites doesn't follow a Gaussian distribution. Thus, the method chosen to perform the differential analysis was the non-parametric test, Wilcoxon rank-sum (also known as the Mann–Whitney U test). The comparison of thousands of cells from each condition often results in extremely low p-values, which can make it challenging to interpret the results. Scanpy also provides another metric named "scores" to address this challenge. This metric uses Z-scores to quantify the difference in the expression levels of metabolites between the experimental groups. Metabolites with a positive score indicate

upregulation, while a negative Z-score suggests downregulation. High absolute values of this Z-score have corresponding low p-values. Thus, high absolute scores indicate significantly different expression.

Differential analysis was performed for every condition using activated cells as the reference group. To simplify the visualization of the results, only the top 5 up and downregulated metabolites were reported here. One of the main goals of this analysis was also to understand the impact of the solvent used to dissolve the compounds on cell metabolism. The differential expression results of the activated cells incubated with H2O or DMSO could help understand if the expression of specific metabolites was associated with one of the solvents. The results of the conditions that shared the same solvent were grouped into different figures to facilitate the visualization and interpretation. **Figure 32** shows the differential expression analysis of naïve cells versus activated cells. The top 5 downregulated metabolites in naive cells were all amino acids, while the top upregulated ones were a mix from different pathways (i.e., TCA cycle, taurine metabolism, and glycolysis). The scores for the top upregulated and downregulated metabolites had an absolute value between 100 and 150. As mentioned above, a higher absolute value indicates a significant change in the metabolite expression. However, comparing these absolute scores with the results from other conditions was necessary before drawing any conclusions.

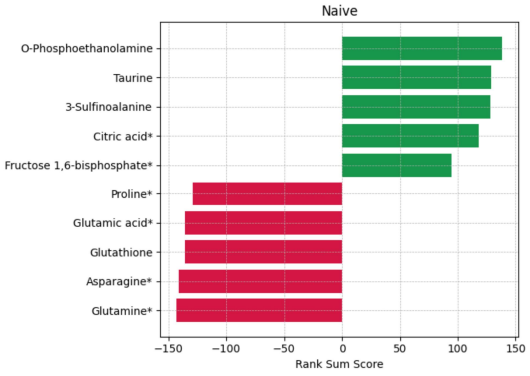

Figure 32 – Differential expression analysis between naïve and activated cells. The top 5 up (green) and down-regulated (red) metabolites are represented. Differential analysis was performed using the non-parametric test Wilcoxon rank-sum.

The results of the conditions where H2O was used as a solvent helped to interpret the significance of these scores (**Figure 33**). The up and downregulated metabolites in H2O and Glucose conditions had absolute scores between 40 and 60. On the other hand, the scores in the 2-DG condition had absolute values above 100, just like in the naïve condition. This indicated that the differences observed in the naïve and 2-DG conditions were more significant than those observed in the H2O and Glucose conditions. These two last conditions shared 4 of the 5 upregulated ions but only shared 2 downregulated ones. The low score indicated that the effect of using H2O as the solvent or adding extra glucose was very dim.

The glycolysis inhibitor, 2-DG, had 3 upregulated metabolites associated with glucose metabolism (glucose*, G6P*, and erythrose 4-phosphate). The downregulated ones were all amino acids, and 4 of these were shared with the naïve condition. However, the curated database annotated the top upregulated marker of the 2-DG condition as fucose 1-phosphate, an intermediate in the reaction that converts fucose into GDP-fucose. This molecule is used by fucosyltransferases to modify lipids and proteins [152]. This was intriguing since the role of this molecule as a metabolite was unclear.

Thus, I hypothesized whether this was just an ion with intensity levels close to noise or a wrong annotation. Because of the small size of the cells and different ionization properties, some metabolites have intensities close to the detection limit. This causes their detection to be unreliable, and any difference observed might be technical and not biological. These metabolites should be excluded during the database curation and processing steps, but it is possible that some could still pass this filtering. Thus, the first step was to check the intensity of this metabolite and the conditions where it was detected (**Figure 34**). The fucose 1-phosphate was uniquely detected in the 2-DG condition, but the intensity was not low. It was comparable to the intensity levels of glutamine*, which is always among the top expressed metabolites in all conditions. Thus, fucose 1-phosphate had a reasonable intensity and could not be considered technical noise, so I focused on the alternative option. Having ambiguous annotations is one of the drawbacks of this method because it cannot differentiate between isomers. Another one is that I am limited to the isomers included in the used databases. This metabolite was only annotated as fucose 1-phosphate, so I wondered if known isomers of this molecule were not included in the database. Searching PubChem, the open chemistry database, gave me the answer I sought.

There was another known molecule with the same formula (C8H13O8P) as fucose 1-phosphate, and it was named 2-Deoxy-Glucose-6-Phosphate [153]. As mentioned above, this product results from the uptake and phosphorylation of 2-DG by hexokinase, the first enzyme in glycolysis. Naturally, this molecule was not included in the database because it is a drug product, not a core metabolite. This information and the evidence that this molecule was only detected in 2-DG treated cells allowed me to assume that this molecule was indeed 2-DG6P* and not fucose-1-phosphate. After being phosphorylated by hexokinase, 2-DG6P competes with glucose 6-phosphate to bind the second enzyme in glycolysis, phosphohexose isomerase. Thus, 2-DG inhibits the first steps of glycolysis, where glucose is converted to glucose 6-phosphate and then fructose-6-phosphate [125]. Thus, the upregulation of 2-DG6P*, and the first two intermediates of glycolysis, G6P* and glucose*, indicated that the 2-DG treatment had successfully worked.

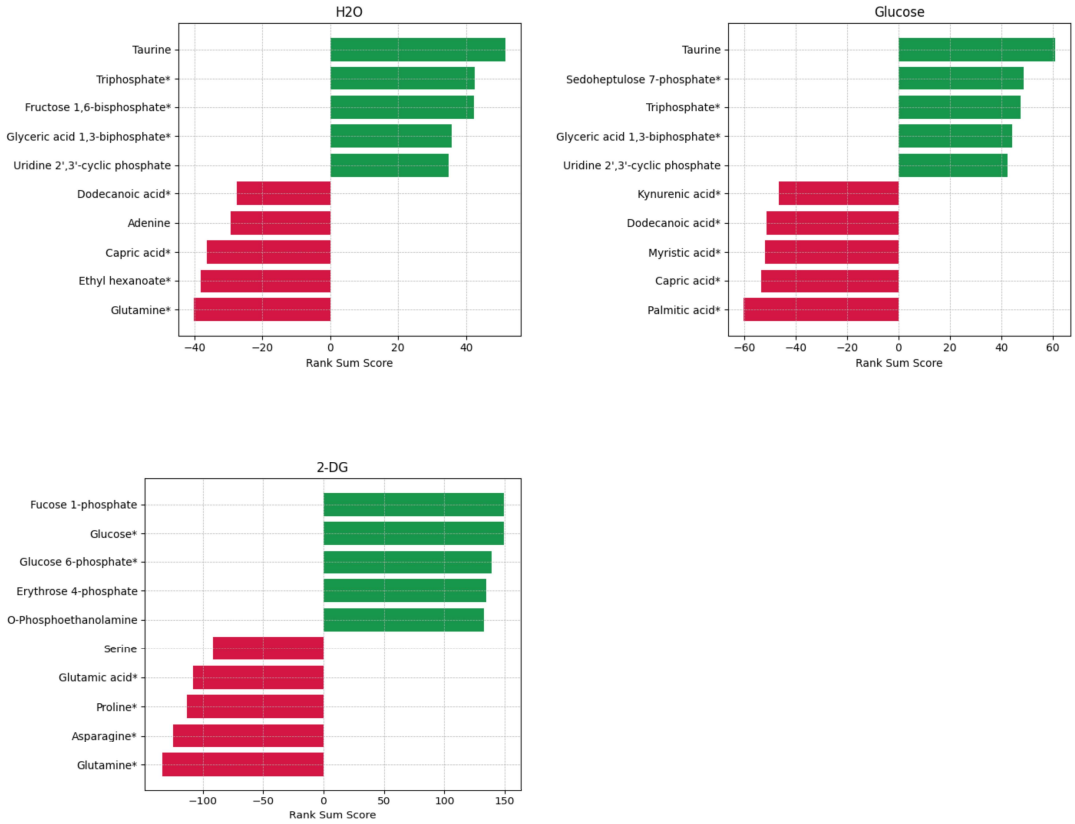

Figure 33 - Differential expression analysis between the indicated conditions and activated cells. The top 5 up (green) and down-regulated (red) metabolites are represented. Differential analysis was performed using the non-parametric test Wilcoxon rank-sum.

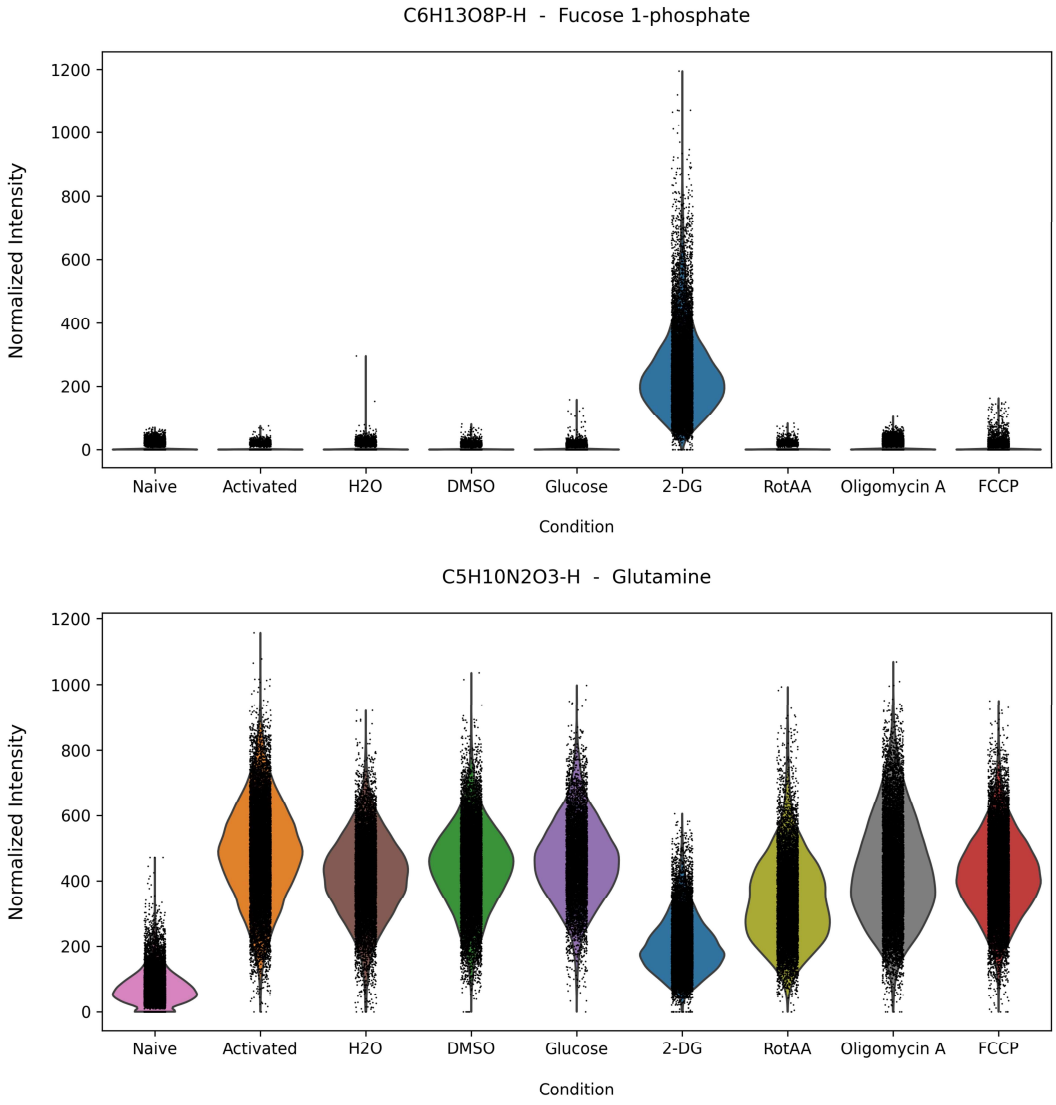

Figure 34 – Distribution of the intensity of fucose 1-phosphate and glutamine* per condition.

The conditions where DMSO was used as solvent also had interesting differential analysis results. The up and downregulated metabolites in the DMSO condition had absolute scores lower than 30. This condition shared some marker metabolites with other ones. However, no single metabolite was observed to be up or downregulated in all the conditions. This and the low score supported the idea that DMSO had no significant effect on the metabolism of cells, and no markers were linked to using DMSO as a solvent.

Similarly, the highest absolute score of FCCP markers was 40, indicating that this treatment's effect was weak.

On the other hand, both RotAA and Oligomycin A had significant results with absolute scores between 50 and -150. The top-downregulated markers of RotAA-treated cells were mainly amino acids already observed in the naïve and 2-DG conditions. Interestingly, the top 3 upregulated markers in the RotAA condition (orotic acid, uracil*, and L-dihydroorotic acid) belonged to the *de novo* pyrimidine biosynthesis pathway [154]. RotAA also shared one upregulated marker with Oligomycin: 2-hydroxyglutaric acid*, a byproduct of the TCA cycle. This metabolite results from the reduction of alpha-ketoglutarate, and its function is still unclear [155]. A study in metazoan species showed that increased alpha-ketoglutarate levels linked to impaired mitochondria and a dysfunctional TCA cycle caused the upregulation of 2-hydroxyglutaric acid [156]. It is still unclear if this reaction also happens in human cells. However, assuming that it does, this would indicate that both RotAA and Oligomycin A conditions had dysfunctional TCA cycle and mitochondria, which resulted in the observed accumulation of 2-hydroxyglutaric acid. Thus making 2-hydroxyglutaric acid a marker of impaired respiration. Oligomycin exhibited high expression of two glycolytic metabolites, FBP* and glyceraldehyde 3-phosphate*. Interestingly, 3 metabolites involved in purine biosynthesis were also differentially expressed in Oligomycin-treated cells. Inosine monophosphate (IMP) expression was upregulated, while the other metabolites, adenine and adenosine monophosphate* (AMP), were downregulated. This imbalance in the purine metabolism indicated a potential effect of Oligomycin on that pathway.

Multiple conclusions could be drawn from the differential analysis results. The first concerns the absolutes scores and their correlation to the significance of the observed effects. The differential expression scores varied greatly among conditions, with some having absolute scores for all metabolites above 100 and others barely having any score above 50. This was already an indication that the score could indicate whether a compound had a significant effect. The second conclusion was that the UMAP visualization was a good representation of the overall impact of the compounds. Conditions with scores closer to 100 clustered apart, while those with scores lower than 50 (i.e., H2O, DMSO, glucose, FCCP) were clustered with the activated condition. Thus, the results of the differential expression in combination with the UMAP visualization were a valid way of assessing the impact of the compounds on the metabolism of $CD4^+$ T cells. The final conclusion was that

the differential analysis results and the UMAP visualization results showed that the used solvents had no significant impact on the metabolism of the treated cells.

Finally, based on these results, I implemented a threshold to determine whether a compound had a significant effect. For a given compound, if all up- or down-regulated metabolites had an absolute score above 50, the effect of this compound was classified as significant. In summary, I demonstrated that the differential expression scores indicate whether a compound had a significant effect. In this case, 2-DG, RotAA, and Oligomycin A had significant effect, while FCCP did not. Besides that, the up-regulated metabolites for the 2-DG condition matched the expected effect from this compound. This showed that HT-SpaceM could differentially detect relevant metabolites and resolve metabolic states.

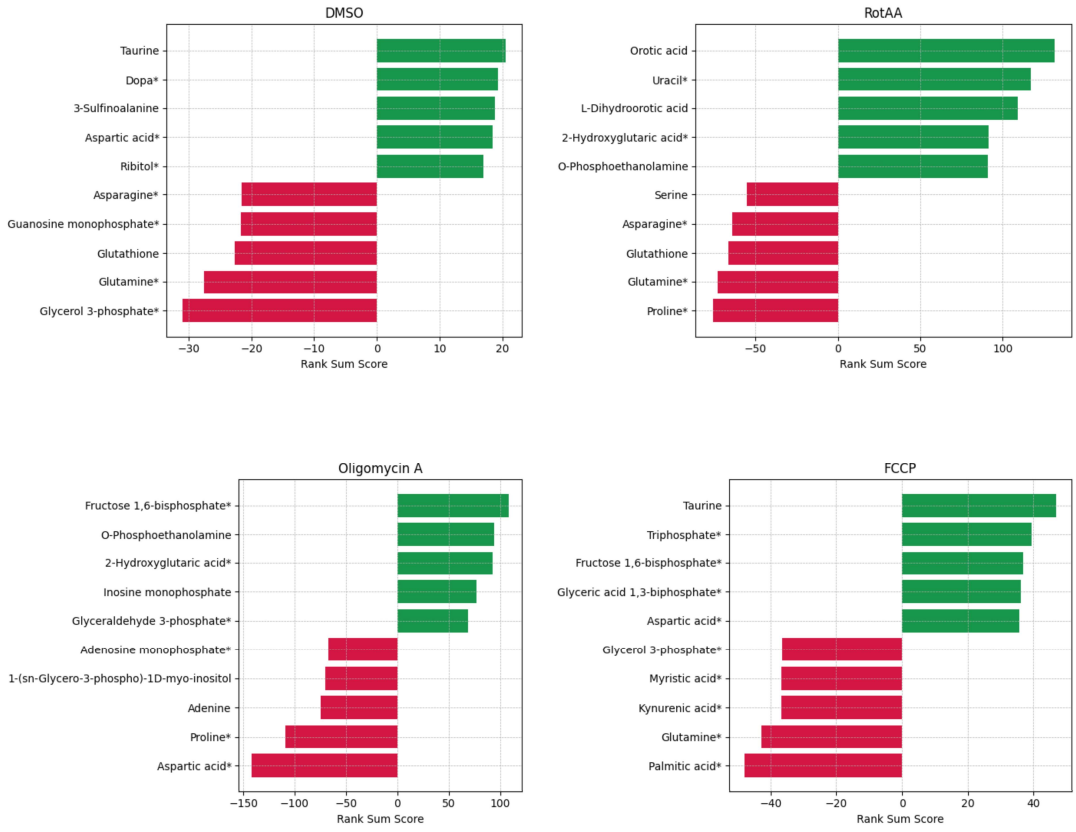

Figure 35 - Differential expression analysis between the indicated conditions and activated cells. The top 5 up (green) and down-regulated (red) metabolites are represented. Differential analysis was performed using the non-parametric test Wilcoxon rank-sum.

4.4.5.3. Structural validation of the identified markers

HT-SpaceM has the potential to detect heterogeneity and focus on rare populations while requiring a small amount of biological material. However, it has the significant drawback of providing ambiguous results due to the inability to differentiate isomers. This is an accepted limitation of the method and is usually surpassed by the provided advantages. However, since this experiment aimed to demonstrate that HT-SpaceM could be used to characterize the metabolome of $CD4^+$ T cells, it was essential to validate the identified markers with LC-MS/MS. The usual experimental workflow was followed with slight modifications. After culturing the cells. Instead of being prepared for HT-SpaceM (i.e., adhered, desiccated, etc.), the cells were frozen for later analysis with LC-MS/MS. Since the bulk method required 3-5 times the number of cells needed by HT-SpaceM, only the significant differentially expressed conditions were validated (Naïve, Activated, 2-DG, RotAA, and Oligomycin A). The data acquisition and processing were done by a postdoc in the Alexandrov team since I was not trained for that. Nevertheless, I generated the plots presented in this section.

Negative polarity was also chosen for LC-MS/MS, and 80 metabolites were detected. However, only 55 were commonly detected between LC-MS/MS and HT-SpaceM. The main goal of this validation was to check which up and downregulated markers identified with HT-SpaceM were also detected with LC-MS/MS. On top of that, I wanted to check if the metabolites that were up and downregulated in single-cell data also showed a similar trend in the bulk data. Thus, I started by checking which of the 5 upregulated and 5 downregulated metabolites for each condition (Naïve, 2-DG, RotAA, and Oligomycin A) were also detected with LC-MS/MS. There was a significant overlap, and for most conditions, around 6/7 of the total up and downregulated metabolites could be commonly detected. The metabolites were divided into two figures according to their differential analysis expression results in single-cell for easier visualization. The LC-MS/MS data was normalized using the Total Ion Count and then transformed using the base 10 logarithm to avoid skewness. Then, plots comparing the intensity of each condition versus activated for a given metabolite were generated.

Figure 36 shows the metabolites detected with LC-MS/MS that were found to be upregulated in Naïve, 2-DG, RotAA, and Oligomycin A conditions with HT-SpaceM. The plot is organized in a way that each row is a different condition and the intensity of each

metabolite is compared between that condition and the activated cells. The red sunburst was used to signal the metabolites and conditions where the results did not match the single-cell observations. In other words, the sunburst signals the metabolites that were upregulated with HT-SpaceM for a given condition but had the opposite trend and were downregulated in LC-MS/MS data. Among the upregulated metabolites, only taurine in naïve cells and G6P in the 2-DG condition did not match the single-cell results and were downregulated in the bulk data. This was a great result because it validated both the structure and the relative intensity of most of the condition markers found with HT-SpaceM.

However, the complete opposite result was observed in the metabolites identified as downregulated with HT-SpaceM in the Naïve, 2-DG, RotAA, and Oligomycin A conditions (**Figure 37**). Although most of them were structurally validated for each condition, their relative intensity compared to the activated cells did not match the single-cell results. In fact, most of these metabolites were actually upregulated in these conditions in LC-MS/MS data, as shown by the red sunbursts. In summary, LC-MS/MS allowed me to validate the detection of some marker metabolites of the Naïve, 2-DG, RotAA, and Oligomycin A conditions. However, the distribution and relative intensity could not be validated for all. The reasons for the observed disparities are not known. Thus, the single-cell results should be interpreted cautiously for such cases. Nevertheless, this was an important step for validating HT-SpaceM as a method for single-cell metabolomics in $CD4^{+}$T cells.

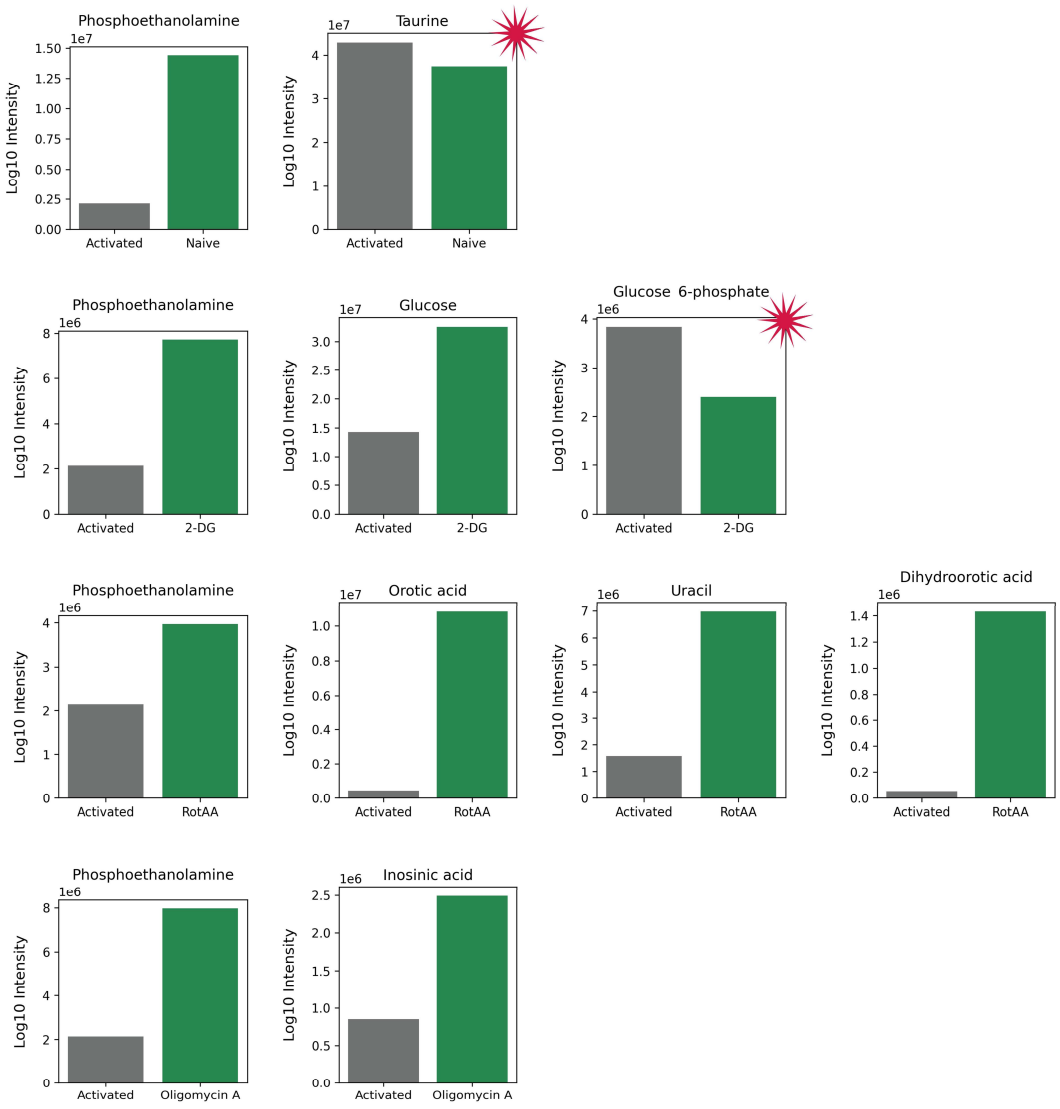

Figure 36 – LC-MS/MS detected metabolites that were upregulated for the indicated conditions in single-cell data. The data was normalized using the Total Ion Count and transformed using the base 10 logarithm. The red sunburst indicates the metabolites and conditions where bulk data does not match single-cell data.

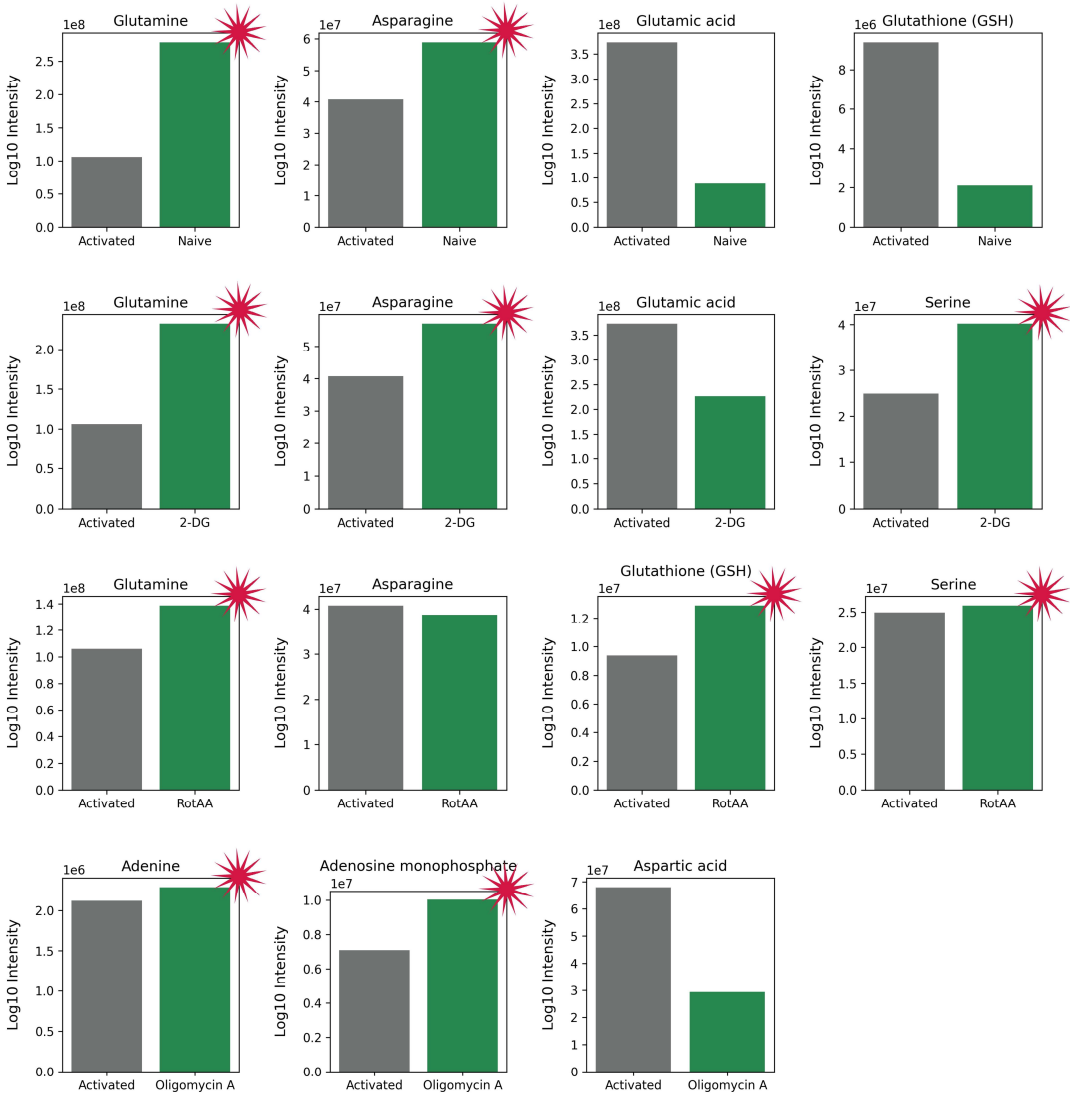

Figure 37 - LC-MS/MS detected metabolites that were downregulated for the indicated conditions in single-cell data. The data was normalized using the Total Ion Count and transformed using the base 10 logarithm. The red sunburst indicates the metabolites and conditions where bulk data does not match single-cell data.

4.4.5.4. Unsupervised clustering reveals metabolic states

The UMAP visualization, reproducibility, and differential analysis indicated that HT-SpaceM could characterize the metabolic state of $CD4^+$ T cells. There was only one analysis left to run that would complete the validation of the method: unsupervised clustering. This would reveal which populations were present in the data and showcase the ability of HT-SpaceM to detect distinct metabolic states. The data was clustered using the Leiden algorithm. Different resolutions were tested, and it was concluded that the ideal resolution was 0.2 because higher resolutions resulted in overclustering. The algorithm identified 5 main clusters (**Figure 38A**), which matched the 5 main populations observed in the UMAP visualization. The distribution of the conditions per cluster revealed that almost all naïve and 2-DG-treated cells were only clustering within their condition (**Figure 38B**). Meanwhile, 5-10% of cells treated with RotAA and Oligomycin were still clustering with the activated cells. This could indicate that this small percentage of cells did not respond to the treatment. Finally, the clustering also reinforced what the differential analysis had shown. The differences between activated and the remaining conditions (H2O, DMSO, glucose, and FCCP) were so dim that they were all assigned to the same cluster.

Differential analysis was performed again, but with settings that were different from before. The analysis was performed on the Leiden clusters, and each cluster was compared to the rest. Thus, the goal was to determine which markers were upregulated on a specific cluster compared to all the others and not just the activated cluster. The top 3 upregulated metabolites for each Leiden cluster are shown in **Figure 39**. For a more comprehensive understanding, the distribution of each metabolite was represented on the UMAP visualization. Since all clusters except cluster 0 were mostly composed of single conditions, it was possible to compare if the markers assigned to the clusters differed from those previously identified for these conditions. Interestingly, no new markers were identified for any cluster. Thus, this showed that these conditions had unique markers not just compared to the activated cells but also to the remaining conditions. However, it was possible to observe that the high expression of some markers was not exclusive to their cluster.

In summary, this last analysis concluded the validation of HT-SpaceM. In this proof-of-concept experiment, I first showed that HT-SpaceM can detect the already reported metabolic dichotomy between activated and naïve cells. This was observed in the UMAP visualization and the differential expression of many metabolites between these two conditions. In this proof-of-concept experiment, I also activated and treated the $CD4^+$ T cells with five modulators known to target glycolysis and OXPHOS. HT-SpaceM could differentially detect metabolites between these modulated conditions and the control condition (Activated). Some of these markers matched the expected effects from the tested compounds and were structurally validated with LC-MS/MS. Dimensionality reduction with the UMAP showed five main populations, three of which were composed of single treatments. The clustering algorithm captured the metabolic states of these five main populations which were linked to the compounds with significant effects. I have also showed that the solvents used to dissolve the compounds (DMSO, H2O) do not significantly affect the metabolism of the cells. Thus, by using modulators with known effects, I have shown that HT-SpaceM is a method that can resolve the metabolome of $CD4^+$ T cells.

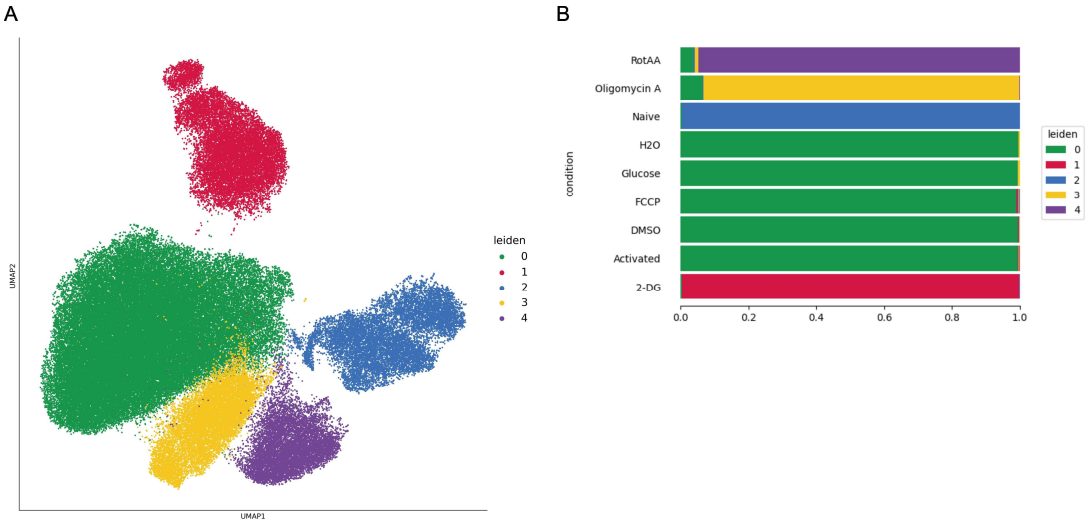

Figure 38 – Unsupervised clustering revealed 5 metabolic states. **(A)** UMAP visualization of 116,148 cells and 143 metabolites colored by the assigned Leiden cluster. **(B)** Visualization of the distribution of conditions within the identified Leiden clusters (resolution=0.2).

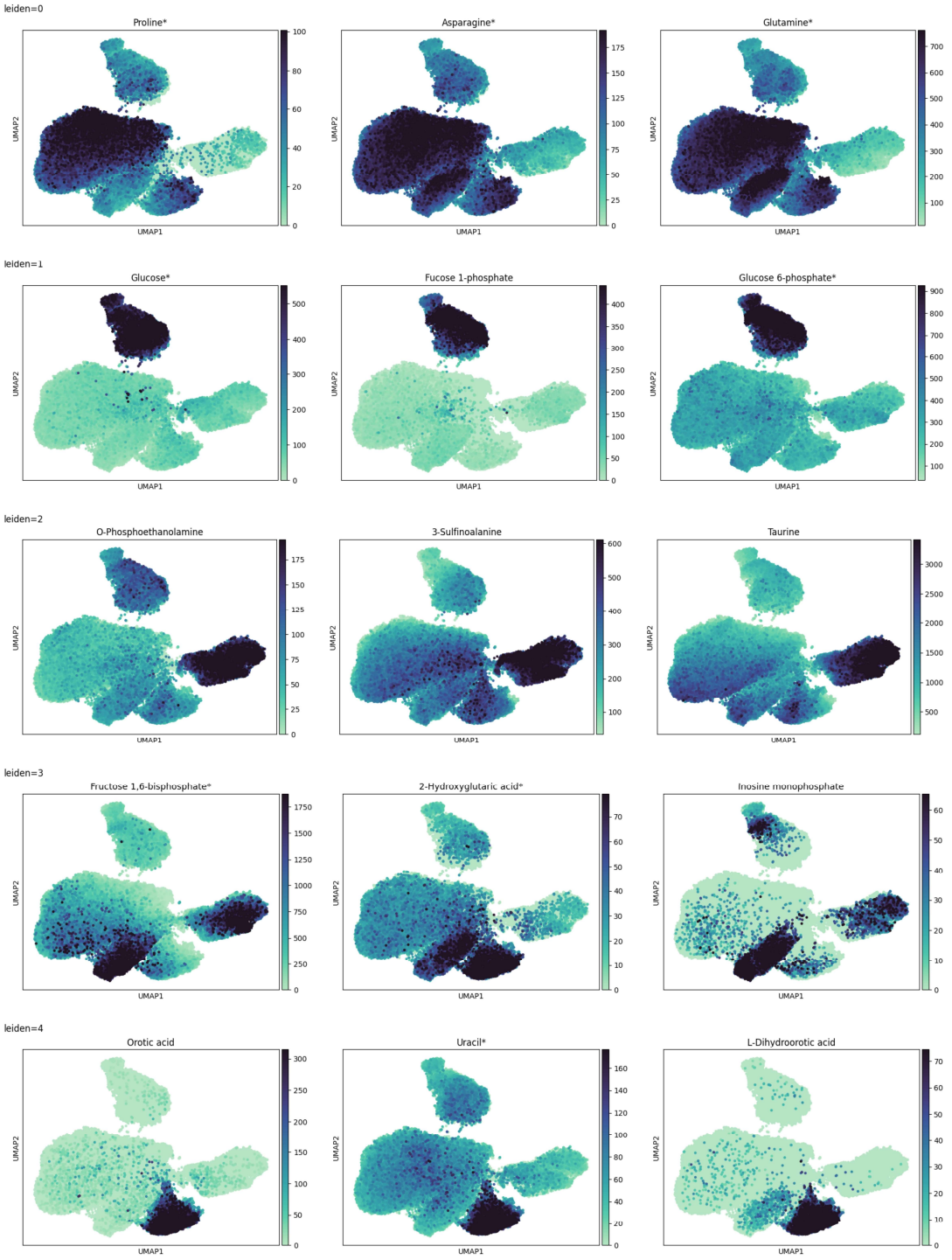

Figure 39 - Differential expression analysis between the Leiden clusters. The top 3 upregulated metabolites for each cluster are shown. The UMAP visualization shows the distribution of the identified upregulated metabolites. Differential analysis was performed using the non-parametric test Wilcoxon rank-sum.

4.5. Evaluating the metabolic response of CD4$^+$ T cells to relevant compounds

4.5.1. Targeting the central metabolic pathways beyond glycolysis and OXPHOS

The successful showcase of the HT-SpaceM method opened the possibility to explore the metabolic modulation of CD4$^+$ T cells further. The proof-of-concept experiment showed that targeting glycolysis and OXPHOS significantly impacted the metabolism of CD4$^+$ T cells. Thus, the following experiment aimed to target other metabolic pathways and prioritized the ones reported as unregulated during the metabolic remodeling of CD4$^+$ T: glutaminolysis and FAS. The first one was targeted with BPTES, a selective inhibitor of glutaminase-1. This enzyme catalyzes the conversion of glutamine into glutamate during the first step of glutaminolysis [157]. The modulation of FAS was achieved by targeting the conversion of acetyl-CoA into malonyl-CoA. This is the commitment step for FAS and is catalyzed by acetyl-CoA carboxylase, an enzyme inhibited by PF-05175157 [158].

The high glycolysis flux upon activation starts with the upregulation of the Glucose transporter 1 (GLUT1) on the cell membrane, which is essential to increase glucose uptake [21]. The GLUT1 inhibitor, STF-31, has been shown to reduce glycolysis and proliferation in activated CD4$^+$T cells [159]. Thus, STF-31 was the third modulator selected, followed by TEPP-46. This small molecule is a known activator of pyruvate kinase M2, the enzyme that catalyzes the last step of glycolysis [160]. The last modulator chosen was MK8722, a direct activator of 5' AMP-Activated Protein Kinase (AMPK) [161]. This metabolic regulator is quickly triggered upon T-cell activation, but its activity declines with proliferation and differentiation. AMPK promotes catabolic processes that generate ATP, like glycolysis and FAO, while inhibiting anabolic processes that consume ATP, like FAS [162]. Thus, TEPP-46 and MK8722 were used to boost glycolysis in activated cells.

Before proceeding with the experiments, choosing the concentration for each compound was necessary. Since some of the chosen modulators had not been tested before in CD4$^+$ T cells, it was necessary to evaluate their optimal concentration. However, due to time restrictions, this was not possible. Thus, a standard concentration of 1µM was chosen for all the modulators not tested in CD4$^+$ T cells before. This choice was based on the concentration range regularly used for other compounds in CD4$^+$ T cells. On the other hand, the concentration chosen for compounds previously tested in CD4$^+$ T cells was similar to the ones reported in the respective studies. Then, the experimental and computational workflow was the same, as shown in **Figure 23**.

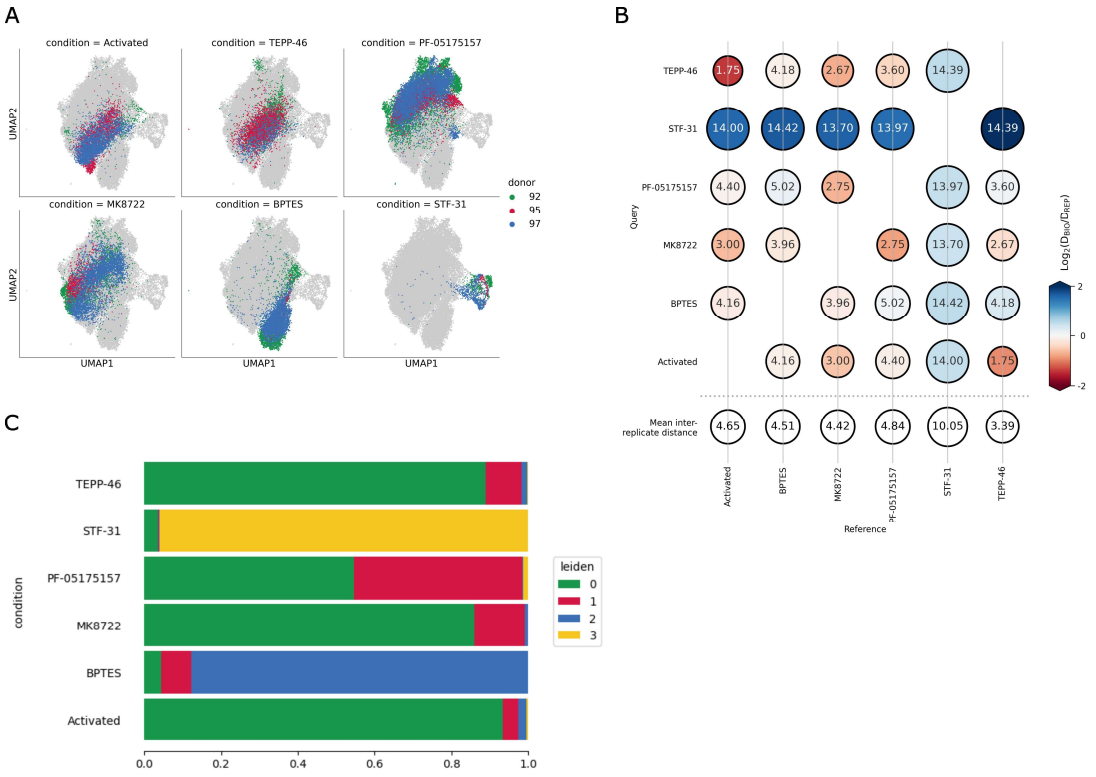

Figure 40 –Treating activated CD4⁺ T cells with known metabolic modulators. **(A)** UMAP visualization of 39,560 cells and 147 metabolites. **(B)** Intra-label vs. inter-label distance plot. The intra-condition distances are represented in the bottom row. The inter-condition distance is represented in the colored circle. A red circle indicates that the intra-condition distance is lower than the inter-condition distance. **(C)** Visualization of the distribution of conditions within the identified Leiden clusters (resolution=0.2).

Data visualization with a UMAP revealed three main populations, two of which were driven individually by BPTES and STF-31, and the third one was a mix of the remaining conditions (**Figure 40A**). Based on the observed intra-condition distance, the reproducibility between replicates seemed to be high, except for STF-31 (**Figure 40B**). Fortunately, the inter-condition distance to the others was higher than the intra-condition distance, which resulted in an isolated population in the UMAP. However, this was not the case for the rest of the conditions, where the intra and inter-condition distances were very similar, which would explain the poor separation observed in the UMAP. Since the intra-condition distance for each condition was relatively low and comparable to previous experiments, the poor distance between replicates was probably not technical but biological. The unsupervised clustering with the Leiden algorithm identified four clusters

(**Figure 40C**). The cells from STF-31 and BPTES conditions were distinctly assigned to individual clusters. While the rest of the conditions evenly populated Cluster 0. There was a fourth cluster (Cluster 1) that was dominated by PF-05175157-treated cells. However, it was not exclusive to this condition and which indicated that the effect of this condition was not strong enough to form its cluster.

Differential expression analysis was run using the activated condition as the reference (**Figure 41**). The results further supported the idea that the modulators had weaker effects than the previous experiment. In fact, none of the conditions had any up or downregulated metabolites with a score above 100. The only exception was PF-05175157, which had one strongly downregulated metabolite. Nevertheless, all the conditions except TEPP-46 had all up or downregulated metabolites with an absolute score above 50. This indicated that TEPP-46 did not have a significant effect in boosting glycolysis in the cells. On the other hand, MK8722, which is also supposed to boost catabolism, had all the downregulated metabolites with a score below -50. Besides the already-known markers like glutamine*, asparagine*, and serine*, which were already observed to be downregulated in other conditions, there were 2 new metabolites downregulated in MK8722-treated cells. These were glycerylphosphorylethanolamine and 1-(sn-glycero-3-phospho)-1D-myo-inositol or glycerophosphoinositol, two phospholipids that play a crucial role in cell membrane integrity [163], [164]. Interestingly, these two downregulated markers were shared with the PF-05175157 condition, where FAS was inhibited. T cells engage in FAS upon activation to generate lipids that will supply the synthesis of new membranes during proliferation [24]. Thus, the downregulation of these two phospholipids in the PF-05175157-treated cells suggested that the treatment worked as expected and inhibited FAS in activated $CD4^+$ T cells. It also indicated that FAS was inhibited in the MK8722 condition. Even though AMPK, the target of MK8722, is usually associated with the activation of catabolism, it can also, in fact, inhibit anabolic processes like FAS. Thus, based on the observed markers, MK8722 did not seem to have the expected effect in boosting glycolysis, but it successfully inhibited FAS.

The inhibition of the conversion of glutamine into glutamic acid resulted in the downregulation of the latter and gamma-aminobutyric acid*(GABA) in BPTES-treated cells. GABA is a downstream product of glutamic acid metabolism [165]. This indicated a significant impairment of glutamine and glutamic acid metabolism by BPTES. The main reason activated T-cells increase glutaminolysis is to generate intermediates that supply the

TCA cycle [26]. Thus, one could expect that inhibiting the first step of glutaminolysis would impair the TCA cycle. However, cells treated with BPTES actually increased the expression of citric acid*. Thus, BPTES inhibited glutamine metabolism in activated $CD4^+$ T cells. However, the effect on the TCA cycle was unclear. Finally, STF-31, the GLUT1 inhibitor, did not have any upregulated metabolites with a score above 50, but it had downregulated ones. Interestingly, the downregulated metabolites were the same ones identified in naïve and 2-DG-treated cells in the previous experiment. This could potentially indicate an impaired activation in STF-31 cells. However, since there are no upregulated markers above the threshold score, no conclusions regarding the metabolic effect of STF-31 can be drawn.

In summary, in this experiment, I treated activated CD4+ T cells with modulators that targeted metabolic pathways upregulated upon activation (glutaminolysis, FAS, glycolysis). The observed effects were not as pronounced as in the proof-of-concept experiment. However, I was able to show that glutaminolysis and FAS synthesis are important in activated $CD4^+$ T cells and that inhibiting these pathways can significantly affect their metabolome.

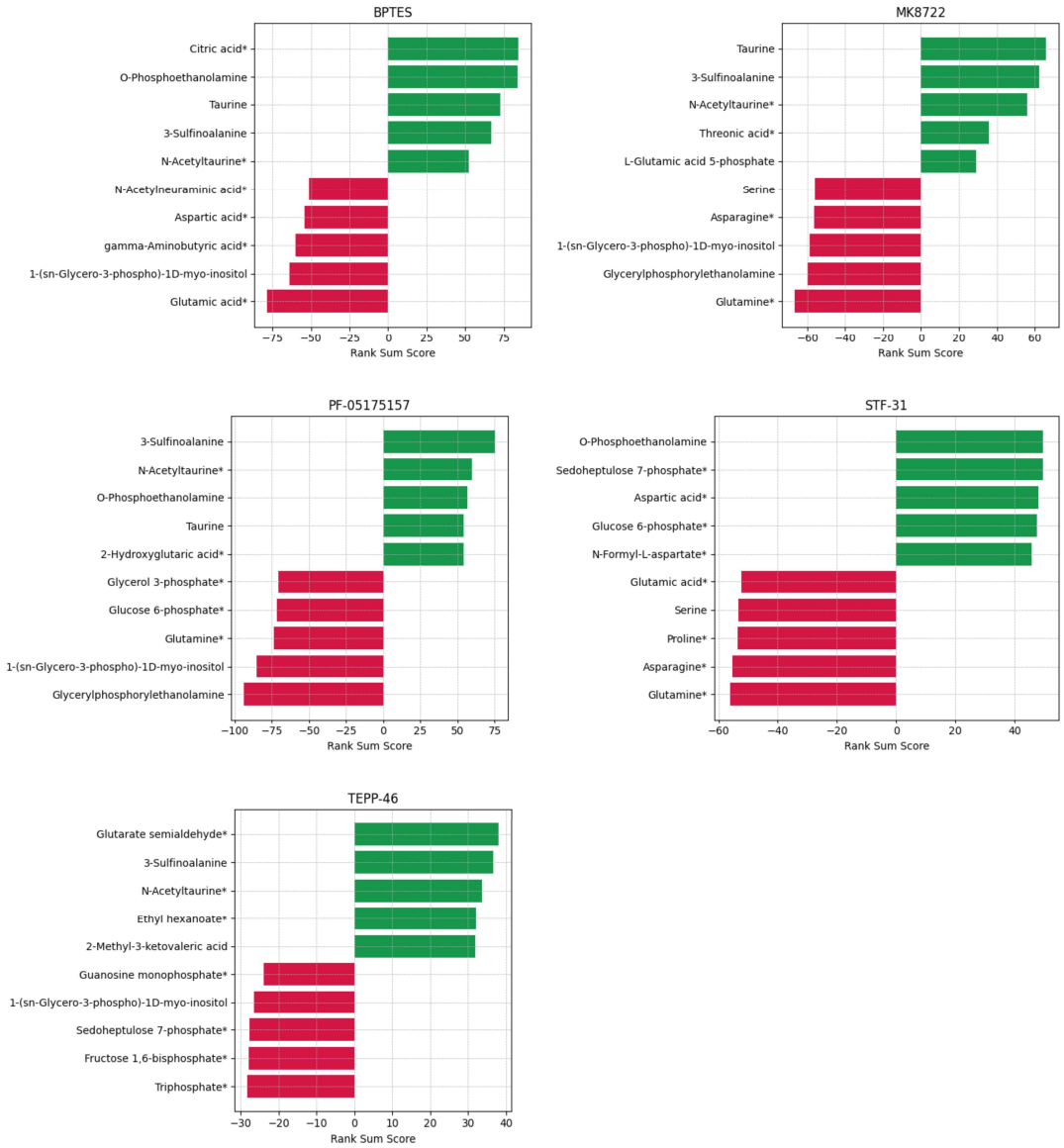

Figure 41 - Differential expression analysis between the indicated conditions and activated cells. The top 5 up (green) and down-regulated (red) metabolites are shown. Differential analysis was performed using the non-parametric test Wilcoxon rank-sum.

4.5.2. Understanding the metabolic effect of JAK inhibitors

The successful characterization of the metabolism of $CD4^+$ T cells with known metabolic modulators in independent experiments empowered the idea of characterizing the impact of non-metabolic modulators. Thus, the experiment described in this section combined a selection of metabolic and T-cell biology modulators. One main pathway that still needed to be targeted was FAO. This pathway plays a key role during the differentiation of Tregs and memory T cells, but it is supposed to be downregulated in activated cells [166]. Nevertheless, it seemed appropriate to cover this pathway, and for this purpose, etomoxir was chosen. This compound blocks the transport of long-chained amino acids into the mitochondria where FAO occurs [166]. Two other compounds targeting the metabolism were chosen: Telaglenastat and AZ-PFKFB3-67 (AZ67). The first targets glutaminase, just like the BPTES compound used in the previous experiment [167]. The main goal behind repeating this modulation was to evaluate if different compounds with the same target would have different modes of action. The second choice also aimed to repeat a pathway that had already been modulated: glycolysis. AZ67 is a potent inhibitor of 6-phosphofructo-2-kinase/fructose-2,6-bisphosphatase-3 (PFKFB3), the most potent activator of glycolysis [168].

The remaining 4 compounds are all approved drugs for distinct diseases. The first one was metformin, a multi-target compound whose primary function is the activation of AMPK. This results in the inhibition of gluconeogenesis, and thus, metformin is commonly used to treat diabetes. However, an increased number of publications have been reporting other potential targets of metformin, which are AMPK-independent, like, for example, complex I of the ETC or glycerol-3-phosphate dehydrogenase [169]. The latter catalyzes the conversion of a glycolic intermediate, dihydroxyacetone phosphate, into glycerol 3-phosphate, which plays a key role in fueling OXPHOS [170]. Rapamycin is an immunosuppressive commonly used to prevent transplant rejection [171]. This compound inhibits the mammalian target of rapamycin (mTOR), a master regulator of cell metabolism. In $CD4^+$ T cells, rapamycin inhibits the differentiation into the T helper lineages and promotes the differentiation into Tregs. The downregulation of mTOR is linked to glycolysis suppression, which impairs the proper differentiation of T helper lineages [172]. The non-metabolic modulators chosen were baricitinib and tofacitinib, inhibitors of the Janus kinase/signal transducer and activator of the transcription (JAK/STAT) pathway. These two approved compounds are commonly used to treat

autoimmune conditions like rheumatoid arthritis. Both compounds inhibit JAK proteins and suppress the downstream signaling in T cells, but their effect on the cell's metabolism is still unknown [173].

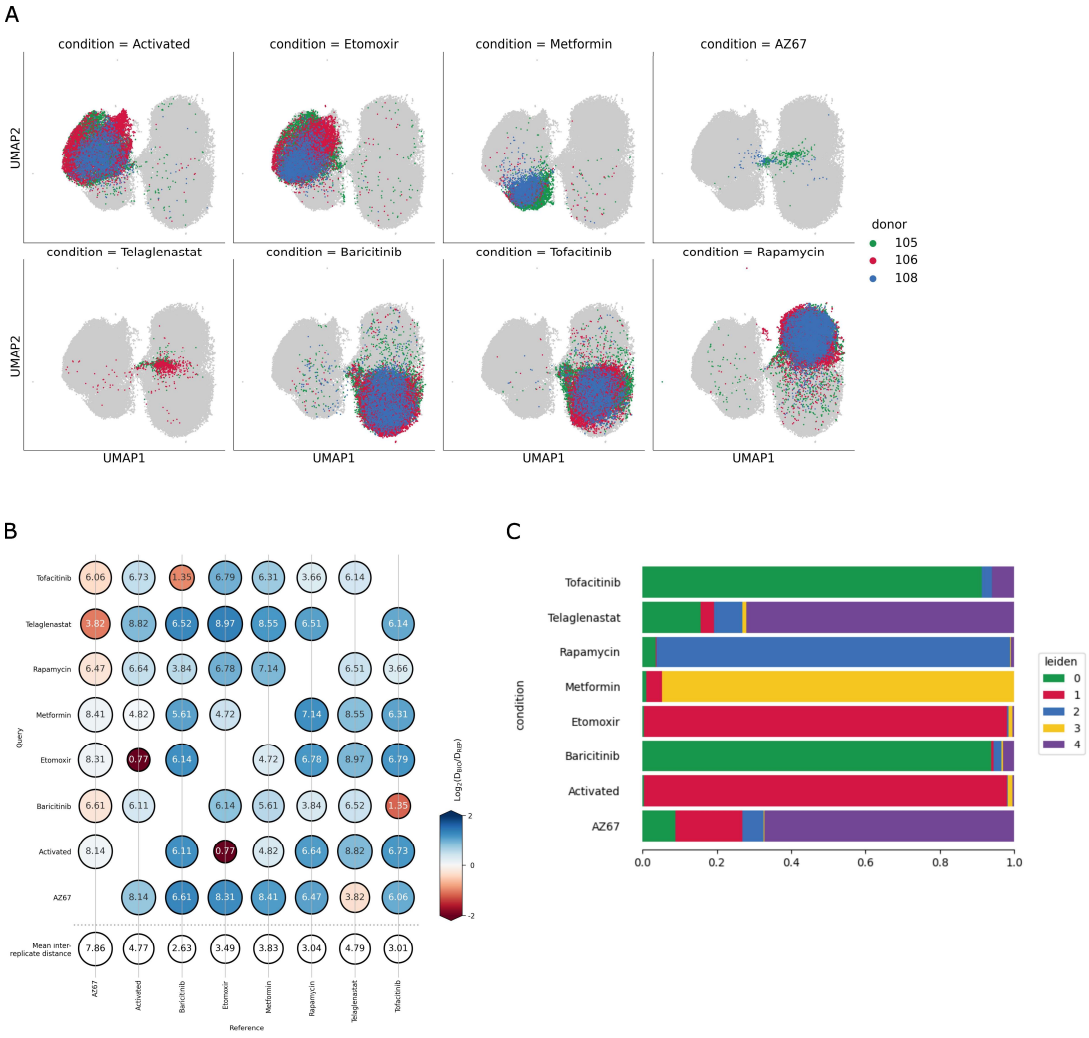

Figure 42 – Treating activated CD4^{+} T cells with a mixed group of modulators. **(A)** UMAP visualization of 89,920 cells and 126 metabolites. **(B)** Intra-label vs. inter-label distance plot. The intra-condition distances are represented in the bottom row. The inter-condition distance is represented in the colored circle. A red circle indicates that the intra-condition distance is lower than the inter-condition distance. **(C)** Visualization of the distribution of conditions within the identified Leiden clusters (resolution=0.3).

The data was processed and filtered as described in the previous sections. Data visualization with a UMAP revealed two main populations of cells (**Figure 42A**). One was populated by activated, etomoxir, and metformin-treated cells, and the other by the remaining conditions. The only condition that was clustering together with the activated cells was Etomoxir. The AZ67 and Telaglenastat conditions had visibly fewer cells than the remaining ones. This resulted from filtering out poor-quality cells (with less than 40 metabolites) in these two conditions, which were the majority. The intra-condition distance was lower than the inter-condition for all conditions except for AZ67, indicating high technical reproducibility (**Figure 42B**). The only pairs of conditions with low inter-condition distance were Activated/Etomoxir and Baricitinib/Tofacitinib. The latter is not unexpected, given that these compounds target the same enzyme. While the low distance between activated and etomoxir-treated cells reflected the poor separation already observed in the UMAP. Unsupervised clustering with the Leiden algorithm found 5 clusters (**Figure 42C**). Etomoxir-treated cells were assigned to the same cluster as the Activated condition, hinting at the dim effect of this compound. AZ67 and telaglenastat-treated cells were also assigned to the same cluster. Given the different modes of action of these compounds, this was unexpected, so it was hypothesized that poor cell quality could drive this.

Differential analysis of metabolite expression was performed using the activated cells as the reference group. The results revealed that all compounds had significant effects except for etomoxir, AZ67, and telaglenastat (**Figure 43**). This conclusion was based on the threshold score defined above. The dim results of etomoxir were not unexpected, given the reported downregulation of FAO by T cells upon activation. However, the non-significant results of AZ67 and telaglenastat were unexpected, given that the previous experiments showed that the metabolism of T cells is impacted when glycolysis and glutaminolysis are inhibited. The low significant results observed for these two compounds could be caused by the low number of cells measured in these conditions. The method used to determine the differential expressed metabolites, Wilcoxon rank-sum, can be greatly influenced by unequal sample sizes, which may increase the likelihood of false negative results.

The accumulation of the TCA-cycle intermediates, malic acid* and fumaric*, and the downregulation of citric acid* indicated that metformin impacted this pathway. However, the direction of the effect was unclear. The taurine metabolism intermediates, taurine and 3-sulfinoalanine, were upregulated in metformin-treated cells. Baricitinib and Tofacitinib conditions shared all the up and downregulated markers, suggesting no difference in these compounds' metabolic mode of action. The downregulation of the glycolysis intermediates FBP* and G6P* indicated that these compounds strongly affected this pathway. The downregulation of these markers was also observed in rapamycin-treated cells, which was expected as mTOR signaling upregulates aerobic glycolysis in T cells [174]. An increased flux of the TCA possibly compensated this, since an upregulation of citric acid* was observed in these cells. Rapamycin also shared some upregulated markers with the Baricitinib and Tofacitinib conditions (e.g., aspartic acid*, adenosine monophosphate*). These results and the UMAP visualization suggested a similar mode of action for these 3 compounds.

Interestingly, one metabolite identified as downregulated in all these conditions was fucose 1-phosphate*. As mentioned before, this compound is an isomer of 2-DG6P, the product of 2-DG phosphorylation by hexokinase. In the proof-of-concept experiments, this metabolite was only detected in 2-DG treated cells, and thus, it was assumed that it was indeed 2-DG6P and not fucose 1-phosphate*. However, in this experiment, no cells were exposed to 2-DG. Therefore, the metabolite detected is very likely fucose 1-phosphate*. This was differentially detected in activated cells, which was unexpected and not observed for this condition in previous experiments. This is a very good example of the variation observed between different experiment batches that was not possible to correct.

In summary, activated $CD4^+$ T cells were treated with additional modulators that covered metabolic and non-metabolic targets. Two of the conditions (AZ67 and Telaglenastat) had a significantly lower number of cells. This was caused by the quality filtered applied where cells with less than 40 metabolites were filtered out. Blocking FAO did not significantly impact the metabolism of $CD4^+$ T cells. On the other hand, JAK inhibition with baricitinib and tofacitinib altered the metabolism of $CD4^+$ T cells similarly to the mTOR inhibitor rapamycin.

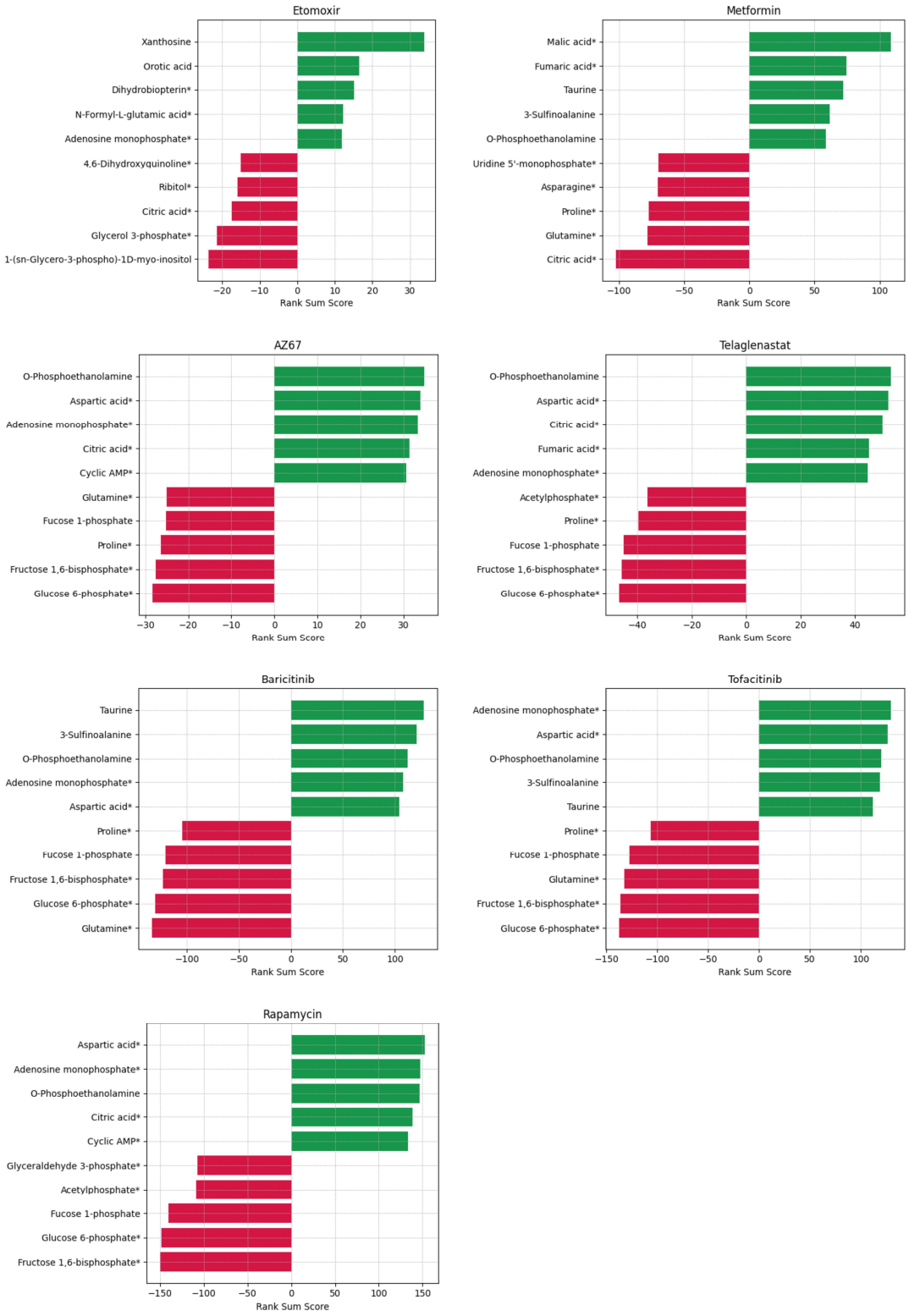

Figure 43- Differential expression analysis between the indicated conditions and activated cells. The top 5 up (green) and down-regulated (red) metabolites are shown. Differential analysis was performed using the non-parametric test Wilcoxon rank-sum.

4.5.3. Modulating CD4$^+$ T cells with compounds used for treating different diseases

The positive results observed with the modulators (e.g., 2-DG, BPTES, oligomycin A) that efficiently targeted metabolic pathways allowed me to start envisioning the idea of building a single-cell atlas. This atlas would be a collection of different metabolic states induced by the known modulators. Then, CD4$^+$ T cells would be modulated with several compounds with unknown metabolic effects and run through the HT-SpaceM pipeline I optimized. Finally, mapping the cells modulated with these compounds into the single-cell atlas of metabolic states would reveal those compounds' likely mode of action. Thus, this experiment aimed to select compounds with known metabolic effects that could be used to expand the single-cell atlas and compounds with unknown effects that would be mapped.

The previous attempts to inhibit glycolysis at a step different from 2-DG did not work. However, targeting this pathway with multiple modulators seemed essential, mainly because OXPHOS was covered with various compounds (oligomycin A, RotAA, metformin). Thus, WZB-117, a GLUT1 inhibitor, was chosen to target glycolysis since it has been reported to block proliferation in CD8$^+$ T cells [175]. The amino acid serine has been reported to be essential for the proper proliferation of T cells [176]. Thus, the second chosen compound, CBR-5884, targeted the *de novo* serine biosynthesis. In this 3-step pathway, where the first one is inhibited by CBR-5884, the glycolytic intermediate, 3-phosphoglycerate, is converted into serine [177]. Mycophenolic acid, which inhibits inosine monophosphate dehydrogenase, was the last metabolic modulator selected [178]. This enzyme participates in the *de novo* purine synthesis, and the modulation of T cells with this compound resulted in impaired proliferation. Mycophenolic acid is classified as an immunosuppressant currently used to prevent organ rejection following a transplant [179].

The non-metabolic modulators were a mix of compounds with distinct functions and applications. The first selected was Torin 1, a synthetic inhibitor of mTOR, which has been reported to be more efficient in inhibiting cell growth and proliferation than rapamycin. Thus, besides unraveling this compound's metabolic mode of action, I also aimed to compare it with rapamycin. Cyclosporine was the second compound selected due to its potent inhibition of T-cell activation. Similarly to rapamycin, this compound is also used to prevent organ rejection following a transplant [180]. The final list of non-metabolic was concluded by selecting one potential anti-cancer compound and one anti-psychotic

compound [181], [182]. The first was named gossypol and has been shown to inhibit the activation of T cells [183]. The second was PF-02545920, which had never been tested in $CD4^+$ T cells.

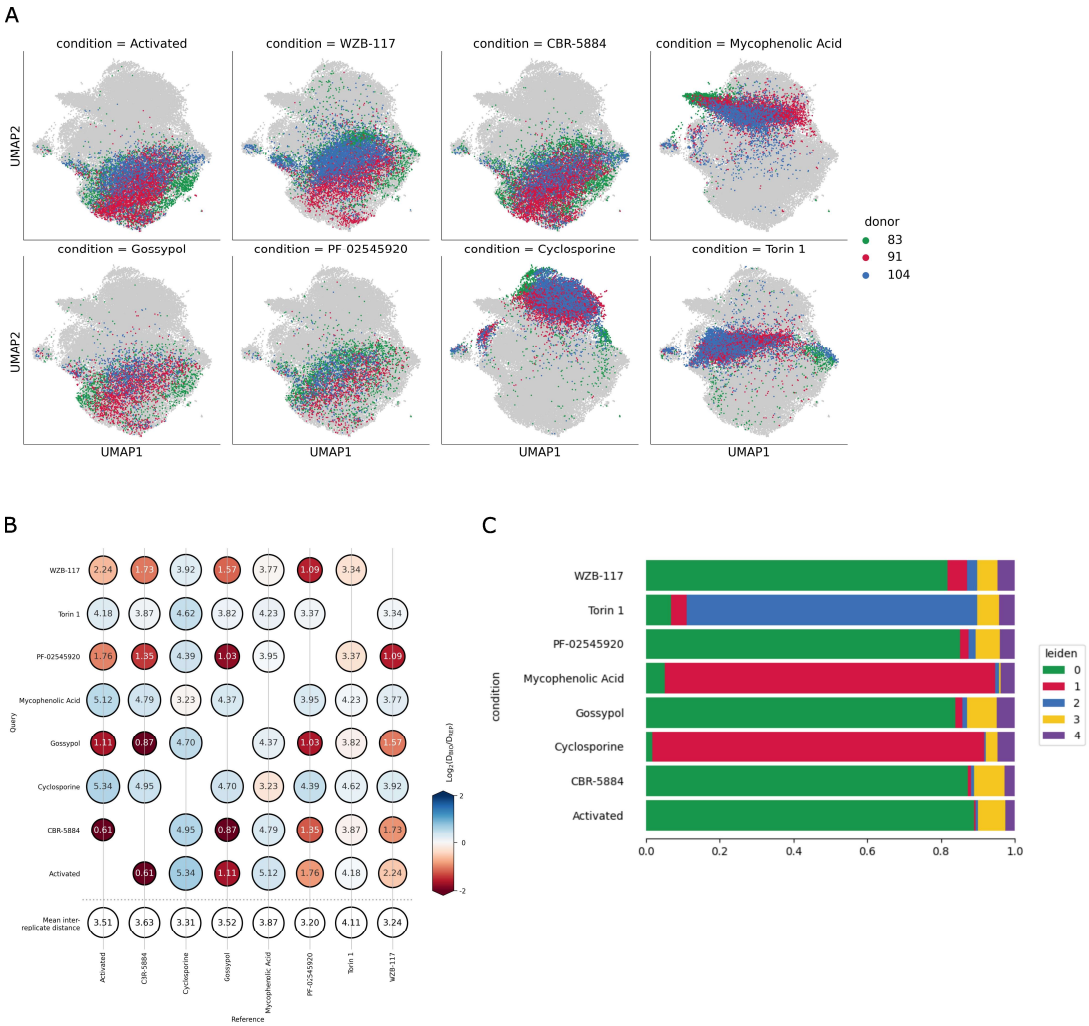

Figure 44 - Treating activated CD4+ T cells with a mixed group of modulators. **(A)** UMAP visualization of 68,249 cells and 103 metabolites. **(B)** Intra-label vs. inter-label distance plot. The intra-condition distances are represented in the bottom row. The inter-condition distance is represented in the colored circle. A red circle indicates that the intra-condition distance is lower than the inter-condition distance. **(C)** Visualization of the distribution of conditions within the identified Leiden clusters (resolution=0.3).

Regrettably, the quality of the data acquired in this batch was inferior to the previous ones. A lower number of metabolites was detected per cell, with most cells not having more than 20. The total number of metabolites detected in at least 1% of all cells was also lower than in the previous batches. Thus, the threshold had to be lowered so that most cells would not be filtered out. The quality filtering was set to select cells that contained at least 20 metabolites. The UMAP visualization revealed one main population with only three conditions clustering apart (**Figure 44A**). The relatively low intra-condition distance observed for every condition suggested that this was not a reproducibility issue (**Figure 44B**). The lower inter-condition distance observed for every condition except Cyclosporine, Torin 1, and Mycophenolic Acid indicated this was a biological effect. Unsupervised Leiden clustering only identified three main clusters, with most conditions sharing their cluster with activated cells (**Figure 44C**). The only conditions assigned to clusters that differed from those of activated cells were Cyclosporine, Torin 1, and Mycophenolic acid. This further indicated that most of the compounds did not affect the metabolism of $CD4^+$ T cells.

Differential expression analysis was run as described before using the activated cells as the reference. The results reinforced what was observed in the UMAP visualization and Leiden clustering. The effect of three of the compounds (CBR-5884, gossypol, and PF-02545920) was very dim, as indicated by the low absolute scores of the top and downregulated metabolites. The GLUT1 inhibitor, WZB-117, only exhibited three metabolites with an absolute score above 50: two downregulated and one upregulated. The downregulated metabolites were the glycolysis intermediates FBP* and G6P*. This suggested glycolysis was downregulated in this condition as expected since glucose uptake was inhibited. However, the low scores indicated a weak effect of this compound and explained the poor separation of these cells from the Activated condition when clustering. The other known metabolic modulator, mycophenolic acid, also exhibited downregulated expression of FBP* and G6P*, while citric acid* expression was upregulated. This indicated glycolysis was downregulated in this condition and an upregulation of oxidation through the TCA cycle. Contrary to the WZB-117, the high absolute score of the down and upregulated metabolites suggested a significant effect of this compound. Treating the cells with the mTOR inhibitor Torin 1 also resulted in the downregulation of FBP* and G6P*. Meanwhile, it also resulted in the accumulation of AMP*, IMP, aspartic acid*, and glutamic acid*. Some of these up and downregulated markers overlapped with the ones

found for Rapamycin condition, the other mTOR inhibitor. This will be discussed in more detail in the discussion chapter. Similarly to all the other conditions, the Cyclosporine condition exhibited downregulation of the glycolysis intermediates, FBP* and G6P*. Interestingly, it also shared some upregulated metabolites with the Torin 1 condition, which suggested that these two compounds had a similar effect.

In summary, in this experiment, I aimed to search for modulators that could be used to expand the envisioned single-cell atlas of metabolic states. I have also searched for compounds that could be used as test cases of this atlas. The data from this batch had lower quality which affected the number of ions detected per cell. Nevertheless, it was still possible to observe significant effect of some compounds. The two immunosuppressants, mycophenolic acid and cyclosporine, and the mTOR inhibitor, Torin 1, significantly changed the metabolism of $CD4^+$ T cells.

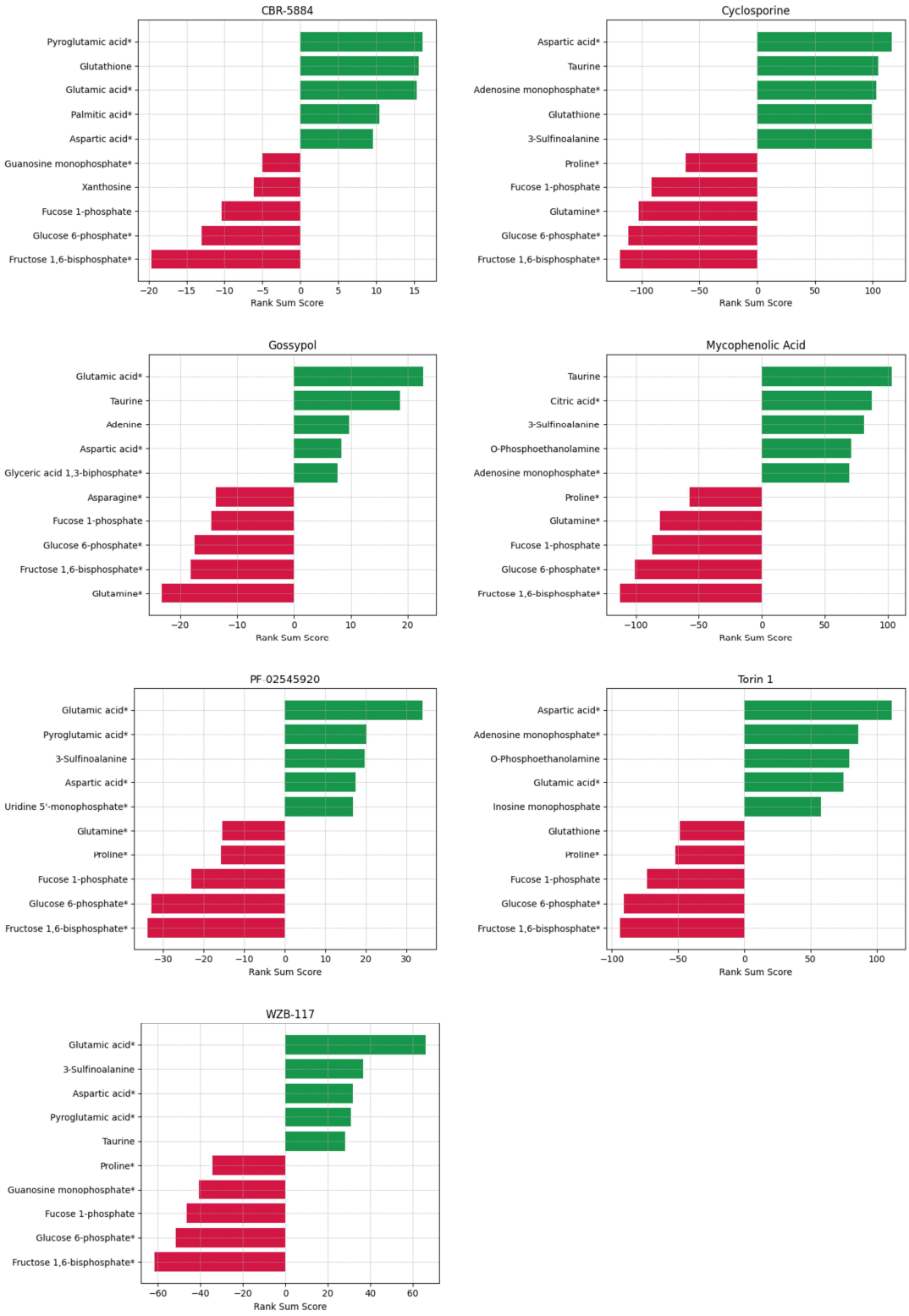

Figure 45 - Differential expression analysis between the indicated conditions and activated cells. The top 5 up (green) and down-regulated (red) metabolites are shown. Differential analysis was performed using the non-parametric test Wilcoxon rank-sum.

4.5.4. Unraveling the metabolic outcome of the polyvalent Methotrexate

Ideally, the single-cell atlas would have as many metabolic states as possible, covering multiple pathways. Due to time restraints, this was not possible, and thus, the last experiment focused on finishing details for the atlas and running one last metabolic modulator. The proof-of-concept experiment was designed based on the modulators used in the Seahorse assay. Because of this, the compounds rotenone and antimycin A were combined in one treatment (RotAA) to mimic the assay. This combination is essential in the Seahorse assay to understand the percentage of oxygen consumed by other cellular enzymes. Thus, this combination is applied after treating the cells with oligomycin A to completely inhibit any remaining flux through the ETC [35]. However, this combination did not fit the purpose of a single-cell atlas of metabolic responses. Because combining the two compounds would hide the individual effects and make it impossible to differentiate them. Thus, one of the main goals of this last experiment was to test rotenone and antimycin A individually. The other chosen modulator was methotrexate (MTX), a compound commonly used to treat cancer and autoimmune diseases. MTX interferes with multiple cell-signaling pathways through different targets. One of those targets is dihydrofolate reductase, an enzyme that participates in folate metabolism, which can lead to reduced nucleotide synthesis. In T cells, MTX inhibits another reaction catalyzed by dihydrofolate reductase, which converts dihydrobiopterin to tetrahydrobiopterin. This results in the accumulation of reactive oxygen species and increased sensitivity to apoptosis [184]. However, MTX has also been shown to inhibit proliferation in T cells and deplete the levels of purines and pyrimidines [185].

The $CD4^+$ T cells were isolated and cultured with the three distinct modulators, and the data was analyzed as previously described. The UMAP visualization revealed three main populations, two individually driven by antimycin A and MTX (**Figure 46A**). Only the Rotenone condition was not clustering separately from the activated cells. This was also reflected in the inter-condition distance between these conditions, which was lower than the intra-condition distance (**Figure 46B**). Nevertheless, the intra-condition distance for all the conditions was relatively low, revealing high reproducibility. The Leiden clustering results also reinforced a potential weak effect of rotenone since it shared a cluster with the activated cells (**Figure 46C**). On the other hand, both Antimycin A and Methotrexate conditions formed their clusters, suggesting stronger effects from these treatments.

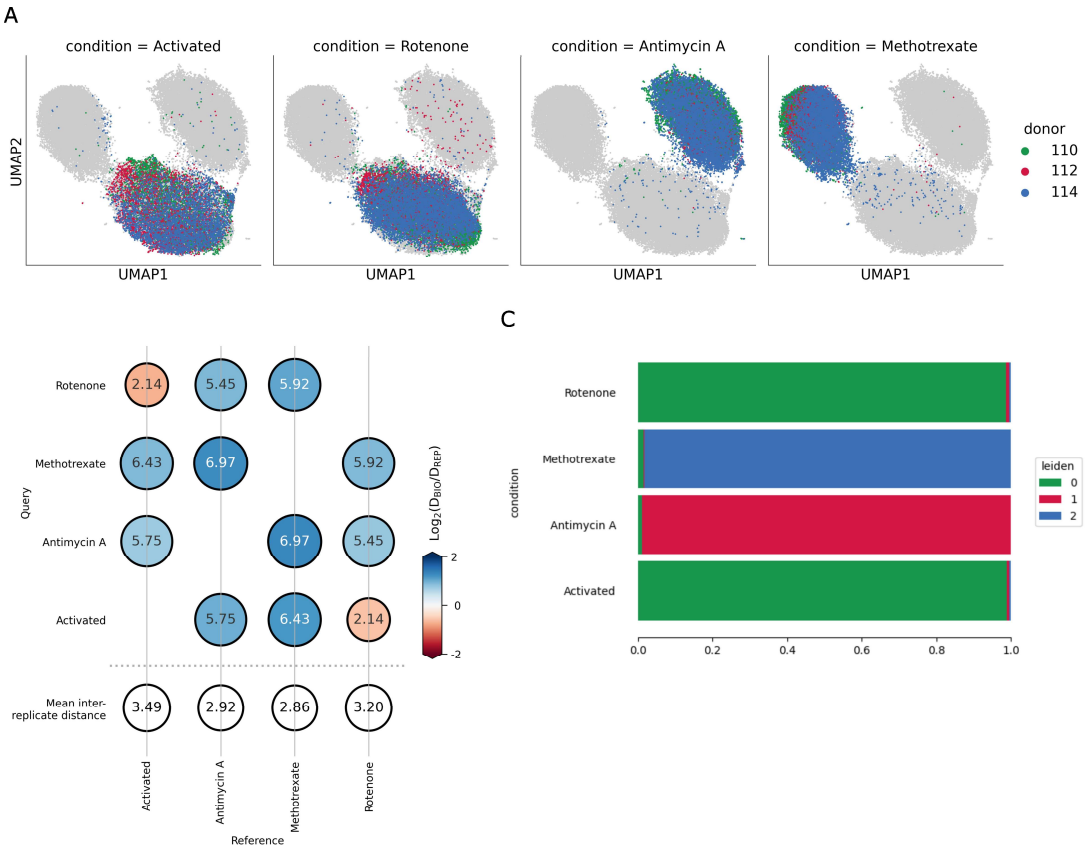

Figure 46 - Treating activated CD4+ T cells with a mixed group of modulators. **(A)** UMAP visualization of 60,866 cells and 123 metabolites. **(B)** Intra-label vs. inter-label distance plot. The intra-condition distances are represented in the bottom row. The inter-condition distance is represented in the colored circle. A red circle indicates that the intra-condition distance is lower than the inter-condition distance. **(C)** Visualization of the distribution of conditions within the identified Leiden clusters (resolution=0.1).

The differential expression analysis results confirmed the weaker effect of rotenone, with the treatment only exhibiting four up and downregulated metabolites above the threshold of 50. On the other hand, $CD4^+$ T cells treated with antimycin A exhibited upregulation of three metabolites from the *de novo* pyrimidine biosynthesis pathway: orotic acid, L-dihydroorotic acid, and uracil*. Interestingly, these three metabolites were also upregulated in the cells treated with RotAA in the proof-of-concept experiment. This indicates that the compound treatment driving the effects of RotAA was actually antimycin A. The impact on the *de novo* pyrimidine synthesis was not expected as the primary known function of this compound is the inhibition of mitochondrial complex III. However, the

inhibition of the biosynthesis of pyrimidines has been observed before in cancer cell lines treated with antimycin A [186], [187]. On the other hand, the top downregulated metabolites were the glycolysis intermediates FBP* and G6P*. This was also observed in cells treated with MTX, along with the downregulation of glutamine*, suggesting that this compound impacts glycolysis and glutaminolysis. Among the downregulated metabolites was guanosine monophosphate*, the end product of the *de novo* purine biosynthesis. While the precursor of this pathway, phosphoribosyl pyrophosphate (PRPP), was the top upregulated metabolite. This suggested that purine synthesis was impaired in cells treated with MTX, as previously reported [185].

In summary, this experiment concludes the long series of testing known and unknown metabolic modulators in $CD4^+$ T cells. In here I showed that the effect observed in the proof-of-concept experiment for RotAA was driven by antimycin A and that rotenone has little effect on the metabolism $CD4^+$ T cells. Treating the cells with antimycin A revealed an unexpected target of this compound, while MTX impacted *de novo* purine biosynthesis. After this, I moved to select the compounds to generate the single-cell atlas of metabolic states of $CD4^+$ T cells.

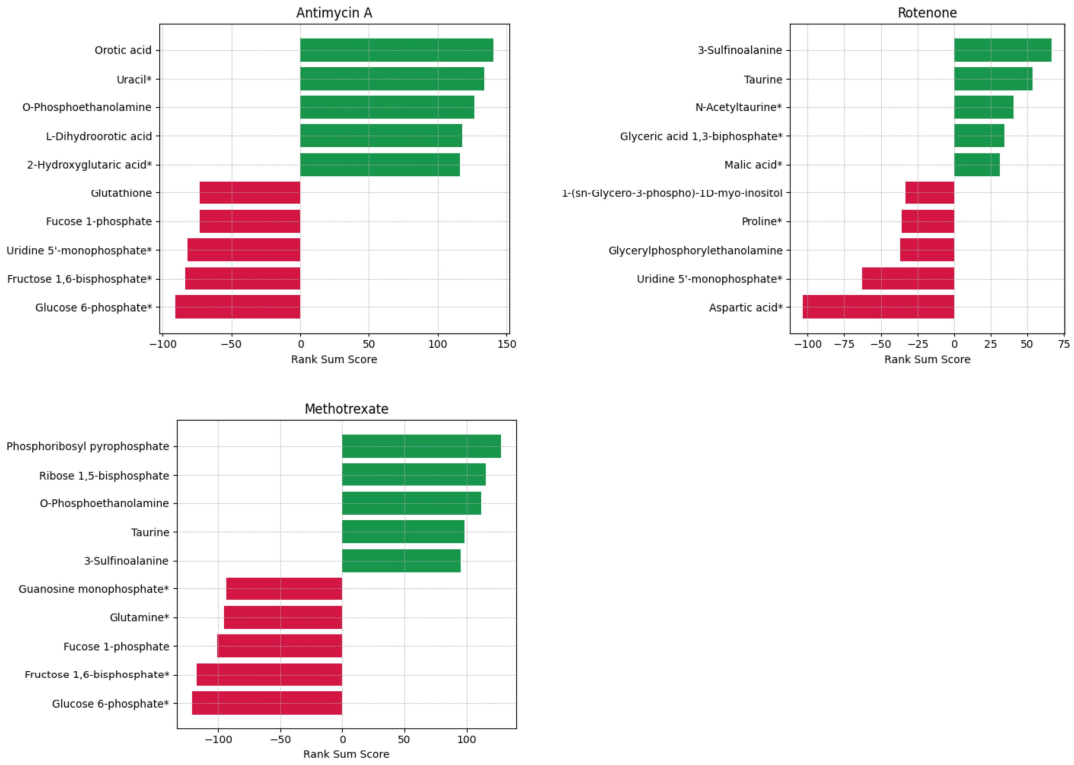

Figure 47 - Differential expression analysis between the indicated conditions and activated cells. The top 5 up (green) and down-regulated (red) metabolites are shown. Differential analysis was performed using the non-parametric test Wilcoxon rank-sum.

4.6. Building a single-cell atlas of CD4$^+$ T cells metabolic states

The initial objective of comparing the metabolic states of naïve and activated cells was pivoted to a more complex idea by adding the known metabolic modulators used in the proof-of-concept experiment. The positive results obtained in that experiment allowed me to keep testing other known modulators. The response of the CD4$^+$ T cells to these different modulators successfully captured by the single-cell method presented here was the foundation for the last objective: the generation of a single-cell atlas of metabolic responses in CD4$^+$ T cells. In total, 31 different states of CD4$^+$ T cells were measured: 21 with known metabolic modulators and 10 with unknown. However, as shown in the previous sections, not all the modulators with known metabolic effects significantly impacted the metabolism of CD4$^+$ T cells (e.g., STF-31 and rotenone). Thus, the choice of the modulators that were included in the atlas was made based on the differential analysis results. Only compounds with all up or downregulated metabolites with an absolute score above 50 were selected for the atlas, as shown in **Table 10**.

The remaining known metabolic modulators were used instead as the test case of the atlas before attempting to project the unknown ones. There were two exceptions to the threshold applied: RotAA and metformin. Both compounds had a score high enough to be included in the atlas but were kept out for different reasons. RotAA was a combination of two modulators (rotenone and antimycin A) and, because of that, was kept out. On the other hand, metformin was initially selected for the atlas. However, this compound had a weaker effect when compared to others (e.g., 2-DG, antimycin A). Because of that, it could not be properly separated from the Activated condition on the atlas. Thus, metformin had to be included in the test set instead. The projection set was then composed of modulators divided into two distinct categories. The first category included modulators with an unknown metabolic effect where the JAK inhibitors fit. The second category was composed of indirect metabolic regulators. This was the case of, for example, AZ67 or MK8722, which target enzymes that regulate specific metabolic pathways.

The compounds selected for the atlas resulted from different experiments run separately. The activated cells were used as the control for possible batch effects since this was the only condition present in all the different experiments. The proof-of-concept experiment demonstrated that donors were reproducible and clustered well together. Thus, observing donors clustering only within their batch and not with the rest would indicate a

batch effect. Inevitably, it was possible to observe batch effect when trying to integrate the conditions for the single-cell atlas, since the clustering of activated cells was not uniform (data not shown). If the observed variability had happened across slides of different donors within the same batch, it could be easily corrected with linear regression, as described before. However, this method was not efficient when integrating multiple batches. Thus, finding a suitable method to correct these batch effects while preserving the biological variability was necessary. Different integration methods commonly used in single-cell pipelines were tested, but only one successfully integrated the different batches without compromising the biological conditions: batch balanced k nearest neighbors (BBKNN) [58]. This method is faster and less resource-demanding than the other alternatives but equally efficient. BBKNN is also available in the Scanpy package, which made it convenient and easy to integrate into my single-cell analysis pipeline.

The BBKNN method corrected the batch effects observed and preserved the differences between conditions. The UMAP visualization of the single-cell atlas showed that some conditions had stronger effects than others (**Figure 48A**). This was already expected since the selected conditions had distinct differential analysis scores. The conditions with the lowest scores (BPTES and PF-05175157) formed a main population together with the activated cells, while the rest were clustering separately. The initial clustering with the Leiden algorithm did not capture individual clusters for BPTES and PF-05175157. These were assigned to a cluster with the activated cells, while the rest of the conditions clustered individually. Thus, increasing the resolution used to see individual clusters that aligned with both BPTES and PF-05175157 was necessary. The drawback of this approach was the overclustering observed with some conditions starting to split into two clusters with increased resolution. In such cases, the clusters assigned to the same condition were merged (**Figure 48B**).

Most clusters were composed of only one condition, except cluster 0, which consisted mainly of activated cells but was also assigned to some cells treated with BPTES and PF-05175157. Nevertheless, each cluster was renamed after the metabolic mode of action of the condition it overlapped with the most. The metabolic mode of action of each compound was determined based on the existing literature and on the results observed in this dissertation. Since most results presented here aligned with the existing literature, defining the metabolic mode of action was quite simple for most compounds. The only exception was antimycin A, whose main function is inhibiting complex III of the ETC. Instead, the

metabolic mode of action assigned to this condition was “Pyrimidine Biosynthesis Inhibition”. This decision was based on the accumulation of metabolites from this pathway and the growing evidence that it is indirectly inhibited by antimycin A [186], [187]. Most cells from each condition were assigned to only one cluster, and the only exceptions were BPTES and PF-05175157 (**Figure 48C**). In these conditions, a significant percentage of the cells was still assigned to the Activation cluster. However, this was not unexpected and reflected the results already observed in the differential analysis and the UMAP visualization. Thus, the single-cell atlas of metabolic states comprised nine different states that covered the metabolism and activation of $CD4^+$ T cells.

Table 10 – Distribution of conditions into their roles in the single-cell atlas generation.

Atlas	Test	Projection
Naïve, Activated, PF-05175157, BPTES, 2-DG, Oligomycin A, Antimycin A, Methotrexate, Mycophenolic Acid	H2O, DMSO, Glucose, STF-31, WZB-117, Metformin, RotAA, Rotenone, FCCP, Telaglenastat, CBR-5884, Etomoxir	TEPP-46, AZ67, Gossypol, PF-02545920, Cyclosporine, MK8722, Rapamycin, Torin 1, Tofacitinib, Baricitinib

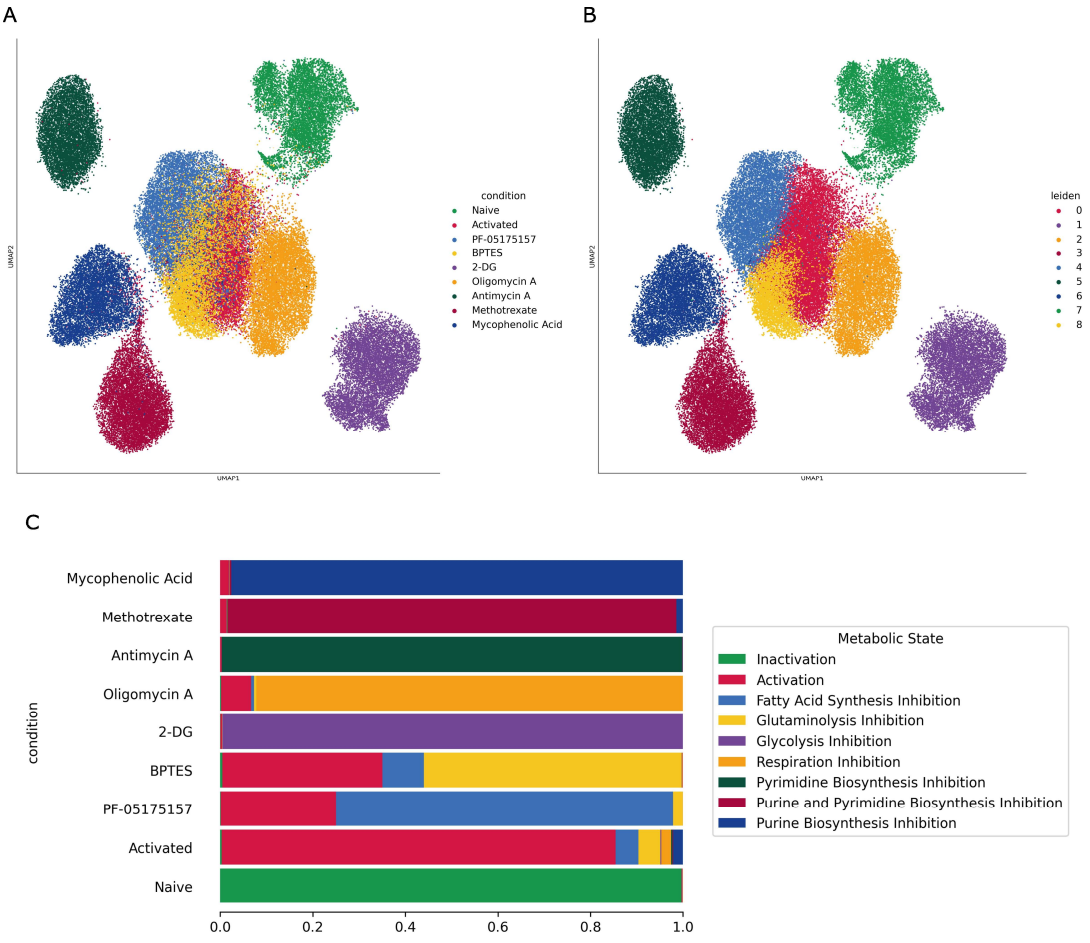

Figure 48 – Single-cell atlas of metabolic states of CD4^{+}T cells. The atlas comprised 9 metabolic states measured for 75,192 cells and 141 metabolites. **(A)** UMAP visualization colored by condition. **(B)** UMAP visualization colored by cluster (resolution=0.9). Each Leiden cluster was renamed to the metabolic mode of action of the condition it overlapped with the most. **(C)** Visualization of the distribution of conditions within the identified the metabolic states.

The generation of single-cell atlases is an emerging topic in the single-cell field. The available methods for integrating and mapping single-cell data onto atlases are not yet fully established. However, there are multiple options, and the proper suitable method is usually heavily dependent on the data characteristics [188]. Some of the most used methods (e.g., Scanorama or Combat) were tried in this project without success. The method that efficiently mapped the test data onto the single-cell atlas was a function in the Scanpy

package named “ingest” [57]. This Scanpy function projects single-cell data onto an existing reference dataset. This is achieved using a k-nearest neighbors algorithm (KNN) to find the closest cells in the reference data for each cell in the query data. The Scanpy “ingest” function also allows the transfer of annotations from the reference dataset to the query data, such as clustering labels.

The results of mapping the test data on the single-cell atlases are presented in **Figure 49**. Most conditions were assigned to the Activation cluster. This was expected, given that most of these conditions were clustering with activated cells and had low differential analysis scores in the original analysis. One of the exceptions was RotAA-treated cells, which were assigned to the “pyrimidine biosynthesis inhibition” cluster or the antimycin A cluster. STF-31 was another exception since it was assigned to the “inactivation” and the “glycolysis inhibition” clusters. This was not unexpected since, in the original analysis, this condition was clustering apart from the activated cells, and the only reason it was not included in the single-cell atlas was the low differential analysis scores. Since the primary function of STF-31 is to block glucose uptake, and the inhibition of glycolysis can impair the activation of T cells, the metabolic states assigned to this condition were aligned with the expected outcome [189]. The complex I inhibitor metformin and the FAO inhibitor etomoxir had about 30% of the cells assigned to the “respiration inhibition” metabolic state. This was consistent with a previous report of etomoxir inhibiting glutamine oxidation in activated $CD8^+$ T cells [190].

The cells from the Telaglenastat condition were mainly assigned to the “activation” metabolic state followed by the “purine biosynthesis inhibition” state. This was not expected since the main function of this compound is to block glutaminolysis. However, the impairment of purine biosynthesis has been suggested before in cancer lines treated with Telaglenastat [191]. The inability of the method to assign the telaglenastat-treated cells to the “glutaminolysis inhibition” state could be due to the weak definition of this cluster. As mentioned before, the cells driving this cluster (BPTES condition) overlapped with the activated condition in the UMAP visualization. And the assignment of this cluster could only be achieved with a higher resolution. Thus, the significant percentage of cells assigned to the “glutaminolysis inhibition” cluster should be interpreted cautiously. Mainly because this was just observed in three conditions from the same batch: FCCP, Glucose and H2O. Nevertheless, the run test of the single-cell atlas revealed that the method used for projection yielded accurate results for most conditions. While the assignment of some

metabolic states may be debatable, most cells for each condition were assigned to the expected clusters. Thus, the projection of the test data showcased the great accuracy of the method in predicting metabolic states.

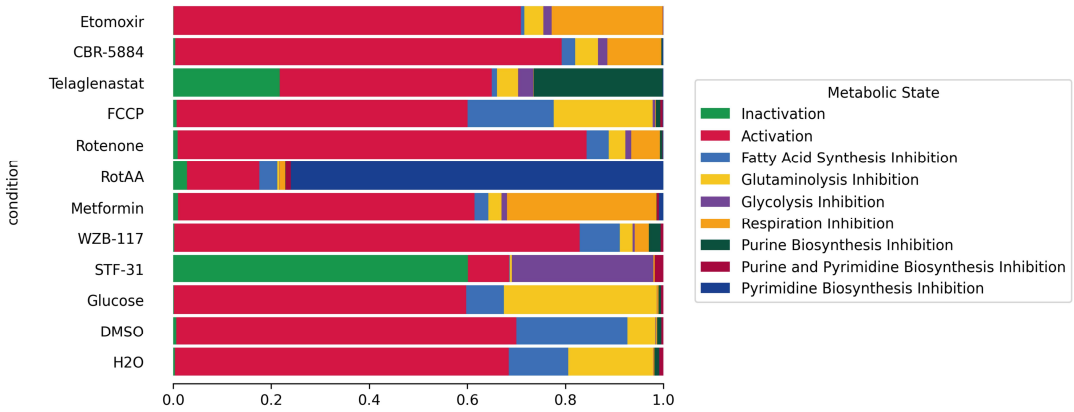

Figure 49 – Distribtuion of the test conditions within the metabolic states of the single cell-atlas.

The results of the projection of the modulators with unknown outcomes and the metabolic regulators onto the single-cell atlas are presented in **Figure 50A**. All the conditions were mainly assigned to the "activation" state. However, a small percentage of cells within some conditions were still assigned to other metabolic states. Cyclosporine was the only condition where most cells were not assigned to the "activation" metabolic state. Instead, they were assigned to "purine biosynthesis inhibition". Since the inhibition of this pathway results in impaired DNA synthesis and proliferation, this assignment could help explain the observed decreased proliferation of T cells treated with this cyclosporin [192], [193]. The JAK inhibitors, baricitinib and tofacitinib, exhibited similar distributions among the possible metabolic states. Although most cells were identified as in the "activation" state, a significant percentage of cells were assigned to the "purine biosynthesis inhibition" state. The effect of these two inhibitors on this pathway is still unknown. However, similar to cyclosporine, this could be linked to the inhibition of proliferation often observed in T

cells treated with these compounds [194]. Interestingly, the two mTOR inhibitors, rapamycin and Torin 1, did not exhibit similar metabolic states. While the cells of both conditions were mainly assigned to the "activation" state, a significant percentage of rapamycin-treated cells were assigned to the "purine biosynthesis inhibition" cluster. However, only a small percentage of cells from the Torin 1 condition were also assigned to this metabolic state. The treatment of cancer cells with rapamycin has been shown to impair the use of purine precursors in RNA and DNA synthesis [195]. This was strong evidence that the observed results were accurate, but why both inhibitors did not exhibit the same response was unclear.

Finally, a significant percentage of cells treated with MK8722, the AMPK activator, were assigned to the "FAS inhibition" and the "glutaminolysis inhibition" states. AMPK has been reported to upregulate glutaminolysis in natural killer cells due to their limited glycolytic capacity [196]. However, there is no information about the role of AMPK under normal conditions. This, however, reinforces that the assignment of cells into the "glutaminolysis inhibition" state should be taken carefully. On the other hand, AMPK is known to inhibit FAS, and treating cancer cell lines with MK8722 resulted in decreased expression levels of fatty acid synthase, which is essential for synthesizing long-chain fatty acids [197], [198]. Thus, the assignment of these cells to the "FAS inhibition" state was very likely accurate. Notably, no significant percentage of cells from any condition was assigned to the metabolic states driven by antimycin and MTX. The only exception was RotAA, which was composed of antimycin. This suggested that these two compounds had unique modes of action compared to the others. On the other hand, "purine biosynthesis inhibition" was assigned to multiple modulators of the projection data (e.g., baricitinib, cyclosporine, etc.). Contrary to what was observed with "glutaminolysis inhibition," this was unlikely a batch effect since these conditions all belonged to different batches. The results were presented in a bar plot for the easiest visualization and comprehension. However, it is also possible to visualize how the cells from each condition are distributed on the UMAP space of the atlas. The UMAP visualization of baricitinib and tofacitinib projection is presented in **Figure 50B**.

Overall, the projection method accurately assigned the different test conditions to the expected metabolic states of the single-cell atlas. However, the inclusion of less pronounced effects should be evaluated if a proper clustering separation cannot be achieved. The assignment of projected data to an erroneous cluster could compromise the

interpretation of the results. Integrating the projection data onto the single-cell atlas revealed the possible metabolic mechanism behind impaired proliferation upon treatment with some compounds. The single-cell atlas presented here demonstrates the capacity provided by single-cell metabolomics and, more precisely, the use of HT-SpaceM data in combining and advancing the growing fields of single-cell and immunometabolism. However, further improvement is required to achieve a practical single-cell atlas of metabolic states in $CD4^+$ T cells. This could consist of adding more metabolic modulators that cover other pathways, testing other integrating methods, or implementing a metric to evaluate the similarity of the projected cells with the assigned cluster. Finally, I demonstrated that SpaceM can be a valuable tool in single-cell omics fields, although some minor improvements and developments are still necessary.

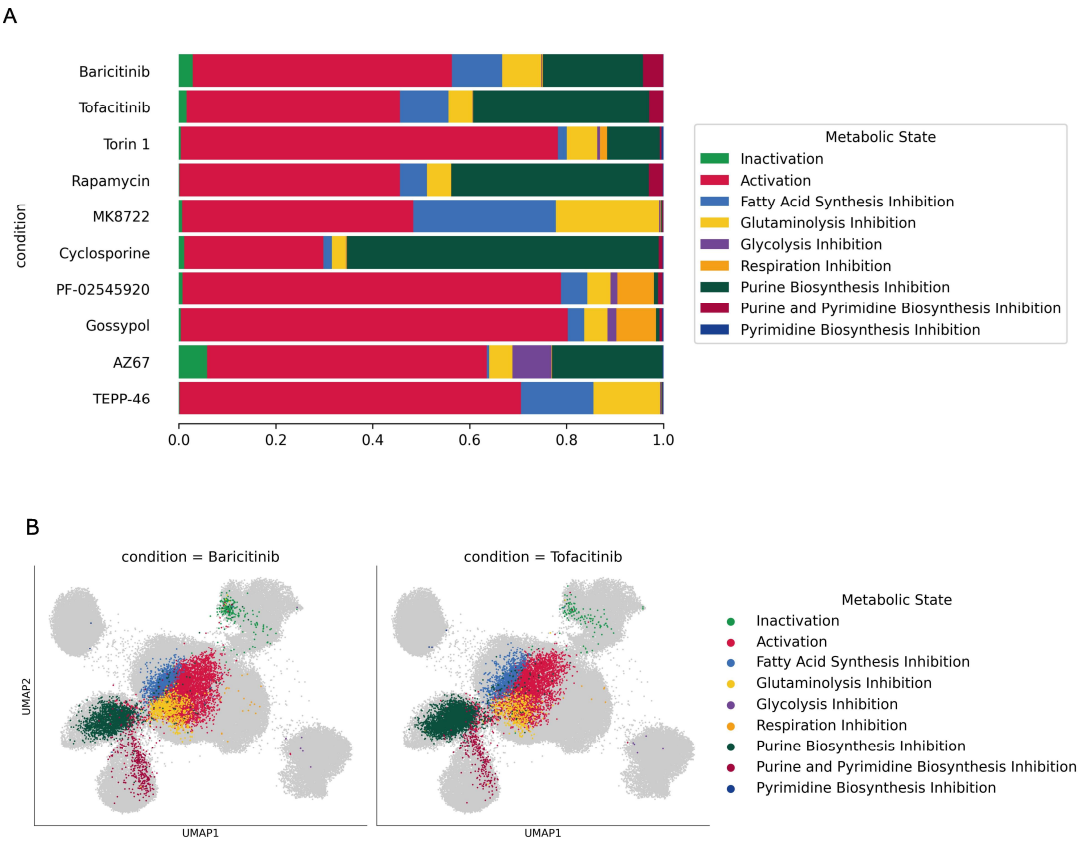

Figure 50 – Projection of the metabolic regulators and the modulators with unknown metabolic outcomes onto the single-cell atlas of metabolic states. **(A)** Distribtuion of the conditions within the metabolic states of the single cell-atlas. **(B)** UMAP visualization of the projection of Baritinib and Tofacitinb condtions onto the atlas.

4.7. Evaluating the effect of the modulators on the viability, proliferation, and activation capacity of $CD4^+$ T cells

The single-cell results were very informative about the impact of the different compounds on the metabolism of $CD4^+$ T cells. Some compounds like baricitinib, tofacitinib, and rapamycin significantly impacted the metabolism of $CD4^+$ T cells. However, the projection into the atlas of metabolic states revealed that most cells treated with these compounds had a metabolic profile similar to the activated cells. Thus, it was necessary to understand if these compounds were affecting other cellular processes like activation and proliferation. These would help interpret and potentially confirm the metabolomic results. The naïve $CD4^+$ T cells were stimulated, modulated, and cultured following the same experimental pipeline used for HT-SpaceM (**Figure 23, Table 9**), with a minor modification where cells were stained with CTV after isolation. After culturing for 72 hours, the $CD4^+$ T cells were stained with CD3, CD4, activation markers (CD25, CD69), and a viability dye (Live/Dead Near-IR). The expression of these markers was assessed using a flow cytometer, and the gating strategy was the same, as shown in **Figure 3**. The SSC and FSC separated the lymphocytes from the debris and clumps. Then, the live cell population was determined by gating on the cells that had low expression of the viability dye. The positive expression of CD3 and CD4 allowed the selection of live $CD4^+$ T cells. The activation state of the cells was determined according to the expression of CD69 and CD25, as described in section 4.2 and **Figure 4**. There were four activation states defined: Inactivation ($CD69^-CD25^-$), Early Activation ($CD69^+CD25^-$), Peak Activation ($CD69^+CD25^+$), and Late Activation ($CD69^-CD25^+$). Finally, the proliferation was determined using the number of CTV peaks, as shown in **Figure 4**. The undivided CTV peak (the most intense peak) was classified as non-proliferation. In contrast, the remaining peaks were classified as proliferation.

After 72 hours of culturing, the viability in most conditions was superior to 80% (**Figure 51**). The only exceptions were DMSO, AZ67, and STF-31. The low viability caused by DMSO was unexpected since this compound had not affected the metabolism of $CD4^+$ T cells in the HT-SpaceM experiment neither did it have fewer cells compared to the other conditions. On the other hand, the low viability of AZ67 and STF-31-treated cells explained the low number of cells observed for these conditions in the single-cell data.

Donor 122 also exhibited very low viability for some conditions (e.g., RotAA, Antimycin A). However, it was not clear if this was biological or technical variability.

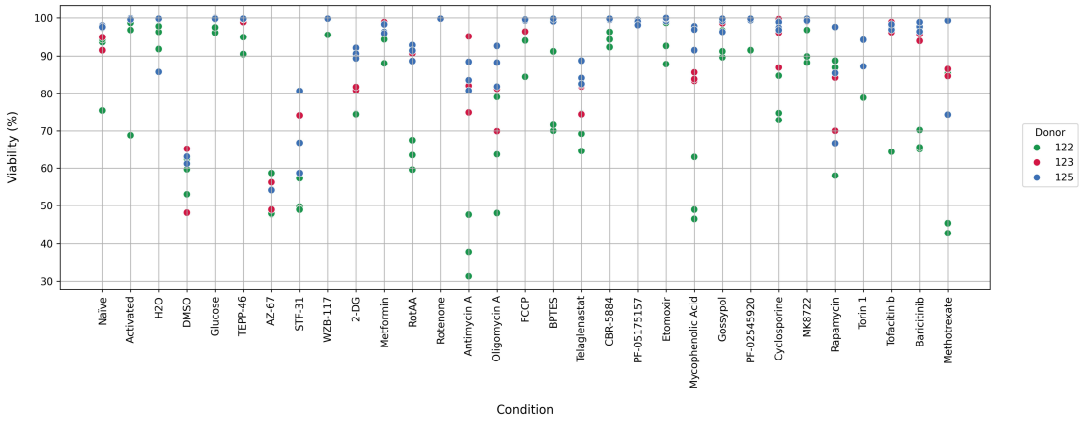

Figure 51 – Viability of activated and modulated CD4$^+$ T cells from three donors. The CD4$^+$ T cells were modulated with 25 different compounds. Percentage of cells that did not express the viability dye Live/Dead Near IR.

On the other hand, the detection of CD69 and CD25 revealed that the compounds had distinct effects on activation (**Figure 52**). Similarly to the viability results, DMSO and AZ67 significantly affected the activation state. Telaglenastat, the glutaminolysis inhibitor, affected activation but did not inhibit it completely, like DMSO and AZ67. Instead, this compound caused a delay in the activation since most cells were still in the Inactivation (~40%) and Early Activation (~30%) stages. This delay in activation was also observed for 2-DG and mycophenolic acid-treated cells. The cells from these two conditions were mostly in the Early and Peak Activation stages. In contrast, the cells from the Activated condition were mainly in the Peak (55%) and Late Activation (40%) stages. The immunosuppressant, cyclosporine, and the JAK inhibitors, tofacitinib and baricitinib, did not impact activation. However, there was also some variability between the technical replicates in these conditions, so the results should be carefully interpreted. The rest of the conditions had most cells in the Peak Activation stage. The only exceptions were H2O, Glucose, TEPP-46, FCCP, and CBR-5884 conditions, where activation was not changed compared to the Activated condition. Interestingly, etomoxir and gossypol affected the

activation of $CD4^+$ T cells, with most treated cells only reaching the Peak Activation stage. However, no significant effect was observed on the single-cell metabolomics data for these two conditions. Thus, these two compounds might affect the activation of the cells, but not the metabolic sates. The results indicated a possible separation between function and metabolism. However, it is also possible that these compounds had indeed a metabolic effect that could not be captured by the method. This is possible if these compounds affect metabolites not detected with HT-SpaceM.

The proliferation results showed that several compounds impacted the capacity of $CD4^+$ T cells to divide upon activation (**Figure 53**). Similarly to what was observed in the viability and activation results, the proliferation was inhibited in DMSO and AZ67 conditions. Interestingly, the proliferation of Methotrexate, Mycophenolic Acid, and Antimycin A conditions was below 20%. The same conditions are included in the single-cell atlas for inhibiting purine and/or pyrimidine biosynthesis. Thus, the proliferation results confirm the mode of action hypothesized for these compounds in $CD4^+$ T cells. The immunosuppressant and mTOR inhibitor, rapamycin, inhibited proliferation greatly, with less than 30% of cells dividing. While the other immunosuppressant, cyclosporine, was less efficient and inhibited proliferation in ~40% of the cells. The JAK inhibitors, baricitinib and tofacitinib, also had a reduced effect on the proliferation. Besides affecting activation, the glycolysis inhibitors, STF-31 and 2-DG, prevented the proliferation of ~80% of the cells. This further reinforced the key role of glycolysis in $CD4^+$ T cell activation and proliferation.

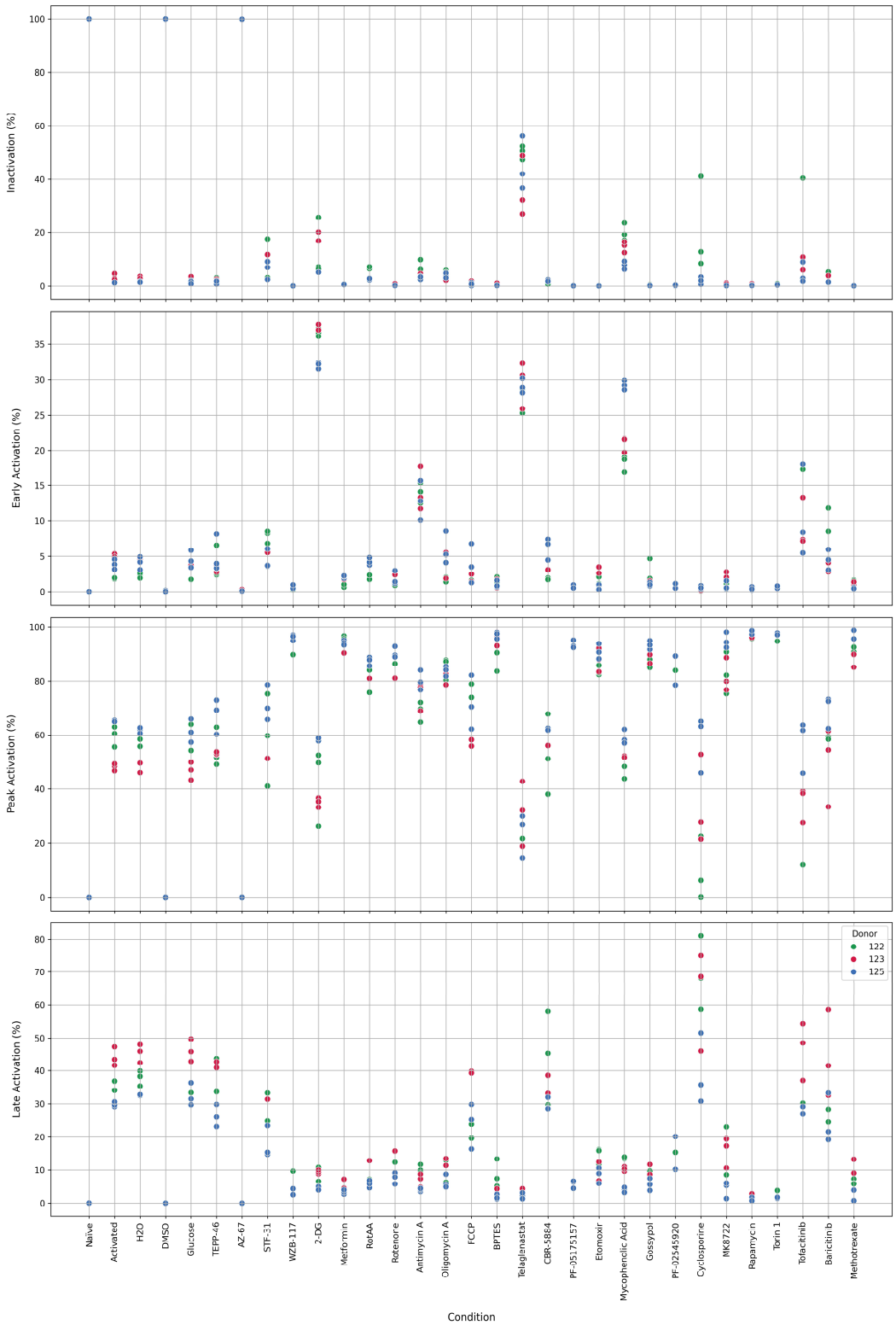

Figure 52 - Activation stages of activated and modulated CD4$^+$ T cells from three donors. The CD4$^+$ T cells were modulated with 25 different compounds. Percentage of total live CD3$^+$CD4$^+$ T cells at each activation stage. The activation stages were determined based on the expression of CD69 and CD25: Inactivation (CD25$^-$ D69$^-$), Early Activation (CD25$^-$D69$^+$), Peak Activation (CD25$^+$D69$^+$), Late Activation (CD25$^+$D69$^-$).

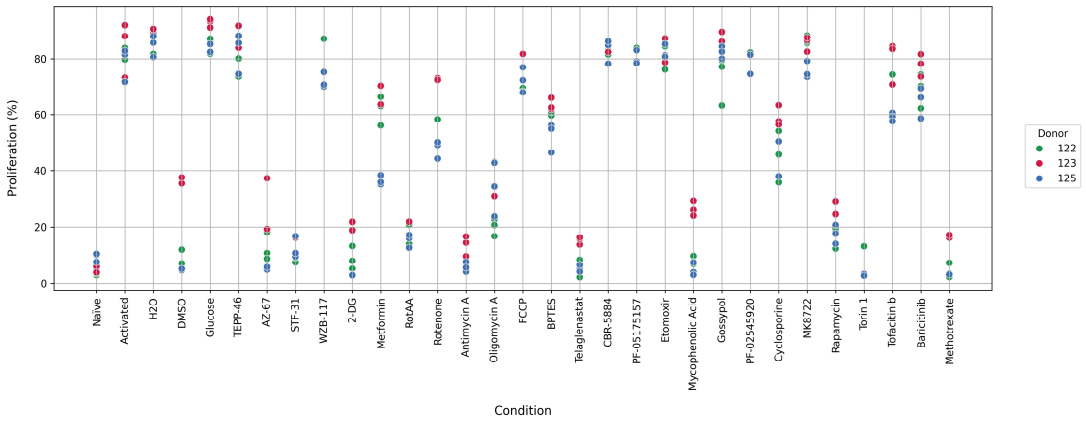

Figure 53 - Proliferation of activated and modulated $CD4^+$ T cells from three donors. The $CD4^+$ T cells were modulated with 25 different compounds. Percentage of total live $CD3^+CD4^+$ T cells that have proliferated. The proliferation was determined based on the number and intensity of CTV peaks: Non-Proliferation (first and most intense peak), Proliferation (remaining peaks). The results exhibited here reflect the percentage of cells in the "Proliferation "stage.

The viability, activation, and proliferation results mostly confirmed the results observed in the single-cell data, with some exceptions. The negative effect of DMSO on viability, activation, and proliferation was one of those examples. This result was unexpected since the single-cell metabolomics results showed that DMSO had no significant impact on the metabolome of the cells. DMSO was included because it is the solvent for most compounds tested. Because the test and stock concentrations varied across compounds, the volume of compound added to each well also differed between conditions. In other words, the amount of DMSO added to each condition varied greatly based on the stock and final concentration of the compounds. Thus, the volume used in the DMSO condition matched the highest volume used among the other conditions. In this experiment, AZ67 was the condition where the highest volume of the compound was added due to the final and stock concentrations. For example, the final volume of AZ67 added to one well was 100 times higher than the volume of rotenone added. Thus, the volume of DMSO was 100 times higher in the AZ67 than in some other wells. Or in other experiments, such as the proof-of-concept experiment where the volume of DMSO was ~75 times lower than in this experiment. The final concentration of DMSO used in these experiments per well was 5% *v/v*. Concentrations of 1% and 2% *v/v* of DMSO were enough to inhibit the proliferation of lymphocytes after 5

days of activation [199]. Thus, this indicated that the observed flow cytometry data for DMSO results cannot be compared with the single-cell results because different concentrations were used in both experiments. This also raises the question of the impact of DMSO on metabolism when used in higher concentrations than in the proof-of-concept experiment. DMSO affected the viability, activation, and proliferation similarly to AZ67. Thus, it is unclear if the results observed for AZ67 are solely caused by this compound or by some synergistic effect with DMSO. This should also be investigated in other conditions where the final concentration of DMSO was at least 1% v/v (i.e. Baricitinib, Tofacitinib, Rapamycin, Torin 1, Cyclosporine, Telaglenastat, Metformin, WZB-117). Thus, different concentrations of DMSO should be tested in both flow cytometry and single-cell metabolomics assays to understand the maximal concentration that can be used before seeing side effects. Finally, the flow cytometry results showed that the functional state was likely correlated with metabolism. More specifically, most conditions where significant metabolic changes were observed also exhibited impaired activation and/or proliferation.

5 DISCUSSION

This project can be split into two main components: method development and biological applications. Since the technical part was extensively dissected in the Results chapter, this discussion will focus on interpreting the biological results. The naïve $CD4^+$ T cells used in this project were subjected to 30 different modulations. To simplify the discussion while still passing a meaningful message, I will only focus on the modulations that significantly impacted the metabolic state of the cells. Thus, this discussion will interpret the metabolic (up and downregulated markers) and functional state (i.e., activation and proliferation) markers. Contrary to the functional state, interpreting the marker metabolites is not straightforward, especially when the metabolic mode of action is unknown. Multiple factors can influence the accumulation of a metabolite, and because of that, the expression level cannot be directly correlated to pathway activity. Indeed, having a highly expressed metabolite from a given pathway could be related to increased activity. However, it could also be caused by a blockage downstream, resulting in pathway arrest and accumulation of that metabolite. Then, some metabolites like leucine and arginine have regulatory roles in cell signaling pathways [200], making interpreting the metabolic outcome challenging.

5.1. Mode of action of metabolic modulators

The current model in the immunometabolism field states that naïve T cells are metabolically quiescent, and upon activation, there is a burst of energy and biomass generation. The published papers on bulk metabolomics in $CD4^+$ T cells also reported that 24 hours of activation is enough to increase the concentration of over 80 metabolites, with this difference augmenting after 72 hours [201], [202]. This extensive list includes the 5 metabolites differentially detected with that HT-SpaceM in $CD4^+$ T cells after activation. These were glutamine*, asparagine*, glutathione, glutamic acid*, and proline*. Upon activation, T cells have been shown to augment glutamine uptake quickly to fuel glutaminolysis. Since the cells are highly engaged in aerobic glycolysis and do not fuel the TCA cycle with carbon units, glutaminolysis is the alternative strategy to keep the cycle going. This happens through converting glutamine into glutamate and subsequently to alpha-ketoglutarate, one of the TCA cycle's intermediates [201], [203]. Activated $CD8^+$ T cells used glutamine as an additional source of asparagine [204]. It is still unclear if this

also happens in $CD4^+$ T cells, but it has been shown that asparagine is essential for proper proliferation and differentiation in these cells [205]. The roles of proline and glutathione are less characterized, but it has been reported that the first is a downstream product of asparagine metabolism in T cells, while the latter is important for reducing oxidative stress [79], [206]. Thus, the data presented in this dissertation reinforces the relevance of glutamine and asparagine metabolism in activated $CD4^+$T cells.

Conversely, the upregulated detection of fructose 1,6-biphosphate* and citric acid* in naïve cells contradicts the previous studies where the intensity of these metabolites was decreased [202]. Fructose 1,6-biphosphate has been proposed to enhance glycolysis while inhibiting OXPHOS in activated T cells [207]. Naïve $CD4^+$ T cells have been shown to accumulate untranslated mRNAs encoding for glycolysis, FAS, and *de novo* purine synthesis enzymes. This strategy is thought to promote the readiness of naïve T cells, allowing them to quickly synthesize these enzymes and consequently engage in metabolic remodeling upon activation. Naïve T cells also exhibited high expression of hexokinase and phosphofructokinase. The latter is one of the key regulators of glycolysis and catalyzes the conversion of fructose 6-phosphate into fructose 1,6-biphosphate [202]. Interestingly, high citrate concentrations inhibit phosphofructokinase and enhance gluconeogenesis [208]. The results might indicate that, similarly to what is observed on the gene expression and enzyme levels, naïve T cells might accumulate fructose 1,6-biphosphate* to rapidly promote glycolysis after activation. The use of glycolysis by naive cells could be prevented by the high levels of citric acid* observed. However, this is just a hypothesis that should be further tested. Taurine and 3-sulfinoalanine (also known as cysteine sulfinic acid), two metabolites involved in taurine synthesis, were also among the naïve cell markers. Taurine maintains homeostasis by protecting against distinct cellular processes like apoptosis or oxidative stress [209]. Thus, the increased detection of taurine and its precursor could be necessary to promote long-term survival while naïve cells wait for activation. The supplementation of taurine to $CD8^+$ T cells simultaneously with activation reduced apoptosis [210]. However, the effect of this metabolite in $CD4^+$ T cells is still unknown and needs to be explored. Thus, accumulating these metabolites could be crucial to protect cells from apoptosis or oxidative stress after activation. The hypothesis that naïve T cells store metabolites to prepare for activation should be further investigated.

The treatment of naïve $CD4^+$ T cells with 2-DG upon activation did not impact the viability of the cells, but it seriously impaired proliferation. On the other hand, activation

was not fully inhibited, with most cells being in the Early and Peak Activation Stages. This delay in the activation has been observed before in human $CD4^+$ T cells also treated with 2-DG [139]. The proliferation of 2-DG-treated cells has also been reported to be delayed compared to activated $CD4^+$ T cells, which I have not observed in this data [139], [211]. There could be two reasons for the observed differences. The first is that the proliferation in these studies was assessed after 96 hours of activation and treatment, while in this project, it was earlier at 72 hours. The second relates to the concentration of 2-DG used in these studies, which was 1.5 to 5 times lower than in this project. Thus, the total inhibition of proliferation observed in this data was likely caused by using a higher concentration of 2-DG. There is no available comprehensive metabolomics study in $CD4^+$ T cells treated with 2-DG that could be used as a reference here. However, there is a study where a human endometrial cancer cell line was treated with 2-DG, where there was a good overlap of the metabolites detected in my project. In that study, it was reported that the intensity of glucose 6-phosphate and erythrose 4-phosphate increased upon treatment with 2-DG [212]. The latter is an intermediate of the non-oxidative branch of PPP and is also one of the upregulated markers that I have identified for this condition [213]. The other 3 accumulated metabolites in 2-DG treated cells were glucose*, G6P*, and 2-DG6P*, the products of the two first steps of glycolysis, which suggested that the pathway was successfully inhibited. Glycolysis and PPP share several intermediates (e.g., glucose 6-phosphate) and can interchangeably fuel one another, which is essential to adapt to metabolic challenges. The blockage in glycolysis caused by 2-DG and the accumulation of G6P* could result in the diversion of this metabolite into PPP, leading to the accumulation of its intermediate, erythrose-4-phosphate. Thus, $CD4^+$ T cells might use PPP as an alternative pathway when glycolysis is inhibited. The 2-DG treated cells shared all the downregulated metabolites with the naïve cells, except for serine. This suggested that these metabolites could have a key role in cellular processes impaired in both naive and 2-DG conditions. The two options were either activation or proliferation. The first was only delayed in 2-DG cells, but proliferation was impaired in both conditions. One of the metabolites in question was glutamine*, which has been shown to be essential for $CD4^+$T cell proliferation but not activation [214]. Arginine* is another downregulated metabolite, and it has been reported to be necessary for the proliferation of $CD4^+$ T cells, as mentioned before [205]. Since the other two metabolites, glutamic acid* and proline*, are downstream products of glutamine* and asparagine*, their downregulation is likely impairing proliferation too. The study mentioned above also observed that treatment of a human cancer cell line with 2-DG

decreased serine levels [212]. Serine has been reported to be essential for the proliferation of $CD4^+$ T cells by supporting *de novo* purine biosynthesis [176]. Thus, the downregulation of serine observed in 2-DG treated cells might also impair proliferation. However, it remains to be elucidated how the glycolysis blockage is connected to the proliferation and downregulation of these metabolites.

The first inhibitor of the ETC that had a significant impact on the metabolism of activated $CD4^+$ T cells was antimycin A. This compound inhibits the complex III of the ETC, but unexpectedly, most of the top-upregulated metabolites were intermediates of the *de novo* pyrimidine biosynthesis pathway. Two of these metabolites were orotic acid and L-dihydroorotic acid, the product and substrate of dihydroorotate dehydrogenase, respectively. This enzyme relies on ubiquinone as the electron acceptor of this oxidative reaction. The reduced ubiquinone will transfer the received electrons from dihydroorotate dehydrogenase to complex III, a reaction that antimycin A inhibits [215]. Thus, dihydroorotate dehydrogenase links mitochondrial respiration to the *de novo* pyrimidine biosynthesis pathway. In addition, uridine 5'-monophosphate*, the end product of the *de novo* pyrimidine biosynthesis pathway, was downregulated. The antimycin A-treated cells also exhibited upregulation of uracil*, a precursor of uridine 5'-monophosphate via the pyrimidine salvage pathway. Thus, this suggested that the *de novo* pyrimidine biosynthesis pathway was indeed blocked due to the complex III inhibition by antimycin A, which caused the accumulation of orotic acid and L-dihydroorotic acid and the downregulation of uridine 5'-monophosphate*. In response, the antimycin A-inhibited cells possibly upregulated the pyrimidine salvage pathway as observed by uracil* accumulation. However, the proliferation of these cells was fully impaired, which suggested that the cells could not compensate for the blockage of pyrimidine synthesis. Among the upregulated metabolites, there was also 2-hydroxyglutaric acid*, the mitochondrial dysfunction marker mentioned before. Thus, this further suggests a severe impairment of mitochondrial respiration caused by antimycin. The downregulation of FBP* and G6P* also suggested the inhibition of glycolysis, which raises the question of which pathway the cells used then as an alternative to respiration blockage. Finally, glutathione was downregulated upon antimycin A treatment, which has also been observed in human fibroblasts [216]. Antimycin A has been shown to increase reactive oxygen species in activated T cells, and the implications of glutathione downregulation in this condition should be investigated further [217]. Thus, antimycin A exhibited great capacity to modulate the metabolism and

impact the proliferation of activated $CD4^+$ T cells. Furthermore, dihydroorotate dehydrogenase has been proposed as a new target for T-cell acute lymphoblastic leukemia [218]. The inhibition of this enzyme should also be explored in the context of autoimmunity.

Oligomycin severely impaired proliferation but only delayed activation of $CD4^+$ T cells. The marker metabolites identified covered distinct dispersed pathways, but when combined, they elucidated oligomycin's effect on $CD4^+$ T cells. First, the accumulation of 2-hydroxyglutaric acid*, a potential marker of mitochondria dysfunction in other species, was the main indication that respiration was successfully inhibited. Oligomycin A blocks the phosphorylation of ADP into ATP. This naturally increases ATP precursors ADP and AMP [129]. This results in the activation of AMPK, which will, in turn, promote catabolism and inhibit anabolism to restore ATP levels [219]. Thus, AMPK upregulates glycolysis and FAO while inhibiting FAS. The accumulation of 2 glycolysis intermediates, fructose- 1,6-biphosphate* and glyceraldehyde 3-phosphate*, indicated that this pathway was upregulated in response to oligomycin A respiration blockage. The downregulation of glycerophosphoinositol, also observed in cells treated with the FAS inhibitor PF-05175157, suggested that FAS was also inhibited. Thus, the inhibition of both glycolysis and FAS indicated that the effect of oligomycin on the ATP levels could indeed have activated AMPK. The accumulation of ADP and AMP also decreases the ATP/ADP ratio, so the AMP is converted into IMP to restore the energy balance and reduce stress levels [220]. This compensation mechanism would explain the downregulation of AMP* and adenine and the upregulation of IMP observed in the oligomycin A-inhibited cells. Finally, aspartic acid* was also downregulated, which was observed before in cell lines treated with oligomycin A, but the cause of this downregulation is still unclear [221]. Aspartate and IMP participate in the first step of *de novo* AMP biosynthesis [222]. This suggests that the aspartic acid* downregulation could be linked to the AMP and IMP regulation in oligomycin A treated cells and should be further investigated. Thus, the Oligomycin A metabolic markers indicated that respiration was inhibited, and the cells had to rearrange a dramatic metabolic shift to adapt. Finally, this also suggests that OXPHOS might be a critical pathway for activated $CD4^+$ T cells, and its therapeutic potential should be further investigated.

The inhibition of the first step of glutaminolysis by BPTES resulted in decreased detection of glutamic acid* and its downstream product, GABA*. On the other hand, it

resulted in the upregulation of citric acid*. This was unexpected since glutaminolysis fuels both the TCA and OXPHOS by converting glutamate into alpha-ketoglutarate [223]. One of the few studies of the effect of BPTES in activated $CD4^+$ T cells reported inhibition of proliferation in cells treated with this compound, which was also observed in my experiments [214]. However, this study did not report how BPTES affected the intervenient metabolites of glutaminolysis. This information was actually reported in cancer cell lines where the effect of BPTES has been heavily studied. These studies observed that treating cancer cells with BPTES resulted in decreased levels of glutamate, aspartate and upregulation of citrate [224], [225]. However, there was no conclusion on what was causing the increased levels of citrate. The upregulation of citric acid* in $CD4^+$ T cells treated with BPTES suggests that glutaminolysis is not essential to fuel the TCA cycle. Thus, the BPTES-inhibited cells found an alternative carbon source and could still increase the cycle flux. The TCA can be fueled by multiple metabolites, including glucose, alanine, or aspartate [226]. The downregulation of aspartic acid* in cells inhibited with BPTES could result from the heavy use of this metabolite to fuel TCA after conversion into oxaloacetate. The results also suggest that activation is delayed and proliferation is inhibited upon treatment with BPTES, even with the cells successfully rewiring their metabolism. Thus, the role of glutamine on $CD4^+$ T cell metabolism should be further studied.

The treatment of $CD4^+$ T cells with PF-05175157, the FAS inhibitor, resulted in the downregulation of two phospholipids that play important roles in membrane structure. The synthesis of new membranes is essential for proliferation in activated cells [24]. Despite the inhibition of FAS, treatment with PF-05175157 did not impair the proliferation of activated $CD4^+$ T cells. This was unexpected because the inhibition of FAS synthesis during T-cell activation was shown before to impair proliferation [227]. Glycerol 3-phosphate* was also found to be downregulated along with glucose-6-phosphate*. Glycerol-3-phosphate is a byproduct of glycolysis and can be used to synthesize phospholipids [228]. Besides that, it also plays a key role in the transport of NADH from the cytosol to the mitochondria for fueling OXPHOS [170]. The treatment with PF-05175157 resulted in the upregulation of 2-hydroxyglutaric acid*, a metabolite potentially linked to mitochondrial and TCA dysfunction [156]. Thus, it is possible that the FAS inhibition caused by PF-05175157 resulted in the downregulation of glycerol 3-phosphate*, one of the building blocks of phospholipids. This consequently affected the shuttle of NADH into the mitochondria, compromising OXPHOS and ATP generation.

However, the role of PF-05175157 in the metabolism of $CD4^+$ T cells needs to be further investigated.

Mycophenolic acid inhibits one arm of the *de novo* biosynthesis of purine nucleotides by blocking the conversion of IMP into xanthosine monophosphate, a precursor of guanosine monophosphate [178]. IMP can be alternatively converted into AMP through the other arm of the *de novo* biosynthesis of purine nucleotides, a set of reactions that also generates fumarate [229]. Thus, this would explain the observed upregulation of AMP* and citric acid* in mycophenolic acid-treated cells since the generated fumarate would fuel the TCA cycle. The accumulation of citric acid* could then lead to the inhibition of glycolysis, explaining the observed downregulation of FBP* and G6P*. However, modulation with mycophenolic acid results in the depletion of the guanosine pool, where guanosine triphosphate is included [230]. Since the conversion of IMP into AMP requires guanosine triphosphate as the energy source, this arm of *de novo* biosynthesis of purines would also be impaired upon treatment with mycophenolic acid. This means that the observed increased levels of AMP* might result from another compensation mechanism. Similarly, the downregulation of glycolysis and upregulation of TCA could be linked to other factors. The treatment of Jukart T cells with mycophenolic acid inhibited glucose uptake and further oxidation [231]. Thus, mycophenolic acid appears to impact glycolysis, although the exact mechanism remains to be elucidated. The functional state results revealed that this compound delayed activation but did not inhibit it, with most cells only reaching the Early and Peak activation stages. On the other hand, cell proliferation was severely impaired, as reported before [179]. Thus, mycophenolic acid affects the metabolism and the functional state of activated $CD4^+$ T cells. However, the exact metabolic impact and outcome remain to be elucidated.

Before being commonly prescribed to treat autoimmune conditions, MTX was used to treat cancer due to its antiproliferative effect. Currently, one of the known targets of MTX is aminoimidazole-4-carboxamide ribonucleotide transformylase, a bifunctional enzyme that catalyzes the last two steps of the *de novo* purine biosynthesis pathway [184]. The treatment of $CD4^+$ T cells with MTX resulted in the upregulation of the precursor of this pathway, PRPP. On the other hand, it also resulted in the downregulation of one product of this pathway, guanosine monophosphate. This and the strong proliferation impairment observed suggested that MTX inhibited *de novo* purine biosynthesis. Since PRPP is required as a co-substrate in the final steps of the *de novo* pyrimidine synthesis, a

potential inhibition of this pathway should also be considered. This would be consistent with previous purine and pyrimidine depletion reports in T cells treated with MTX [185]. The only significant change observed in the *de novo* pyrimidine biosynthesis pathway was the downregulation of its precursor, glutamine*. However, since no other significant change was observed for the intermediates, the methotrexate's impact on this pathway remained unclear. Among the upregulated metabolites was ribose 1,5-biphosphate, an understudied metabolite reported to be an activator of the glycolytic enzyme phosphofructokinase. One study in macrophages reported this metabolite to be a product of PRPP dephosphorylation [232]. However, this reaction was never reported in another cell type, so it remains unclear what the origin of this metabolite is in $CD4^+$ T cells. The role of ribose 1,5-biphosphate as an activator of glycolysis also remains unclear because the glycolytic intermediates FBP and G6P* were found to be downregulated. Thus, MTX treatment in $CD4^+$ T cells inhibited purine biosynthesis, but the effect on pyrimidines remained unclear. Ribose 1,5-biphosphate was significantly upregulated upon treatment with MTX. However, its role in CD4+ T cell metabolism is unclear and should be explored.

Metformin is one of the compounds in the grey zone between the known and unknown metabolic modulators. This is because of the multiple targets of metformin and the dispersed array responses. However, this also means that it is very well studied, which should help when it comes to conclusions regarding its metabolic mode of action in $CD4^+$ T cells. The functional state markers revealed a delay in activation (with most cells in the peak activation stage) and a considerable impairment of proliferation for metformin-treated cells. Similar activation and proliferation patterns have been observed before in $CD4^+$ T cells treated with metformin. However, it was concluded that metformin did not affect the glucose uptake or lactate production in activated cells [233]. This is not unexpected since metformin activates AMPK, which promotes catabolic processes like glycolysis. The downregulation of citric acid* and the upregulation of malic acid* and fumaric acid* hinted at a dysregulation of the TCA cycle. Metformin has been reported to suppress the conversion of malate to citrate in cancer cell lines [234]. Metformin has also been reported to impair the TCA cycle flux by promoting reserve exchange flux, leading to malate and fumarate accumulation [235]. This is thought to be a compensation mechanism for complex I inhibition. Metformin has also been reported to inhibit glutaminase, the enzyme that catalyzes the conversion of glutamine to glutamate [236]. However, this is insufficient to explain the observed downregulation of glutamine*. Metformin reportedly inhibited

asparagine synthesis, but the exact process remains unclear [237]. However, this correlates with the downregulation of asparagine and proline observed in the results shown here. Thus, Metformin might be inhibiting complex I in activated $CD4^+$ T cells, resulting in a change of dynamics in the TCA cycle. Moreover, the effect of metformin on amino acid metabolism should also be explored.

5.2. Mode of action of non-metabolic modulators

Despite belonging to different batches, the mTOR inhibitors, rapamycin and Torin 1, exhibited a significant overlap of the up and downregulated metabolites. In fact, these two compounds shared three of the five top-downregulated metabolites: FBP*, G6P*, and fucose 1-phosphate. The interpretation of fucose 1-phosphate will be skipped since its primary known function is to be an intermediate in fucosylation, and little is known about its metabolic role [152]. The downregulation of the glycolysis intermediates FBP* and G6P* indicated the inhibition of this pathway. Additionally, the treatment with rapamycin also resulted in the inhibition of a third glycolysis intermediate, glyceraldehyde 3-phosphate*. Since mTOR promotes glycolysis, this indicates that the modulation with rapamycin and Torin 1 worked [174]. Rapamycin and Torin 1 condition also shared the top 3 upregulated metabolites: aspartic acid*, AMP*, and O-phosphoethanolamine. Aspartate participates in the branch of the *de novo* biosynthesis of purine nucleotides that converts IMP into AMP. Interestingly, the first was upregulated in the Torin 1 condition but not Rapamycin. The AMP can be converted into ATP, which can be further used for RNA and DNA synthesis [192]. Unfortunately, it is not possible to detect any nucleoside triphosphate with this method, so there is no information on how the levels of ATP are affected in these conditions. Alternatively, ATP can be converted into cyclic AMP, a known inhibitor of proliferation and cytokine production in activated T cells [238]. The expression of cAMP* was upregulated in rapamycin but not in Torin 1-treated cells. The treatment of $CD4^+$ T cells with either rapamycin or Torin 1 resulted in the almost complete inhibition of proliferation but not activation. Thus, cyclic AMP accumulation is not the only cause of impaired proliferation. Moreover, it has been reported that mTOR activates *de novo* purine biosynthesis, and treatment with rapamycin prevented the use of precursors of this pathway in the synthesis of RNA and DNA in cancer cell lines [195]. This suggests that the accumulation of *de novo* purine biosynthesis intermediates does not result from the

activation but rather from inhibiting this pathway, which would result in the depletion of nucleotides necessary for proliferation. The accumulation of AMP*, IMP, and aspartic acid* suggests the inhibition of a downstream step. However, it is essential to investigate further how mTOR inhibition is causing this. Thus, de novo purine biosynthesis inhibition appears to be causing the proliferation impairment in Torin 1 treated cells. Meanwhile, in rapamycin-treated cells, this might result from the combination of cyclic AMP accumulation and the inhibition of *de novo* purine biosynthesis. $CD4^+$ T cells treated with Torin 1 also exhibited upregulation of glutamic acid* and downregulation of its downstream product, glutathione. The accumulation of glutamate and glutamine has also been observed in cancer cell lines treated with rapamycin [239]. However, it is still not clear how glutathione is affected by mTOR inhibition. Finally, rapamycin-treated cells also exhibited high levels of citric acid*, indicating increased activity of the TCA cycle, which would compensate for the inhibited glycolysis. However, the citric acid* accumulation could also be related to the AMP* and aspartic acid* accumulation. The *de novo* purine biosynthesis links nucleotide metabolism to the TCA cycle through the generation of fumarate when converting IMP to AMP, as mentioned above. Thus, the connection between these two metabolites (AMP* and aspartic acid*) and the TCA cycle needs to be further explored in rapamycin-treated $CD4^+$ T cells. Thus, the up and downregulated metabolites found indicate that both mTOR inhibitors have overlapping metabolic outcomes with minor differences.

Baricitinib and Tofacitinib are JAK inhibitors commonly used to treat autoimmune diseases. One of the observed effects of these compounds is the inhibition of proliferation in activated T cells [194]. The results presented here showed a modest impact on the proliferation, while there was a heterogeneous response to activation. These compounds have also been shown to decrease the amount of lactate produced and the ratio of glycolysis to OXPHOS [240]. Similar results were observed here with the downregulation of glucose-6-phosphate* and fructose 1,6-biphosphate*. Thus, this indicates that besides inhibiting JAK enzymes, baricitinib and tofacitinib might also downregulate glycolysis in activated $CD4^+$ T cells. The mechanism by which this happens remains to be elucidated. The downregulation of glutamine also suggests some effect on glutaminolysis. However, without detecting other markers, it is impossible to hypothesize the direction of the pathway. Finally, two upregulated metabolites, AMP* and aspartic acid, were also observed in Torin 1 and rapamycin-treated cells. Since proliferation was not severely

impaired in baricitinib and tofacitinib-treated cells, it is unclear if the effect on this pathway is the same as in the mTOR-inhibited conditions. However, these results suggest that baricitinib and tofacitinib indirectly affect the metabolism of $CD4^+$ T cells.

Treating $CD4^+$ T cells with cyclosporin had a heterogeneous effect on activation with high variability between replicates, likely due to sample preparation or technical errors. Conversely, the reproducibility of proliferation was higher between technical replicates. The percentage of cells that divided was lower than in the activated control, indicating that this compound impaired proliferation. Given its role as an immunosuppressant, the capacities of cyclosporin to inhibit the proliferation of activated T cells have been known for a long time [241]. Interestingly, this condition's up and downregulated metabolites fully overlapped with those found either for the mTOR or the JAK inhibitors. Cyclosporin inhibits the activation of the nuclear factor of activated T cells, a family of transcription factors that can induce the expression of c-Myc [193]. This transcription factor, in turn, is responsible for the upregulation of glycolysis and glutaminolysis in activated T cells [201]. Thus, it has been hypothesized that cyclosporin might inhibit these two pathways. The significant downregulation of the glycolysis intermediates FBP* and G6P*, observed in this project, supported this hypothesis. However, the downregulation of glutamine* and the upregulation of glutathione suggested otherwise since this metabolite is likely synthesized from glutamic acid obtained through glutaminolysis. Reactive oxygen species are thought to be involved in the side effects experienced by patients treated with cyclosporine [242]. It is unclear if this also happens on the cellular level, but it would explain the increased glutathione levels observed. Thus, the results suggest that glycolysis might be downregulated, but the state of glutaminolysis is unclear. The Cyclosporine condition also exhibited increased levels of aspartic acid* and AMP* and impaired proliferation, as mentioned before. Several effector enzymes from the *de novo* purine biosynthesis are also regulated by the transcription factor c-Myc [243]. Thus, the indirect inhibition of c-Myc by cyclosporine might be causing the inhibition of this pathway and proliferation. However, the exact mechanisms that lead cyclosporin to inhibit these metabolic pathways must be explored.

5.3. Metabolites to investigate in CD4$^+$ T cells

Two metabolites were constantly upregulated in the modulated conditions mentioned in this chapter: O-phosphoethanolamine and taurine. Interestingly, these two metabolites were also identified as markers of the Naïve condition. Their interpretation was purposely skipped when discussing each condition individually to avoid repetition so that it will be discussed here. O-phosphoethanolamine detection was upregulated in all conditions except in cells treated with cyclosporine. The role of this metabolite is still being explored, not just in the immunometabolism field, and it might have different roles depending on the context. For example, supplementing a melanoma cancer cell line with a low concentration of phosphoethanolamine increased proliferation. However, higher concentrations were cytotoxic and induced cell death [244]. O-phosphoethanolamine is a precursor of phosphatidylethanolamine, an essential phospholipid present in membranes [245]. The role of this phospholipid is only starting to be explored in T cells, but it has been recently shown that blocking the synthesis of this phosphatidylethanolamine resulted in impaired cell proliferation [246]. In all conditions where O-phosphoethanolamine was upregulated, impaired proliferation was also observed, although in varying degrees. This indicates that the accumulation of O-phosphoethanolamine was correlated with decreased proliferation. However, the role of this metabolite on T cell activation and proliferation should be further explored. Finally, it would also be worth exploring the role of O-phosphoethanolamine on naïve T cells. The accumulation of this metabolite in this non-proliferative population suggested that the cells could store it to quickly engage in membrane biosynthesis upon activation. However, O-phosphoethanolamine could also have additional functions in the metabolism of naïve and activated CD4$^+$ T cells that still need to be explored. The accumulation of taurine in naïve cells was already discussed above, and the main conclusion was that it might help promote long-term survival while the cells wait for activation. Taurine was also upregulated in several conditions (i.e., metformin, BPTES, PF-05175157, mycophenolic acid, methotrexate, cyclosporine, baricitinib, tofacitinib), which exhibited varying degrees of proliferation impairment. The supplementation of taurine to CD8$^+$ T cells simultaneously with activation increased proliferation and cytotoxic activity [210]. Since taurine was detected in conditions where proliferation was impaired and in conditions where it was only slightly affected, the correlation between the accumulation of this metabolite and proliferation is unclear. Thus, taurine might have a role in CD4$^+$ T cells that needs to be explored.

5.4. Limitations and Future Directions

HT-SpaceM has many advantages compared to other single-cell methods, such as the throughput or the standard format of the output data, which is compatible with other single-cell analysis packages. One main advantage not emphasized in the results chapter is the in-house software that can be used for all the processing steps, such as microscopy data stitching, mass spectrometry data conversion, data uploading to METASPACE, cell segmentation, and single-cell data generation. This centralization of all steps in a single software facilitates data processing. HT-SpaceM also requires a low number of cells per well (technical replicate), a significant advantage over bulk methods.

However, the method and the project also have some limitations that must be considered. The main limitation of HT-SpaceM is the type of mass spectrometry data acquired. During HT-SpaceM, only one round of ionization is performed in the mass analyzer. Since no fragmentation is done, it is not possible to distinguish the different isomers of the detected ions. For example, this can be problematic when leading with pentose or hexose sugars. Performing fragmentation would be possible and easy to integrate into the pipeline. However, it would also significantly increase the time required to measure one single well. To achieve this, it could also be necessary to focus on a specific group of metabolites, which would defeat the untargeted purpose of the method. Thus, this limitation cannot be overcome without compromising the main strengths of the method. Currently, it takes 40 minutes to image half of one well. This is enough to sample 500 to 1000 cells and it means that imaging one entire slide takes around 27 hours. Although no difference was observed between wells sampled at the beginning and the end of the acquisition, this is still a limitation when wanting to run larger projects. However, this is a limitation of the instrument and should be overcome in the next years with the technological advancements in the MALDI-imaging MS field. Finally, steady-state measurement of metabolites is also a known limitation in metabolomics. This can make interpreting the results difficult since the presence of a metabolite does not always correlate with pathway activity. One way to overcome this would be combining HT-SpaceM with other modalities that detect the enzymes, such as mass cytometry or MALDI-IHC, a novel technique that combines MALDI with immunohistochemistry [247].

Finally, there were also many limitations related to the experimental design. The main limitation was that multiple concentrations and incubation times were not tested for the different compounds. This was not possible because of time constraints. Although most compounds had the expected effect, some compounds like rotenone and WZB-117 did not reproduce the previous effects in $CD4^+$ T cells [134], [248]. In future applications of the method, it would be advisable to test different concentrations and time points to understand the effects of short versus long-term incubations and if there are off-target effects above specific concentrations. Another limitation was that the different conditions were run in separate batches, which made it necessary to find ways to integrate them. The results presented in this dissertation extensively showed the capacity of HT-SpaceM to detect distinct metabolic states. However, the results failed to exhibit the single-cell capacities of the method, such as heterogeneity or spatial relationships. This was something not pursued due to time constraints. The atlas projection was the only analysis demonstrating the heterogeneity among conditions, with some splitting across different metabolic states. However, the atlas also presented limitations, such as the number of metabolic states included. Ideally, it should cover more metabolic pathways. It should contain compounds that affect different targets in the same pathway, as the metabolic outcome might differ. This was partially achieved by including the OXPHOS inhibitors antimycin A (complex III) and oligomycin A (complex V), but it should be done for other pathways. Only a comprehensive and extensive atlas can give insightful outcomes. The method used to integrate the projected data into the atlas should also be evaluated. There are now available resources to benchmark methods for atlas integration, which provide metrics to decide on the optimal method [188].

HT-SpaceM extensively demonstrated that it can be used for single-cell metabolomics analysis of $CD4^+$ T cells. The future directions of the method should prioritize integrating with other techniques, such as immunohistochemistry. This would make it possible to study heterogeneous populations such as PBMCs, which cannot be differentiated based on morphology alone. The metabolic coverage should also be optimized to provide a more complete overview of the metabolome. This could be achieved by, for example, imaging the slides in both negative and positive polarity. Finally, once this is optimized and standardized, HT-SpaceM could have the capacity to be applied in the clinical context by providing the metabolomic composition of heterogeneous populations (e.g., tumor microenvironment).

6 CONCLUSION

In this dissertation, I have presented a novel method for single-cell metabolomics in $CD4^+$ T cells. The method presented here, HT-SpaceM, is a high-throughput updated version of the method originally developed by the Alexandrov team. In my project, I have adapted the many steps of the original method, SpaceM, including sample preservation and the chemical matrix used. I have demonstrated that HT-SpaceM can resolve the metabolic state of naïve, activated, and modulated $CD4^+$ T cells. Notably, some of the 25 different compounds used to modulate the $CD4^+$ T cells have never been tested in these cells before (e.g. AZ-PFKFB3-67). The modulation of the cells with these compounds has revealed potential metabolic mechanisms not reported before in $CD4^+$ T cells that should be further explored. These include the role of antimycin A in inhibiting *de novo* pyrimidine biosynthesis or the role of cyclosporine in purine biosynthesis. Additionally, I reported specific metabolites that were identified with HT-SpaceM and should be further studied. This is the case of O-phosphoethanolamine or taurine, which were present in many conditions with impaired activation and proliferation. However, their role in the metabolism of activated $CD4^+$ T cells is understudied. Finally, I have presented a single-cell atlas of metabolic states in $CD4^+$ T cells. The atlas comprised 9 metabolic states and could predict the mode of action of known modulators. It also predicted the mode of action of modulators with unknown metabolic effects. For example, it predicted that the JAK inhibitors, baricitinib and tofacitinib, inhibited the purine biosynthesis pathway. However, the coverage of the atlas was limited and it should be further expanded for a more comprehensive interpretation. The expanded single-cell atlas of metabolic states in $CD4^+$ T cells has the potential to be helpful in the clinical context, such as in the discovery of metabolic targets for new therapies. The single-cell metabolomics method presented in this dissertation helps advance the fields of single-cell metabolomics and immunometabolism by providing a novel way of studying the metabolism of $CD4^+$ T cells.

7 REFERENCES

[1] D. D. Chaplin, “Overview of the immune response,” *J. Allergy Clin. Immunol.*, vol. 125, pp. S3-23, 2010, doi: 10.1016/j.jaci.2009.12.980.

[2] K. M. Yatim and F. G. Lakkis, “A brief journey through the immune system,” *Clin. J. Am. Soc. Nephrol.*, vol. 10, no. 7, pp. 1274–1281, 2015, doi: 10.2215/CJN.10031014.

[3] J. Parkin and B. Cohen, “An Overview of the Immune System,” *Lancet*, vol. 357, no. 9270, pp. 1777–1789, 2001, doi: 10.1016/S0140-6736(00)04904-7.

[4] D. L. Woodland and J. E. Kohlmeier, “Migration, maintenance and recall of memory T cells in peripheral tissues,” *Nat. Rev. Immunol.*, vol. 9, no. 3, pp. 153–161, 2009, doi: 10.1038/nri2496.

[5] A. J. Pollard and E. M. Bijker, “A guide to vaccinology: from basic principles to new developments,” *Nat. Rev. Immunol.*, vol. 21, no. 2, pp. 83–100, 2021, doi: 10.1038/s41577-020-00479-7.

[6] N. Lam, Y. S. Lee, and D. L. Farber, “A guide to adaptive immune memory,” *Nat. Rev. Immunol.*, 2024, doi: 10.1038/s41577-024-01040-6.

[7] B. V. Kumar, T. J. Connors, and D. L. Farber, “Human T Cell Development, Localization, and Function throughout Life,” *Immunity*, vol. 48, no. 2, pp. 202–213, 2018, doi: 10.1016/j.immuni.2018.01.007.

[8] L. Chopp, C. Redmond, J. J. O’Shea, and D. M. Schwartz, “From thymus to tissues and tumors: A review of T-cell biology,” *J. Allergy Clin. Immunol.*, vol. 151, no. 1, pp. 81–97, 2023, doi: 10.1016/j.jaci.2022.10.011.

[9] T. Van Den Broek, J. A. M. Borghans, and F. Van Wijk, “The full spectrum of human naive T cells,” *Nat. Rev. Immunol.*, vol. 18, no. 6, pp. 363–373, 2018, doi: 10.1038/s41577-018-0001-y.

[10] X. Zhu and J. Zhu, “CD4 T helper cell subsets and related human immunological disorders,” *Int. J. Mol. Sci.*, vol. 21, no. 21, pp. 1–26, 2020, doi: 10.3390/ijms21218011.

[11] A. Corthay, “How do regulatory T cells work?,” *Scand. J. Immunol.*, vol. 70, pp. 326–336, 2009, doi: 10.1111/j.1365-3083.2009.02308.x.

[12] L. Sun, Y. Su, A. Jiao, X. Wang, and B. Zhang, “T cells in health and disease,” *Signal Transduct. Target. Ther.*, vol. 8, no. 1, 2023, doi: 10.1038/s41392-023-01471-y.

[13] M. Dominguez-Villar and D. A. Hafler, “Regulatory T cells in autoimmune disease,” *Nat. Immunol.*, vol. 19, pp. 665–673, 2018, doi: 10.1038/s41590-018-0120-4.

[14] L. Makowski, M. Chaib, and J. C. Rathmell, “Immunometabolism: From basic mechanisms to translation,” *Immunol. Rev.*, vol. 295, no. 1, pp. 5–14, 2020, doi: 10.1111/imr.12858.

[15] J. Traba, M. N. Sack, T. A. Waldmann, and O. M. Anton, “Immunometabolism at the Nexus of Cancer Therapeutic Efficacy and Resistance,” *Front. Immunol.*, vol. 12, no. May, pp. 1–16, 2021, doi: 10.3389/fimmu.2021.657293.

[16] M. Galgani, S. Bruzzaniti, and G. Matarese, “Immunometabolism and autoimmunity,” *Curr. Opin. Immunol.*, vol. 67, pp. 10–17, 2020, doi: 10.1016/j.coi.2020.07.002.

[17] D. Roos and J. A. Loos, “Changes in the Carbohydrate Metabolism of Mitogenically Stimulated Human Peripheral Lymphocytes: II Relative Importance of Glycolysis and Oxidative Phosphorylation on Phytohaemagglutinin Stimulation,” *Exp. Cell Res.*, vol. 77, pp. 127–135, 1973.

[18] H. W. Chen, H.-J. Heiniger, and A. A. Kandutsch, “Relationship Between Sterol Synthesis and DNA Synthesis in Phytohemagglutinin-Stimulated Mouse Lymphocytes,” *Proc. Natl. Acad. Sci.*, vol. 72, no. 5, pp. 1950–1954, 1975.

[19] E. L. Pearce, M. C. Poffenberger, C. H. Chang, and R. G. Jones, “Fueling immunity: Insights into metabolism and lymphocyte function,” *Science (80-.).*, vol. 342, no. 6155, 2013, doi: 10.1126/science.1242454.

[20] L. Almeida, M. Lochner, L. Berod, and T. Sparwasser, “Metabolic pathways in T cell activation and lineage differentiation,” *Semin. Immunol.*, vol. 28, no. 5, pp. 514–524, 2016, doi: 10.1016/j.smim.2016.10.009.

[21] C. S. Palmer, M. Ostrowski, B. Balderson, N. Christian, and S. M. Crowe, “Glucose metabolism regulates T cell activation, differentiation, and functions,” *Front. Immunol.*, vol. 6, no. JAN, pp. 1–6, 2015, doi: 10.3389/fimmu.2015.00001.

[22] M. Y. Braun, “The Natural History of T Cell Metabolism,” *Int. J. Mol. Sci.*, vol. 22, no. 13, pp. 1–16, 2021, doi: 10.3390/ijms22136779.

[23] M. M. Delmastro-Greenwood and J. D. Piganelli, “Changing the energy of an immune response,” *Am. J. Clin. Exp. Immunol.*, vol. 2, no. 1, pp. 30–54, 2013.

[24] M. D. Buck, D. O’Sullivan, and E. L. Pearce, “T cell metabolism drives immunity,” *J. Exp. Med.*, vol. 212, no. 9, pp. 1345–1360, 2015, doi: 10.1084/jem.20151159.

[25] E. L. Carr *et al.*, “Glutamine Uptake and Metabolism Are Coordinately Regulated by ERK/MAPK during T Lymphocyte Activation,” *J. Immunol.*, vol. 185, no. 2, pp. 1037–1044, 2010, doi: 10.4049/jimmunol.0903586.

[26] R. J. DeBerardinis *et al.*, “Beyond aerobic glycolysis: Transformed cells can engage in glutamine metabolism that exceeds the requirement for protein and nucleotide synthesis,” *Proc. Natl. Acad. Sci.*, vol. 104, no. 49, pp. 19345–19350, 2007, doi: 10.1073/pnas.0709747104.

[27] R. M. Loftus and D. K. Finlay, “Immunometabolism: cellular metabolism turns immune regulator,” *J. Biol. Chem.*, vol. 291, no. 1, pp. 1–10, 2016, doi: 10.1074/jbc.R115.693903.

[28] G. J. W. van der Windt and E. L. Pearce, “Metabolic switching and fuel choice during T-cell differentiation and memory development,” *Immunol. Rev.*, vol. 249, pp. 27–42, 2012, doi: 10.1111/j.1600-065X.2012.01150.x.

[29] G. Andrejeva and J. C. Rathmell, “Similarities and Distinctions of Cancer and Immune Metabolism in Inflammation and Tumors,” *Cell Metab.*, vol. 26, pp. 49–70, 2017, doi: 10.1016/j.cmet.2017.06.004.

[30] Y. Cao, J. C. Rathmell, and A. N. Macintyre, “Metabolic reprogramming towards aerobic glycolysis correlates with greater proliferative ability and resistance to metabolic inhibition in CD8 versus CD4 T cells,” *PLoS One*, vol. 9, no. 8, pp. 1–15, 2014, doi: 10.1371/journal.pone.0104104.

[31] M. Corrado and E. L. Pearce, “Targeting memory T cell metabolism to improve immunity,” *J. Clin. Invest.*, vol. 132, no. 1, pp. 1–11, 2022, doi: 10.1172/JCI148546.

[32] B. Wu, J. J. Goronzy, and C. M. Weyand, “Metabolic Fitness of T Cells in Autoimmune Disease,” *Immunometabolism*, vol. 2, no. 2, p. e200017, 2020, doi: 10.20900/immunometab20200017.

[33] G. O. Rangel Rivera *et al.*, “Fundamentals of T Cell Metabolism and Strategies to Enhance Cancer Immunotherapy,” *Front. Immunol.*, vol. 12, no. March, pp. 1–17, 2021, doi: 10.3389/fimmu.2021.645242.

[34] K. Voss, H. S. Hong, J. E. Bader, A. Sugiura, C. A. Lyssiotis, and J. C. Rathmell, “A guide to interrogating immunometabolism,” *Nat. Rev. Immunol.*, vol. 21, no. 10, pp. 637–652, 2021, doi: 10.1038/s41577-021-00529-8.

[35] M. C. Ludikhuize, M. Meerlo, B. M. T. Burgering, and M. J. Rodríguez Colman, “Protocol to profile the bioenergetics of organoids using Seahorse,” *STAR Protoc.*, vol. 2, no. 1, 2021, doi: 10.1016/j.xpro.2021.100386.

[36] M. N. Artyomov and J. Van den Bossche, “Immunometabolism in the Single-Cell Era,” *Cell Metab.*, vol. 32, no. 5, pp. 710–725, Nov. 2020, doi: 10.1016/j.cmet.2020.09.013.

[37] V. Purohit, A. Wagner, N. Yosef, and V. K. Kuchroo, “Systems-based approaches to study immunometabolism,” *Cell. Mol. Immunol.*, vol. 19, no. 3, pp. 409–420, 2022, doi: 10.1038/s41423-021-00783-9.

[38] D. Hilovsky, J. Hartsell, J. D. Young, and X. Liu, “Stable Isotope Tracing Analysis in Cancer

Research: Advancements and Challenges in Identifying Dysregulated Cancer Metabolism and Treatment Strategies," *Metabolites*, vol. 14, no. 6, p. 318, 2024, doi: 10.3390/metabo14060318.

[39] M. N. Artyomov and J. Van den Bossche, "Immunometabolism in the Single-Cell Era," *Cell Metab.*, vol. 32, no. 5, pp. 710–725, 2020, doi: 10.1016/j.cmet.2020.09.013.

[40] A. Baysoy, Z. Bai, R. Satija, and R. Fan, "The technological landscape and applications of single-cell multi-omics," *Nat. Rev. Mol. Cell Biol.*, vol. 24, no. 10, pp. 695–713, 2023, doi: 10.1038/s41580-023-00615-w.

[41] F. W. M. Verheijen, T. N. M. Tran, J. C. Chang, F. Broere, E. A. Zaal, and C. R. Berkers, "Deciphering metabolic crosstalk in context: lessons from inflammatory diseases," *Mol. Oncol.*, vol. 18, pp. 1759–1776, 2024, doi: 10.1002/1878-0261.13588.

[42] M. Heinemann and R. Zenobi, "Single cell metabolomics," *Curr. Opin. Biotechnol.*, vol. 22, no. 1, pp. 26–31, 2011, doi: 10.1016/j.copbio.2010.09.008.

[43] K. D. Duncan, J. Fyrestam, and I. Lanekoff, "Advances in mass spectrometry based single-cell metabolomics," *Analyst*, vol. 144, no. 3, pp. 782–793, 2019, doi: 10.1039/c8an01581c.

[44] A. Ali *et al.*, "Single cell metabolism: current and future trends," *Metabolomics*, vol. 18, no. 10, pp. 1–22, 2022, doi: 10.1007/s11306-022-01934-3.

[45] I. Lanekoff, V. V. Sharma, and C. Marques, "Single-cell metabolomics: where are we and where are we going?," *Curr. Opin. Biotechnol.*, vol. 75, pp. 1–7, 2022, doi: 10.1016/j.copbio.2022.102693.

[46] G. R. D. Prabhu, E. R. Williams, M. Wilm, and P. L. Urban, "Mass spectrometry using electrospray ionization," *Nat. Rev. Methods Prim.*, vol. 3, no. 1, 2023, doi: 10.1038/s43586-023-00203-4.

[47] X. Guo, X. Wang, C. Tian, J. Dai, Z. Zhao, and Y. Duan, "Development of mass spectrometry imaging techniques and its latest applications," *Talanta*, vol. 264, no. January, p. 124721, 2023, doi: 10.1016/j.talanta.2023.124721.

[48] E. K. Neumann, T. J. Comi, S. S. Rubakhin, and J. V. Sweedler, "Lipid Heterogeneity between Astrocytes and Neurons Revealed by Single-Cell MALDI-MS Combined with Immunocytochemical Classification," *Angew. Chemie - Int. Ed.*, vol. 58, no. 18, pp. 5910–5914, 2019, doi: 10.1002/anie.201812892.

[49] M. Niehaus, J. Soltwisch, M. E. Belov, and K. Dreisewerd, "Transmission-mode MALDI-2 mass spectrometry imaging of cells and tissues at subcellular resolution," *Nat. Methods*, vol. 16, no. 9, pp. 925–931, 2019, doi: 10.1038/s41592-019-0536-2.

[50] C. Zhang, S. E. Le Dévédec, A. Ali, and T. Hankemeier, "Single-cell metabolomics by mass spectrometry: ready for primetime?," *Curr. Opin. Biotechnol.*, vol. 82, p. 102963, 2023, doi: 10.1016/j.copbio.2023.102963.

[51] L. Rappez *et al.*, "SpaceM reveals metabolic states of single cells," *Nat. Methods*, vol. 18, no. 7, pp. 799–805, 2021, doi: 10.1038/s41592-021-01198-0.

[52] T. Alexandrov *et al.*, "METASPACE: A community-populated knowledge base of spatial metabolomes in health and disease," *bioRxiv*, pp. 1–22, 2019, doi: 10.1101/539478.

[53] M. C. Chambers *et al.*, "A cross-platform toolkit for mass spectrometry and proteomics," *Nat. Biotechnol.*, vol. 30, no. 10, pp. 918–920, 2012, doi: 10.1038/nbt.2377.

[54] A. M. Race, I. B. Styles, and J. Bunch, "Inclusive sharing of mass spectrometry imaging data requires a converter for all," *J. Proteomics*, vol. 75, no. 16, pp. 5111–5112, 2012, doi: 10.1016/j.jprot.2012.05.035.

[55] J. Schindelin *et al.*, "Fiji: An open-source platform for biological-image analysis," *Nat. Methods*, vol. 9, no. 7, pp. 676–682, 2012, doi: 10.1038/nmeth.2019.

[56] C. Stringer, T. Wang, M. Michaelos, and M. Pachitariu, "Cellpose: a generalist algorithm for cellular segmentation," *Nat. Methods*, vol. 18, no. 1, pp. 100–106, 2021, doi: 10.1038/s41592-020-01018-x.

[57] F. A. Wolf, P. Angerer, and F. J. Theis, "SCANPY: large-scale single-cell gene expression data

analysis," *Genome Biol.*, vol. 19, no. 1, p. 15, Dec. 2018, doi: 10.1186/s13059-017-1382-0.

[58] K. Polański, M. D. Young, Z. Miao, K. B. Meyer, S. A. Teichmann, and J. E. Park, "BBKNN: Fast batch alignment of single cell transcriptomes," *Bioinformatics*, vol. 36, no. 3, pp. 964–965, 2020, doi: 10.1093/bioinformatics/btz625.

[59] M. Waskom, "Seaborn: Statistical Data Visualization," *J. Open Source Softw.*, vol. 6, no. 60, p. 3021, 2021, doi: 10.21105/joss.03021.

[60] J. A. Kirwan *et al.*, "Quality assurance and quality control reporting in untargeted metabolic phenotyping: mQACC recommendations for analytical quality management," *Metabolomics*, vol. 18, no. 9, pp. 1–16, 2022, doi: 10.1007/s11306-022-01926-3.

[61] I. Mondragão-Rodrigues and M. F. Macedo, "Buffy Coat Processing Impacts on Monocytes' Capacity to Present Lipid Antigens," *Biomedicines*, vol. 11, no. 3, 2023, doi: 10.3390/biomedicines11030833.

[62] J. Domínguez-Andrés *et al.*, "In vitro induction of trained immunity in adherent human monocytes," *STAR Protoc.*, vol. 2, no. 1, 2021, doi: 10.1016/j.xpro.2021.100365.

[63] C. R. Kleiveland, "Peripheral Blood Mononuclear Cells," *Impact Food Bioact. Gut Heal.*, vol. Chapter 15, pp. 1–327, 2015, doi: 10.1007/978-3-319-16104-4.

[64] F. Naeim, P. N. Rao, S. X. Song, and R. T. Phan, "Principles of Immunophenotyping," *Atlas Hematop. Morphol. Immunophenotype, Cytogenet. Mol. Approaches, Second Ed.*, pp. 29–56, 2018, doi: 10.1016/B978-0-12-809843-1.00002-4.

[65] J. M. Thompson, J. R. Gralow, R. Levy, and R. A. Miller, "The optimal application of forward and ninety-degree light scatter in flow cytometry for the gating of mononuclear cells," *Cytometry*, vol. 6, no. 5, pp. 401–406, 1985, doi: 10.1002/cyto.990060503.

[66] H. M. Shapiro, *Practical Flow Cytometry*. Wiley, 2003.

[67] T. Wu *et al.*, "Cell Granularity Reflects Immune Cell Function and Enables Selection of Lymphocytes with Superior Attributes for Immunotherapy," *Adv. Sci.*, vol. 10, no. 28, pp. 1–15, 2023, doi: 10.1002/advs.202302175.

[68] J. Akagi *et al.*, "Real-time cell viability assays using a new anthracycline derivative DRAQ7®," *Cytom. Part A*, vol. 83 A, no. 2, pp. 227–234, 2013, doi: 10.1002/cyto.a.22228.

[69] M. A. Nokta, X. D. Li, J. Nichols, A. Pou, D. Asmuth, and R. B. Pollard, "Homeostasis of naive and memory T cell subpopulations in peripheral blood and lymphoid tissues in the context of human immunodeficiency virus infection," *J. Infect. Dis.*, vol. 183, no. 9, pp. 1336–1342, 2001, doi: 10.1086/319868.

[70] I. M. Rea, S. E. McNerlan, and H. D. Alexander, "CD69, CD25, and HLA-DR activation antigen expression on CD3+ lymphocytes and relationship to serum TNF-α, IFN-γ, and sIL-2R levels in aging," *Exp. Gerontol.*, vol. 34, no. 1, pp. 79–93, 1999, doi: 10.1016/S0531-5565(98)00058-8.

[71] C. G. Sagerström, E. M. Kerr, J. P. Allison, and M. M. Davis, "Activation and differentiation requirements of primary T cells in vitro," *Proc. Natl. Acad. Sci. U. S. A.*, vol. 90, no. 19, pp. 8987–8991, 1993, doi: 10.1073/pnas.90.19.8987.

[72] G. Iezzi, K. Karjalainen, and A. Lanzavecchia, "The duration of antigenic stimulation determines the fate of naive and effector T cells," *Immunity*, vol. 8, no. 1, pp. 89–95, 1998, doi: 10.1016/S1074-7613(00)80461-6.

[73] S. M. Kaech, E. J. Wherry, and R. Ahmed, "Effector and memory T-cell differentiation: Implications for vaccine development," *Nat. Rev. Immunol.*, vol. 2, no. 4, pp. 251–262, 2002, doi: 10.1038/nri778.

[74] J. Jiao *et al.*, "Comparison of two commonly used methods for stimulating T cells," *Biotechnol. Lett.*, vol. 41, no. 12, pp. 1361–1371, 2019, doi: 10.1007/s10529-019-02743-w.

[75] Lemieszek, Marina B., S. D. Findlay, and G. M. Siegers, "CellTrace™ Violet Flow Cytometric Assay to Assess Cell Proliferation Proliferation," *Cancer Cell Biol. Methods Protoc.*, vol. Chapter 9, pp. 44–45, 2022.

[76] C. Binder *et al.*, "CD2 Immunobiology," *Front. Immunol.*, vol. 11, no. June, pp. 1–14, 2020, doi: 10.3389/fimmu.2020.01090.

[77] G. E. Moore, R. E. Gerner, and H. A. Franklin, "Culture of Normal Human Leukocytes," *JAMA J. Am. Med. Assoc.*, vol. 199, no. 8, pp. 519–524, 1967, doi: 10.1001/jama.1967.03120080053007.

[78] A. R. Medvec *et al.*, "Improved Expansion and In Vivo Function of Patient T Cells by a Serum-free Medium," *Mol. Ther. Methods Clin. Dev.*, vol. 8, no. March, pp. 65–74, 2018, doi: 10.1016/j.omtm.2017.11.001.

[79] R. Geiger *et al.*, "L-Arginine Modulates T Cell Metabolism and Enhances Survival and Anti-tumor Activity," *Cell*, vol. 167, no. 3, pp. 829-842.e13, 2016, doi: 10.1016/j.cell.2016.09.031.

[80] S. MacPherson *et al.*, "Clinically relevant T cell expansion media activate distinct metabolic programs uncoupled from cellular function," *Mol. Ther. Methods Clin. Dev.*, vol. 24, no. March, pp. 380–393, 2022, doi: 10.1016/j.omtm.2022.02.004.

[81] J. R. Cantor *et al.*, "Physiologic Medium Rewires Cellular Metabolism and Reveals Uric Acid as an Endogenous Inhibitor of UMP Synthase," *Cell*, vol. 169, no. 2, pp. 258-272.e17, 2017, doi: 10.1016/j.cell.2017.03.023.

[82] H. Gatla *et al.*, "Enabling Allogeneic T Cell-Based Therapies: Scalable Stirred-Tank Bioreactor Mediated Manufacturing," *Front. Med. Technol.*, vol. 4, no. May, pp. 1–15, 2022, doi: 10.3389/fmedt.2022.850565.

[83] X. Jiang *et al.*, "MRI of tumor T cell infiltration in response to checkpoint inhibitor therapy," *J. Immunother. cancer*, vol. 8, no. 1, pp. 4–8, 2020, doi: 10.1136/jitc-2019-000328.

[84] K. S. Sidhu, E. Amiel, R. C. Budd, and D. E. Matthews, "Determination of cell volume as part of metabolomics experiments," *Am. J. Physiol. - Cell Physiol.*, vol. 321, no. 6, pp. C947–C953, 2021, doi: 10.1152/AJPCELL.00613.2020.

[85] T. M. Villanueva-Cabello and I. Martinez-Duncker, "Preparation of CD4+ T cells for analysis of GD3 and GD2 ganglioside membrane expression by microscopy," *J. Vis. Exp.*, vol. 2016, no. 117, pp. 1–8, 2016, doi: 10.3791/54569.

[86] A. Ariel *et al.*, "IL-2 Induces T Cell Adherence to Extracellular Matrix: Inhibition of Adherence and Migration by IL-2 Peptides Generated by Leukocyte Elastase," *J. Immunol.*, vol. 161, no. 5, pp. 2465–2472, 1998, doi: 10.4049/jimmunol.161.5.2465.

[87] K. I. Jankowska *et al.*, "Integrins modulate T cell receptor signaling by constraining actin flow at the immunological synapse," *Front. Immunol.*, vol. 9, no. JAN, pp. 1–19, 2018, doi: 10.3389/fimmu.2018.00025.

[88] A. Sadoun *et al.*, "Controlling T cells spreading, mechanics and activation by micropatterning," *Sci. Rep.*, vol. 11, no. 1, pp. 1–15, 2021, doi: 10.1038/s41598-021-86133-1.

[89] M. H. Nelson *et al.*, "Identification of human CD4+T cell populations with distinct antitumor activity," *Sci. Adv.*, vol. 6, no. 27, pp. 1–10, 2020, doi: 10.1126/sciadv.aba7443.

[90] A. R. Korte and Y. J. Lee, "MALDI-MS analysis and imaging of small molecule metabolites with 1,5-diaminonaphthalene (DAN)," *J. Mass Spectrom.*, vol. 49, no. 8, pp. 737–741, 2014, doi: 10.1002/jms.3400.

[91] B. Wadie, L. Stuart, C. M. Rath, B. Drotleff, S. Mamedov, and T. Alexandrov, "METASPACE-ML: Metabolite annotation for imaging mass spectrometry using machine learning," *bioRxiv*, 2024, [Online]. Available: https://www.biorxiv.org/content/10.1101/2023.05.29.542736v2%0Ahttps://www.biorxiv.org/content/10.1101/2023.05.29.542736v2.abstract.

[92] A. Ponjavic *et al.*, "Single-Molecule Light-Sheet Imaging of Suspended T Cells," *Biophys. J.*, vol. 114, no. 9, pp. 2200–2211, 2018, doi: 10.1016/j.bpj.2018.02.044.

[93] M. Tsang, J. Gantchev, F. M. Ghazawi, and I. V. Litvinov, "Protocol for adhesion and immunostaining of lymphocytes and other non-adherent cells in culture," *Biotechniques*, vol. 63, no.

5, pp. 230–233, 2017, doi: 10.2144/000114610.

[94] J. Wang *et al.*, "MALDI-TOF MS imaging of metabolites with a N -(1-Naphthyl) ethylenediamine dihydrochloride matrix and its application to colorectal cancer liver metastasis," *Anal. Chem.*, vol. 87, no. 1, pp. 422–430, 2015, doi: 10.1021/ac504294s.

[95] Q. Ma, Y. Wang, A. S. Y. Lo, E. M. Gomes, and R. P. Junghans, "Cell density plays a critical role in ex vivo expansion of T cells for adoptive immunotherapy," *J. Biomed. Biotechnol.*, vol. 2010, 2010, doi: 10.1155/2010/386545.

[96] M. Takeichi and T. S. Okada, "Roles of magnesium and calcium ions in cell-to-substrate adhesion," *Exp. Cell Res.*, vol. 74, no. 1, pp. 51–60, 1972, doi: 10.1016/0014-4827(72)90480-6.

[97] M. Strazza, I. Azoulay-Alfaguter, A. Pedoeem, and A. Mor, "Static adhesion assay for the study of integrin activation in T lymphocytes," *J. Vis. Exp.*, no. 88, pp. 1–5, 2014, doi: 10.3791/51646.

[98] B. S. Kong, C. Lee, and Y. M. Cho, "Protocol for the assessment of human T cell activation by real-time metabolic flux analysis," *STAR Protoc.*, vol. 3, no. 1, p. 101084, 2022, doi: 10.1016/j.xpro.2021.101084.

[99] B. K. Lundholt, K. M. Scudder, and L. Pagliaro, "A simple technique for reducing edge effect in cell-based assays," *J. Biomol. Screen.*, vol. 8, no. 5, pp. 566–570, 2003, doi: 10.1177/1087057103256465.

[100] M. Babič *et al.*, "Poly(L-lysine)-modified iron oxide nanoparticles for stem cell labeling," *Bioconjug. Chem.*, vol. 19, no. 3, pp. 740–750, 2008, doi: 10.1021/bc700410z.

[101] Z. Qiao and F. Lissel, "MALDI Matrices for the Analysis of Low Molecular Weight Compounds: Rational Design, Challenges and Perspectives," *Chem. - An Asian J.*, vol. 16, no. 8, pp. 868–878, 2021, doi: 10.1002/asia.202100044.

[102] R. Cheng, F. Zhang, M. Li, X. Wo, Y. W. Su, and W. Wang, "Influence of Fixation and Permeabilization on the Mass Density of Single Cells: A Surface Plasmon Resonance Imaging Study," *Front. Chem.*, vol. 7, no. August, pp. 1–7, 2019, doi: 10.3389/fchem.2019.00588.

[103] H. Zhao *et al.*, "Dual-Ion-Mode MALDI MS Detection of Small Molecules with the O-P,N-Doped Carbon/Graphene Matrix," *ACS Appl. Mater. Interfaces*, vol. 10, no. 43, pp. 37732–37742, 2018, doi: 10.1021/acsami.8b14643.

[104] K. Chen, D. Baluya, M. Tosun, F. Li, and M. Maletic-Savatic, "Imaging mass spectrometry: A new tool to assess molecular underpinnings of neurodegeneration," *Metabolites*, vol. 9, no. 7, 2019, doi: 10.3390/metabo9070135.

[105] C. Keller *et al.*, "Comparison of Vacuum MALDI and AP-MALDI Platforms for the Mass Spectrometry Imaging of Metabolites Involved in Salt Stress in Medicago truncatula," *Front. Plant Sci.*, vol. 9, no. August, pp. 1–15, 2018, doi: 10.3389/fpls.2018.01238.

[106] S. Banerjee and R. N. Zare, "Influence of Inlet Capillary Temperature on the Microdroplet Chemistry Studied by Mass Spectrometry," *J. Phys. Chem. A*, vol. 123, no. 36, pp. 7704–7709, 2019, doi: 10.1021/acs.jpca.9b05703.

[107] R. R. Roiffé *et al.*, "Development of a sensitive and fast method for detection of catecholamines and metabolites by HRMS," *Microchem. J.*, vol. 150, no. August, p. 104173, 2019, doi: 10.1016/j.microc.2019.104173.

[108] F. Hillenkamp and M. Karas, "The MALDI Process and Method," *MALDI MS A Pract. Guid. to Instrumentation, Methods Appl.*, pp. 1–28, 2007, doi: 10.1002/9783527610464.ch1.

[109] S. J. Wetzel, C. M. Guttman, and J. E. Girard, "The influence of matrix and laser energy on the molecular mass distribution of synthetic polymers obtained by MALDI-TOF-MS," *Int. J. Mass Spectrom.*, vol. 238, no. 3 SPEC. ISS., pp. 215–225, 2004, doi: 10.1016/j.ijms.2004.04.019.

[110] M. Tuck, F. Grélard, L. Blanc, and N. Desbenoit, "MALDI-MSI Towards Multimodal Imaging: Challenges and Perspectives," *Front. Chem.*, vol. 10, no. May, pp. 1–11, 2022, doi: 10.3389/fchem.2022.904688.

[111] V. Saharuka *et al.*, "Large-Scale Evaluation of Spatial Metabolomics Protocols and Technologies,"

bioRxiv, p. 2024.01.29.577354, 2024, [Online]. Available: https://www.biorxiv.org/content/10.1101/2024.01.29.577354v1%0Ahttps://www.biorxiv.org/content/10.1101/2024.01.29.577354v1.abstract.

[112] B. Sarvin *et al.*, "Fast and sensitive flow-injection mass spectrometry metabolomics by analyzing sample-specific ion distributions," *Nat. Commun.*, vol. 11, no. 1, pp. 1–11, 2020, doi: 10.1038/s41467-020-17026-6.

[113] S. Sah *et al.*, "Targeted Microchip Capillary Electrophoresis-Orbitrap Mass Spectrometry Metabolomics to Monitor Ovarian Cancer Progression," *Metabolites*, vol. 12, no. 6, pp. 1–14, 2022, doi: 10.3390/metabo12060532.

[114] R. T. Steven *et al.*, "Atmospheric-Pressure Infrared Laser-Ablation Plasma-Postionization Mass Spectrometry Imaging of Formalin-Fixed Paraffin-Embedded (FFPE) and Fresh-Frozen Tissue Sections with No Sample Preparation," *Anal. Chem.*, vol. 94, no. 28, pp. 9970–9974, 2022, doi: 10.1021/acs.analchem.2c00690.

[115] C. C. J. Fitzgerald *et al.*, "Profiling Urinary Sulfate Metabolites With Mass Spectrometry," *Front. Mol. Biosci.*, vol. 9, no. February, pp. 1–14, 2022, doi: 10.3389/fmolb.2022.829511.

[116] T. Porta, A. Lesur, E. Varesio, and G. Hopfgartner, "Quantification in MALDI-MS imaging: what can we learn from MALDI-selected reaction monitoring and what can we expect for imaging?," *Anal. Bioanal. Chem.*, vol. 407, no. 8, pp. 2177–2187, 2015, doi: 10.1007/s00216-014-8315-5.

[117] S. Laugesen and P. Roepstorff, "Combination of two matrices results in improved performance of MALDI MS for peptide mass mapping and protein analysis," *J. Am. Soc. Mass Spectrom.*, vol. 14, no. 9, pp. 992–1002, 2003, doi: 10.1016/S1044-0305(03)00262-9.

[118] M. Šebela, "Solid mixed matrices and their advantages in matrix- assisted laser desorption / ionisation time-of-flight mass spectrometry," *Spectrosc. Eur.*, vol. 28, no. 1, pp. 10–14, 2016.

[119] M. Laštovičková, J. Chmelik, and J. Bobalova, "The combination of simple MALDI matrices for the improvement of intact glycoproteins and glycans analysis," *Int. J. Mass Spectrom.*, vol. 281, no. 1–2, pp. 82–88, 2009, doi: 10.1016/j.ijms.2008.12.017.

[120] S. R. Shanta *et al.*, "A new combination MALDI matrix for small molecule analysis: Application to imaging mass spectrometry for drugs and metabolites," *Analyst*, vol. 137, no. 24, pp. 5757–5762, 2012, doi: 10.1039/c2an35782h.

[121] M. Bianco *et al.*, "Development of a New Binary Matrix for the Comprehensive Analysis of Lipids and Pigments in Micro- and Macroalgae Using MALDI-ToF/ToF Mass Spectrometry," *Int. J. Mol. Sci.*, vol. 25, no. 11, 2024, doi: 10.3390/ijms25115919.

[122] L. A. J. O'Neill, R. J. Kishton, and J. Rathmell, "A guide to immunometabolism for immunologists," *Nat. Rev. Immunol.*, vol. 16, pp. 553–565, 2016, doi: 10.1038/nri.2016.70.

[123] J. N. Koberstein *et al.*, "Monitoring glycolytic dynamics in single cells using a fluorescent biosensor for fructose 1,6-bisphosphate," *Proc. Natl. Acad. Sci. U. S. A.*, vol. 119, no. 31, pp. 1–8, 2022, doi: 10.1073/pnas.2204407119.

[124] G. J. W. van der Windt, C. H. Chang, and E. L. Pearce, "Measuring bioenergetics in T cells using a seahorse extracellular flux analyzer," *Curr. Protoc. Immunol.*, vol. 2016, pp. 3.16B.1-3.16B.14, 2016, doi: 10.1002/0471142735.im0316bs113.

[125] R. L. Aft, F. W. Zhang, and D. Gius, "Evaluation of 2-deoxy-D-glucose as a chemotherapeutic agent: Mechanism of cell death," *Br. J. Cancer*, vol. 87, no. 7, pp. 805–812, 2002, doi: 10.1038/sj.bjc.6600547.

[126] C. S. Pereira, M. H. Teixeira, D. A. Russell, J. Hirst, and G. M. Arantes, "Mechanism of rotenone binding to respiratory complex I depends on ligand flexibility," *Sci. Rep.*, vol. 13, no. 1, pp. 1–9, 2023, doi: 10.1038/s41598-023-33333-6.

[127] E. Goetzman, Z. Gong, B. Zhang, and R. Muzumdar, "Complex II Biology in Aging, Health, and Disease," *Antioxidants*, vol. 12, no. 7, pp. 1–11, 2023, doi: 10.3390/antiox12071477.

[128] M. Ogita, A. Ogita, Y. Usuki, K. I. Fujita, and T. Tanaka, "Antimycin A-induced cell death depends on AIF translocation through NO production and PARP activation and is not involved in ROS generation, cytochrome c release and caspase-3 activation in HL-60 cells," *J. Antibiot. (Tokyo).*, vol. 62, no. 3, pp. 145–152, 2009, doi: 10.1038/ja.2009.2.

[129] J. Symersky, D. Osowski, D. E. Walters, and D. M. Mueller, "Oligomycin frames a common drug-binding site in the ATP synthase," *Proc. Natl. Acad. Sci. U. S. A.*, vol. 109, no. 35, pp. 13961–13965, 2012, doi: 10.1073/pnas.1207912109.

[130] B. Plitzko and S. Loesgen, "Measurement of Oxygen Consumption Rate (OCR) and Extracellular Acidification Rate (ECAR) in Culture Cells for Assessment of the Energy Metabolism," *Bio-Protocol*, vol. 8, no. 10, pp. 1–13, 2018, doi: 10.21769/bioprotoc.2850.

[131] M. Y. Ng, Z. J. Song, C. H. Tan, M. Bassetto, and T. Hagen, "Structural investigations on the mitochondrial uncouplers niclosamide and FCCP," *FEBS Open Bio*, vol. 14, pp. 1057–1071, 2024, doi: 10.1002/2211-5463.13817.

[132] K. Renner *et al.*, "Metabolic plasticity of human T cells: Preserved cytokine production under glucose deprivation or mitochondrial restriction, but 2-deoxy-glucose affects effector functions," *Eur. J. Immunol.*, vol. 45, no. 9, pp. 2504–2516, 2015, doi: 10.1002/eji.201545473.

[133] C. H. Chang *et al.*, "Posttranscriptional control of T cell effector function by aerobic glycolysis," *Cell*, vol. 153, no. 6, p. 1239, 2013, doi: 10.1016/j.cell.2013.05.016.

[134] L. Holthaus, V. Sharma, D. Brandt, A. G. Ziegler, M. Jastroch, and E. Bonifacio, "Functional and metabolic fitness of human CD4+ T lymphocytes during metabolic stress," *Life Sci. Alliance*, vol. 4, no. 12, pp. 1–13, 2021, doi: 10.26508/lsa.202101013.

[135] N. Jones *et al.*, "Metabolic adaptation of human CD4+ and CD8+ T-cells to T-cell receptor-mediated stimulation," *Front. Immunol.*, vol. 8, no. NOV, p. 1516, Nov. 2017, doi: 10.3389/FIMMU.2017.01516/BIBTEX.

[136] R. E. Yanes, H. Zhang, Y. Shen, C. M. Weyand, and J. J. Goronzy, "Metabolic reprogramming in memory CD4 T cell responses of old adults," *Clin. Immunol.*, vol. 207, no. July, pp. 58–67, 2019, doi: 10.1016/j.clim.2019.07.003.

[137] A. V. Menk *et al.*, "Early TCR Signaling Induces Rapid Aerobic Glycolysis Enabling Distinct Acute T Cell Effector Functions," *Cell Rep.*, vol. 22, no. 6, pp. 1509–1521, 2018, doi: 10.1016/j.celrep.2018.01.040.

[138] H. Wu *et al.*, "Mitochondrial dysfunction promotes the transition of precursor to terminally exhausted T cells through HIF-1α-mediated glycolytic reprogramming," *Nat. Commun.*, vol. 14, no. 1, 2023, doi: 10.1038/s41467-023-42634-3.

[139] X. Chen, L. Kozhaya, C. Wang, L. Placek, E. Karhan, and D. Unutmaz, "Modulation of glucose metabolism by 2-Deoxy-D-Glucose (2DG) promotes IL-17 producing human T cell subsets," *bioRxiv*, p. 2022.03.13.484135, 2022, [Online]. Available: https://www.biorxiv.org/content/10.1101/2022.03.13.484135v2%0Ahttps://www.biorxiv.org/content/10.1101/2022.03.13.484135v2.abstract.

[140] S. A. Mookerjee, D. G. Nicholls, and M. D. Brand, "Determining maximum glycolytic capacity using extracellular flux measurements," *PLoS One*, vol. 11, no. 3, pp. 1–20, 2016, doi: 10.1371/journal.pone.0152016.

[141] Y. Darzi, I. Letunic, P. Bork, and T. Yamada, "IPath3.0: Interactive pathways explorer v3," *Nucleic Acids Res.*, vol. 46, no. W1, pp. W510–W513, 2018, doi: 10.1093/nar/gky299.

[142] M. D. Luecken and F. J. Theis, "Current best practices in single-cell RNA-seq analysis: a tutorial," *Mol. Syst. Biol.*, vol. 15, no. 6, 2019, doi: 10.15252/msb.20188746.

[143] V. A. Traag, L. Waltman, and N. J. van Eck, "From Louvain to Leiden: guaranteeing well-connected communities," *Sci. Rep.*, vol. 9, no. 1, pp. 1–12, 2019, doi: 10.1038/s41598-019-41695-z.

[144] R. Satija, J. A. Farrell, D. Gennert, A. F. Schier, and A. Regev, "Spatial reconstruction of single-cell gene expression data," *Nat. Biotechnol.*, vol. 33, no. 5, pp. 495–502, 2015, doi: 10.1038/nbt.3192.

[145] L. Heumos *et al.*, “Best practices for single-cell analysis across modalities,” *Nat. Rev. Genet.*, vol. 24, no. 8, pp. 550–572, 2023, doi: 10.1038/s41576-023-00586-w.

[146] X. Zhu, T. K. Wolfgruber, A. Tasato, C. Arisdakessian, D. G. Garmire, and L. X. Garmire, “Granatum: A graphical single-cell RNA-Seq analysis pipeline for genomics scientists,” *Genome Med.*, vol. 9, no. 1, pp. 1–12, 2017, doi: 10.1186/s13073-017-0492-3.

[147] X. Chen, B. Zhang, T. Wang, A. Bonni, and G. Zhao, “Robust principal component analysis for accurate outlier sample detection in RNA-Seq data,” *BMC Bioinformatics*, vol. 21, no. 1, pp. 1–20, 2020, doi: 10.1186/s12859-020-03608-0.

[148] I. T. Jollife and J. Cadima, “Principal component analysis: A review and recent developments,” *Philos. Trans. R. Soc. A Math. Phys. Eng. Sci.*, vol. 374, no. 2065, 2016, doi: 10.1098/rsta.2015.0202.

[149] P. J. Rousseeuw, “Silhouettes: A graphical aid to the interpretation and validation of cluster analysis,” *J. Comput. Appl. Math.*, vol. 20, no. C, pp. 53–65, 1987, doi: 10.1016/0377-0427(87)90125-7.

[150] L. J. Salomon, J. P. Bernard, and Y. Ville, “Analysis of Z-score distribution for the quality control of fetal ultrasound measurements at 20-24 weeks,” *Ultrasound Obstet. Gynecol.*, vol. 26, no. 7, pp. 750–754, 2005, doi: 10.1002/uog.2640.

[151] J. W. Squair *et al.*, “Confronting false discoveries in single-cell differential expression,” *Nat. Commun.*, vol. 12, no. 1, 2021, doi: 10.1038/s41467-021-25960-2.

[152] M. Schneider, E. Al-Shareffi, and R. S. Haltiwanger, “Biological functions of fucose in mammals,” *Glycobiology*, vol. 27, no. 7, pp. 601–618, 2017, doi: 10.1093/glycob/cwx034.

[153] PubChem, “PubChem Compound Summary for CID 46936435, 2-Deoxy-glucose-6-phosphate,” *National Center for Biotechnology Information*. https://pubchem.ncbi.nlm.nih.gov/compound/46936435 (accessed Jul. 18, 2024).

[154] R. L. Levine, N. J. Hoogenraad, and N. Kretchmer, “A review: Biological and clinical aspects of pyrimidine metabolism,” *Pediatr. Res.*, vol. 8, no. 7, pp. 724–734, 1974, doi: 10.1203/00006450-197407000-00008.

[155] X. Du and H. Hu, “The Roles of 2-Hydroxyglutarate,” *Front. Cell Dev. Biol.*, vol. 9, no. March, pp. 1–13, 2021, doi: 10.3389/fcell.2021.651317.

[156] W. M. Oldham, C. B. Clish, Y. Yang, and J. Loscalzo, “Hypoxia-Mediated Increases in l-2-hydroxyglutarate Coordinate the Metabolic Response to Reductive Stress,” *Cell Metab.*, vol. 22, no. 2, pp. 291–303, 2015, doi: 10.1016/j.cmet.2015.06.021.

[157] Y. Zhang *et al.*, “The Glutaminase-1 Inhibitor [11C-carbony]BPTES: Synthesis and Positron Emission Tomography Study in Mice,” *Pharmaceuticals*, vol. 16, no. 7, 2023, doi: 10.3390/ph16070963.

[158] B. Batchuluun, S. L. Pinkosky, and G. R. Steinberg, “Lipogenesis inhibitors: therapeutic opportunities and challenges,” *Nat. Rev. Drug Discov.*, vol. 21, no. 4, pp. 283–305, 2022, doi: 10.1038/s41573-021-00367-2.

[159] H. Fu *et al.*, “The glucose transporter 2 regulates CD8+ T cell function via environment sensing,” *Nat. Metab.*, vol. 5, no. 11, pp. 1969–1985, 2023, doi: 10.1038/s42255-023-00913-9.

[160] Z. Zhang, X. Deng, Y. Liu, Y. Liu, L. Sun, and F. Chen, “PKM2, function and expression and regulation,” *Cell Biosci.*, vol. 9, no. 1, pp. 1–25, 2019, doi: 10.1186/s13578-019-0317-8.

[161] C. Wang *et al.*, “MK8722, an AMPK activator, inhibiting carcinoma proliferation, invasion and migration in human pancreatic cancer cells,” *Biomed. Pharmacother.*, vol. 144, no. October, p. 112325, 2021, doi: 10.1016/j.biopha.2021.112325.

[162] E. H. Ma, M. C. Poffenberger, A. H. T. Wong, and R. G. Jones, “The role of AMPK in T cell metabolism and function,” *Curr. Opin. Immunol.*, vol. 46, pp. 45–52, 2017, doi: 10.1016/j.coi.2017.04.004.

[163] S. Daniele, G. Mangano, L. Durando, L. Ragni, and C. Martini, “The nootropic drug A-glyceryl-phosphoryl-ethanolamine exerts neuroprotective effects in human hippocampal cells,” *Int. J. Mol.*

Sci., vol. 21, no. 3, 2020, doi: 10.3390/ijms21030941.

[164] D. Corda, P. Zizza, A. Varone, K. S. Bruzik, and S. Mariggiò, "The glycerophosphoinositols and their cellular functions," *Biochem. Soc. Trans.*, vol. 40, no. 1, pp. 101–107, 2012, doi: 10.1042/BST20110679.

[165] O. A. C. Petroff, "GABA and glutamate in the human brain," *Neuroscientist*, vol. 8, no. 6, pp. 562–573, 2002, doi: 10.1177/1073858402238515.

[166] B. Raud *et al.*, "Etomoxir Actions on Regulatory and Memory T Cells Are Independent of Cpt1a-Mediated Fatty Acid Oxidation," *Cell Metab.*, vol. 28, no. 3, pp. 504-515.e7, 2018, doi: 10.1016/j.cmet.2018.06.002.

[167] E. Emberley *et al.*, "The glutaminase inhibitor telaglenastat enhances the antitumor activity of signal transduction inhibitors everolimus and cabozantinib in models of renal cell carcinoma," *PLoS One*, vol. 16, no. 11 November, pp. 1–20, 2021, doi: 10.1371/journal.pone.0259241.

[168] B. Emini Veseli, P. Van Wielendaele, M. Delibegovic, W. Martinet, and G. R. Y. De Meyer, "The PFKFB3 Inhibitor AZ67 Inhibits Angiogenesis Independently of Glycolysis Inhibition," *Int. J. Mol. Sci.*, vol. 22, no. 11, 2021, doi: 10.3390/ijms22115970.

[169] H. Zhu, Z. Jia, Y. R. Li, and I. Danelisen, "Molecular mechanisms of action of metformin: latest advances and therapeutic implications," *Clin. Exp. Med.*, vol. 23, no. 7, pp. 2941–2951, 2023, doi: 10.1007/s10238-023-01051-y.

[170] S. Oh, X. L. Mai, J. Kim, A. C. V. de Guzman, J. Y. Lee, and S. Park, "Glycerol 3-phosphate dehydrogenases (1 and 2) in cancer and other diseases," *Exp. Mol. Med.*, vol. 56, no. 5, pp. 1066–1079, 2024, doi: 10.1038/s12276-024-01222-1.

[171] A. P. Turner *et al.*, "Sirolimus enhances the magnitude and quality of viral-specific CD8 + T-cell responses to vaccinia virus vaccination in rhesus macaques," *Am. J. Transplant.*, vol. 11, no. 3, pp. 613–618, 2011, doi: 10.1111/j.1600-6143.2010.03407.x.

[172] H. Chi, "Regulation and function of mTOR signalling in T cell fate decisions," *Nat. Rev. Immunol.*, vol. 12, no. 5, pp. 325–338, 2012, doi: 10.1038/nri3198.

[173] Y. Tanaka, Y. Luo, J. J. O'Shea, and S. Nakayamada, "Janus kinase-targeting therapies in rheumatology: a mechanisms-based approach," *Nat. Rev. Rheumatol.*, vol. 18, no. 3, pp. 133–145, 2022, doi: 10.1038/s41584-021-00726-8.

[174] R. J. Salmond, "mTOR Regulation of Glycolytic Metabolism in T Cells," *Front. Cell Dev. Biol.*, vol. 6:122, 2018, doi: 10.3389/fcell.2018.00122.

[175] C. Di Dedda, D. Vignali, L. Piemonti, and P. Monti, "Pharmacological targeting of GLUT1 to control autoreactive T cell responses," *Int. J. Mol. Sci.*, vol. 20, no. 19, pp. 1–15, 2019, doi: 10.3390/ijms20194962.

[176] E. H. Ma *et al.*, "Serine Is an Essential Metabolite for Effector T Cell Expansion," *Cell Metab.*, vol. 25, no. 2, pp. 345–357, 2017, doi: 10.1016/j.cmet.2016.12.011.

[177] E. Mullarky *et al.*, "Identification of a small molecule inhibitor of 3-phosphoglycerate dehydrogenase to target serine biosynthesis in cancers," *Proc. Natl. Acad. Sci. U. S. A.*, vol. 113, no. 7, pp. 1778–1783, 2016, doi: 10.1073/pnas.1521548113.

[178] J. E. S. Kitchin, M. K. Pomeranz, G. Pak, K. Washenik, and J. L. Shupack, "Rediscovering mycophenolic acid: A review of its mechanism, side effects, and potential uses," *J. Am. Acad. Dermatol.*, vol. 37, no. 3 I, pp. 445–449, 1997, doi: 10.1016/S0190-9622(97)70147-6.

[179] L. Quéméneur, M. Flacher, L.-M. Gerland, M. Ffrench, J.-P. Revillard, and N. Bonnefoy-Berard, "Mycophenolic Acid Inhibits IL-2-Dependent T Cell Proliferation, But Not IL-2-Dependent Survival and Sensitization to Apoptosis," *J. Immunol.*, vol. 169, no. 5, pp. 2747–2755, 2002, doi: 10.4049/jimmunol.169.5.2747.

[180] D. Tedesco and L. Haragsim, "Cyclosporine: A Review," *J. Transplant.*, vol. 2012, pp. 1–7, 2012, doi: 10.1155/2012/230386.

[181] D. Paunovic *et al.*, "The potential roles of gossypol as anticancer agent: advances and future directions," *Chinese Med. (United Kingdom)*, vol. 18, no. 1, pp. 1–17, 2023, doi: 10.1186/s13020-023-00869-8.

[182] F. S. Menniti, T. A. Chappie, and C. J. Schmidt, "PDE10A Inhibitors—Clinical Failure or Window Into Antipsychotic Drug Action?," *Front. Neurosci.*, vol. 14, no. January, pp. 1–18, 2021, doi: 10.3389/fnins.2020.600178.

[183] B. Song *et al.*, "Gossypol suppresses mouse T lymphocytes via inhibition of NFκB, NFAT and AP-1 pathways," *Immunopharmacol. Immunotoxicol.*, vol. 35, no. 5, pp. 615–621, 2013, doi: 10.3109/08923973.2013.830126.

[184] B. N. Cronstein and T. M. Aune, "Methotrexate and its mechanisms of action in inflammatory arthritis," *Nat. Rev. Rheumatol.*, vol. 16, no. 3, pp. 145–154, 2020, doi: 10.1038/s41584-020-0373-9.

[185] B. Friedman and B. Cronstein, "Methotrexate mechanism in treatment of rheumatoid arthritis," *Jt. Bone Spine*, vol. 86, no. 3, pp. 301–307, 2019, doi: 10.1016/j.jbspin.2018.07.004.

[186] A. A. Khutornenko, V. V. Roudko, B. V. Chernyak, A. B. Vartapetian, P. M. Chumakov, and A. G. Evstafieva, "Pyrimidine biosynthesis links mitochondrial respiration to the p53 pathway," *Proc. Natl. Acad. Sci. U. S. A.*, vol. 107, no. 29, pp. 12828–12833, 2010, doi: 10.1073/pnas.0910885107.

[187] Y. Zhang *et al.*, "Inhibition of mitochondrial complex III induces differentiation in acute myeloid leukemia," *Biochem. Biophys. Res. Commun.*, vol. 547, pp. 162–168, 2021, doi: 10.1016/j.bbrc.2021.02.027.

[188] M. D. Luecken *et al.*, "Benchmarking atlas-level data integration in single-cell genomics," *Nat. Methods*, vol. 19, no. 1, pp. 41–50, 2022, doi: 10.1038/s41592-021-01336-8.

[189] S. Liu, S. Liao, L. Liang, J. Deng, and Y. Zhou, "The relationship between CD4+ T cell glycolysis and their functions," *Trends Endocrinol. Metab.*, vol. 34, no. 6, pp. 345–360, 2023, doi: 10.1016/j.tem.2023.03.006.

[190] R. S. O'Connor *et al.*, "The CPT1a inhibitor, etomoxir induces severe oxidative stress at commonly used concentrations," *Sci. Rep.*, vol. 8, no. 1, pp. 1–9, 2018, doi: 10.1038/s41598-018-24676-6.

[191] J. De los Santos-Jiménez *et al.*, "Metabolic Adjustments following Glutaminase Inhibition by CB-839 in Glioblastoma Cell Lines," *Cancers (Basel).*, vol. 15, no. 2, 2023, doi: 10.3390/cancers15020531.

[192] N. J. Mullen and P. K. Singh, "Nucleotide metabolism: a pan-cancer metabolic dependency," *Nat. Rev. Cancer*, vol. 23, no. 5, pp. 275–294, 2023, doi: 10.1038/s41568-023-00557-7.

[193] D. T. Tran, K. Sundararaj, C. Atkinson, and S. N. Nadig, "T-cell immunometabolism: Therapeutic implications in organ transplantation," *Transplantation*, vol. 105, no. 11, pp. E191–E201, 2021, doi: 10.1097/TP.0000000000003767.

[194] S. Kubo *et al.*, "Janus kinase inhibitor baricitinib modulates human innate and adaptive immune system," *Front. Immunol.*, vol. 9, no. JUN, pp. 1–11, 2018, doi: 10.3389/fimmu.2018.01510.

[195] I. Ben-Sahra, G. Hoxhaj, S. J. H. Ricoult, J. M. Asara, and B. D. Manning, "mTORC1 induces purine synthesis through control of the mitochondrial tetrahydrofolate cycle," *Science (80-.).*, vol. 351, no. 6274, pp. 728–733, Feb. 2016, doi: 10.1126/science.aad0489.

[196] A. Kumar, E. L. Yarosz, A. Andren, L. Zhang, C. A. Lyssiotis, and C. H. Chang, "NKT cells adopt a glutamine-addicted phenotype to regulate their homeostasis and function," *Cell Rep.*, vol. 41, no. 4, p. 111516, 2022, doi: 10.1016/j.celrep.2022.111516.

[197] R. Ke, Q. Xu, C. Li, L. Luo, and D. Huang, "Mechanisms of AMPK in the maintenance of ATP balance during energy metabolism," *Cell Biol. Int.*, vol. 42, no. 4, pp. 384–392, 2018, doi: 10.1002/cbin.10915.

[198] L. Wang *et al.*, "MK8722 initiates early-stage autophagy while inhibiting late-stage autophagy via FASN-dependent reprogramming of lipid metabolism," *Theranostics*, vol. 14, no. 1, pp. 75–95, 2024, doi: 10.7150/thno.83051.

[199] L. De Abreu Costa *et al.*, "Dimethyl sulfoxide (DMSO) decreases cell proliferation and TNF-α, IFN-, and IL-2 cytokines production in cultures of peripheral blood lymphocytes," *Molecules*, vol. 22, no. 11, pp. 1–10, 2017, doi: 10.3390/molecules22111789.

[200] R. Milanesi, P. Coccetti, and F. Tripodi, "The regulatory role of key metabolites in the control of cell signaling," *Biomolecules*, vol. 10, no. 6, 2020, doi: 10.3390/biom10060862.

[201] R. Wang *et al.*, "The Transcription Factor Myc Controls Metabolic Reprogramming upon T Lymphocyte Activation," *Immunity*, vol. 35, no. 6, pp. 871–882, 2011, doi: 10.1016/j.immuni.2011.09.021.

[202] S. Ricciardi *et al.*, "The Translational Machinery of Human CD4 + T Cells Is Poised for Activation and Controls the Switch from Quiescence to Metabolic Remodeling," *Cell Metab.*, vol. 28, no. 6, pp. 895-906.e5, 2018, doi: 10.1016/j.cmet.2018.08.009.

[203] E. L. Carr *et al.*, "Glutamine Uptake and Metabolism Are Coordinately Regulated by ERK/MAPK during T Lymphocyte Activation," *J. Immunol.*, vol. 185, pp. 1037–1044, 2010, doi: 10.4049/jimmunol.0903586.

[204] H. C. Hope, R. J. Brownlie, C. M. Fife, L. Steele, M. Lorger, and R. J. Salmond, "Coordination of asparagine uptake and asparagine synthetase expression modulates CD8+ T cell activation," *JCI Insight*, vol. 6, no. 9, 2021, doi: 10.1172/jci.insight.137761.

[205] H. C. Hope and R. J. Salmond, "The Role of Non-essential Amino Acids in T Cell Function and Anti-tumour Immunity," *Arch. Immunol. Ther. Exp. (Warsz).*, vol. 69, no. 1, pp. 1–9, 2021, doi: 10.1007/s00005-021-00633-6.

[206] T. W. Mak *et al.*, "Glutathione Primes T Cell Metabolism for Inflammation," *Immunity*, vol. 46, no. 4, pp. 675–689, 2017, doi: 10.1016/j.immuni.2017.03.019.

[207] P. Icard, M. Alifano, E. Donnadieu, and L. Simula, "Fructose-1,6-bisphosphate promotes PI3K and glycolysis in T cells?," *Trends Endocrinol. Metab.*, vol. 32, no. 8, pp. 540–543, 2021, doi: 10.1016/j.tem.2021.04.013.

[208] P. Icard *et al.*, "Understanding the central role of citrate in the metabolism of cancer cells and tumors: An update," *Int. J. Mol. Sci.*, vol. 22, no. 12, pp. 1–19, 2021, doi: 10.3390/ijms22126587.

[209] S. Baliou *et al.*, "Protective role of taurine against oxidative stress (Review)," *Mol. Med. Rep.*, vol. 24, no. 2, pp. 1–19, 2021, doi: 10.3892/mmr.2021.12242.

[210] Y. Ping *et al.*, "Taurine enhances the antitumor efficacy of PD-1 antibody by boosting CD8+ T cell function," *Cancer Immunol. Immunother.*, vol. 72, no. 4, pp. 1015–1027, 2023, doi: 10.1007/s00262-022-03308-z.

[211] S. Y. Tan, Y. Kelkar, A. Hadjipanayis, A. Shipstone, T. A. Wynn, and J. P. Hall, "Metformin and 2-Deoxyglucose Collaboratively Suppress Human CD4+ T Cell Effector Functions and Activation-Induced Metabolic Reprogramming," *J. Immunol.*, vol. 205, no. 4, pp. 957–967, 2020, doi: 10.4049/jimmunol.2000137.

[212] K. Urakami, V. Zangiacomi, K. Yamaguchi, and M. Kusuhara, "Impact of 2-deoxy-D-glucose on the target metabolome profile of a human endometrial cancer cell line," *Biomed. Res.*, vol. 34, no. 5, pp. 221–229, 2013, doi: 10.2220/biomedres.34.221.

[213] A. Stincone *et al.*, "The return of metabolism: Biochemistry and physiology of the pentose phosphate pathway," *Biol. Rev.*, vol. 90, no. 3, pp. 927–963, 2015, doi: 10.1111/brv.12140.

[214] Z. Sener, F. H. Cederkvist, R. Volchenkov, H. L. Holen, and B. S. Skålhegg, "T helper cell activation and expansion is sensitive to glutaminase inhibition under both hypoxic and normoxic conditions," *PLoS One*, vol. 11, no. 7, pp. 1–18, 2016, doi: 10.1371/journal.pone.0160291.

[215] Y. Zhou *et al.*, "DHODH and cancer: promising prospects to be explored," *Cancer Metab.*, vol. 9, no. 1, pp. 1–25, 2021, doi: 10.1186/s40170-021-00250-z.

[216] W. H. Park and B. R. You, "Antimycin A induces death of the human pulmonary fibroblast cells via ROS increase and GSH depletion," *Int. J. Oncol.*, vol. 48, no. 2, pp. 813–820, 2016, doi:

10.3892/ijo.2015.3276.

[217] N. E. Scharping *et al.*, "Mitochondrial stress induced by continuous stimulation under hypoxia rapidly drives T cell exhaustion," *Nat. Immunol.*, vol. 22, no. 2, pp. 205–215, 2021, doi: 10.1038/s41590-020-00834-9.

[218] A. N. Sexauer *et al.*, "DHODH: a promising target in the treatment of T-cell acute lymphoblastic leukemia," *Blood Adv.*, vol. 7, no. 21, pp. 6685–6701, 2023, doi: 10.1182/bloodadvances.2023010337.

[219] G. R. Steinberg and D. Carling, "AMP-activated protein kinase: the current landscape for drug development," *Nat. Rev. Drug Discov.*, vol. 18, no. 7, pp. 527–551, 2019, doi: 10.1038/s41573-019-0019-2.

[220] M. A. Zabielska, T. Borkowski, E. M. Slominska, and R. T. Smolenski, "Inhibition of AMP deaminase as therapeutic target in cardiovascular pathology," *Pharmacol. Reports*, vol. 67, no. 4, pp. 682–688, 2015, doi: 10.1016/j.pharep.2015.04.007.

[221] K. Davidsen, J. S. Marvin, A. Aggarwal, T. A. Brown, and L. B. Sullivan, "An engineered biosensor enables dynamic aspartate measurements in living cells," *Elife*, vol. 12, 2024, doi: 10.7554/eLife.90024.

[222] C. V. Iancu, Y. Zhou, T. Borza, H. J. Fromm, and R. B. Honzatko, "Cavitation as a mechanism of substrate discrimination by adenylosuccinate synthetases," *Biochemistry*, vol. 45, no. 38, pp. 11703–11711, 2006, doi: 10.1021/bi0607498.

[223] X. Feng, X. Li, N. Liu, N. Hou, X. Sun, and Y. Liu, "Glutaminolysis and CD4+ T-cell metabolism in autoimmunity: From pathogenesis to therapy prospects," *Front. Immunol.*, vol. 13, no. September, pp. 1–12, 2022, doi: 10.3389/fimmu.2022.986847.

[224] G. A. Nagana Gowda *et al.*, "A Metabolomics Study of BPTES Altered Metabolism in Human Breast Cancer Cell Lines," *Front. Mol. Biosci.*, vol. 5, no. May, pp. 1–13, 2018, doi: 10.3389/fmolb.2018.00049.

[225] C. A. Schoonjans *et al.*, "Targeting endothelial cell metabolism by inhibition of pyruvate dehydrogenase kinase and glutaminase-1," *J. Clin. Med.*, vol. 9, no. 10, pp. 1–14, 2020, doi: 10.3390/jcm9103308.

[226] P. K. Arnold and L. W. S. Finley, "Regulation and function of the mammalian tricarboxylic acid cycle," *J. Biol. Chem.*, vol. 299, no. 2, p. 102838, 2023, doi: 10.1016/j.jbc.2022.102838.

[227] M. Angela *et al.*, "Fatty acid metabolic reprogramming via mTOR-mediated inductions of PPARγ directs early activation of T cells," *Nat. Commun.*, vol. 7, pp. 1–15, 2016, doi: 10.1038/ncomms13683.

[228] E. Possik *et al.*, "New Mammalian Glycerol-3-Phosphate Phosphatase: Role in β-Cell, Liver and Adipocyte Metabolism," *Front. Endocrinol. (Lausanne).*, vol. 12, no. July, pp. 1–9, 2021, doi: 10.3389/fendo.2021.706607.

[229] V. Pareek, A. M. Pedley, and S. J. Benkovic, "Human de novo purine biosynthesis," *Crit. Rev. Biochem. Mol. Biol.*, vol. 56, no. 1, pp. 1–16, 2021, doi: 10.1080/10409238.2020.1832438.

[230] V. Lamba, K. Sangkuhl, K. Sanghavi, A. Fish, R. B. Altman, and T. E. Klein, "PharmGKB summary: mycophenolic acid pathway," *Pharmacogenet. Genomics*, vol. 24, no. 1, pp. 73–79, 2014, doi: 10.1097/FPC.0000000000000010.

[231] A. A. Fernández-Ramos *et al.*, "A comprehensive characterization of the impact of mycophenolic acid on the metabolism of Jurkat T cells," *Sci. Rep.*, vol. 7, no. 1, pp. 1–11, 2017, doi: 10.1038/s41598-017-10338-6.

[232] T. Kawaguchi, R. L. Veech, and K. Uyeda, "Regulation of energy metabolism in macrophages during hypoxia: Roles of fructose 2,6-bisphosphate and ribose 1,5-bisphosphate," *J. Biol. Chem.*, vol. 276, no. 30, pp. 28554–28561, 2001, doi: 10.1074/jbc.M101396200.

[233] R. Cartes-vel, B. Antilef, S. Sanhueza, L. Lamperti, M. Gonz, and E. Nova-lamperti, "Metformin

Restrains the Proliferation of CD4 + T Lymphocytes by Inducing Cell Cycle Arrest in Normo- and Hyperglycemic Conditions," 2024.

[234] S. Andrzejewski, S.-P. Gravel, M. Pollak, and J. St-Pierre, "Metformin directly acts on mitochondria to alter cellular bioenergetics," *Cancer Metab.*, vol. 2, no. 1, pp. 1–14, 2014, doi: 10.1186/2049-3002-2-12.

[235] X. Liu, I. L. Romero, L. M. Litchfield, E. Lengyel, and J. W. Locasale, "Metformin Targets Central Carbon Metabolism and Reveals Mitochondrial Requirements in Human Cancers," *Cell Metab.*, vol. 24, no. 5, pp. 728–739, 2016, doi: 10.1016/j.cmet.2016.09.005.

[236] S. Saladini *et al.*, "Metformin impairs glutamine metabolism and autophagy in tumour cells," *Cells*, vol. 8, no. 1, 2019, doi: 10.3390/cells8010049.

[237] A. S. Krall *et al.*, "Asparagine couples mitochondrial respiration to ATF4 activity and tumor growth," *Cell Metab.*, vol. 33, no. 5, pp. 1013-1026.e6, 2021, doi: 10.1016/j.cmet.2021.02.001.

[238] K. W. Brudvik and K. Taskén, "Modulation of T cell immune functions by the prostaglandin E 2 - CAMP pathway in chronic inflammatory states," *Br. J. Pharmacol.*, vol. 166, no. 2, pp. 411–419, 2012, doi: 10.1111/j.1476-5381.2011.01800.x.

[239] A. Csibi *et al.*, "The mTORC1 pathway stimulates glutamine metabolism and cell proliferation by repressing SIRT4," *Cell*, vol. 153, no. 4, pp. 840–854, 2013, doi: 10.1016/j.cell.2013.04.023.

[240] P. Kvacskay *et al.*, "Increase of aerobic glycolysis mediated by activated T helper cells drives synovial fibroblasts towards an inflammatory phenotype: new targets for therapy?," *Arthritis Res. Ther.*, vol. 23, no. 1, pp. 1–15, 2021, doi: 10.1186/s13075-021-02437-7.

[241] C. Flores, G. Fouquet, I. C. Moura, T. T. Maciel, and O. Hermine, "Lessons to learn from low-dose cyclosporin-A: A new approach for unexpected clinical applications," *Front. Immunol.*, vol. 10, no. MAR, pp. 1–7, 2019, doi: 10.3389/fimmu.2019.00588.

[242] J. Lee, "Use of antioxidants to prevent cyclosporine a toxicity," *Toxicol. Res.*, vol. 26, no. 3, pp. 163–170, 2013, doi: 10.5487/TR.2010.26.3.163.

[243] H. De Vitto, D. B. Arachchige, B. C. Richardson, and J. B. French, "The intersection of purine and mitochondrial metabolism in cancer," *Cells*, vol. 10, no. 10, pp. 1–16, 2021, doi: 10.3390/cells10102603.

[244] L. I. Mambelli *et al.*, "Phosphoethanolamine induces caspase-independent cell death by reducing the expression of C-RAF and inhibits tumor growth in human melanoma model," *Biomed. Pharmacother.*, vol. 103, no. November 2017, pp. 18–28, 2018, doi: 10.1016/j.biopha.2018.03.135.

[245] E. Calzada, O. Onguka, and S. M. Claypool, *Phosphatidylethanolamine Metabolism in Health and Disease*, vol. 321. Elsevier Inc., 2016.

[246] C. Ma *et al.*, "Upregulated ethanolamine phospholipid synthesis via selenoprotein I is required for effective metabolic reprogramming during T cell activation," *Mol. Metab.*, vol. 47, no. January, p. 101170, 2021, doi: 10.1016/j.molmet.2021.101170.

[247] B. S. R. Claes *et al.*, "MALDI-IHC-Guided In-Depth Spatial Proteomics: Targeted and Untargeted MSI Combined," *Anal. Chem.*, vol. 95, no. 4, pp. 2329–2338, 2023, doi: 10.1021/acs.analchem.2c04220.

[248] M. K. Williamson *et al.*, "Upregulation of glucose uptake and hexokinase activity of primary human CD4+ T cells in response to infection with HIV-1," *Viruses*, vol. 10, no. 3, 2018, doi: 10.3390/v10030114.

APPENDICES

Appendix A

Composition of the curated database used to annotate the single-cell data presented in this dissertation. The information provided here includes all molecular formulas, the candidate molecules reported by METASPACE and the chosen molecules ones to report.

Molecular Formula	Candidate Molecules	Selected Molecule
C10H12N2O3	4-Aminobenzoyl-(beta)-alanine, Formyl-5-hydroxykynurenamine, L-Kynurenine	Kynurenine
C10H12N4O6	Xanthosine	Xanthosine
C10H12N5O5P	3',5'-Cyclic dAMP	3',5'-Cyclic dAMP
C10H12N5O6P	Adenosine 2',3'-cyclic phosphate, Cyclic AMP	Cyclic AMP
C10H12N5O7P	Cyclic GMP, Guanosine 2',3'-cyclic phosphate	Cyclic GMP
C10H13N4O8P	INOSINE-MONOPHOSPHATE, Inosine 2'-phosphate, Inosinic acid	Inosine monophosphate
C10H13N5O4	Adenosine, Deoxyguanosine, Vidarabine, Zidovudine	Adenosine
C10H13N5O5	8-Hydroxy-deoxyguanosine, Guanosine	Guanosine
C10H14N5O6P	Deoxyadenosine monophosphate	Deoxyadenosine monophosphate
C10H14N5O7P	2'-Deoxyguanosine 5'-monophosphate, 2-hydroxy-dAMP, 3'-AMP, Adenosine 2'-phosphate, Adenosine monophosphate, DEOXYGUANOSINE-MONOPHOSPHATE	Adenosine monophosphate
C10H14N5O8P	8-Oxo-dGMP, Cyclic pyranopterin monophosphate, Guanosine monophosphate	Guanosine monophosphate
C10H15N2O8P	5-Thymidylic acid	Thymidine monophosphate

C10H16O2	(+/-)-2-(5-Methyl-5-vinyltetrahydrofuran-2-yl)propionaldehyde, (+/-)-Dihydromintlactone, (-)-(Z)-Tetrahydro-6-(2-pentenyl)-2H-pyran-2-one, (xi)-(Z)-5-(3-Hexenyl)dihydro-2(3H)-furanone, 2,4-Hexadienyl butyrate, 2,4-Hexadienyl isobutyrate, 4-Isopropyl-3-cyclohexene-1-carboxylic acid, 5,6-Dihydro-6-pentyl-2H-pyran-2-one, 6-Hydroxy-2,6-dimethyl-2,7-octadien-4-one, Ascaridole, Dihydronepetalactone, Epoxyartemisia ketone, Epoxycampholenic aldehyde, Ethyl (4Z)-4,7-octadienoate, Geranic acid, Methyl octynecarboxylate, cis-3-Hexenyl crotonate, gamma-Diosphenol, trans-4,5-epoxy-2(E)-decenal, xi-1,8,8-Trimethyl-2-oxabicyclo[3.2.1]octan-3-one	2,4-Hexadienyl butyrate
C10H17N3O6	Glutaminylglutamic acid, Glutamylglutamine, N-gamma-Glutamylglutamine, N2-gamma-Glutamylglutamine, Norophthalmic acid	Norophthalmic acid
C10H17N3O6S	Glutathione	Glutathione
C10H18O2	(+)-6-Hydroxy-2,6-dimethyl-7-octen-4-one, (E)-3-(Tetrahydro-5,5-dimethyl-2-furanyl)-2-buten-1-ol, (S,E)-2,6-Dimethyl-5,7-octadiene-2,3-diol, (\u00b1)-6-Methyl-5-hepten-2-yl acetate, (\u00b1)-cis-Linalyl oxide, (\u00b1)-trans-Linalyl oxide, 1-Cyclopropyl-4-methyl-1,3-cyclohexanediol, 1-Octen-3-yl acetate, 2,6-Dimethyl-3,7-octadiene-2,6-diol, 2-Exo-hydroxy-1,8-cineole, 2-Hexenyl butanoate, 2-Hydroxycineol, 2-Methylbutyl 3-methyl-2-butenoate, 2-Octenyl acetate, 2-Propenyl heptanoate, 3-Decenoic acid, 3-Methyl-2,4-nonanedione, 4-Hydroxy-2,6-dimethyl-7-octen-3-one, 5-Decenoic acid, 5Z-Octenyl acetate, 6-Decanolide, 6-Decenoic acid, 8-Methylnonenoate, 9-Decenoic acid, 9-Hydroxygeraniol, Citronellic acid, Cnidiol C, Cyclohexyl butanoate, Cyclohexylethyl acetate, Ethyl (E)-2-octenoate, Ethyl 3-octenoate, Ethyl 4Z-octenoate, Hexyl crotonate, Isopentyl 3-methyl-2-butenoate, Lilac alcohol, Linalool oxide (trans-pyranoid), Linalool oxide III, Linalyl oxide, Menthone lactone, Methyl (xi)-3-nonenoate, Methyl 2-nonenoate, cis-3-Hexenyl butyrate, cis-3-Hexenyl isobutyrate, cis-4-Decenoic acid, delta-Decalactone, trans-Dec-2-enoic acid, trans-p-Menth-2-ene-1,4-diol, xi-5-Hexyldihydro-2(3H)-furanone, xi-Tetrahydro-3-pentyl-2H-pyran-2-one	8-Methylnonenoate

C10H20O2	(1R,2S,3S,4R)-p-Menthane-2,3-diol, (1S,3R,4R)-p-Menthane-1,3-diol, (2S)-2-Ethylhexyl acetate, (Z)-1-(1-Ethoxyethoxy)-3-hexene, (\u00b1)-3-Octyl acetate, 1,1-Diethoxy-2-hexene, 1-Methylethyl heptanoic acid, 2,6-Dimethyl-7-octene-2,6-diol, 2-Methylbutyl 2-methylbutanoate, 2-Methylbutyl 3-methylbutanoate, 2-Methylpropyl hexanoate, 3-Methylbutyl 2-methylbutanoate, 3-Methylbutyl pentanoate, 4-Ethyloctanoic acid, 4-Methylnonanoic acid, 7-Hydroxy-3,7-dimethyloctanal, Acetaldehyde 1,3-octanediol acetal, Butyl hexanoate, Capric acid, Ethyl 2-ethylhexanoate, Ethyl octanoate, Heptanal propyleneglycol acetal, Hexanal butane-2,3-diol acetal, Hexyl 2-methylpropanoate, Hexyl butyrate, Isooctyl acetate, Isopentyl isopentanoate, Methyl nonanoate, Octyl acetate, Pentyl 3-methylbutanoate, Propyl heptanoate, p-Menthane-3,8-diol, trans-p-Menthane-1,8-diol	Capric acid
C10H20O7P2	Geranyl-PP	Geranyl-PP
C10H7NO3	1-Nitronaphthalene-5,6-oxide, 1-Nitronaphthalene-7,8-oxide, Kynurenic acid	Kynurenic acid
C11H12N2O2	(\u00b1)-Tryptophan, 3-Hydroxymethylantipyrine, 4-Hydroxyantipyrine, D-Tryptophan, Ethotoin, L-Tryptophan, Nirvanol, S-nirvanol	Tryptophan
C11H15N5O3S	5'-Methylthioadenosine	5'-Methylthioadenosine
C11H19NO8	(3R)-3,4-Dihydroxy-3-(hydroxymethyl)butanenitrile 4-glucoside, 4-Hydroxyproline galactoside, Galactosyl 4-hydroxyproline, N-Acetylmuramate	N-Acetylmuramate
C11H19NO9	N-ACETYLNEURAMINATE, N-Acetyl-a-neuraminic acid, N-Acetylneuraminic acid, O-Acetylneuraminic acid	N-Acetylneuraminic acid
C11H20NO12P	N-Acetylneuraminate 9-phosphate, N-Acetylneuraminic acid 9-phosphate	N-Acetylneuraminic acid 9-phosphate
C11H9NO3	Indolepyruvate	Indolepyruvate
C12H24O2	(R)-Dihydrocitronellol acetate, 2-Heptyl butyrate, Decyl acetate, Dodecanoic acid, Ethyl decanoate, Hexyl hexanoate, Isobutyl octanoate, Isopropyl nonanoate, Nonanal propyleneglycol acetal, Octyl 2-methylpropanoate, Octyl butanoate, Pentyl heptanoate	Dodecanoic acid
C14H20N2O3S	Methionyl-Phenylalanine, Phenylalanyl-Methionine	Methionyl-Phenylalanine
C14H28O2	10-Methyltridecanoic acid, 12-Methyltridecanoic acid, 2,6,10-Trimethylundecanoic acid, 3-Methylbutyl nonanoate, Decyl butanoate, Dodecyl acetate, Ethyl dodecanoate, Heptyl heptanoate, Hexanal octane-1,3-diol acetal, Hexyl octanoate, Isobutyl decanoate, Myristic acid, Nonyl isovalerate, Undecanal propyleneglycol acetal	Myristic acid

C15H17N3O5	2-cyano-N,N-diethyl-3-(4-hydroxy-3-methoxy-5-nitrophenyl)prop-2-enamide, Aspartyl-Tryptophan, Tryptophyl-Aspartate	Tryptophyl-Aspartate
C16H32O2	Butyl dodecanoate, Dodecyl 2-methylpropanoate, Dodecyl butyrate, Ethyl tetradecanoate, Hexyl decanoate, Isopalmitic acid, Octyl octanoate, Palmitic acid, Trimethyltridecanoic acid	Palmitic acid
C20H32O2	7,13-Eperudien-15-oic acid, Arachidonic acid, Cis-8,11,14,17-Eicosatetraenoic acid, Copalic acid, Drostanolone, Junicedral, Mesterolone, Oryzalexin E, Oryzalexin S, Sideridiol, Yucalexin P21, ent-17-Hydroxy-16beta-kauran-19-al	Arachidonic acid
C20H34O5	(5Z,9E,12S,14Z)-8,11,12-Trihydroxyicosa-5,9,14-trienoate, 11,12,15-THETA, 11,12,15-TriHETRE, 11,12,15-trihydroxyeicosatrienoic acid, 11,14,15-THETA, 11-Epi-PGF2a, 11b-PGF2a, 13,14-Dihydro- lipoxin A4, 13,14-Dihydro-15-keto PGF2a, 15-keto-PGF1alpha, 8-Isoprostaglandin E1, 8-Isoprostaglandin F2a, 8-iso-13,14-dihydro-15-keto-PGF2a, 8-isoprostaglandin PGF2b, Prostaglandin D1, Prostaglandin E1, Prostaglandin F2a, Prostaglandin F2b, Prostaglandin H1, Sterebin G, Trioxilin A3, Troxilin B3	8-Isoprostaglandin F2a
C2H5O5P	Acetylphosphate, Phosphonoacetate	Acetylphosphate
C2H5O6P	Phosphoglycolic acid	Phosphoglycolic acid
C2H7NO3S	Taurine	Taurine
C2H8NO3P	Ciliatine	Ciliatine
C2H8NO4P	O-Phosphoethanolamine	O-Phosphoethanolamine
C3H4O4	Hydroxypyruvic acid, Malonic acid, Tartronate semialdehyde	Malonic acid
C3H5O6P	Phosphoenolpyruvic acid	Phosphoenolpyruvic acid
C3H7NO2S	D-Cysteine, L-Cysteine	Cysteine
C3H7NO3	D-Serine, L-Serine, Protein serine	Serine
C3H7NO4S	3-Sulfinato-L-alaninate, 3-Sulfinoalanine	3-Sulfinoalanine
C3H7NO5S	Cysteic acid	Cysteic acid
C3H7O6P	D-Glyceraldehyde 3-phosphate, Dihydroxyacetone phosphate	Glyceraldehyde 3-phosphate
C3H7O7P	(2R)-2-Hydroxy-3-(phosphonatooxy)propanoate, 2-Phospho-D-glyceric acid, 2-Phosphoglyceric acid, 2-phosphonato-D-glycerate(3-), 3-Phosphoglyceric acid	2-Phosphoglyceric acid
C3H8NO6P	DL-O-Phosphoserine, Phosphoserine	Phosphoserine
C3H8O10P2	2,3-Diphosphoglyceric acid, 3-phosphonato-D-glyceroyl Phosphate(4-), Glyceric acid 1,3-biphosphate	Glyceric acid 1,3-biphosphate
C3H9O6P	Beta-Glycerophosphoric acid, Glycerol 3-phosphate	Glycerol 3-phosphate
C4H10NO6P	Iminoerythrose 4-phosphate, O-Phosphohomoserine, O-Phosphothreonine	O-Phosphothreonine
C4H4N2O2	4-Carboxypyrazole, Uracil	Uracil
C4H4O4	Fumaric acid, Maleic acid	Fumaric acid

C4H4O5	Oxalacetic acid	Oxalacetic acid
C4H5N3O	Cytosine	Cytosine
C4H6N2O2	Dihydrouracil, L-3-Cyanoalanine, N-Methylhydantoin	Dihydrouracil
C4H6O3	(S)-Methylmalonic acid semialdehyde, 2-Ketobutyric acid, 2-Methyl-3-oxopropanoic acid, 4-Hydroxycrotonic acid, Acetic anhydride, Acetoacetic acid, Succinic acid semialdehyde	Acetoacetic acid
C4H6O4	3-methoxy-3-oxopropanoic acid, 4-Hydroxy-2-oxobutanoic acid, Erythrono-1,4-lactone, Methylmalonic acid, Succinic acid, Threonolactone, xi-3-Hydroxy-2-oxobutanoic acid	Succinic acid
C4H6O5	D-Malic acid, L-Malic acid, Malic acid, Velcorin	Malic acid
C4H7NO3	Acetylglycine, L-2-Amino-3-oxobutanoic acid, L-Aspartate-semialdehyde	L-Aspartate-semialdehyde
C4H7NO4	1-deoxy-1-(N6-lysino)-D-fructose, D-Aspartic acid, Iminodiacetic acid, L-Aspartic acid	Aspartic acid
C4H8N2O3	D-Asparagine, Glycyl-glycine, L-Asparagine, N-Carbamoylsarcosine, Ureidopropionic acid	Asparagine
C4H8NO7P	L-Aspartyl-4-phosphate	L-Aspartyl-4-phosphate
C4H8O3	(R)-3-Hydroxybutyric acid, (R)-3-Hydroxyisobutyric acid, (S)-3-Hydroxybutyric acid, (S)-3-Hydroxyisobutyric acid, 2-Hydroxybutyric acid, 2-Methyl-3-hydroxypropanoate, 3-Hydroxybutyric acid, 3-hydroxy-2-methylpropanoic acid, 4-Hydroxybutyric acid, Alpha-Hydroxyisobutyric acid, Ethoxyacetic acid	4-Hydroxybutyric acid
C4H8O5	Erythronic acid, L-threonic Acid, Threonic acid	Threonic acid
C4H9NO2	(R)-b-aminoisobutyric acid, (S)-b-aminoisobutyric acid, 2-Aminoisobutyric acid, 3-Aminobutanoic acid, 3-Aminoisobutanoic acid, Butyl nitrite, D-Alpha-aminobutyric acid, D-alpha-Aminobutyric acid, Dimethylglycine, Gamma-Aminobutyric acid, L-Alpha-aminobutyric acid, L-alpha-Aminobutyric acid, N-Ethylglycine, N-Methylalanine, O-Acetylethanolamine, gamma-Aminobutyric acid	gamma-Aminobutyric acid
C4H9NO3	4-Amino-3-hydroxybutyrate, Hydroxyethyl glycine, L-Allothreonine, L-Homoserine, L-Threonine	L-Threonine
C4H9NO4S	Homocysteinesulfinic acid, N-Acetyltaurine	N-Acetyltaurine
C4H9O7P	D-Erythrose 4-phosphate	Erythrose 4-phosphate
C5H10N2O3	Alanylglycine, D-Glutamine, L-Glutamine, Ureidoisobutyric acid	Glutamine
C5H10N2O3S	Cysteinylglycine, Glycyl-Cysteine	Cysteinylglycine
C5H10NO7P	L-Glutamic acid 5-phosphate	L-Glutamic acid 5-phosphate

C5H10O5	2-Deoxypentonic acid, 2-Deoxyribonic acid, 3-hydroxy-2,2-bis(hydroxymethyl)propanoic acid, Aldehydo-D-xylose, Arabinofuranose, Beta-D-ribopyranose, D-Apiose, D-Arabinose, D-Ribose, D-Ribulose, D-Xylose, D-Xylulose, L-Arabinose, L-Ribulose, L-Threo-2-pentulose, beta-Arabinose	Ribose
C5H10O6	2,3,4,5-Tetrahydroxypentanoic acid, Arabinonic acid, L-Xylonate, Ribonic acid	Arabinonic acid
C5H11N3O2	4-Guanidinobutanoic acid	4-Guanidinobutanoic acid
C5H11NO2	5-Aminopentanoic acid, Amyl Nitrite, Betaine, L-Valine, N-Methyl-a-aminoisobutyric acid, Norvaline, Vaporole	Valine
C5H11NO2S	L-Methionine, Penicillamine, Racemethionine	Methionine
C5H11O7P	1-Deoxy-D-xylulose 5-phosphate, 5-Deoxyribose-1-phosphate, Deoxyribose 1-phosphate, Deoxyribose 5-monophosphate, Deoxyribose 5-phosphate	Deoxyribose 5-phosphate
C5H11O8P	Beta-L-arabinose 1-phosphate, D-Arabinose 5-phosphate, D-Ribose 5-phosphate, D-Ribulose 5-phosphate, D-Xylulose 1-phosphate, Ribose 1-phosphate, Xylulose 5-phosphate	Ribulose 5-phosphate
C5H12N2O2	D-Ornithine, Ornithine	Ornithine
C5H12O11P2	Ribose 1,5-bisphosphate	Ribose 1,5-bisphosphate
C5H12O5	D-Arabitol, D-Xylitol, L-2-(Hydroxymethyl)-1,2,3,4-butanetetrol, L-Arabitol, Ribitol	Ribitol
C5H13O14P3	Phosphoribosyl pyrophosphate	Phosphoribosyl pyrophosphate
C5H14NO6P	Glycerylphosphorylethanolamine, sn-glycero-3-Phosphoethanolamine	Glycerylphosphorylethanolamine
C5H4N2O4	Orotic acid	Orotic acid
C5H4N4O	Allopurinol, Hypoxanthine	Hypoxanthine
C5H4N4O2	6,8-Dihydroxypurine, Oxypurinol, Xanthine	Xanthine
C5H4N4O3	Uric acid	Uric acid
C5H5N5	Adenine	Adenine
C5H5N5O	2-Hydroxyadenine, 8-Hydroxyadenine, Guanine	Guanine
C5H6N2O2	1H-Imidazole-1-acetic acid, Imidazoleacetic acid, Thymine	Thymine
C5H6N2O4	4,5-Dihydroorotic acid, L-Dihydroorotic acid	L-Dihydroorotic acid
C5H6O4	2,5-Dioxopentanoate, 2-Hydroxyglutaric acid lactone, 2-Pentendioate, Citraconic acid, Gamma-delta-Dioxovaleric acid, Glutaconic acid, Itaconic acid, Mesaconic acid, Methyl hydrogen fumarate	Itaconic acid
C5H6O5	3-Oxoglutaric acid, 3-methylmalate(2-), Oxoglutaric acid	Oxoglutaric acid
C5H7NO2	1-Pyrroline-2-carboxylic acid, 1-Pyrroline-5-carboxylic acid	1-Pyrroline-5-carboxylic acid
C5H7NO3	(3R,5S)-1-pyrroline-3-hydroxy-5-carboxylic Acid, 1-Pyrroline-4-hydroxy-2-carboxylate, N-Acryloylglycine, Pyroglutamic acid, Pyrrolidonecarboxylic acid, Pyrroline hydroxycarboxylic acid, dimethadione	Pyroglutamic acid
C5H7NO5	4-Hydroxy-L-glutamic acid, A-Ketoglutaric acid oxime, N-Formyl-L-aspartate	N-Formyl-L-aspartate

C5H8N2O2	Dihydrothymine, L-Cyclo(alanylglycyl), Pyroglutamine, Squamolone	Dihydrothymine
C5H8O3	(2E)-4-hydroxy-3-methylbut-2-enoic acid, (2Z)-2-(hydroxymethyl)but-2-enoic acid, 2,3-dimethyloxirane-2-carboxylic acid, 2-(hydroxymethyl)but-2-enoic acid, 2-Methylacetoacetic acid, 2-Oxovaleric acid, 3-keto-2-Methylbutyrate, 4-hydroxy-2-methylbut-2-enoic acid, 4-hydroxy-3-methylbut-2-enoic acid, Acetoxyacetone, Alpha-ketoisovaleric acid, Ethyl pyruvate, Glutarate semialdehyde, Levulinic acid, Methylacetoacetic acid, alpha-Ketoisovaleric acid, dimethyloxirane-2-carboxylic acid	Glutarate semialdehyde
C5H8O4	(S)-2-Acetolactate, (S)-Methylbutanethioic acid, 2-Acetolactate, 2-C-Methyl-1,4-erythrono-D-lactone, 2-Deoxy-L-ribono-1,4-lactone, 2-Hydroxy-4-oxopentanoic acid, Dimethylmalonic acid, Ethylmalonic acid, Glutaric acid, Methylsuccinic acid, Monoethyl malonic acid	Glutaric acid
C5H8O5	2-Hydroxyglutarate, 3-Hydroxyglutaric acid, Citramalic acid, D-2-Hydroxyglutaric acid, D-Xylono-1,5-lactone, L-2-Hydroxyglutaric acid, Ribonolactone	2-Hydroxyglutaric acid
C5H9NO2	4-Amino-2-methylenebutanoic acid, Acetamidopropanal, D-Proline, L-Proline, Pterolactam	Proline
C5H9NO3	3-Hydroxy-L-proline, 4-Hydroxy-2-pyrrolidinecarboxylic acid, 4-Hydroxy-L-proline, 4-Hydroxyproline, 5-Amino-2-oxopentanoic acid, 5-Aminolevulinic acid, L-Glutamic gamma-semialdehyde, N-Acetyl-L-alanine, N-Acetyl-beta-alanine, Propionylglycine, Trans-3-hydroxy-L-proline, cis-4-Hydroxy-D-proline, cis-4-Hydroxyproline	L-Glutamic gamma-semialdehyde
C5H9NO4	3-(Carboxymethylamino)propanoic acid, D-Glutamic acid, DL-Glutamate, L-4-Hydroxyglutamate semialdehyde, L-Glutamic acid, N-Acetylserine, N-Methyl-D-aspartic acid, N-lactoyl-Glycine, O-Acetylserine	Glutamic acid
C6H10N2O4	Formiminoglutamic acid, N-Acetylasparagine	Formiminoglutamic acid
C6H10O3	(4S,6S)-3,4,5,6-Tetrahydro-4-hydroxy-6-methyl-2H-pyran-2-one, 2-Ketohexanoic acid, 2-Methyl-3-ketovaleric acid, 3-Methyl-2-oxovaleric acid, 3-Oxohexanoic acid, 4-Acetylbutyrate, 5-Ethoxy-4,5-dihydro-2(3H)furanone, Acetoin acetate, Adipate semialdehyde, Ethyl acetoacetate, Ketoleucine, Methyl levulinate, Mevalonolactone, Pantolactone, Sherry lactone	2-Methyl-3-ketovaleric acid
C6H10O4	(S)-2-Aceto-2-hydroxybutanoic acid, 2,2-Dimethylsuccinic acid, 2-Methylglutaric acid, 4-Ethoxy-4-oxobutanoic acid, Adipic acid, Dimethyl succinate, Methylglutaric acid, Monomethyl glutaric acid, Solerol	2-Aceto-2-hydroxybutanoic acid

C6H10O7	2-Keto-L-gluconate, 3,4,5,6-tetrahydroxyoxane-2-carboxylic acid, 3-Dehydro-L-gulonate, 5-Keto-D-gluconate, D-Glucuronic acid, Galacturonic acid, Iduronic acid, L-Altruronic acid, Pectic acid, Pectin	Iduronic acid
C6H10O8	D-Glucaric acid, Galactaric acid, Glucaric acid	Glucaric acid
C6H11NO2	(2E)-Decenoyl-ACP, 1-Piperidine carboxylic acid, 2-Pyrrolidineacetic acid, 3-Acetamidobutanal, D-Pipecolic acid, D-pipecolate, L-Pipecolic acid, L-trans-4-Methyl-2-pyrrolidinecarboxylic acid, N-Methyl proline, N4-Acetylaminobutanal, Pipecolic acid, Vigabatrin	4-Methylproline
C6H11NO3	(S)-2-amino-6-oxohexanoate, (S)-5-Amino-3-oxohexanoate, 2-Keto-6-aminocaproate, 4-Acetamidobutanoic acid, Allysine, Isobutyrylglycine, L-cis-4-(Hydroxymethyl)-2-pyrrolidinecarboxylic acid, L-trans-5-Hydroxy-2-piperidinecarboxylic acid, Methyl aminolevulinate, N-(2-Carboxymethyl)-morpholine, N-Butyrylglycine, N-Propionylalanine	4-Acetamidobutanoic acid
C6H11NO4	(\u00b1)-2,2'-Iminobispropanoic acid, Acetylhomoserine, Aminoadipic acid, Glutamate, gamma-methyl ester, N-Acetylthreonine, N-methyl-L-glutamic Acid, hydroxybutyrylglycine	Aminoadipic acid
C6H11O9P	2-Keto-3-deoxy-6-phosphogluconic acid, 6-Phosphonoglucono-D-lactone	6-Phosphonoglucono-D-lactone
C6H12N2O3	Alanyl-Alanine, D-Alanyl-D-alanine	Alanyl-Alanine
C6H12O4	(2-Methoxyethoxy)propanoic acid, (R) 2,3-Dihydroxy-3-methylvalerate, (R)-mevalonate, Glycerol 1-propanoate, Mevalonic acid	2,3-Dihydroxy-3-methylvalerate
C6H12O5	1,5-Anhydrosorbitol, 2-Deoxygalactopyranose, 2-Deoxyglucose, 2-O-Methyl-D-xylose, 3-Deoxyfructose, 6-methyloxane-2,3,4,5-tetrol, Beta-D-Fucose, D-Fucose, L-Fucose, L-Fucose-1P, L-Fuculose, L-Rhamnulose, Rhamnose, beta-L-fucose	Fucose
C6H12O6	2,5-bis(hydroxymethyl)oxolane-2,3,4-triol, 3(S)-hydroxy-all-cis-8,11,14,17-eicosatetraenoyl-CoA, 3-Deoxyarabinohexonic acid, Allose, Alpha-D-Glucopyranoside, Alpha-D-Glucose, Beta-D-Galactose, Beta-D-Glucose, D-Fructose, D-Galactose, D-Glucopyranoside, D-Glucose, D-Mannose, D-Tagatose, D-chiro-inositol, Dihydroxyacetone (dimer), Fructose-1P, Glycoprotein-phospho-D-mannose, L-Galactose, L-Gulose, L-Sorbose, Levoinositol, allo-inositol, cis-inositol, epi-Inositol, muco-Inositol, myo-Inositol, neo-inositol, scyllo-Inositol	Glucose
C6H12O7	Galactonic acid, Gluconic acid, Gulonic acid	Gluconic acid

C6H13NO2	(\u00b1)-erythro-Isoleucine, 3,3,5-triiodo-L-thyronine-beta-D-glucuronoside, 3-Aminocaproic acid, 6-Deoxyfagomine, Aminocaproic acid, Beta-Leucine, D-Leucine, L-Alloisoleucine, L-Isoleucine, L-Leucine, L-Norleucine, N-(2-Hydroxyethyl)-morpholine, N-methylvaline	Leucine
C6H13O10P	2-Carboxyarabinitol 5-phosphate, 6-Phosphogluconic acid	6-Phosphogluconic acid
C6H13O7P	Mevalonic acid-5P	Mevalonic acid-5P
C6H13O8P	Fucose 1-phosphate	Fucose 1-phosphate
C6H13O9P	1D-myo-Inositol 3-phosphate, Beta-D-Fructose 2-phosphate, Beta-D-Fructose 6-phosphate, Beta-D-Glucose 6-phosphate, D-Mannose 1-phosphate, D-Myo-inositol 4-phosphate, D-Tagatose 1-phosphate, D-Tagatose 6-phosphate, D-fructose 1-phosphate, D-galactopyranose 1-phosphate, Dolichyl phosphate D-mannose, Fructose 1-phosphate, Fructose 6-phosphate, Galactose 1-phosphate, Glucose 1-phosphate, Glucose 6-phosphate, Inositol phosphate, Mannose 6-phosphate, Myo-inositol 1-phosphate, Sorbose 1-phosphate	Glucose 6-phosphate
C6H14N2O2	D-Lysine, L-Lysine	Lysine
C6H14N4O2	D-Arginine, L-Arginine	Arginine
C6H14NO8P	Aminofructose 6-phosphate, Glucosamine 6-phosphate, Glucosamine-1P	Glucosamine-1P
C6H14O12P2	1-phosphatidyl-1D-myo-inositol-3,4-bisphosphate, 1D-Myo-inositol 1,3-bisphosphate, 1D-Myo-inositol 1,4-bisphosphate, 1D-Myo-inositol 3,4-bisphosphate, Alpha-D-Glucose 1,6-bisphosphate, D-Fructose 2,6-bisphosphate, D-Mannose 1,6-bisphosphate, D-Tagatose 1,6-bisphosphate, Fructose 1,6-bisphosphate, beta-D-Fructose 1,6-bisphosphate	Fructose 1,6-bisphosphate
C6H14O6	Galactitol, L-Iditol, Mannitol, Sorbitol	L-Iditol
C6H15O9P	Sorbitol-6-phosphate	Sorbitol-6-phosphate
C6H6N2O2	(E)-Urocanic acid, 2-Aminonicotinic acid, 5-Oxo-2(5H)-isoxazolepropanenitrile, Nicotinamide N-oxide, Trans-urocanate, Urocanic acid	Urocanic acid
C6H6O4	2,3-Methylenesuccinic acid, 5-Hydroxymaltol, Kojic acid, Sumiki's acid, benzene-1,2,3,4-tetrol, benzene-1,2,3,5-tetrol, cis,cis-Muconic acid, trans-trans-Muconic acid	Sumiki's acid
C6H6O6	Dehydroascorbic acid, cis-Aconitic acid, trans-Aconitic acid	Dehydroascorbic acid
C6H8N2O3	4-Imidazolone-5-propionic acid, 5-Hydroxymethyl-4-methyluracil, Imidazolelactic acid	4-Imidazolone-5-propionic acid
C6H8O5	2-Methyl-4-oxopentanedioic acid, 3-Methyl-3-hydroxypentanedioate, 3-Oxoadipic acid, Oxoadipic acid	Oxoadipic acid

C6H8O7	(1R,2R)-Isocitric acid, 2,3-Diketo-L-gulonate, Citric acid, D-Glucaro-1,4-lactone, D-threo-Isocitric acid, Diketogulonic acid, Isocitric acid	Citric acid
C6H9N3O2	L-2-Amino-3-(1-pyrazolyl)propanoic acid, L-Histidine	Histidine
C6H9NO5	2-Amino-3-oxoadipate, D-N-(Carboxyacetyl)alanine, N-Acetyl-L-aspartic acid, N-Formyl-L-glutamic acid	N-Formyl-L-glutamic acid
C7H10O5	2,6-dimethyl-trans-2-heptenoyl-CoA, 2-Isopropyl-3-oxosuccinate, 3,4,5-trihydroxycyclohex-1-ene-1-carboxylic acid, Dimethyl 2-oxoglutarate, Shikimic acid	Dimethyl 2-oxoglutarate
C7H10O6	2-Hydroxy-2-(2-oxopropyl)butanedioic acid, 2-O-Methylascorbic acid, 3-Dehydroquinate	3-Dehydroquinate
C7H10O7	2-Methylcitric acid, 3-(Carboxymethyl)-3-hydroxypentanedioic acid, Homocitric acid, Methylisocitric acid	Methylisocitric acid
C7H11NO5	Glutarylglycine, N-Acetylglutamic acid	Glutarylglycine
C7H12N2O3	Glycylproline, Prolylglycine	Glycylproline
C7H12O4	2,2-Dimethylglutaric acid, 2-Ethylglutaric acid, 2-Methyladipic acid, 3,3-Dimethylglutaric acid, 3-Methyladipic acid, Diethyl malonate, Ethyl methyl_succinate, Mono-methyl-adipate, Pimelic acid, Propyleneglycol diacetate	Pimelic acid
C7H12O5	(\u00b1)-Glycerol 1,2-diacetate, 2,3-Dimethyl-3-hydroxyglutaric acid, 2-Isopropylmalic acid, 3-Hydroxy-2-methylglutarate, 3-Isopropylmalate	3-Isopropylmalate
C7H14N2O4S	Allocystathionine, Cysteinyl-Threonine, L-Cystathionine, Threoninyl-Cysteine	Allocystathionine
C7H15O10P	D-Sedoheptulose 7-phosphate, Sedoheptulose 1-phosphate	Sedoheptulose 7-phosphate
C7H6O4	2,4,6-trihydroxybenzaldehyde, 2,4-Dihydroxybenzoic acid, 2,6-Dihydroxybenzoic acid, 2-Pyrocatechuic acid, 3,5-Dihydroxybenzoic acid, Gentisic acid, Patulin, Protocatechuic acid	2-Pyrocatechuic acid
C7H8O	Anisole, Benzyl alcohol, m-Cresol, o-Cresol, p-Cresol	p-Cresol
C7H8O2	1-(2-Furanyl)-1-propanone, 1-(2-Furanyl)-2-propanone, 2-Acetyl-3-methylfuran, 2-Acetyl-5-methylfuran, 2-Hydroxybenzyl alcohol, 3-Hydroxybenzyl alcohol, 3-methoxyphenol, 4,6-Heptadiyne-1,3-diol, 4-Hydroxybenzyl alcohol, 4-Methylcatechol, Guaiacol, Mequinol	4-Methylcatechol
C8H10N4O4	5-Acetylamino-6-formylamino-3-methyluracil	5-Acetylamino-6-formylamino-3-methyluracil
C8H10O4	2,3-dimethoxybenzene-1,4-diol, 2,6-dimethoxybenzene-1,4-diol, 3,4-Dihydroxyphenylglycol, 3,4-Methyleneadipic acid, 3,4-dimethoxybenzene-1,2-diol, 3,5-dimethoxybenzene-1,2-diol, 4,5-dimethoxybenzene-1,3-diol, Furaneol acetate, Herierin III, Herierin IV	3,4-Dihydroxyphenylglycol
C8H14N2O5S	Glutamylcysteine, gamma-Glutamylcysteine	Glutamylcysteine

C8H14O2S2	(R)-lipoic acid, (S)-lipoic acid	Lipoic acid
C8H15N3O4	Alanyl-Gamma-glutamate, Alanyl-Glutamine, Glutaminylalanine, N-a-Acetylcitrulline	N-a-Acetylcitrulline
C8H16NO9P	N-Acetyl-D-Glucosamine 6-Phosphate, N-Acetyl-D-galactosamine 1-phosphate, N-Acetyl-D-mannosamine 6-phosphate, N-Acetyl-glucosamine 1-phosphate, N-Acetylglucosamine 6-phosphate, N-acetyl-alpha-D-galactosamine 1-phosphate	N-Acetylglucosamine 6-phosphate
C8H16O2	(3R,5Z)-5-Octene-1,3-diol, (\u00b1)-5-Hydroxy-4-octanone, 1,1-Dimethoxy-trans-2-hexene, 1-Hydroxy-3-octanone, 2-Ethylbutyl acetate, 2-Ethylhexanoic acid, 2-Methylheptanoic acid, 2-Methylpropyl butanoate, 2-ethylhexanoate (isobar with 2-propylpentanoate), 3-(Hydroxymethyl)-2-heptanone, 3-Hydroxy-2-octanone, 3-Methylbutyl propanoate, 6-Methylheptanoic acid, Butyl butyrate, Butyl isobutyrate, Caprylic acid, Ethyl (\u00b1)-2-methylpentanoate, Ethyl (\u00b1)-3-methylpentanoate, Ethyl 2-ethylbutanoate, Ethyl 4-methylpentanoate, Ethyl hexanoate, Heptyl formate, Hexyl acetate, Isobutyl isobutyrate, Isopropyl 2-methylbutanoate, Isopropyl 3-methylbutanoate, Methyl 5-methylhexanoate, Methyl heptanoate, Pentyl propanoate, Propyl 3-methylbutanoate, Propyl pentanoate, Tetrahydro-2,5-dimethyl-2H-pyranmethanol, Valeraldehyde propyleneglycol acetal, Valproic acid, cis- and trans-2-Isobutyl-4-methyl-1,3-dioxolane	Ethyl hexanoate
C8H8O2	2'-Hydroxyacetophenone, 2-Hydroxy-4-methylbenzaldehyde, 2-Methoxybenzaldehyde, 2-Methylbenzoic acid, 3-(3-Furanyl)-2-methyl-2-propenal, 3-(5-Methyl-2-furyl)prop-2-enal, 3-Methoxybenzaldehyde, 4-(2-Furanyl)-3-buten-2-one, 4-Hydroxyphenylacetaldehyde, 4-Methoxybenzaldehyde, 4-Methylbenzoic acid, 4-ethenylbenzene-1,2-diol, 4-ethenylbenzene-1,3-diol, 5-ethenylbenzene-1,3-diol, Benzyl formate, M-toluic Acid, Methyl benzoate, Phenyl acetate, Phenylacetic acid, alpha-Methyl-2-furanacrolein	4-Hydroxyphenylacetaldehyde

C8H8O3	(R)-mandelic Acid, 1-(2-Furanyl)-1,3-butanedione, 1-(5-Methyl-2-furanyl)-1,2-propanedione, 2',3'-Dihydroxyacetophenone, 2',4'-Dihydroxyacetophenone, 2',5'-Dihydroxyacetophenone, 2',6'-Dihydroxyacetophenone, 2,4'-Dihydroxyacetophenone, 2-(Hydroxymethyl)benzoic acid, 2-Methoxybenzoic acid, 2-Propenyl 2-furancarboxylate, 2-hydroxy-2-phenylacetic acid, 3',4'-Dihydroxyacetophenone, 3',5'-Dihydroxyacetophenone, 3,4-Dihydroxyphenylacetaldehyde, 3-Cresotinic acid, 3-Hydroxyphenylacetic acid, 3-Methoxybenzoic acid, 4-Hydroxy-3-methylbenzoic acid, 4-Hydroxyphenyl acetate, 4-[(E)-2-hydroxyethenyl]benzene-1,2-diol, 5-ethenylbenzene-1,2,3-triol, Ethyl 2-furanyl diketone, Mandelic acid, Methyl 2-hydroxybenzoate, Methyl furfuracrylate, Methylparaben, Ortho-Hydroxyphenylacetic acid, Phenoxyacetic acid, Vanillin, p-Anisic acid, p-Hydroxyphenylacetic acid	3,4-Dihydroxyphenylacetaldehyde
C8H8O4	2',4',6'-Trihydroxyacetophenone, 2,6-Dimethoxy-1,4-benzoquinone, 2-hydroxy-4-methoxybenzoic acid, 3, 5-Dihydroxyphenylacetic acid, 3,4-Dihydroxybenzeneacetic acid, 3,4-Dihydroxymandelaldehyde, 3-Acetyl-4-hydroxy-6-methyl-2H-pyran-2-one, 3-Hydroxymandelic acid, 3-Methoxysalicylic acid, 3-hydroxy-2-methoxybenzoic acid, 3-hydroxy-5-methoxybenzoic acid, 5-Methoxysalicylic acid, Homogentisic acid, Isovanillic acid, Thermophillin, Vanillic acid, p-Hydroxymandelic acid	3,4-Dihydroxybenzeneacetic acid
C8H9NO3	3-Methoxyanthranilate, 3alpha,4,5,7alpha-Tetrahydro-5-hydroxy-1H-isoindole-1,3(2H)-dione, 3alpha,4,7,7alpha-Tetrahydro-4-hydroxy-1H-isoindole-1,3(2H)-dione, Isopyridoxal, Pyridoxal	Pyridoxal
C8H9NO4	4-Pyridoxic acid	4-Pyridoxic acid

C9H10O3	2-(2-hydroxyphenyl)propanoic acid, 2-(3-hydroxyprop-1-en-1-yl)benzene-1,4-diol, 2-[3-(hydroxymethyl)oxiran-2-yl]phenol, 2-hydroxy-2-phenylpropanoic acid, 2-hydroxy-3-(2-hydroxyphenyl)propanal, 3,4-Dihydroxyphenylacetone, 3,4-Dimethoxybenzaldehyde, 3,5-Dimethoxybenzaldehyde, 3-(2,3-dihydroxyphenyl)propanal, 3-(2,5-dihydroxyphenyl)propanal, 3-(2-Hydroxyphenyl)propanoic acid, 3-(3-Hydroxyphenyl)propanoic acid, 3-(3-hydroxyprop-1-en-1-yl)benzene-1,2-diol, 3-Hydroxy-1-(4-hydroxyphenyl)-1-propanone, 3-Methoxyphenylacetic acid, 3-Phenoxypropionic acid, 3-hydroxy-3-(2-hydroxyphenyl)propanal, 3-hydroxy-3-phenylpropanoic acid, 4-Hydroxyphenyl-2-propionic acid, 4-Methoxybenzyl formate, 4-Methoxyphenylacetic acid, 4-[(1E)-3-hydroxyprop-1-en-1-yl]benzene-1,2-diol, 4-[(E)-2-hydroxyethenyl]-2-methoxyphenol, 4-[3-(hydroxymethyl)oxiran-2-yl]phenol, 4-ethenyl-2-methoxybenzene-1,3-diol, 4-ethenyl-6-methoxybenzene-1,3-diol, 5-ethenyl-3-methoxybenzene-1,2-diol, D-Phenyllactic acid, Desaminotyrosine, Ethyl 2-furanacrylate, Ethyl salicylate, Ethyl vanillin, Ethylparaben, Guaicyl acetate, Homovanillin, Ipomeanine, L-3-Phenyllactic acid, Methyl 2-methoxybenzoate, Methyl 4-methoxybenzoate, Phenyllactic acid, Tropate	Homovanillin
C9H11N2O8P	Uridine 2',3'-cyclic phosphate	Uridine 2',3'-cyclic phosphate
C9H11NO2	3-Pyridinebutanoic acid, 4-Hydroxy-1-(3-pyridinyl)-1-butanone, 5-(3-Pyridyl)-2-hydroxytetrahydrofuran, Benzocaine, Benzyl glycinate, Ethyl 2-aminobenzoate, Gentiatibetine, L-Phenylalanine, Methyl N-methylanthranilate, Norsalsolinol	Phenylalanine
C9H11NO3	4,6,7-Trihydroxy-1,2,3,4-tetrahydroisoquinoline, 4-Hydroxy-4-(3-pyridyl)-butanoic acid, Beta-Tyrosine, L-Threo-3-Phenylserine, L-Tyrosine, Meta-Tyrosine, o-Tyrosine	Tyrosine
C9H11NO4	2-Hydroxy-3-(3,4-dihydroxyphenyl)propanamide, DL-Dopa, L-Dopa, N-Hydroxy-L-tyrosine	Dopa
C9H12N2O6	Pseudouridine, Uridine	Uridine

C9H12O4	(\u00b1)-threo-1-(4-Hydroxyphenyl)-1,2,3-propanetriol, 1-(3-Hydroxy-4-methoxyphenyl)-1,2-ethanediol, 2-(hydroxymethyl)-3,5-dimethoxyphenol, 2-(hydroxymethyl)-5-methoxy-4-methylbenzene-1,3-diol, 3,4-Methylenepimelic acid, 4-(hydroxymethyl)-5-methoxy-2-methylbenzene-1,3-diol, 4-Formyl-3-(formylmethyl)-4-hexenoic acid, 4-ethyl-6-methoxybenzene-1,2,3-triol, 5-ethyl-3-methoxybenzene-1,2,4-triol, 6-methoxy-3,5-dimethylbenzene-1,2,4-triol, Genipic acid, Vanylglycol	Vanylglycol
C9H13N2O9P	3'-UMP, Pseudouridine 5'-phosphate, Uridine 2'-phosphate, Uridine 5'-monophosphate	Uridine 5'-monophosphate
C9H13N5O3	1-hydroxy-2-Oxopropyl tetrahydropterin, 4a-Carbinolamine tetrahydrobiopterin, 6-Lactoyltetrahydropterin, Dihydrobiopterin, O2'-4a-cyclic-tetrahydrobiopterin	Dihydrobiopterin
C9H14N2O11P2	dUDP	dUDP
C9H14N3O8P	Cytidine 2'-phosphate, Cytidine monophosphate	Cytidine monophosphate
C9H14N4O3	(6R)-6-(L-Erythro-1,2-Dihydroxypropyl)-5,6,7,8-tetrahydro-4a-hydroxypterin, Alanyl-Histidine, Carnosine, Histidinyl-Alanine	Carnosine
C9H15N4O8P	AICAR	AICAR
C9H16N2O5	4-(Glutamylamino) butanoate, Aspartyl-Valine, Hydroxyprolyl-Threonine, L-N-(3-Carboxypropyl)glutamine, N2-Succinyl-L-ornithine, Threoninyl-Hydroxyproline, Valyl-Aspartate	4-(Glutamylamino) butanoate
C9H17NO5	(R)-pantothenic Acid, Pantothenic acid	Pantothenic acid
C9H19O11P	1-(sn-Glycero-3-phospho)-1D-myo-inositol	1-(sn-Glycero-3-phospho)-1D-myo-inositol
C9H7NO2	2-Indolecarboxylic acid, 3-Formyl-6-hydroxyindole, 4,6-Dihydroxyquinoline, Indole-3-carboxylic acid, Quinoline-4,8-diol	4,6-Dihydroxyquinoline
C9H8O3	(2E)-3-(3,4-dihydroxyphenyl)prop-2-enal, 2-Hydroxycinnamic acid, 3-(2,3-dihydroxyphenyl)prop-2-enal, 3-(2,5-dihydroxyphenyl)prop-2-enal, 3-(2-hydroxyphenyl)oxirane-2-carbaldehyde, 3-(2-hydroxyphenyl)prop-2-enoic acid, 3-(3-hydroxyphenyl)prop-2-enoic acid, 3-(4-hydroxyphenyl)oxirane-2-carbaldehyde, 3-(4-hydroxyphenyl)prop-2-enoic acid, 3-phenyloxirane-2-carboxylic acid, 4-Hydroxycinnamic acid, 4-methoxy-1-benzofuran-6-ol, Coumaric acid, Enol-phenylpyruvate, Methyl Phenylglyoxalate, Phenylpyruvic acid, cis-p-Coumaric acid, m-Coumaric acid	Phenylpyruvic acid
CH4NO5P	Carbamoyl phosphate	Carbamoyl phosphate
H4O7P2	Pyrophosphate	Pyrophosphate
H5O10P3	PPPi, Triphosphate	Triphosphate